ABSTRACT

HEACOCK, BENJAMIN JAMES. Neutron Dynamical Diffraction: Interferometer Improvement and Precision Structure Factor Measurements. (Under the direction of Albert Young).

Neutron wave diffraction from periodic potentials, termed dynamical diffraction, may be classified into two categories: (1) diffraction from optical potentials, where the spatial period of the potential is much larger than the neutron wavelength, and (2) diffraction from crystalline potentials, where the neutron wavelength and the period of the potential are of similar size. This dissertation describes neutron optical experiments at both length scales.

Micromachined gratings used by neutron grating interferometers fall into the first category. The non-ideal shape of phase-gratings is probed with neutrons using a double crystal diffractometer. It is found that grating alignment to the beam strongly affects the diffracted wave amplitudes which impacts the interference fringe visibility of phase-grating neutron interferometers. Additionally, a phase-recovered computed tomography algorithm for double crystal diffractometers is developed. The reconstructed images of the gratings taken from passing neutron scattering data through the algorithm matches the grating shape measured with a scanning electron microscope.

Diffraction from crystalline potentials enables single crystal neutron interferometry, where unlike phase-grating interferometry, complete path separation on the order of centimeters is achieved. A series of experiments is described where strain in single crystal neutron interferometers is characterized by studying the neutron interference patterns associated with double and triple crystal rocking curves. The measured angular misalignments of the diffracting components that make up the interferometer are found to be on the order of nanoradians, which is large enough to cause systematic effects in some types of experiments. Specifically, a long-standing discrepancy between the acceleration due to Earth's gravity measured using single crystal neutron interferometry and other quantum interference methods is shown to be approximately the same size as would be expected from the typical nanoradian Bragg plane misalignments measured in a few single crystal interferometers. Fortunately, it is shown that these misalignments may be lessened by annealing the entire interferometer at $800°$C.

Dynamical diffraction in a crystal slab exhibits pendellösung interference, where the diffracted intensity oscillates as a function of neutron wavelength, crystal thickness, and the neutron-lattice potential. The phase of pendellösung oscillations is used to perform precision measurements of the (111), (220), and (400) neutron structure factors in silicon. By comparing the measured structure factors to their predicted momentum transfer dependence, the silicon mean square thermal displacement and neutron charge radius are measured. Additionally, using prior measurements of the silicon mean square displacement and neutron charge radius, these data provide sensitive limits to extensions of the standard model of particle physics for force mediators that couple to mass. The measured neutron mean square charge radius is -0.1088 ± 0.0093 fm^2, which is consistent the Particle Data

Group suggested value of -0.1161 ± 0.0022 fm^2. Assuming the Particle Data Group's recommended value and uncertainty for the neutron charge radius, the measured Debye-Waller B parameter is $0.477\,11 \pm 0.000\,70$ Å^2 at 295.5 K. Previous experimental limits on the strength of a beyond the standard model force mediator with mass range 10 eV to 10 keV are improved by nearly an order of magnitude over most of the mass range and almost two orders of magnitude for a 25 eV force mediator. Extending the experiment to higher order Bragg reflections and/or other crystal species will be sensitive to anharmonic contributions to lattice dynamics and further improve sensitivity to the neutron charge radius and beyond the standard model forces.

Neutron Dynamical Diffraction: Interferometer Improvement and Precision Structure Factor
Measurements

by
Benjamin James Heacock

A dissertation submitted to the Graduate Faculty of
North Carolina State University
in partial fulfillment of the
requirements for the Degree of
Doctor of Philosophy

Physics

Raleigh, North Carolina

2019

APPROVED BY:

Michael Huber
External Member

Paul Huffman

Chueng Ji

Jacob Jones

Albert Young
Chair of Advisory Committee

DEDICATION

To my wife, Kate.

BIOGRAPHY

I was born in Lansing, Michigan to Nancy Darr and James Heacock. My brother Jon, sister Sarah, and I spent our early childhoods in San Bernardino, CA, before my family moved across the country to Franklin, TN. I later went to college at Belmont University in Nashville, TN. After graduating from college, I moved to Denver, CO to be with and marry Kate Gregory. Since getting married, Kate, our dog Bonnie, and I have never stayed put long. We moved to Raleigh, NC for two years so I could start my PhD program at NCSU. After finishing my course work, we moved to Rockville, MD so I could work on research full time at the NIST Center for Neutron Research, in Gaithersburg, MD. A year later, Kate had landed her dream job as a helicopter transport nurse, and we found ourselves living on a twenty seven foot sailboat in Baltimore's inner harbor. Less than a year later we upgraded to a thirty four footer. In October 2017, we sailed our home to Annapolis, MD for a change of pace. We are excited to be "land lubbers" again and enjoy the comforts of single-use kitchen appliances.

ACKNOWLEDGEMENTS

It takes a village to raise a physicist. I cannot possibly thank everyone who has helped me along the way. My advisor, Albert Young, has an energy and talent for science that I have very thoroughly enjoyed during my time as a graduate student. When science got tough, he was always there to keep me motivated and get me on track. Two other mentors stand out as critical to my development as a physicist: Michael Huber taught me how to function in a laboratory, was always there to help me when I got stuck, and provided rapid and helpful feedback on my writing. Dmitry Pushin is a joy to collaborate with and guided me in my work on Chapter 2 of this dissertation.

I would like to thank the NCSU physics department and the Triangle Universities Nuclear Laboratory for financial support. Special thanks to Rhonda Bennett, Chastity Buehring, and Leslie Cochran for their patience and administrative support which allowed me to focus on physics. I am grateful to my committee members: Michael Huber, Paul Huffman, Chueng Ji, and Jacob Jones for their time and insights. Many thanks to Srikanth Patala for filling in at the eleventh hour.

I am deeply grateful to all of my colleagues at the NCNR. Whenever I needed help, there was always someone to talk to. Special thanks to Rob Shankle and Eli Baltic for their technical support, Mikala Shremshock for teaching me how to work with acid safely, Michelle Jamer for doing x-ray diffraction measurements, Juscelino Leao for help with annealing, Martha Neviaser for her administrative support, and Shannon Hoogerheide and the rest of the fundamental physics group for allowing me to rely on their expertise. A very special thank you to Robert Haun who is a good friend and was always willing to go above and beyond to keep my experiments running.

Thank you to Michael Snow for getting Albert and I involved with interferometry in the first place. I am grateful for my collaborators at the University of Waterloo, especially Dusan Sarenac, Ivar Taminiau, Connor Kapahi, and David Cory. Thank you to Sam Werner for fathering the field of neutron interferometry and warning me about parasitic reflections in the pendellösung measurements.

I would like to thank Hirohiko Shimizu for bringing me to Japan for a month, and Tomoki Yamamoto, Anju Okada, Masaaki Kitaguchi, and Katsuya Hirota for welcoming me there. Most of my dissertation would have been impossible if not for the talents of Yutaka Yamagata, Takuya Hosobata and the rest of the RIKEN Center for Advanced Photonics team. Thank you to Tomoki Yamamoto, Masaya Nakaji, and Takuhiro Fujiie for travelling half way across the world to visit the NCNR and work on experiments with me.

Special thanks to Muhammad Arif for his scientific inspiration and insights, building up the NCNR interferometry program, being a wonderful mentor to my mentors, and believing in me. I am so very grateful to have known him.

Finally, thank you to my family for always encouraging and supporting me. I wholeheartedly agree: "The best dissertation is a done dissertation." I am especially grateful to my wife, Kate. I cannot thank her enough for her support, patience, and sacrifice.

TABLE OF CONTENTS

LIST OF TABLES

LIST OF FIGURES

1.1 The Neutron and Its Interactions

The neutron is a composite particle made up of one up and two down quarks. While electrically neutral, it carries a magnetic moment and has a radial charge distribution. The neutron scatters from nuclei primarily via the strong force. The lifetime of the free neutron is approximately fifteen minutes, after which time it decays into a proton, an electron and an electron antineutrino. Correlation coefficients between the decay particles and the lifetime of the neutron itself probe the electroweak interaction [Nic09]. Finally, the neutron interacts with Earth's gravitational field, which is measurable with interference measurements [Wer75] and bound gravitational states with ultracold neutrons [Nes02]. Thus, the neutron's interactions with all of the four fundamental forces, (1) electricity and magnetism, (2) the strong force, (3) the weak interaction, and (4) gravity, are experimentally relevant.

The utility of neutrons as a scattering probe for a wide variety of researchers has lead to a number of user facilities around the world of both reactor and accelerator types. Reactor sources function by drawing on the large fluence of neutrons in a nuclear fission reactor, while accelerator sources focus a high energy proton beam onto a spallation target. The proton beams at spallation sources are typically pulsed, permitting the moderated neutron time-of-flight (TOF) to be used for energy discrimination without loss of intensity, and improving signal to background ratios for many measurements. Reactor sources tend to be more intense than spallation sources; however, energy discrimination from a reactor source must be performed by either chopping the beam or using Bragg scattering from monochromator crystals.

As de Broglie particles, non-relativistic neutrons having kinetic energy

$$E = \frac{p^2}{2m} \tag{1.1}$$

with momentum p and mass m, exhibit a wavelength given by

$$\lambda = \frac{h}{p}, \tag{1.2}$$

where h is Plank's constant. Alternatively, a neutron with wave vector $\vec{k}$ has momentum

$$\vec{p} = \hbar\vec{k}. \tag{1.3}$$

This fundamental relation causes factors of $\hbar$ to be pervasive in calculations dealing with neutron optics. For simplicity, unless $\hbar$ appears explicitly in an expression, this dissertation uses natural units where $\hbar = c = 1$, with c the speed of light. It should be noted that even when using natural units, dimensional analysis is both possible and important. Specifically, quantities must have units of energy (equivalent to inverse length) to some power (including zero and negative powers). As such, it is useful to keep the mass

$$m_n = 939.6 \text{ MeV} \tag{1.4}$$

and reduced Compton wavelength

$$\lambdabar_n = \frac{1}{m_n} = 0.2100 \text{ fm} \tag{1.5}$$

of the neutron at hand.

All of the experiments presented in this dissertation use cold neutrons with kinetic energies on the order of 10 meV, which corresponds to velocities of about 1000 m/s and wavelengths of a few ångströms. Because cold neutrons have wavelengths similar to x-rays, some imaging and scattering techniques work for both x-rays and neutrons. This includes radiography, computed tomography, phase-contrast imaging, small-angle scattering, reflectometry, Bonse-Hart cameras, perfect crystal and grating interferometers, and more. While neutrons are severely limited by intensity relative to x-rays, neutrons are deeply penetrating due to their electric neutrality and low absorption. Additionally, the scattering cross sections for x-rays tend to scale with the atomic number Z, while the scattering cross sections for neutrons do not follow such a pattern across the periodic table. The complementary information available from both x-rays and neutrons is such that the two have even been combined into a single computed tomography (CT) apparatus [LaM17], housed at the National Institute of Standards and Technology (NIST) Center for Neutron Research (NCNR).

1.2 Cold Neutron Optics

Neutrons scatter from nuclei primarily via the strong force. Because the femtometer length scale of the strong force is much smaller than the wavelength of the cold neutron wave, scattering can be described by a single parameter, the scattering length b, and the potential between a neutron located at $\vec{x}$ and a nucleus located at $\vec{x}'$ is given by the Fermi pseudopotential

$$V = \frac{2\pi}{m} b \, \delta^3 \left(\vec{x} - \vec{x}' \right), \tag{1.6}$$

where δ^3 is the three dimensional Dirac delta function. In a material, this potential is averaged over many scattering centers leading to an optical potential

$$V(\vec{x}) = \begin{cases} V_0, & \text{inside material} \\ \\ 0, & \text{outside material} \end{cases} \tag{1.7}$$

where

$$V_0 = \frac{2\pi}{m} \langle b \rangle, \tag{1.8}$$

and $\langle b \rangle$ is the scattering length density of the material.

The optical potential of a material creates an index of refraction given by

$$n = \frac{p_{\mathrm{mat}}}{p_{\mathrm{vac}}} = \sqrt{\frac{p_{\mathrm{vac}}^2 - 2mV_0}{p_{\mathrm{vac}}^2}}, \tag{1.9}$$

where the "vac" and "mat" subscripts denote the velocity v and momentum p of the neutron in vacuum or within the material, respectively. Neutron optical potentials have magnitudes on the order of 100 neV, while cold neutrons have kinetic energies on the order of 10 meV. With $E_{\mathrm{kin}} = 10^6 \times V_0$, the first order expansion of Equation 1.9 is an excellent approximation

$$n \simeq 1 - \frac{V_0}{2E_{\mathrm{kin}}} = 1 - \frac{\langle b \rangle \lambda^2}{2\pi} \sim 1 - 10^{-6}. \tag{1.10}$$

With cold neutron indices of refraction close to unity, refraction by large angles is an impossibility. However, this is also a feature of neutron optics. Using a refracting prism, it is a relatively simple matter to deflect neutron beams at very small angles with precision. For example, in Chapter 3, refracting prisms are used to measure angular misalignments between crystals with uncertainties on the order of picoradians!
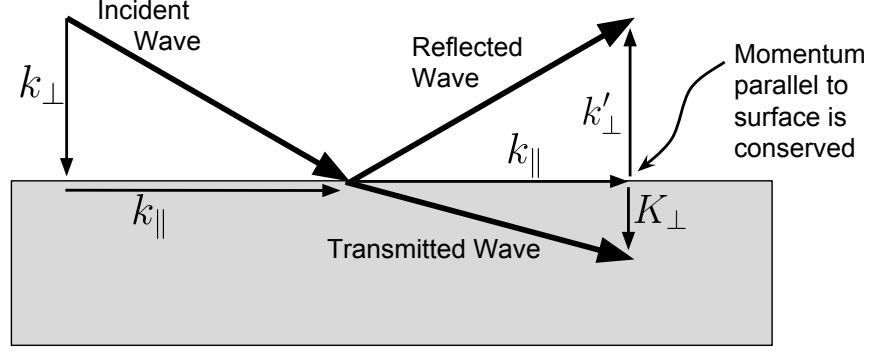
Figure 1.1 An incident neutron wave is partially reflected and partially transmitted from a material surface. Both the reflected and transmitted waves conserve momentum parallel to the boundary.

1.2.1 Optical Boundaries and Momentum Conservation

When a neutron wave passes from vacuum into a material, the neutron's momentum along the boundary is conserved. Additionally, some portion of the wave will also be reflected at the boundary (see Figure 1.1). This is a common pedagogical problem in quantum mechanics.

However, in regards to momentum conservation laws for neutron optical components with complicated shapes, consider the time evolution operator across the boundary (up to a normalization constant)

$$\mathcal{U} = \int_S d^2 x \, \mathcal{U}_{\text{mat}} |\vec{x}\rangle\langle\vec{x}| \mathcal{U}_{\text{vac}}, \tag{1.11}$$

where the subscripts have the same meaning as Equation 1.9; the integral is computed over the surface between the material and vacuum; and

$$\mathcal{U} = \mathcal{T}\left\{ e^{-i \int dt \, \mathcal{H}} \right\} \tag{1.12}$$

is the time evolution operator, with $\mathcal{T}\{\cdots\}$ denoting the time-ordered product. Let $|\vec{k}\rangle$ and $|\vec{K}\rangle$ be the energy eigenstates in vacuum and within the material, respectively. Also, I will assume energy conservation across the boundary

$$\frac{K^2}{2m} + V_0 = \frac{k^2}{2m}. \tag{1.13}$$

The relevant integral over the surface becomes

$$\int_S d^2 x \langle \vec{K} | \vec{x} \rangle \langle \vec{x} | \vec{k} \rangle = \frac{1}{(2\pi)^3} \int_S d^2 x \, e^{i(\vec{k} - \vec{K}) \cdot \vec{x}} \tag{1.14}$$

For a mostly flat surface with a local radius of curvature that is much larger than the neutron wavelength, the integral becomes a delta function, conserving the neutron momentum parallel to the material surfaces. Combining this expression with energy conservation determines the wave vector inside the material.

Note that I took energy conservation in Equation 1.13 without proof. Energy conservation may be imposed mathematically by allowing the surface integration in Equation 1.14 to also be an integration over time. In other words, any canonical momenta, including the Hamiltonian itself, that commute with the Hamiltonian are conserved

$$\frac{dP^\mu}{dt} = -i \left[x^\mu, P^0 \right] = g^{\mu\nu} \frac{\partial \mathcal{H}}{\partial x^\nu} \tag{1.15}$$

where $[A, B] = AB - BA$ is the commutator; P^μ is a four vector with $P^0 = \mathcal{H}$ the Hamiltonian; P^i are the canonical momenta conjugate to x^i; and $g^{\mu\nu} = [1, -1, -1, -1]$ is the metric. For the case of neutron refraction from a material, the gradient of $\mathcal{H}$ is zero parallel to the boundary and nonzero perpendicular to the boundary.

The application of Equation 1.15 to neutron optics is as follows: Generally the optical potential will be slowly varying relative to the neutron wavelength. The surfaces of a material that the neutron wave penetrates locally conserve momentum along the surfaces. This is to say if a neutron enters a material through a surface with surface normal $\hat{n}$ and exits the material through a surface with surface normal $\hat{n}'$, then refraction can occur in the plane defined by $\hat{n}$ and $\hat{n}'$.

Partial reflection from the surface also occurs. Simplifying Equation 1.13 by noting that the wave vectors parallel to the surface are equal inside and outside of the material $\vec{K}_\parallel = \vec{k}_\parallel$, while the wave vectors perpendicular to the material are not equal $\vec{K}_\perp \neq \vec{k}_\perp$

$$K_\perp^2 = k_\perp^2 - 2mV_0, \tag{1.16}$$

gives the criteria for total external reflection. If $2mV_0$ is greater than $\vec{k}_\perp^2$, then $K_\perp$ is imaginary. This is the principle behind neutron guides, where a material with very high scattering length density is used to make the angle of total external reflection relatively high (on the order of 0.5 degrees for typical cold neutron wavelengths). It is also possible to select neutrons with total momentum small enough for $E_{\text{kin}} < V_0$. Neutrons with such energies are referred to as ultracold neutrons (UCN). Ultracold neutrons may be trapped in material or magnetic bottles, rendering them especially useful for experiments requiring long interrogation times, such as measurements of the neutron lifetime, or searches for the neutron electric dipole moment (nEDM) [LG09].

While identifying which momenta are conserved is a nice qualitative tool, quantitatively analyzing refraction from complicated shapes in this way would be difficult. A simpler approach is to use the eikonal approximation to compute the neutron's phase

$$\phi = \int dt\, L \tag{1.17}$$

where the integral is taken over the neutron's classical trajectory, and $L = \vec{p} \cdot \dot{\vec{x}} - \mathcal{H}$ is the Lagrangian. The eikonal approximation is valid when the potential is slowly varying compared to the neutron wavelength [SN11]. Another way of writing Equation 1.17 is

$$\phi = -\int g_{\mu\nu} P^\mu dx^\nu. \tag{1.18}$$

This helps illustrate that the particle's phase is a Lorentz invariant quantity. For interferometry, the phase shift between two paths

$$\Delta\phi = \phi_2 - \phi_1 = \oint g_{\mu\nu} P^\mu dx^\nu, \tag{1.19}$$

is measured, with the contour going forward through path 1 and backward through path 2. Alternatively, the phase shift from a perturbation to the free space Hamiltonian is

$$\phi - \phi_{\text{vac}} = -\int g_{\mu\nu} \left(P^\mu - P^\mu_{\text{vac}} \right) dx^\nu. \tag{1.20}$$

Using the momentum conservation rules at each boundary, implies that only the $\hat{n} \cdot (\vec{P} - \vec{P}_{\text{vac}})$ term is nonzero, and constitutes the contribution to neutron phase from the optical component

$$\phi - \phi_{\text{vac}} = -\int \hat{n} \cdot \left(\vec{P} - \vec{P}_{\text{vac}} \right) \hat{n} \cdot d\vec{x}. \tag{1.21}$$

This illustrates how keeping track of momentum conservation throughout an optical system can simplify phase calculations and help avoid confusion.

If the classical equations of motion are solved and the phase shift is computed according to Equation 1.21, the quantum mechanical neutron state $|\psi\rangle$ may be propagated through time in the eikonal approximation. This produces

$$\langle \vec{x}|\mathcal{U}|\psi\rangle = e^{i\phi(\vec{x})}\langle \vec{x}|\psi\rangle \tag{1.22}$$

which may computed in momentum space by taking the Fourier transform, in which case gradients in $\phi(\vec{x})$ create changes in momentum. Such effects are treated in detail in Chapter 2.

1.3   Dynamical Diffraction from Optical Potentials

Dynamical diffraction refers the the diffraction of a wave by a periodic potential. Before exploring crystalline dynamical diffraction, where the period of the potential is of similar size to the neutron

wavelength and the eikonal approximation is invalid, I will describe dynamical diffraction from optical potentials. In this case the phase shift may be expanded in a Fourier series

$$\phi(\vec{x}) = \sum_n \phi_n e^{in\vec{q_0}\cdot\vec{x}}, \tag{1.23}$$

where n is an integer, and $|\vec{q_0}| = \frac{2\pi}{\lambda_G}$ with λ_G the period of the potential. The vector form of $\vec{q_0}$ also describes the diffraction direction. The phase shift causes the momentum state $|\vec{k}\rangle$ to be scattered into the momentum state $|\vec{k}'\rangle$ via

$$\left\langle \vec{k}' \left| e^{i\phi(\vec{x})} \right| \vec{k} \right\rangle = \frac{1}{(2\pi)^3} \int d^3x \, e^{i\vec{Q}\cdot\vec{x}+i\phi(\vec{x})} \tag{1.24}$$

where $\vec{Q} = \vec{k}' - \vec{k}$ is the momentum transfer. If Equation 1.23 is inserted into this expression for $\phi(\vec{x})$, then only integer values of $\vec{q_0}$ are possible for the momentum transfer $\vec{Q}$, creating sharp diffraction peaks. While the momentum transfer is constrained to certain values, the amplitudes of the diffracted waves depend on the shape of the potential through the ϕ_n terms. This effect is described in detail in Chapter 2 where phase-recovered CT from neutron scattering data is performed.

The very well-defined momentum transfers of dynamical diffraction make periodic potentials ideal for creating neutron beam splitters, enabling many varieties of neutron interferometers. Dynamical diffraction from optical potentials takes the form of micromachined gratings, where material is removed from silicon or quartz wafers with photo lithography and etchants [Dav07; Lyn12]. Gratings made from absorbing materials, such as gadolinium, are also needed for some types of grating interferometers. See, for example, [Grü08]. While there are many types of grating interferometers, all of them split and coherently recombine beams using an array of diffracting components. The alignment and spacing of the gratings, as well as any samples within the array, affect the phase and fringe visibility of the interference image.

Finally, consider that Equation 1.23 may be expressed as an operator

$$D(\vec{Q}) = \frac{1}{(2\pi)^6} \int d^3k \, d^3x \, \left| \vec{k} + \vec{Q} \right\rangle e^{i\vec{Q}\cdot\vec{x}+i\phi(\vec{x})} \left\langle \vec{k} \right|, \tag{1.25}$$

which upon translation by $\vec{\Delta x}$ using the translation operator $\mathcal{J} = e^{-i\vec{p}\cdot\vec{\Delta x}}$

$$\mathcal{J}^{-1}D(\vec{Q})\mathcal{J} = e^{-i\vec{Q}\cdot\vec{\Delta x}}D(\vec{Q}) \tag{1.26}$$

creates a phase shift. This result depends only on $D(\vec{Q})$ being a diffraction operator, and the phase shift upon translation does not depend on the magnitude of $D(\vec{Q})$. Equation 1.26 is a useful tool for many neutron grating interferometers, whereby translating one of the gratings modulates the phase of the interference pattern at the detector [Mia16].

1.4 Dynamical Diffraction from Crystals

Bragg diffraction is unlike dynamical diffraction from optical potentials, in that the eikonal approximation is not longer valid because the period of the potential and the neutron wavelength are both on the ångström length scale. Instead, the Hamiltonian inside the crystal must be solved. When expanded in an internal wave vector basis, energy and momentum conservation at the boundary still holds, following the same discussion as for optical potentials in Section 1.2.1. In this section, I will give a solution to the dynamical diffraction Hamiltonian, which has been previously derived by many authors under a myriad of notations. Some notable treatments of dynamical diffraction used to create the following discussion include [Sea78; Abo02; Lem13; RW15]. I suggest newcomers to the theory see [Sea89] and [RW15] first, while [Abo02] provides an excellent detailed treatment, and [Lit97; Lit98; Lem13; Pot15] describe how dynamical diffraction can create phase shifts in a neutron interferometer. This is the subject of Chapter 3, where a more general version of the analysis performed by [Lit97; Lit98] is developed to account for strain in a crystalline neutron interferometer. To provide a derivation as thorough as [Abo02] would be a daunting task. Instead, I will try to highlight the critical physical concepts within the theory.

In order to solve the crystalline dynamical diffraction Hamiltonian, I will begin by writing the potential as a diffraction operator

$$\left\langle \vec{k}' \right| \sum_{\vec{\ell},v} V_{\ell,v}(\vec{x} - \vec{x}_{\vec{\ell},v}) \left| \vec{k} \right\rangle = \frac{1}{(2\pi)^3} \sum_{\vec{\ell},v} \widetilde{V}_{\vec{\ell},v}(Q) e^{i\vec{Q}\cdot\vec{x}_{\vec{\ell},v}} \tag{1.27}$$

where $\vec{\ell}$ is a vector of integers that indexes the unit cells; v indexes the positions within the unit cell; and $V_{\vec{\ell},v}$ and $\widetilde{V}_{\vec{\ell},v}$ are the potential and its Fourier transform, respectively, for the scattering center located at $\vec{x}_{\vec{\ell},v} = \vec{\ell}a + \vec{x}_v$ with a the lattice constant. I have assumed a cubic unit cell, but this need not be the case. The computation of this expression is treated in detail in Chapter 4. For now, it is sufficient to recognize that the sum over $\vec{\ell}$ is a discrete Fourier transform, which equates to zero when adding over the many scattering centers in the crystal, except in the case where the momentum transfer is equal to a reciprocal lattice vector

$$\vec{Q} = \vec{H} = \frac{2\pi}{a}\vec{\ell}'. \tag{1.28}$$

Letting

$$\sum_{\vec{\ell}} \rightarrow \frac{1}{a^3} \int d^3x, \tag{1.29}$$

Equation 1.27 becomes

8

$$\left\langle \vec{k}' \middle| \sum_{\vec{\ell},v} V_{\ell,v}(\vec{x} - \vec{x}_{\vec{\ell},v}) \middle| \vec{k} \right\rangle = \frac{1}{a^3} \sum_{\vec{H},v} \widetilde{V}_{\vec{\ell},v}(H) e^{i\vec{H}\cdot\vec{x}_v} \delta^3 \left(\vec{Q} - \vec{H} \right), \qquad (1.30)$$

and the sum over $\vec{\ell}$ becomes a sum over different $\vec{H}$. In most experiments, only one reciprocal lattice vector will be relevant. This is due to the Bragg condition where the component of the incoming wave vector along $\vec{H}$ must be very close to $\vec{H}/2$ for diffraction to occur. I will take only one reciprocal lattice vector as being relevant as an assumption. Physically, this stems from the fact that the strength of the potential between the scattering centers and the neutron is very small compared to the kinetic energy of the neutron, which is identical to the statement made in Equation 1.9 concerning optical potentials. Even in the case where an incoming neutron beam is diffracted by more than one Bragg vector, the overlap in the relevant volumes of momentum space for the two Bragg conditions is extremely small.

Using only one $\vec{H}$, I can write the crystalline dynamical diffraction Hamiltonian in a $\left| \vec{K} \right\rangle$, $\left| \vec{K} + \vec{H} \right\rangle$, basis, where $\vec{K}$ is the wave vector inside the crystal. Using the definition of the reduced structure factor

$$v_Q = 2m \sum_v \widetilde{V}_v \left(\vec{Q} \right) \left\langle e^{i\vec{Q}\cdot\vec{x}_v} \right\rangle, \qquad (1.31)$$

where the Brackets around the $e^{i\vec{Q}\cdot\vec{x}_v}$ term indicate that the phase factor must be averaged over the position space wave function of the scattering center at $\vec{x}_v$, I can write the Hamiltonian in matrix form

$$\mathcal{H} = \frac{1}{2m} \begin{pmatrix} K^2 + v_0 & v_H \\ v_{-H} & K_H^2 + v_0. \end{pmatrix}, \qquad (1.32)$$

where $\vec{K}_H \equiv \vec{K} + \vec{H}$. Note that v_0 is given by Equation 1.31 with $\vec{Q} = 0$, and that $V_0 = v_0/(2m)$ is the optical potential. This is the Hamiltonian for a two state system, where the off-diagonal element v_H cause $|\vec{K}\rangle$ to diffract into $|\vec{K}_H\rangle$ and the element v_{-H} is diffraction from $|\vec{K}_H\rangle$ into $|\vec{K}\rangle$.

1.4.1 Energy Eigenstates of the Dynamical Diffraction Hamiltonian

The Hamiltonian in Equation 1.32 produces the secular equation

$$(K^2 + v_0 - k^2)(K_H^2 + v_0 - k^2) = v_H v_{-H}, \qquad (1.33)$$

where I have used energy conservation to label the eigenvalue (with $2m$ factored out) as k^2 with $\vec{k}$ the wave vector outside the crystal. The two solutions for k^2 are

9

$$k^2 = K^2 + v_0 + \frac{1}{2}(K_H^2 - K^2) \mp \sqrt{\frac{1}{4}(K^2 - K_H^2)^2 + v_H v_{-H}}. \tag{1.34}$$

The energy states of the dynamical diffraction Hamiltonian make up a continuous spectrum with a two-fold energy degeneracy. The problem is inherently two-dimensional in $\vec{K}$, with the diffraction plane described by $\vec{K}$ and $\vec{H}$. It is useful to define K_ζ as the component of $\vec{K}$ in the direction perpendicular to $\vec{H}$, and K_ξ as the component of $\vec{K}$ parallel to $\vec{H}$. Letting $K_\xi = \delta K - H/2$, and solving Equation 1.34 for K_ζ^2

$$K_\zeta^{\pm^2} = k^2 - \frac{1}{4}H^2 + (\delta K)^2 - v_0 \pm \sqrt{(\delta K\, H)^2 + v_H v_{-H}}. \tag{1.35}$$

Note that the $(\delta K)^2 \sim 5 \times 10^{-6} v_H$ term is small enough to be ignored. Many crystalline dynamical diffraction effects can be seen directly in this result. First, $\delta K = 0$ corresponds to neutrons with momenta corresponding to the exact Bragg condition, and K_ζ is the component of the internal wave vector along the Bragg planes. The plus and minus solutions in Equation 1.35 form two dispersion surfaces as shown in Figure 1.2. The average value of K_ζ is

$$K_{\zeta B} = \sqrt{k^2 - \frac{1}{4}H^2 - v_0}. \tag{1.36}$$

The separation between the dispersion surfaces depends on v_H and thus the strength of the potential between the scattering centers and the neutron. Equation 1.34 may also be used to compute an effective refractive index

$$n = \frac{K}{k} \simeq 1 - \frac{1}{2k}\left(v_0 + \delta K\, H \mp \sqrt{(\delta K\, H)^2 + v_H v_{-H}}\right). \tag{1.37}$$

From this expression, it is apparent that the two degenerate eigenstates have different indices of refraction. Physically, the two states are said to have overlap maximally with the scattering centers (plus sign in Equation 1.37) or with the space between the scattering centers (minus sign in Equation 1.37). These are usually referred to the $|\beta\rangle$ and $|\alpha\rangle$ states, respectively.

The difference in absorption of the $|\alpha\rangle$ and $|\beta\rangle$ states [Abo02] is also apparent from this expression. Allowing v_0 and $\sqrt{v_H v_{-H}}$ to have imaginary parts due to the imaginary part of the scattering length density, the $|\alpha\rangle$ state will have less absorption than the $|\beta\rangle$ state, as would be expected. Additionally, the level of absorption depends on the misalignment from the exact Bragg condition δK. Finally, note that the magnitude of the imaginary part of v_0 must be larger than that of $\sqrt{v_H v_{-H}}$, otherwise neutrons would be created in the crystal, which is not physical.

The reflectivity of the crystal depends on the misalignment from the exact Bragg condition with the width of a crystal's momentum-space acceptance dependent on $v_H v_{-H}$. It is convenient to weight factors of $\delta K\, H$ by $\sqrt{v_H v_{-H}}$
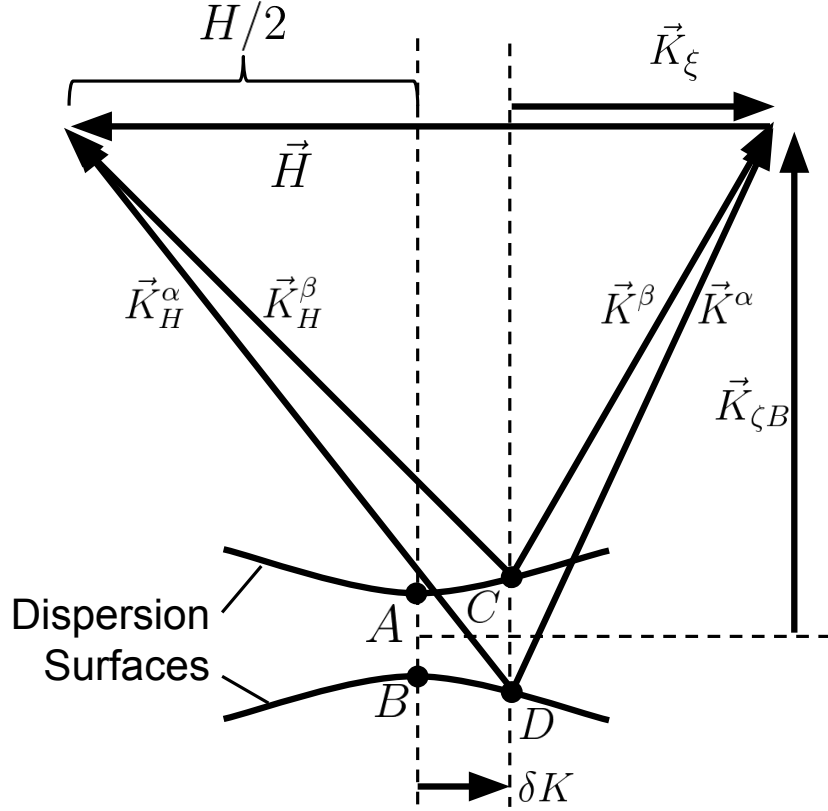
Figure 1.2 Dispersion surfaces for crystalline dynamical diffraction. The momentum space segments $\overline{AB}$ and $\overline{CD}$ are given by $\overline{AB} = \sqrt{v_H v_{-H}}/K_{\zeta B}$ and $\overline{CD} = \sqrt{(\delta K\, H)^2 + v_H v_{-H}}/K_{\zeta B}$. The separation of the dispersion surfaces and the magnitude of δK are greatly exaggerated for clarity.

$$\eta \equiv \frac{\delta K\, H}{\sqrt{v_H v_{-H}}}, \tag{1.38}$$

such that η spanning ± 1 corresponds to the angular momentum space acceptance of the crystal, called the Darwin width Θ_D, when δK is expressed as an angle $\Theta_D = 2\sqrt{v_H v_{-H}}/(HK)$.

Solving for the energy eigenstates of the dynamical diffraction Hamiltonian in the $|\vec{K}\rangle$, $|\vec{K}_H\rangle$ basis gives

$$\left|\alpha, \beta\right\rangle = a_0^{\pm}(K)\left|\vec{K}\right\rangle + a_H^{\pm}(K)\left|\vec{K}_H\right\rangle \tag{1.39}$$

with the coefficients

$$a_0^\pm(K) = \frac{1}{\sqrt{2}} \left(1 \pm \frac{K_H^2 - K^2}{\sqrt{\frac{1}{4}\left(K_H^2 - K^2\right)^2 + v_H v_{-H}}} \right)^{\frac{1}{2}}$$

$$a_H^\pm(K) = \mp \frac{1}{\sqrt{2}} \left(\mp 1 + \frac{K_H^2 - K^2}{\sqrt{\frac{1}{4}\left(K_H^2 - K^2\right)^2 + v_H v_{-H}}} \right)^{\frac{1}{2}} \sqrt{\frac{v_H}{v_{-H}}},$$

or in terms of η

$$a_0^\pm(\eta) = \frac{1}{\sqrt{2}} \left(1 \pm \frac{\eta}{\sqrt{\eta^2 + 1}} \right)^{\frac{1}{2}} \tag{1.40}$$

$$a_H^\pm(\eta) = \mp \frac{1}{\sqrt{2}} \left(1 \mp \frac{\eta}{\sqrt{\eta^2 + 1}} \right)^{\frac{1}{2}} \sqrt{\frac{v_H}{v_{-H}}}. \tag{1.41}$$

The phase factor $\sqrt{v_H/v_{-H}}$ can lead to interesting effects, such as neutron spin rotation down a channel cut crystal [Dom01]. However, it does not affect any of the experiments in this work, and I will therefore leave off this term in the following discussion for brevity.

1.4.2   Laue Geometry

With the solution to the dynamical diffraction Hamiltonian, the reflectivity of two distinct geometries may be computed. The first, called the Laue geometry is the geometry used by all the experiments in this dissertation. The Laue geometry consists of a crystal slab with faces parallel to $\vec{H}$ (Figure 1.3). Momentum conservation across the boundary implies that the misalignment from the exact Bragg condition δK is conserved across the boundary. A single incoming plane wave then excites the two degenerate $|\alpha\rangle$ and $|\beta\rangle$ states simultaneously. The two states propagate down the Bragg planes in a direction given by

$$\dot{\xi} = \frac{\partial \mathcal{H}^{\alpha,\beta}}{\partial(\delta K)} = \mp \frac{\delta K\, H^2}{2m\sqrt{(\delta K\, H)^2 + v_H v_{-H}}} \tag{1.42}$$

and

$$\dot{\zeta} = \frac{\partial \mathcal{H}^{\alpha,\beta}}{\partial K_\zeta} = \frac{1}{m} K_\zeta^{\alpha,\beta}. \tag{1.43}$$

Noting that $\delta K\, H \sim v_H v_{-H}$, $\dot{\xi}$ lies between $\pm H/(2m)$. This causes the neutron wave to fill the Borrmann fan, which is outlined by $\dot{\xi}/\dot{\zeta}$ in the case where $\delta K \gg \sqrt{v_H v_{-H}}/H$
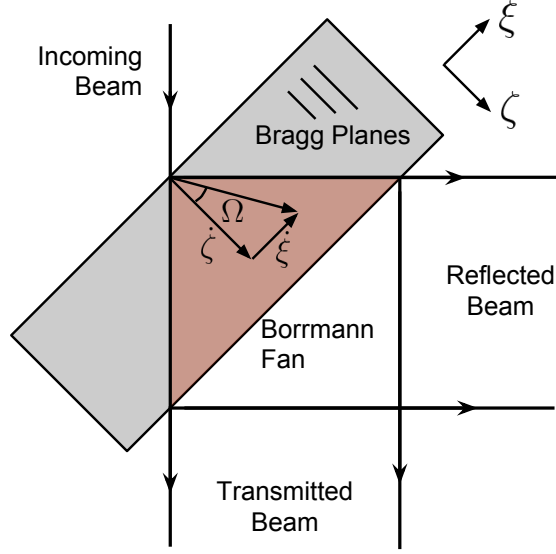
Figure 1.3 Borrmann fan in the Laue geometry.

$$\lim_{\delta K \gg \frac{\sqrt{v_H v_{-H}}}{H}} \frac{\dot{\xi}}{\dot{\zeta}} = \mp \frac{H}{2K_{\zeta B}} = \mp \tan(\theta_B) \tag{1.44}$$

where θ_B is the angle between $\vec{K}$ and $\vec{K}_{\zeta B}$, called the Bragg angle. In the Laue geometry, the angle between the propagation direction in the crystal for the component of the neutron wave packet satisfying the exact Bragg condition $\delta K = 0$ and the components slightly off Bragg $\delta K \sim \sqrt{v_H v_{-H}}/H$ (see Figure 1.4) is given by

$$\Omega = \tan^{-1}\left[\frac{\dot{\xi}(\delta K)}{\dot{\zeta}}\right] \tag{1.45}$$

where I have noted that $\dot{\xi}$ is a function of δK.

When the neutron wave $|\vec{k}\rangle$ enters the crystal, it excites $|\alpha\rangle$ and $|\beta\rangle$ states which propagate through the crystal until reaching the exit surface. At the exit surface, the α and β states both excite $|\vec{k}\rangle$ and $|\vec{k} + \vec{H}\rangle$ states outside the crystal. The reflection coefficients in the Laue geometry are then given by the partial wave amplitudes Equations 1.40 and 1.41 of the α and β states

$$r^{\alpha,\beta}(\eta) = \left\langle \vec{k} + \vec{H} \middle| \alpha, \beta \right\rangle \left\langle \alpha, \beta \middle| \vec{k} \right\rangle = a_H^{\pm}(\eta) a_0^{\pm *}(\eta) = \mp \frac{1}{2} \left(1 - \frac{\eta^2}{\eta^2 + 1}\right)^{\frac{1}{2}}. \tag{1.46}$$

13

The α and β states also accrue unique phases according to Equation 1.23. Only the K_ζ component contributes to the phase shift relative to vacuum, because the Hamiltonian and the other two momenta are conserved in the Laue geometry

$$\Delta\phi_{\text{Laue}} = \int (\vec{K}_\zeta^\alpha - \vec{K}_\zeta^\beta)d\zeta = D\frac{\sqrt{v_H v_{-H}}}{K_{\zeta B}}\sqrt{\eta^2 + 1} \tag{1.47}$$

where D is the thickness of the crystal. Inserting this result into Equation 1.46 gives

$$r(\eta) = r^\alpha(\eta) + r^\beta(\eta) = -i\frac{\sin(\Delta\phi_{\text{Laue}})}{\sqrt{\eta^2 + 1}}. \tag{1.48}$$

The argument of the sine function creates oscillations in the diffracted intensity called pendellösung oscillations. The phase of the oscillation depends on the crystal thickness, and has a spatial period of

$$\Delta_H = \frac{\pi H}{\sqrt{v_H v_{-H}}}\cot\theta_B. \tag{1.49}$$

This phase shift and beating period depend on v_H, making pendellösung interference a useful tool for precision measurements of the structure factor. This is the subject of Chapter 4.

The average reflectivity is computed by averaging over pendellösung oscillations

$$\mathcal{R} = \langle r^2(\eta)\rangle = \frac{\langle\sin^2(\Delta\phi_{\text{Laue}})\rangle}{\eta^2 + 1} = \frac{1}{2(\eta^2 + 1)}. \tag{1.50}$$

This function is plotted in Figure 1.4a and has a full width half maximum (FWHM) of 2 in η-space, corresponding to a relative FWHM for $\delta K/K = \Theta_D$ of

$$\Theta_D = \frac{2\sqrt{v_H v_{-H}}}{HK} \simeq 10^{-5} \text{ rad}. \tag{1.51}$$

The very small value of Θ_D is due to the diffraction operator coming from a weak potential. Put another way, the scattering length $b \sim 5$ fm is small compared to the lattice constant of $a \sim 5$ Å.

1.4.3 Bragg Geometry

The Bragg geometry has some important physical differences compared to the Laue geometry. In this case, the boundary is perpendicular to $\vec{H}$, and K_ζ, and not K_ξ, is conserved. Energy and momentum conservation then determines δK inside the crystal

$$\delta K = \pm\frac{1}{H}\sqrt{(\delta K_B H)^2 - v_H v_{-H}}, \tag{1.52}$$

where
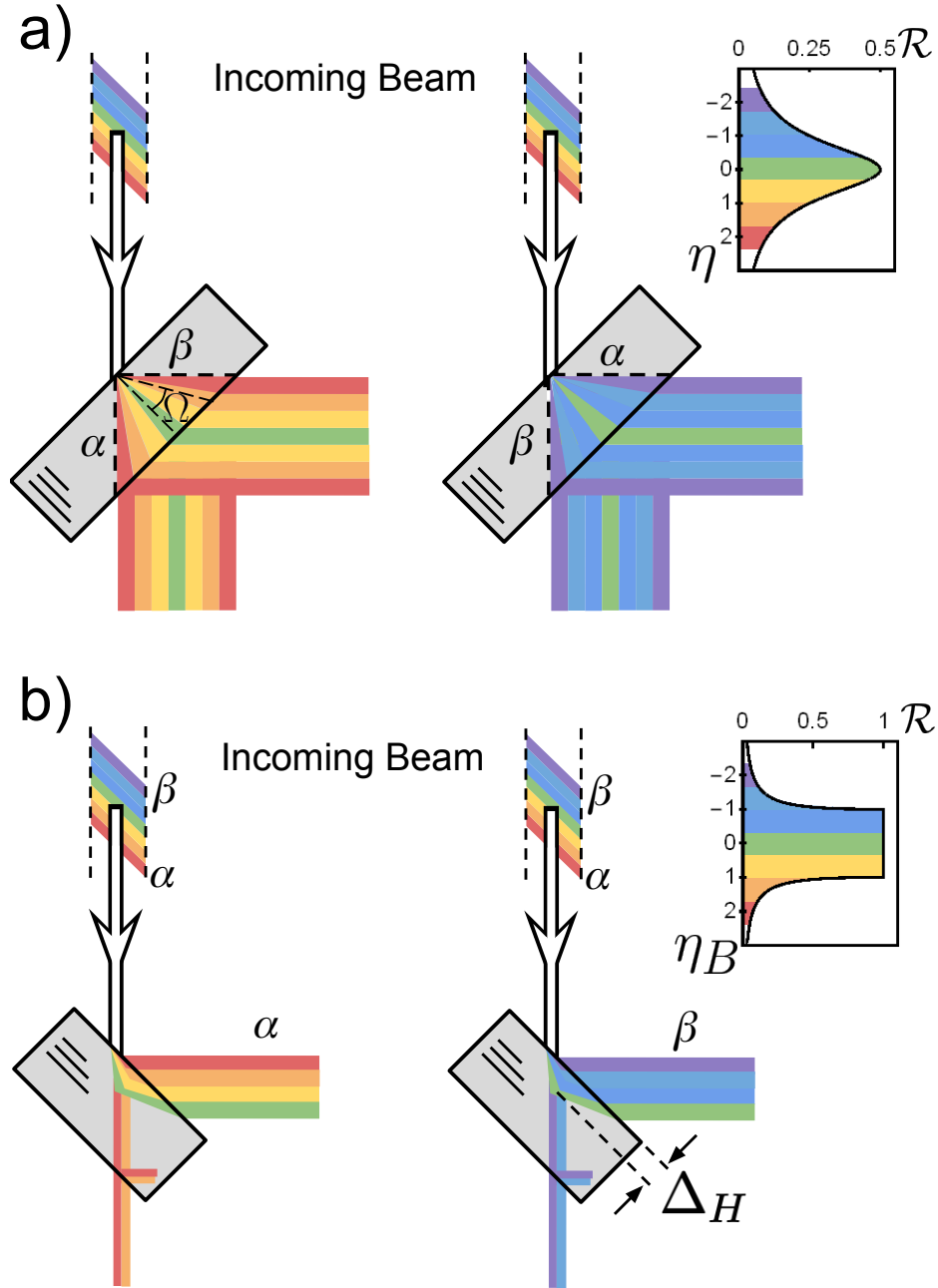
Figure 1.4 Dispersion in the Laue and Bragg geometries. Deviation from the Bragg condition is denoted by color and depends on the component of the incoming momentum along the direction of the reciprocal lattice vector. In the Laue geometry (a) two degenerate solutions are excited within the crystal. In the Bragg geometry (b), each δK excites either the α or β branch. The average reflectivity as a function of η or η_B is also shown for both geometries. The central portion of $\mathcal{R}(\eta_B)$ for the Bragg geometry, called the Darwin plateau, produces a reflectivity of 100%. The neutron wave penetrates the crystal to a depth given by the pendellösung length Δ_H, which is on the order of 50 μm.

$$\delta K_B = \frac{1}{H} \left(k_\xi^2 - \frac{1}{4} H^2 - v_0 \right) \tag{1.53}$$

is analogous to δK in the Laue geometry and is the deviation from the exact Bragg condition, defined in terms of the momentum of the incoming neutron wave. Notice that δK can be imaginary if $\delta K_B^2 < v_H v_{-H}$. This range defines the Darwin width for 100% reflectivity, in analogy with the case of total external reflection for cold neutrons of glancing incidence or UCN from an optical potential. Similar to Equation 1.38, it is convenient to define the normalized quantity

$$\eta_B = \frac{\delta K_B \, H}{\sqrt{v_H v_{-H}}}. \tag{1.54}$$

Physically, η and η_B correspond to the canonical momentum conjugate to ξ inside and outside of the crystal, respectively.

The reflection coefficient for the Bragg geometry is a slightly more complicated than that of the Laue geometry. For the Laue geometry, I noted that conservation of energy and momentum along the crystal surface causes an incoming neutron wave to excite an internal crystal state that is a linear combination of $|\vec{K}\rangle$ and $|\vec{K}_H\rangle$ and propagates from one surface to another. For the Bragg geometry, the entrance and exit surfaces are the same and while the $|\vec{K}_H\rangle$ term in the dynamical diffraction eigenstate still clearly creates a reflected beam, the $|\vec{K}\rangle$ term recreates the original wave $|\vec{k}\rangle$, with a reduced amplitude

$$r_1 \left| \vec{k} \right\rangle = \left(\left| \vec{k} + \vec{H} \right\rangle a_H + \left| \vec{k} \right\rangle a_0 \right) a_0^*. \tag{1.55}$$

Repeated applications of r_1 generates

$$r_\infty = \sum_{n=0}^{\infty} |a_0|^{2n} \, a_H a_0^*. \tag{1.56}$$

Writing $a_0(\eta)$ and $a_H(\eta)$ in terms of η_B given the relationship between η_B and η (Equation 1.54), the infinite sum converges and the total reflectivity is

$$\mathcal{R} = |r_\infty|^2 = \begin{cases} 1, & \eta_B^2 < 1 \\ \left(\eta_B - \sqrt{\eta_B^2 - 1} \right)^2, & \eta_B^2 > 1 \end{cases}, \tag{1.57}$$

which is plotted in Figure 1.4b. Note that this is the solution for an infinitely thick crystal. Some authors quote a slightly different result [Sea89]

$$\mathcal{R} = |r_\infty|^2 = \begin{cases} 1, & \eta_B^2 < 1 \\ \left(1 - \sqrt{1 - \eta_B^{-2}}\right)^2, & \eta_B^2 > 1 \end{cases}, \tag{1.58}$$

which averages the beam reflected by the crystal surface with the beam reflected on the back surface of the crystal over oscillations that are similar to pendellösung in the Laue geometry. In reality, this portion of the reflected beam will be translated by $n2D \cot \theta_B$ relative to beam reflected by the crystal surface, with n an odd integer describing the number of internal reflections [Abo02]. Whether this portion of the beam is relevant depends on the thickness of the crystal and Bragg angle. Only the shape of $\mathcal{R}$ outside of the Darwin width is affected.

1.5 NIOF Facilities

All of the experimental work in this dissertation was performed at at the NCNR Neutron Interferometry and Optics Facility (NIOF). The NIOF is in the cold neutron guide hall off of neutron guide 7 (NG7). The layout of the guide hall and the containment building at the NCNR is shown in Figure 1.5a. All of the beams in the guide hall are cold neutron beams extracted from a liquid hydrogen cold source. With the exception of the Multi Axis Crystal Spectrometer (MACS), the instruments in the confinement building use thermal neutrons. For more information on the NCNR, including the user program, see the NCNR website [Ncn].

The NIOF consists of two beamlines. The original beamline, simply called "NIOF", uses an advanced vibrational isolation system (Figure 1.5c). The NIOF wavelength is adjustable, though it has remained at 2.7 Å for a number of years. This is a convenient wavelength, as it corresponds to a 45 degree Bragg angle for the (220) reflection of silicon.

The NIOFa beamline uses 4.4 Å neutrons, but also has a strong $\lambda/2$ component. The 4.4 Å wavelength is also convenient, as it corresponds to an approximately 45 degree Bragg angle for the (111) reflection of silicon. The existence of the 2.2 Å portion of the beam is often also utilized. For experiments that suffer from $\lambda/2$ pollution, such as spin precession experiments, the shorter wavelengths may be filtered out with a beryllium filter.

1.6 Overview

The remaining chapters detail a number of experiments concerning neutron dynamical diffraction. Chapter 2 deals with dynamical diffraction from optical potentials, namely micromachined silicon phase-gratings. A double crystal diffractometer was used to measure neutron diffraction from the phase-gratings. It was found due to the high aspect ratio of the gratings that the diffracted wave amplitudes were very sensitive to the alignment of the grating to the neutron beam, providing
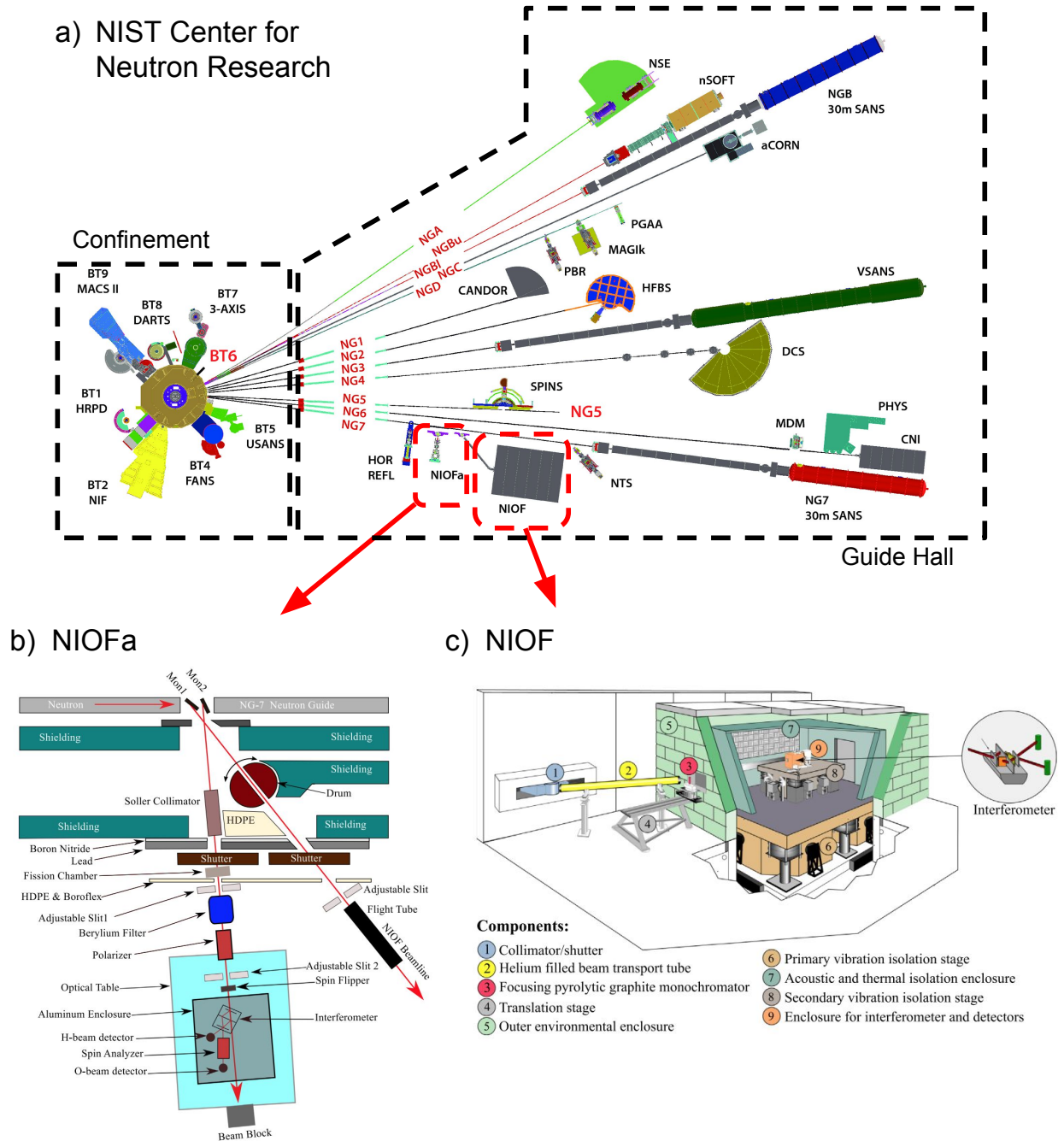
Figure 1.5 Layout of the NCNR (a) from [Ncn]. The NIOF beamlines are located on NG7 at the NCNR. The original NIOF beamline (c) uses an advanced vibrational isolation system. The NIOFa beamline (b) is a more flexible setup. Some minor changes have been made. For example the Söller collimator inside the shielding for NIOFa has been removed, and the beryllium filter, spin polarizer, and spin analyzer may be translated in and out of the beam. NIOF and NIOFa schematics from [Sha16].

a potential explanation for why some types of neutron grating interferometers have not been demonstrated with high interference fringe visibility. The high sensitivity of the sample-beam alignment prompted the creation of a phase-recovered CT algorithm which produces reconstructions of the gratings from double crystal diffractometer data. Prospects for using phase recovered CT at user neutron scattering instruments for periodic samples is promising.

Chapter 3 details how very small levels of strain may be measured in crystalline neutron interferometers using refracting prisms inserted in one arm of an interferometer. Intrinsic angular misalignments on the order of tens of nanoradians are measured. It is found that comparable strain strongly perturbs the dynamical phase corrections employed by prior precision measurements of acceleration due to Earth's gravity using crystalline neutron interferometers. The size of the predicted correction given the measured Bragg plane misalignments in typical interferometers would produce a systematic shift to the measured acceleration due to Earth's gravity of approximately the same size as the historical discrepancy. It is then shown that annealing an entire interferometer at 800°C can alleviate enough residual strain to bring the Bragg planes of the interferometer into an improved alignment. Finally, the construction of a two-crystal neutron interferometer is described, where the interferometer performance is tracked as a function of post-fabrication measures.

Chapter 4 uses pendellösung interferometry to perform precision measurements of the silicon structure factors for the (111), (220), and (400) Bragg reflections. The forward scattering phase shift of the pendellösung sample is also measured by placing the sample in a neutron interferometer. By taking the ratio of the pendellösung and forward scattering interferometer measurements, the need for an extremely flat sample with very little residual strain is alleviated. This is critical to the success of the experiment, as the work of Chapter 3 indicates that a strain-free optically polished crystal would be very difficult to create. The three measured structure factors are already enough to provide a precision measurement of the Debye-Waller factor from lattice dynamics, with some sensitivity to the neutron charge radius and beyond the standard model (BSM) force mediators on the 2 keV mass scale. If recent high quality neutron inelastic scattering data sets, along with improved lattice dynamical models [Kim15; Kim18], may be used as an independent measure of the Debye-Waller factor, then the sensitivity to the neutron charge radius and BSM forces could be improved. Furthermore, there are many more Bragg reflections whose structure factors could be measured. This would allow for a higher sensitivity to anharmonic force contributions to the Debye-Waller factor and BSM force mediators. Finally, the precision measurements of lattice dynamical quantities can alleviate uncertainties in the evaluation of x-ray structure factors used to map the charge density in silicon.

CHAPTER 2

NEUTRON PHASE-GRATING DIFFRACTION AND
PHASE-RECOVERED TOMOGRAPHY

2.1 Introduction

The following chapter details the characterization of neutron phase-gratings via the diffraction of neutrons from the gratings. The diffraction angles are very small, on the order of 0.5 minutes of arc, which necessitated the use of a double crystal diffractometer to resolve the diffraction spectra from the phase-gratings. Initially, it was found that the diffraction spectra could be predicted from scanning electron microscope (SEM) micrographs of the gratings and that distortions of the gratings are large enough to hurt the performance of phase-grating neutron interferometers. A manuscript detailing the results is currently in the publication process [Hea18a]. Additionally, my colleagues and I realized that the inverse of the transform which allows for the grating SEMs to predict the diffraction spectra can be reversed. An algorithm that does this was developed, drawing on existing phase-recovery and computed tomography (CT) methods. This resulted in high resolution (300 nm) spatial images of the gratings. Unlike creating a SEM micrograph, which entails cleaving the gratings, the method is nondestructive and may be broadly applicable to a wide class of scientific samples that already benefit from neutron scattering methods. The development and performance of the algorithm is described in another manuscript which is also in the publication process [Hea18b].

2.2 Neutron Phase Grating Diffraction

When a neutron passes through an optical potential, the magnitude of the potential is much smaller than the kinetic energy of the neutron. Additionally, if the length scale over which the potential

varies is much larger than the wavelength of the neutron, the phase accrued by the neutron wave is given by its semiclassical path integral

$$\phi(\vec{x}) = -\int dt V(\vec{x}) \simeq -\frac{m}{k} \int d\ell V(\vec{x}) \tag{2.1}$$

where the integral is taken over the neutron trajectory, and the semiclassical nature of the computation comes from the change of variables from time to space. In the case of optical potentials, this can be further reduced to the form

$$\phi(\vec{x}) = -\lambda \int d\ell \langle b(\vec{x}) \rangle \tag{2.2}$$

where $\langle b(\vec{x}) \rangle$ is the scattering length density of the material. Note that because the integral is over the neutron trajectory, the phase $\phi(\vec{x})$ is only a function of the transverse coordinates and not the longitudinal coordinate of the neutron. In the case of phase gratings, the material is cut to a shape such that

$$\langle b \rangle = \begin{cases} \sum_i N_i b_i & \text{inside material} \\ 0 & \text{outside material} \end{cases}, \tag{2.3}$$

where N_i is the number density and b_i is the scattering length of the ith species in the sample. The position space Green's function for transmission through the sample is

$$G(x', x) = e^{-i\phi(\vec{x})} \delta^{(3)} \left(\vec{x}' - \vec{x} \right). \tag{2.4}$$

Rewriting as an operator in momentum space gives

$$
\begin{aligned}
\hat{G} &= \int d^3k' d^3k \, \left| \vec{k}' \right\rangle \left\langle \vec{k}' \right| G \left| \vec{k} \right\rangle \left\langle \vec{k} \right| \\
&= \int d^3k' d^3k d^3x \, \left| \vec{k}' \right\rangle e^{-i\phi(\vec{x}) - i(\vec{k}' - \vec{k}) \cdot \vec{x}} \left\langle \vec{k} \right| \\
&= \int d^3k' d^3k \, \left| \vec{k}' \right\rangle \tilde{G} \left(\vec{k}' - \vec{k} \right) \left\langle \vec{k} \right|.
\end{aligned}
\tag{2.5}
$$

The task is to now study the structure of

$$\tilde{G} = \mathcal{F} \left\{ e^{-i\phi(\vec{x})} \right\}. \tag{2.6}$$

For a periodic phase shifter, $\phi(\vec{x})$ may be expanded in a Fourier series. For simplicity, I will take $\phi(\vec{x}) \rightarrow \phi(x)$ to be a one-dimensional profile, though the extension to two dimensional profiles is straightforward.

$$\phi(x) = \sum_{n=-\infty}^{\infty} \phi_n e^{inq_0 x} \tag{2.7}$$

where n is an integer and

$$q_0 = \frac{2\pi}{\lambda_G} \tag{2.8}$$

with λ_G the period of the phase grating. Expanding the function $G(x)$ in a Fourier series gives

$$G(x) = \sum_{m=0}^{\infty} \frac{1}{m!} \left(-i \sum_n \phi_n e^{inq_0 x} \right)^m. \tag{2.9}$$

Noting that the phase factor must be integer values of $q_0 x$ for all m and n, this expression can be rewritten as a single sum over some integer n'

$$G(x) = \sum_{n'} a_{n'} e^{in'q_0 x}. \tag{2.10}$$

Writing this in momentum space

$$\widetilde{G}(q) = \sum_{n'} a'_n \delta \left(q - n'q_0 \right), \tag{2.11}$$

I can identify the $a_{n'}$ as the diffracted wave amplitudes by propagating an incoming neutron state $|\psi_0\rangle$ through the phase grating

$$\begin{aligned}
|\psi\rangle &= \sum_{n'} a_{n'} \int d^3k d^3k' \left| \vec{k}' \right\rangle \delta^{(3)} \left(\vec{k}' - \vec{k} - n'\vec{q}_0 \right) \left\langle \vec{k} \middle| \psi_0 \right\rangle \\
&= \sum_{n'} a_{n'} \int d^3k' \left| \vec{k}' \right\rangle \left\langle \vec{k} + n'\vec{q}_0 \middle| \psi_0 \right\rangle.
\end{aligned} \tag{2.12}$$

The relation of the ϕ_n Fourier coefficients to the $a_{n'}$ diffracted wave amplitudes can be done through a recursive series (Appendix A). However, it is not immediately useful to compute diffracted wave amplitudes in terms of the Fourier coefficients making up $\phi(x)$. Inverting the wave amplitudes $a_{n'}$ to recover the phase profile is a more interesting task, and can be done via phase recovery algorithms. This forms the basis of phase-recovered tomography and is described in Section 2.4.

The sum over m in Equation 2.9 is equivalent to the Born approximation. Thus, for phase profiles with a smaller amplitude, higher order in m become less meaningful. The sum over n, on the other hand, depends on the shape of the grating. Finally, note that the shape of the wave packet is not altered by diffraction from the grating. However, if the wave packet's spread in momentum space

is broader than the separation between diffraction peaks, the location and amplitudes will become difficult to resolve experimentally.

2.3 Phase Grating Characterization for Interferometer Improvement

The recent advances in far-field phase-grating moiré interferometry extends phase-grating neutron interferometry to high intensity sources of thermal neutrons, showing promise for impactful long-path-length experiments and providing new methods of characterizing materials by scanning the autocorrelation length over many orders of magnitude [Pus17a; Hus16; Sar18; Bro17; Bro18]. This technique has proven to be advantageous due to its relatively broad wavelength acceptance and less stringent alignment requirements. However, the observed contrast of 3 % [Sar18] needs to be substantially improved.

A major contributor to the achieved poor contrast is suspected to be the sub-optimal quality and alignment of the high aspect ratio phase-gratings. Fortunately, phase-grating characterization and improved grating alignment are enabled by measuring the diffraction pattern of a neutron beam scattered from a phase-grating. The analogous method for optimizing the orientation of phase-gratings for x-rays is crucial for obtaining high interferometer contrast [Mia16]. What follows is a characterization of the diffraction of neutrons and the function $\widetilde{G}$ from some of the phase gratings used in the original demonstration of a far-field neutron interferometer. Distortions measured in the diffraction pattern which would impact the theoretical maximum contrast of the interferometer are found. Improved phase-grating quality will be important in improving interferometer performance.

2.3.1 Experiment

The experiment was performed at the NIOFa beamline at the National Institute of Standards and Technology (NIST) Center for Neutron Research (NCNR) in Gaithersburg, MD [Sha16; Pus15]. A schematic of the experiment is shown in Figure 2.1a. A 4.4 Å wavelength neutron beam is extracted from the neutron guide using a pyrolytic graphite (PG) crystal. The beam passes through a 2 mm slit before being Bragg diffracted (Laue geometry) by a perfect-silicon crystal (111) monochromator. A 4.4 mm wide cadmium block is used to select the forward-diffracted beam from the monochromator. To measure the outgoing momentum distribution modified by the phase-grating, a second perfect-silicon crystal (111) analyzer was placed after the grating, forming a double crystal diffractometer. The monochromator was rotated relative to the analyzer by a rotation stage with an embedded optical encoder, allowing arcsecond precision motion. The apparatus functions as a double crystal diffractometer; more advanced double crystal diffractometers are usually referred to as ultra small angle neutron scattering (USANS) spectrometers, and USANS user instruments, such as those
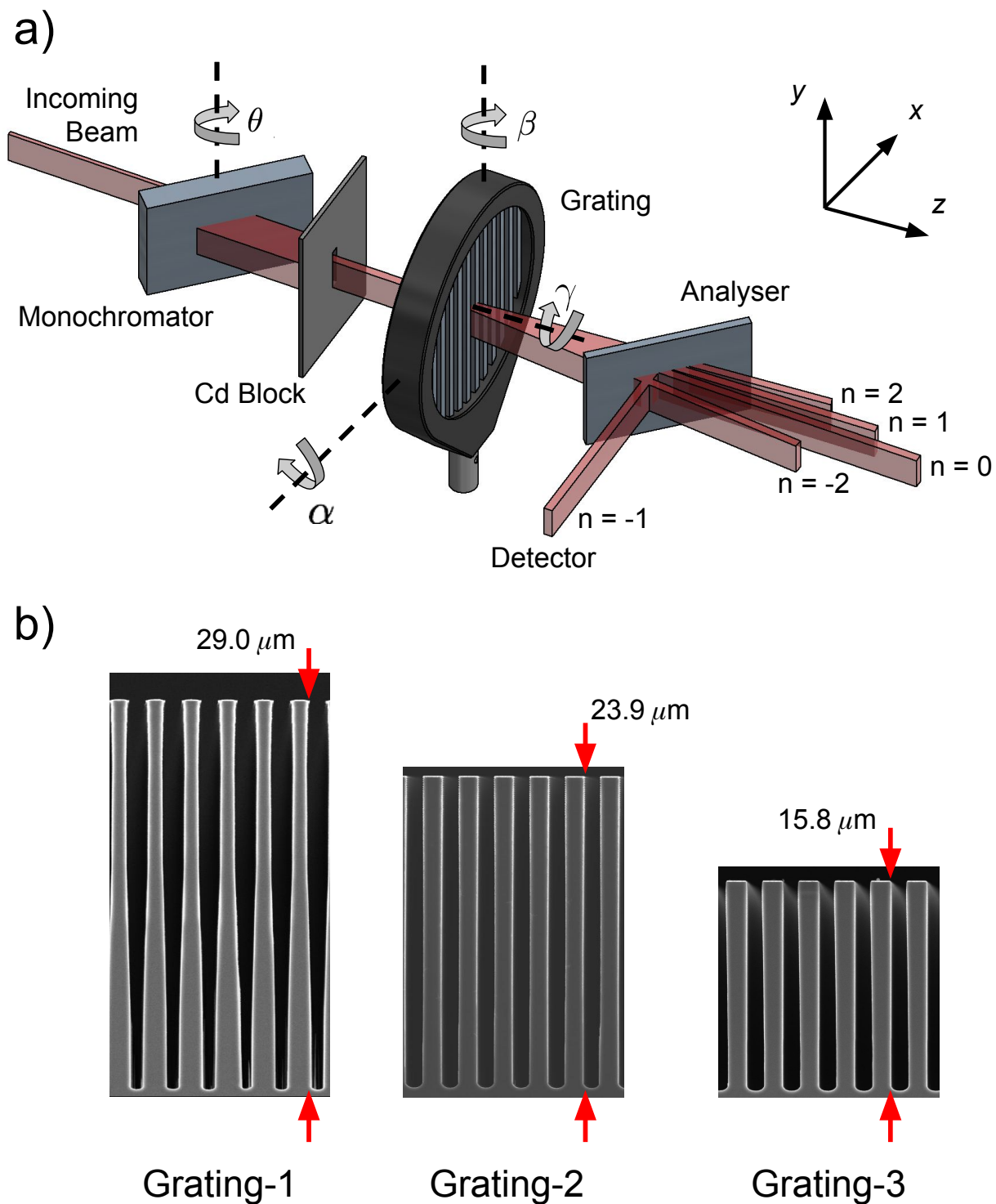
Figure 2.1 (a) Experimental setup. A $\lambda = 4.4$ Å neutron beam passes through a monochromator crystal, then through a phase-grating whose effect is measured by an analyzer crystal and a ^{3}He proportional counter. The grating may be rotated by angles α, β, and γ about the x, y, and z axes respectively. (b) SEM of the gratings.

described in [Bar05] or [Str07], can perform the same type of measurements. The diffraction pattern was measured as a function of sample rotation angles α, β, and γ, as defined in Figure 2.1a.

The Bragg diffracted wave packets are Lorentzian in shape in momentum-space (see the reflectivity function $\mathcal{R}$ in the Laue geometry, Equation 1.50). Their nominal transverse coherence length is given by the pendellösung length $\Delta_H = 35$ μm for the (111) reflection from silicon at $\lambda = 4.4$ Å. Diffraction peaks were clearly visible, the angular locations of which are given by

$$\theta_n = \sin^{-1}\left(\frac{n\lambda}{\lambda_G}\right),\tag{2.13}$$

where λ_G is the period of the grating, and n is an integer that represents the diffraction order. The relative amplitudes of the diffraction peaks depend on the shape and amplitude of the phase profile for a given angle of sample rotation β.

Three gratings were analyzed in this experiment. The period of each grating was $\lambda_G = 2.4$ μm. The grating depths were $h = 29.0$ μm, $h = 23.9$ μm, and $h = 15.8$ μm, with corresponding phase amplitudes of 2.6 rad, 2.2 rad, and 1.4 rad, respectively for $\lambda = 4.4$ Å neutrons. Scanning electron micrographs of the three gratings are shown in Figure 2.10.

Diffraction spectra as a function of grating rotation β about the y-axis were taken from approximately -2 degrees to 4 degrees in 1 degree steps y-axis rotation for Grating-1, -6 degrees to 6 degrees in 1 degree steps for Grating-2, and -6 degrees to 6 degrees in 1.5 degree steps for Grating-3. The -3 degree y-axis rotation diffraction spectrum for Grating-1 was substituted with the 5 degree spectrum, because the -3 degree spectrum was out of the measured range. The grating rotation was severe enough for there to be no diffraction peaks expected in the -3 degree spectrum.

2.3.2 Results

y-axis rotations

Rotations about the y-axis cause the effective grating period to decrease. However, the severe aspect ratio of these gratings causes a change in the phase path integral to be the dominant effect. Integrating over the neutron's trajectory through a phase-grating as a function of rotation about the y-axis modifies the effective phase profile from a nominal square wave. This is referred to as a Radon transform, and is addressed in detail in Section 2.4, where a phase-recovered tomography algorithm for imaging the gratings is presented. One can also predict the momentum distribution from the SEM micrographs, from which the impact of the grating shape on interferometer performance can be assessed. Note that this effect is not as pronounced for very cold neutron (VCN) phase-gratings, neutron diffraction from which has been characterized in the past, because the phase-gratings used for VCN have aspect ratios close to unity [Ede91].

The effective phase profiles were computed from the SEM micrographs as a function of rotation about the y-axis using silicon's neutron scattering length density of 2.1×10^{-6} Å^{-2} [Ncn]. The momentum distributions were computed by transforming the phase profiles taken from the SEM micrographs via a Radon transform followed by a fast Fourier transform (FFT). The power spectra of the FFT compared to experimental momentum space distributions for Grating-1, along with the effective phase profiles, are shown in Figure 2.2.

The diffraction peaks were characterized by fitting the measured intensity versus monochromator rotation to multiple Lorentzians. Figure 2.3 compares the areas of the fitted Lorentzians to the areas of the peaks in the FFT power spectra computed from the SEM micrographs. The computed diffraction peak areas from the SEM micrographs were scaled to match the absolute peak areas of the measured distributions, with the relative areas between diffraction orders and grating rotations preserved. The asymmetry between the two first-order diffraction peak areas was unique to Grating-1. This effect can be understood by inspecting the spatial phase profiles computed from the SEM micrographs (see Fig 2.2). As the grating is rotated, the phase profile has an asymmetrical slope. The sign of the slope changes as the grating rotation crosses zero. This unique phase profile is only seen in Grating-1 because of the trapezoidal grating walls which are visible in the SEM micrograph of Figure 2.1b.

Due to the high aspect ratio of neutron phase-gratings, the phase profile vanishes as the rotation about the y-axis approaches $\lambda_G/h \sim 5$ degrees. The quality of the grating further diminishes the angular range over which the grating is effective. This can be seen by inspecting the relative peak areas in Figure 2.3. Because of the distorted walls of Grating-1, the first order peak areas have a large slope as a function of y-axis rotation when the grating is aligned to the beam. This adds a transverse momentum dependence to the diffracted wave amplitudes when the grating is used in a phase-grating neutron interferometer, which diminishes interferometer contrast. Even for the typical beam divergence of ~ 0.5 degrees, the angular edges of the beam probe drastically different grating profiles. This effect is absent in Grating-2 and Grating-3, where the diffracted peak areas form a maximum when the grating is aligned to the beam.

The impact of a non-ideal grating profile on the contrast of a three phase-grating moiré interferometer is is illustrated in Figure 2.4. Maximum achievable contrast was calculated by computing the diffracted wave amplitudes from the Grating-1 SEM as previously described. This was combined with the closed-form solution for the diffracted wave amplitudes for square gratings with heights of 15 μm and 16 μm. The three phase-grating moiré pattern contrast was then computed according to the equations set out in [Mia16], with Grating-1 used as the central grating. Contrast is computed as a function of wavelength and the angular alignment of the central grating about the y-axis. The resulting function can then be integrated over a wavelength and/or angular distribution. In this case, the angular distribution was assumed to be Gaussian with width σ with either a monochromatic or Maxwell-Boltzmann distributed source. A reduction in contrast from the non-square profile of
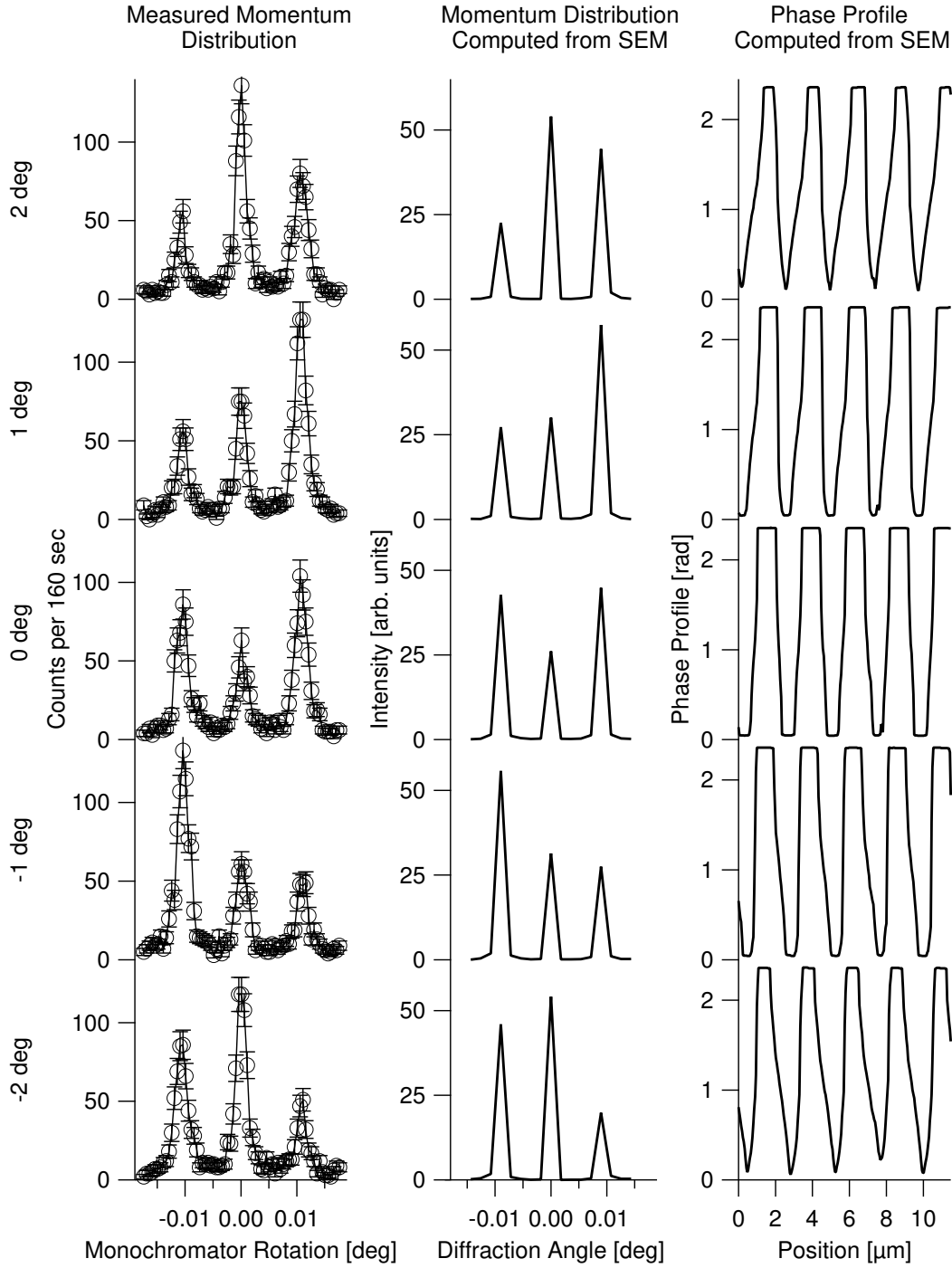
Figure 2.2 The left column of plots is the measured momentum distributions as a function of grating rotation about the y-axis β for Grating-1. Grating rotation ranges from -2 degrees to 2 degrees in one degree steps from bottom to top. Uncertainties are purely statistical, and lines connecting data points are shown for clarity. The middle (right) column shows the diffracted momentum distributions (phase profiles) computed from the SEM micrographs.
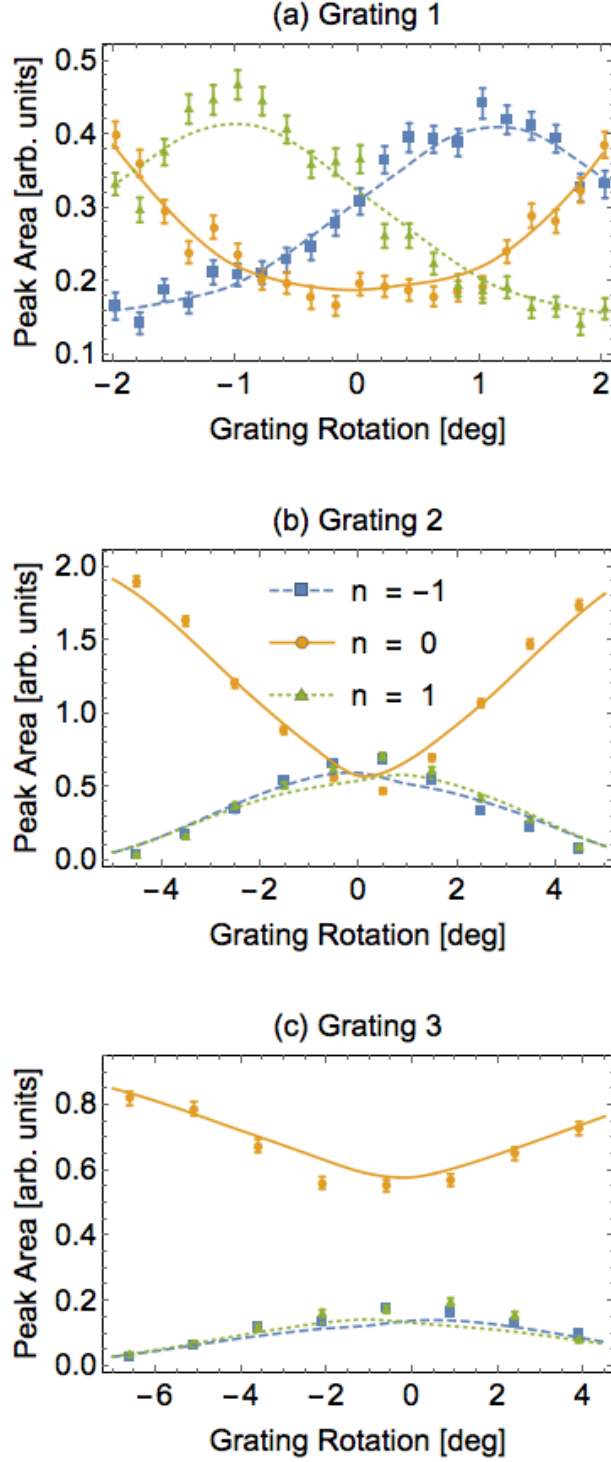
Figure 2.3 Zeroth and first order diffraction peak areas from the measured momentum distributions (data points) and the diffracted momentum distributions computed from the SEM micrographs (solid lines) as a function of grating rotation about the y-axis for (a) Grating-1, (b) Grating-2, and (c) Grating-3. Uncertainties shown are purely statistical.

Grating-1 is clearly visible for all wavelengths (Figure 2.4a), and beam divergence at the level of most neutron experiments ($\sim 0.5°$) also reduces contrast. Note that the effect of beam divergence is only considered for the central grating, which would dominate the effect, as it is twice the height of the other two gratings. Finally, computing contrast versus the angular alignment of the central grating for a neutron beam with a wavelength distribution given by a Maxwell-Boltzmann distribution with average wavelength $\lambda = 5$ Å, as was the case in the first demonstration of a neutron three phase-grating moiré interferometer [Sar18], I show that the lower-than-expected contrast could have occurred from a 3.5 degree misalignment of the central grating about the y-axis. This is a feasible cause of the observed low contrast, because while the grating rotations about the z-axis were optimized for the far-field neutron interferometer demonstration [Sar18], less effort was spent aligning the gratings about the y-axis [Pus18].

x-axis Rotations

Rotations about the x-axis only change the effective thickness of the grating, and therefore the phase profile of the grating changes as

$$\phi(x) \to \frac{\phi(x)}{\cos \alpha}. \tag{2.14}$$

A square wave grating with a phase amplitude $\phi_0 = Nb\lambda h$ with the h the height of the grating of $\phi_0 = \pi$ exhibits no zeroth order peak. The amplitude of the zeroth order peak is proportional to $\cos^2(\phi_0/2)$, and the peak reappears slowly as a function of grating thickness. Demonstration of the zeroth-order peak suppression is shown in Figure 2.5 by rotating Grating-2 about the x-axis.

However, the disappearance of the zeroth-order peak does not hold true for a π phase-grating with sloped walls. Thus, if a π phase-grating is known to be aligned to the y-axis, as in the previous section, the lack of a zeroth order peak is a measure of the squareness of the grating. The almost complete suppression of the zeroth order peak seen in Figure 2.5b matches the SEM micrograph in Figure 2.1b in that Grating-2 is of very high quality and closely estimates a square wave.

z-axis rotations

Grating rotations about the z-axis rotate the diffraction plane of the grating out of the diffraction plane of the monochromator-analyzer pair (the x-z plane in Figure 2.1a). This can be interpreted as effectively lengthening the grating's period by

$$\lambda_G \to \frac{\lambda_G}{\cos \gamma}, \tag{2.15}$$

where γ is the angle of elevation between the crystal and grating diffraction planes about the z-axis. Because the momentum distribution is only narrow in the crystal diffraction direction, rotating the
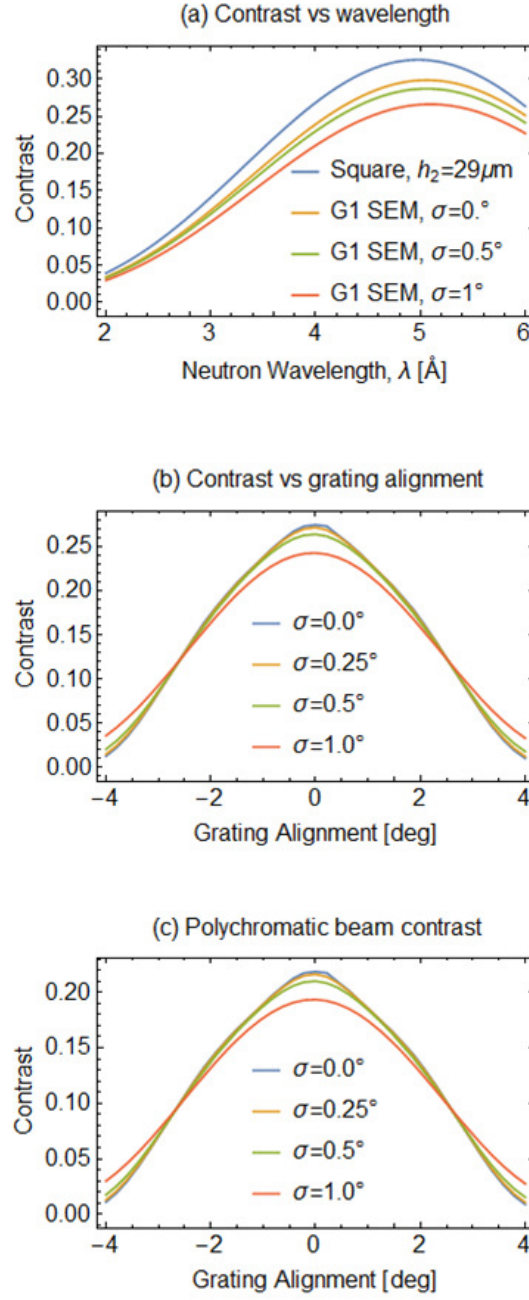
Figure 2.4 Predicted contrast of a three phase-grating moiré interferometer, with the first and third gratings ideal square gratings with heights 15 μm and 16 μm respectively, and the central grating given by the SEM of Grating-1. Contrast is plotted (a) versus wavelength with all gratings aligned to the beam for a few beam divergences and versus central grating angular alignment about the y-axis with (b) $\lambda = 4.4$ Å and (c) λ given by a Maxwell-Boltzmann distribution with average wavelength 5 Å. Also shown in (a) is the ideal contrast for a square grating of height 29 μm. Note the loss of contrast for all wavelengths given the non-square shape of Grating-1.
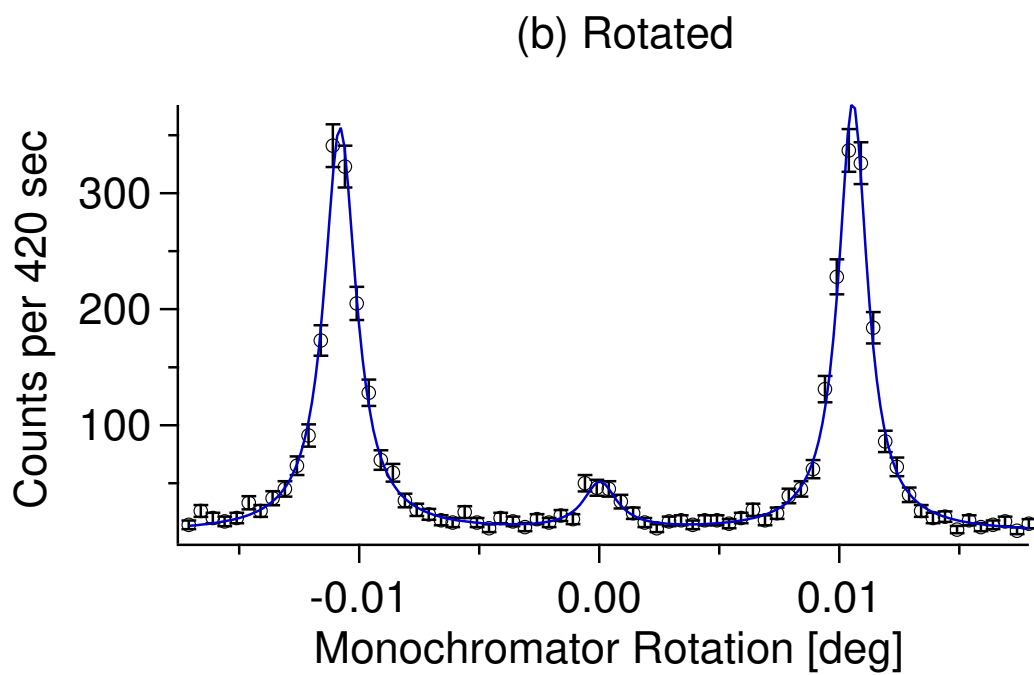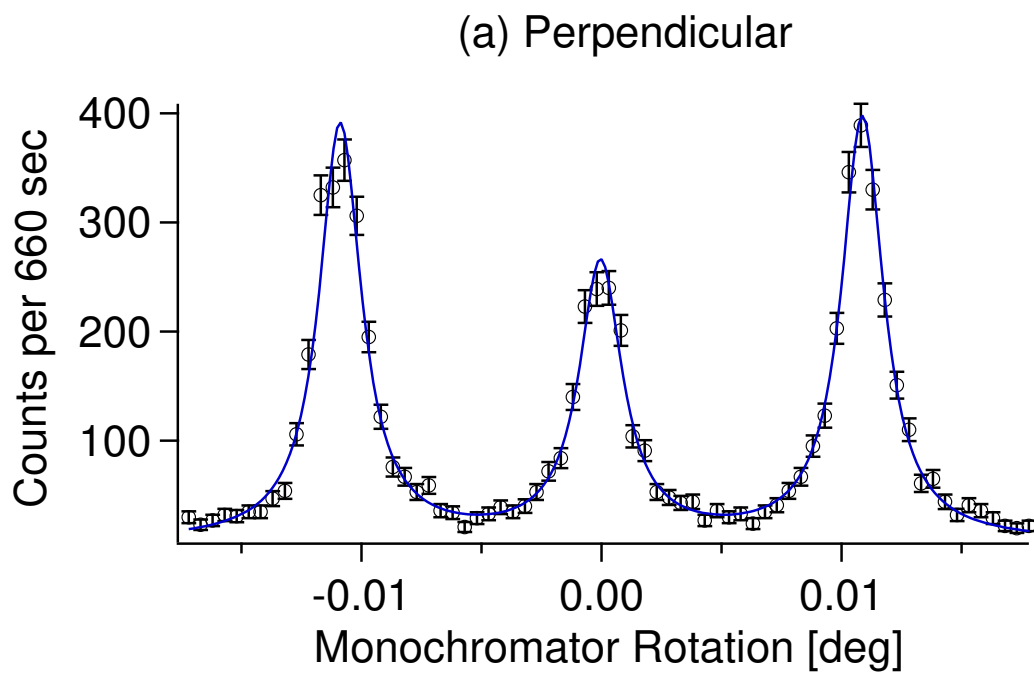
Figure 2.5 Grating-2 diffraction peaks when the grating is (a) perpendicular to the incoming beam and (b) rotated by ~ 40 degrees about the x-axis so that it is approximately acts as a π phase-grating. Uncertainties shown are purely statistical. Lines are fitted Lorentzians.
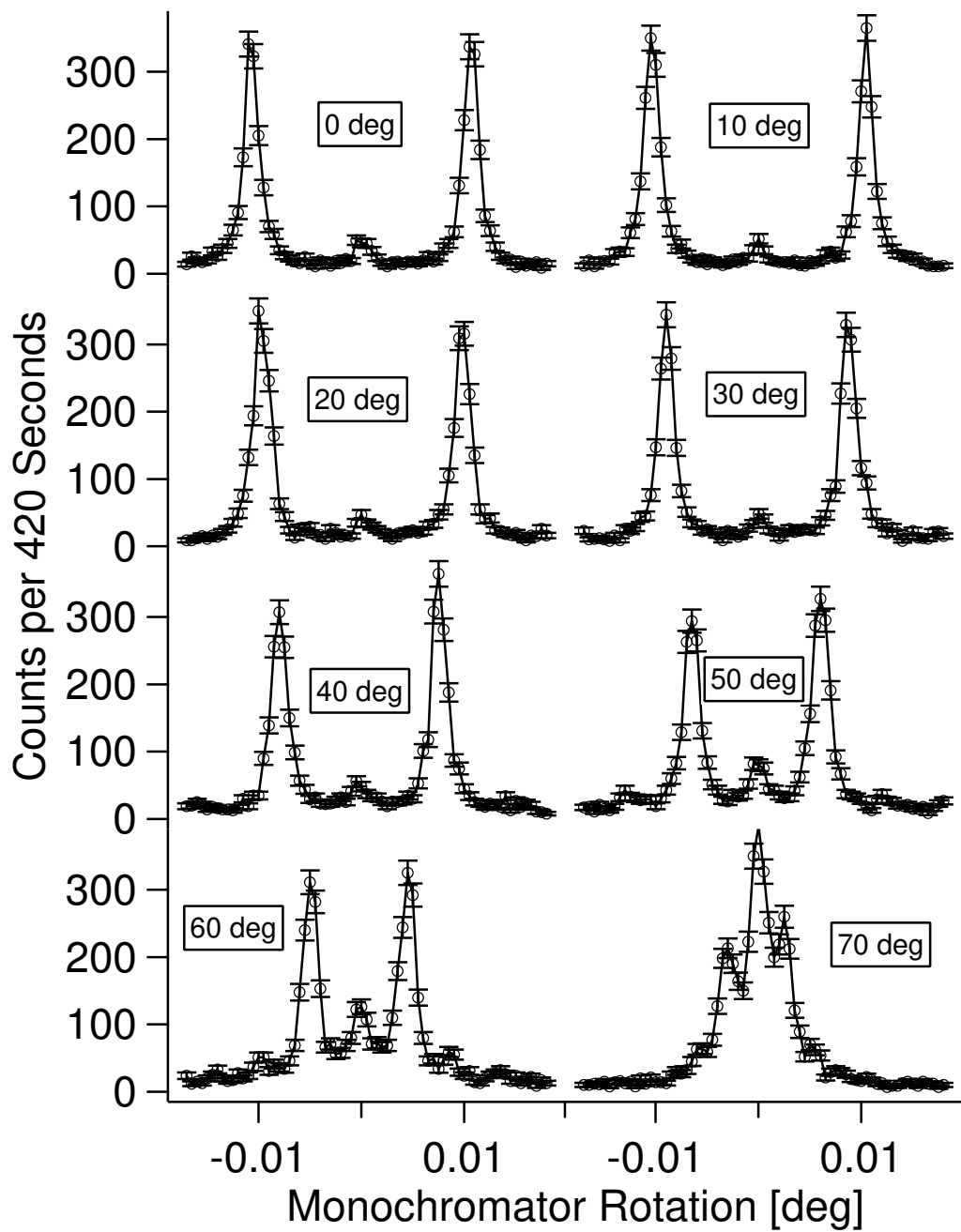
Figure 2.6 Grating-2 diffraction peaks in the $\sim \pi$ orientation as a function of rotation about the z-axis. Uncertainties shown are purely statistical. Lines connecting data points are shown for clarity.
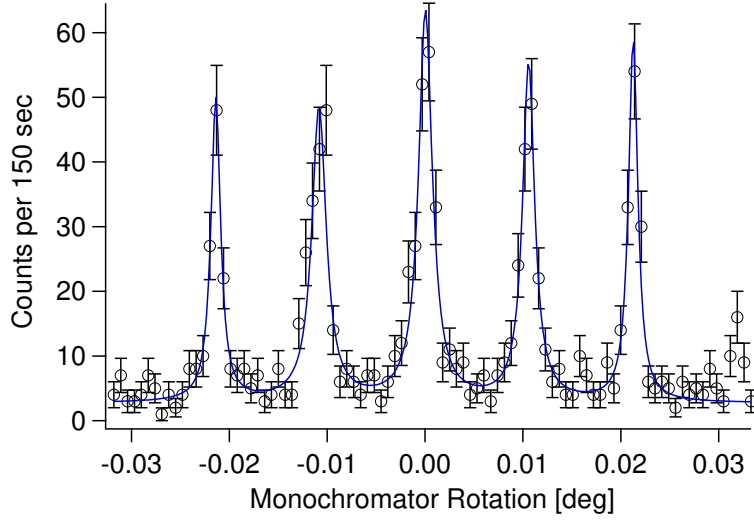
Figure 2.7 Double grating momentum distribution with Grating-1 and Grating-2 and fitted Lorentzians. Each grating was aligned to the beam about the y-axis separately. Uncertainties shown are purely statistical.

σ_x / λ_G. This causes the measured diffraction peaks to overlap as the grating is rotated as shown in Figure 2.6.

z-axis rotations with two gratings

When two gratings with the same period are used in series, the nth-order diffraction peaks from the first grating are diffracted into $(n + m)^{th}$ order peaks, where m is the diffraction order of the second grating. The measured momentum distribution of Grating-1 and Grating-2 operated in series is shown in Figure 2.7. Second order diffraction peaks now have amplitudes similar to the first and zeroth order peaks.

If one or both of the gratings are rotated about the z-axis, Equation 2.13 is modified and the crystal monochromator / analyzer pair will measure peak locations of

$$\theta = \sin^{-1} \left[\frac{\lambda}{\lambda_G} (n \cos \gamma_1 + m \cos \gamma_2) \right] \tag{2.16}$$

for two gratings of the same period λ_G, with γ_1 and γ_2 the z-axis rotation of Grating-1 and Grating-2, respectively. The effect of rotating one grating about the z-axis while leaving the other aligned is shown in Figure 2.8. The number of observable peaks increases because $n + m \cos \gamma$ need not add to an integer between -2 and 2 for n and m restricted to $\{0, \pm 1\}$. As shown in Figure 2.8b seven diffraction peaks were resolvable; though up to nine peaks are possible.

33
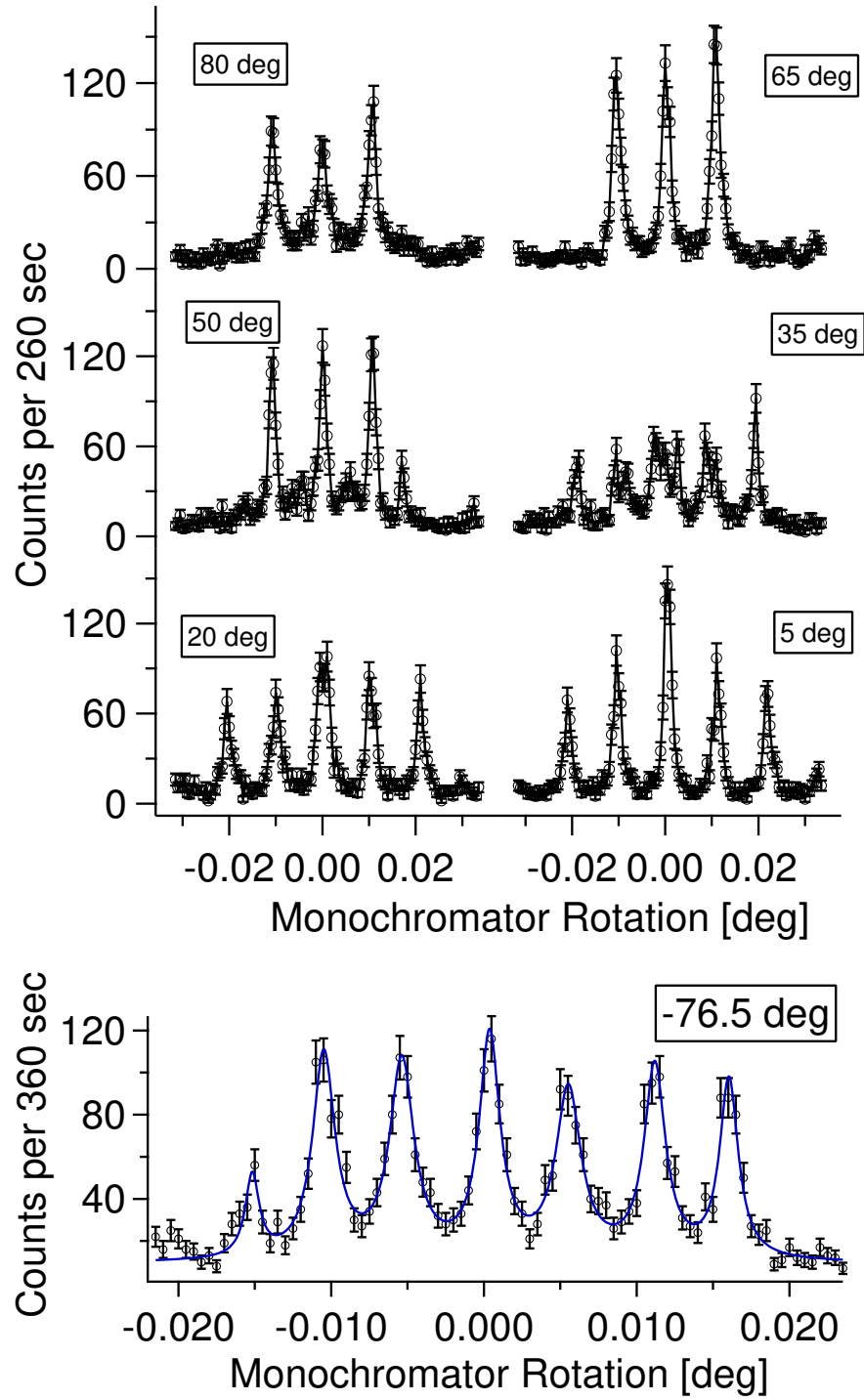
Figure 2.8 Two grating measured momentum distributions with Gratings-1 and -2. Grating-1 is being rotated about the z-axis while Grating-2 was held fixed. Each grating was aligned to the beam about the y-axis separately. Uncertainties shown are purely statistical. In the upper array of plots, lines between data points are shown for clarity. Fitted Lorentzians are shown in the bottom plot.

2.3.3 Conclusion

Characterizing the diffraction spectrum of a neutron phase-grating with a crystal monochromator-analyzer pair elucidates how the grating's alignment with the beam impacts the resulting momentum distribution. Rotations about each of the three axes for the coordinate system defined by the diffraction plane of the grating resulted in different effects.

Rotations about the $y-$axis change the effective phase profile of the grating. This alters the relative diffracted wave amplitudes in a way that can be predicted from the SEM micrographs of the grating. A grating with distorted walls exhibits a gradient in the measured first order diffraction peak areas as a function of rotation about the y-axis, which degrades contrast in a phase-grating neutron interferometer. The overall phase of the grating is set by its depth and the neutron wavelength; rotating the grating about the x-axis changes the effective depth of the grating. This degree of freedom was used to tune a grating to have a phase amplitude of $\phi_0 = \pi$ and almost completely suppress the zeroth order diffraction peak. Rotations about the z-axis tilt the diffraction plane of the grating relative to the monochromator-analyzer pair. This enabled measurements of the outgoing momentum distribution as the grating period approached and became larger than the coherence length of the neutron wave packet.

Measuring the momentum distribution of a neutron beam diffracted by a phase-grating provides a useful grating characterization tool. A crystal monochromator-analyzer pair could also be used in situ for the pre-alignment of grating neutron interferometers, where each grating could be aligned to the incoming beam separately. Finally, the demonstration of the neutron three phase-grating moiré interferometer achieved a low contrast of 3% most likely because it used the trapezoidal-shaped Grating-1, without any rotational optimization, as the middle grating.

2.4 Phase-Recovered Tomography

In the previous section I showed that the SEM micrograph of a phase-grating may be used to correctly predict the momentum distribution of a neutron diffracted by the grating, which can be done as a function of rotational alignment to the beam. The natural question is then whether this operation can be reversed. Whereas, instead of starting with the SEM micrograph and ending with predictions for the diffracted wave amplitudes as a function of grating alignment, is it possible to measure diffraction spectra as a function of grating rotation, then recover the shape of the grating? It turns out that this can be accomplished through a combination of phase-recovery and computed tomographic reconstruction. While in its current state this technique only really applies to periodic samples, it is nonetheless remarkable that the resolution of the reconstructions are on the order of 300 nm. This is much smaller than the typical resolution of neutron imaging, which is sensitive to sample features larger than roughly 20 μm. The spatial resolution of neutron imaging is limited by

the resolution of neutron position sensitive detectors (PSDs), though a range of techniques can push neutron imaging resolution down to a few micrometers [Hus17; Har17; Wil12; Str09].

The present work develops algorithms for using scattering data with a phase retrieval algorithm to perform neutron computed tomography (CT) with a spatial resolution more than an order of magnitude smaller than other neutron imaging techniques. Neutron CT is a very useful form of neutron imaging in its own right that has already been demonstrated with radiographic, phase contrast, differential phase contrast, and dark field signals [All00; Str04; Pus06; Pus07; Str08; Str09], but its image resolution is no better than single projection neutron imaging. By measuring neutron diffraction spectra as a function of sample rotation and using a phase retrieval algorithm to recover the phase in position-space, the need for a high resolution neutron PSD is eliminated. The recovered phase as a function of sample rotation is then tomographically reconstructed, giving a two-dimensional density map of the sample.

The periodic structure of the phase-gratings need only stay constant over the neutron's coherence length ($\sim 35~\mu$m in this case), rendering this technique insensitive to many types of sample defects. The gratings with periods of 2.4 μm were imaged over a beam size of 4.4 mm, but the neutron coherence length and momentum-space resolution of the double crystal diffractometer are such that the resulting real-space image size is the width of ten to twenty grating periods. While the technique is insensitive to a low-density of grating defects, such as a vacancies or dislocations, the overall shape and period of the grating is assumed to be uniform over the entire beam. If a PSD were used instead of the proportional counter used in this experiment, the periodic portions of the sample would need only extend to the pixel size, putting the sub-micrometer imaging of quasi-periodic samples firmly in reach. In practice, the per pixel count rate in such a setup would set an effective minimum beam size.

The phase retrieval and tomographic reconstruction techniques demonstrated here may be useful for a sophisticated USANS spectrometer, such as those described in [Bar05] or [Str07] for a wide variety of sample types. Phased retrieved CT is also used for x-ray coherent diffractive imaging (CDI), though not using a double crystal diffractometer [She15; Rod13; Mar12; Bur11; Lan08], and phase retrieval using the transport of intensity equation (TIE) method for intermediate-field applications is used by phase-contrast neutron imaging [All00; Str09]. The techniques described here are also directly applicable to other neutron scattering measurements, such as small-angle neutron scattering (SANS) [Gli98], where the measured Fourier images are inherently two-dimensional, instead of one-dimensional, as is the case for USANS spectrometers.

The basic outline of the phase retrieved CT algorithm is shown in Figure 2.9. The position-space phase of each measured diffraction spectra is computed using a phase retrieval algorithm. The retrieved phase as a function of β forms a sinogram which is then tomographically reconstructed, giving two-dimensional images of the scattering length density of the gratings. See Section 2.4.1 for a detailed description of the reconstruction algorithm. The reconstructions of the grating scattering length density and SEM micrographs of the three gratings are shown in Figure 2.10. The vertical
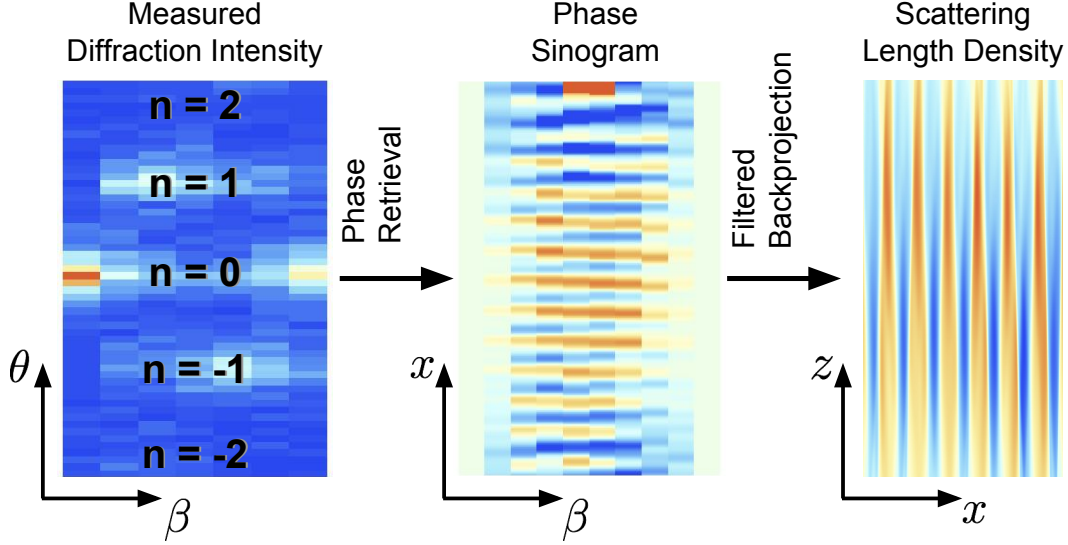
Figure 2.9 Outline of the phase-recovery algorithm. From the measured diffraction intensity, the position-space phase is retrieved, giving the phase sinogram, which is then used to reconstruct the scattering length density of the grating.

walls of Grating-2 and Grating-3 are captured by the reconstructions, while the slope and curvature of the walls of Grating-1 visible in the SEM micrograph are well-represented in the reconstruction. The good agreement between the SEM micrographs and the reconstructions also imply that the grating profile is uniform over a much larger region than what is visible to the SEM. A uniform phase profile is critical for neutron morié interferometers, the recent demonstrations of which used the same phase-gratings [Pus17b; Sar18].

The spatial resolution of the reconstructions are a fraction of the 2.4 μm period. The spatial resolution can be estimated to be about one fourth of $\lambda_G/n_{\max}$. The diffraction spectra were measured over a large enough range to resolve $n = 2$ (which was highly suppressed for these phase-gratings), so the ultimate spatial resolution is estimated to be 300 nm.

2.4.1 Reconstruction Algorithm

As previously discussed, the phase profile $\phi(x)$ of a neutron propagating in the z-direction through a material is given in the Eikonal approximation by

$$\phi(x) = -\frac{1}{\hbar} \int dt \, V_0 \simeq -\lambda \int dz \, \langle b(x,z) \rangle, \tag{2.17}$$
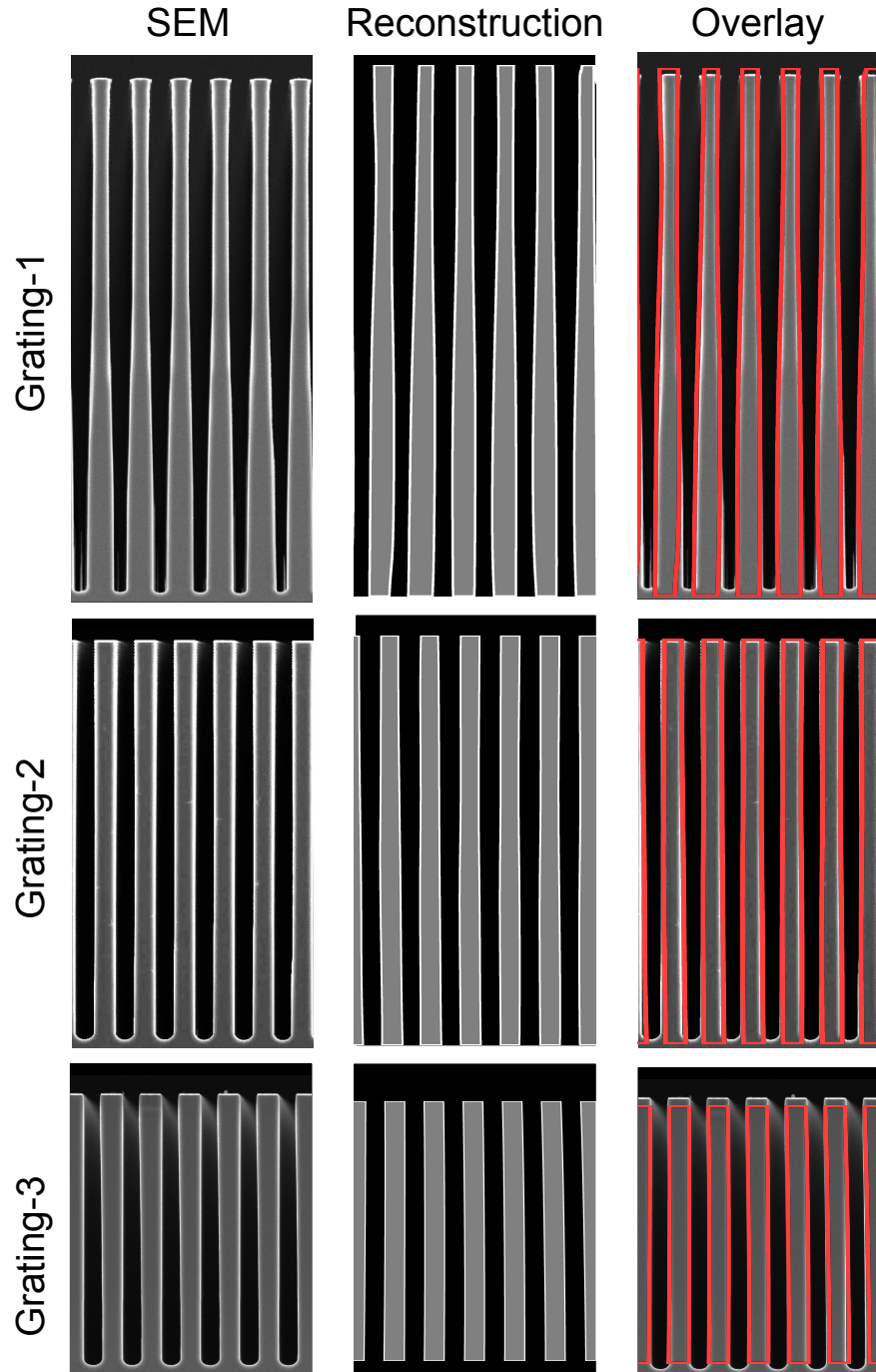
Figure 2.10 SEM micrographs of the phase-gratings (left column) compared to their neutron tomographic reconstructions (middle column). Also shown is an overlay (right column) of the outline of the reconstruction over the SEM. The good agreement between the SEM and reconstructions indicate that the shape of the gratings are uniform over a large range. The walls of Grating-2 and Grating-3 are shown to be very straight, while the sloped walls of Grating-1 appear in both the SEM micrograph and the reconstruction. Edge highlights added to the reconstructions for clarity.
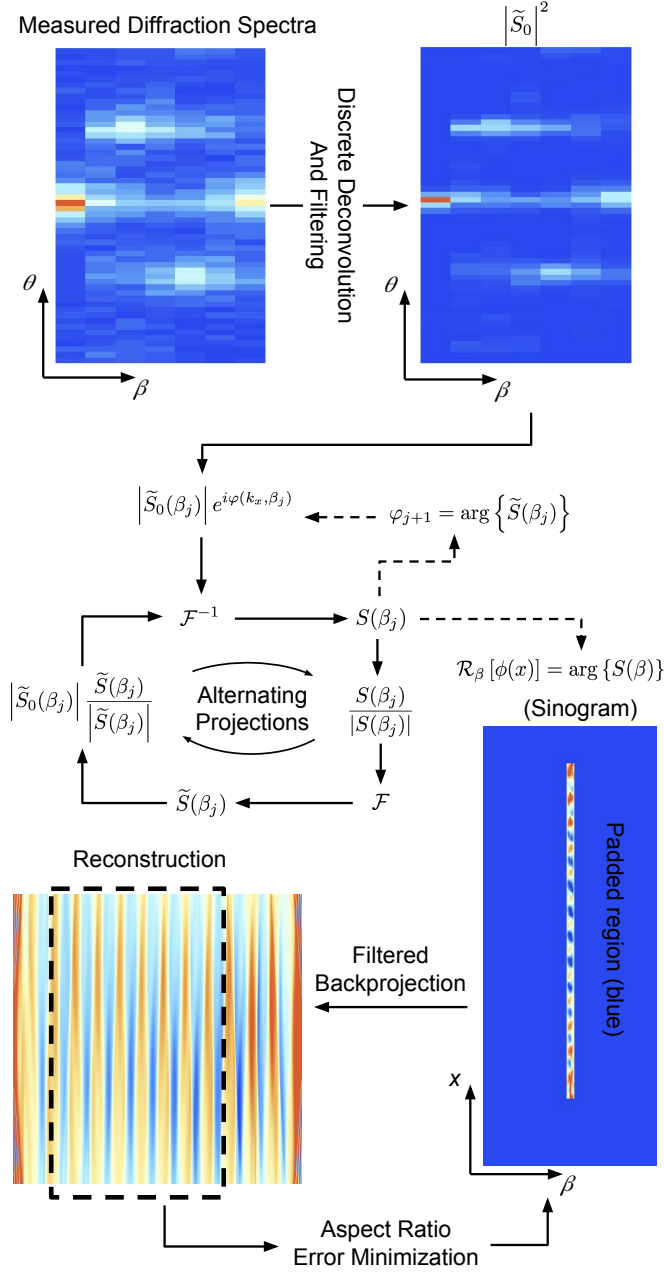
Figure 2.11 Outline of the entire reconstruction process. The raw data is filtered and deconvolved from the average diffraction spectrum of the maximum and minimum measured sample rotation angles. The output is passed into an alternating projections algorithm for each sample rotation angle β, with the previous solution seeding the next step in β. The retrieved position-space phase as a function of x and β forms a sinogram, which is padded with zeros so that β extends from $-\pi/2$ to $\pi/2$. A filtered back projection of the sinogram creates the reconstructed scattering length density. The high-fidelity portion of the reconstruction is made into a binary image, Radon-transformed back into a sinogram, and compared to the original sinogram over the relevant range. The sinogram error is minimized with respect to the aspect ratio of the reconstruction. See text for details.

The goal of tomography is then to reconstruct $\langle b(x, z) \rangle$. I will consider one-dimensional phase profiles, though the extension to two dimensions is straightforward, in which case the reconstruction of the scattering length density is three-dimensional instead of two-dimensional.

To begin, consider writing the momentum space wave function after diffraction

$$\widetilde{\psi} = \mathcal{F}\{e^{-i\phi(x)}\} * \widetilde{\psi}_0, \tag{2.18}$$

where $*$ is the convolution operator. The raw data for phase-recovered tomography is the diffraction spectrum, which is the modulus square of this wave function $P(k_x) = |\widetilde{\psi}(k_x)|^2$.

If diffraction spectra are taken as a function of sample rotation, then the resulting momentum-space wave function is given by

$$\widetilde{\psi} = \widetilde{S}(k_x, \beta) * \widetilde{\psi}_0, \tag{2.19}$$

with the function $\widetilde{S}(k_x, \beta)$ defined in terms of the the grating rotation angle β about the y-axis (see Figure 2.1a) and

$$\widetilde{S}(k_x, \beta) = \mathcal{F}\{S(x, \beta)\}, \tag{2.20}$$

given that

$$S(x, \beta) = e^{-i\mathcal{R}_\beta[\phi(x)]}, \tag{2.21}$$

where integrating over the neutron's trajectory through a sample as a function of sample rotation modifies the effective phase profile (Equation 2.17) via a Radon transformation $\mathcal{R}_\beta[\phi(x)]$. For clarity, I will now drop the k_x and x arguments in $\widetilde{S}(\beta)$ and $S(\beta)$, respectively.

Because the size of the beam is much larger than the grating period, when $P(k_x)$ is averaged over translations x_0 of the incoming state, $\widetilde{\psi}_0(k_x) \to \widetilde{\psi}_0(k_x)e^{ik_x x_0}$, the measured momentum distribution reduces to

$$P_f(k_x, \beta) = \left|\widetilde{S}(\beta)\right|^2 * \left|\widetilde{\psi}_0\right|^2. \tag{2.22}$$

This reduction can also be viewed as an averaging over the phase, or physical translation in the x-direction, of the periodic structure contained in $\phi(x)$. Thus the result is independent of the translation of the periodic structure, rendering this technique insensitive to many types of sample defects.

Before recovering the phase profile $\phi(x)$, the measured momentum distribution is deconvolved with $\left|\widetilde{\psi}_0\right|^2$, which is simply the measured diffraction spectrum with no sample present. For this experiment, discrete deconvolutions are performed between the measured momentum distributions

for each y-axis rotation and the average of the first and last momentum distributions (largest grating rotations), where there were no visible diffraction peaks. Additionally, a two-dimensional Gaussian filter is applied to the resulting $\left|\widetilde{S}(\beta)\right|^2$ with respect to diffraction angle θ and grating rotation β for noise suppression. While this step is sufficient for this data, there are other methods for modifying phase recovery algorithms for noisy data [Lan08; Mar12; Rod13]. With the deconvolved diffraction spectra $\left|\widetilde{S}(\beta)\right|^2$ isolated, I can compute

$$\mathcal{F}^{-1}\left\{\left|\widetilde{S}(\beta)\right|e^{i\varphi(k_x,\beta)}\right\} = e^{-i\mathcal{R}_\beta[\phi(x)]}, \tag{2.23}$$

where $\varphi(k_x, \beta)$ is an unknown function. While the absolute value of $\widetilde{S}(\beta)$ is known from the deconvolution of the incoming and outgoing momentum distributions, the phase $\varphi(k_x, \beta)$ has not been measured. Both the momentum-space phase $\varphi(k_x, \beta)$ and the position-space phase $\mathcal{R}_\beta[\phi(x)]$ can be retrieved with an alternating projections algorithm [She15], an outline of which is shown in Figure 2.11.

2.4.1.1 Phase Recovery

Phase recovery by alternating projections works by alternating between real-space and Fourier-space magnitude constraints [She15]. In this case, the Fourier-space magnitude constraint step is imposed by updating $\widetilde{S}(\beta)$ according to

$$\widetilde{S}(\beta_j) \rightarrow \left|\widetilde{S}_0(\beta_j)\right|\frac{\widetilde{S}(\beta_j)}{\left|\widetilde{S}(\beta_j)\right|} \tag{2.24}$$

in Figure 2.11, where j indexes the grating rotation angle, and $\left|\widetilde{S}_0(\beta_j)\right|$ is the deconvolved measured diffraction spectrum. The real-space magnitude constraint comes from assuming that absorption is negligible, in which case $|S_0(\beta)| = 1$. The function $S(\beta)$ is updated with each iteration of the algorithm by taking

$$S(\beta_j) \rightarrow \frac{S(\beta_j)}{|S(\beta_j)|}. \tag{2.25}$$

Note that there are methods for extending the real-space constraint or phase recovery in general to samples with non-negligible absorption [She15; Bur11].

It is well-known that alternating projection algorithms can be sensitive to the initial phase guess $\varphi(k_x, \beta)$, as many global minima are possible [She15]. Some of these minima may be physical, while others are not. In general, solutions are impervious to complex conjugations, phase offsets, and real-space translations of $S(\beta)$ [GSF12]. This complicates phase retrieval for the purposes of tomography, because the solution space needs to be continuous between rotation steps, $\beta_j \rightarrow \beta_{j\pm1}$.

A number of phase retrieval algorithms for tomography exist [Bur11; Lan08], but a suitable way to ensure a continuous solution space as a function of grating rotation is to initiate the next iteration of $\beta_{j\pm1}$ with the previous solution of $\varphi(k_x, \beta_j)$. Therefore continuity in β-space is imposed by taking

$$\varphi(k_x, \beta_{j\pm1}) \rightarrow \varphi(k_x, \beta_j) \tag{2.26}$$

for an initial guess at each step in β. This is done from the middle out, choosing the initial value of β to correspond to the grating approximately perpendicular with the beam, then seeding subsequent $\varphi(k_x, \beta)$ with that of the previous β in both the positive and negative sample rotation directions.

The initial $\widetilde{S}(\beta)$ is found by passing a random phase $\varphi(k_x, \beta)$ into the alternating projections algorithm. This is repeated two hundred times, and the resulting solution with a minimum error in $\widetilde{S}(\beta)$ and $S(\beta)$ is selected. The error is defined as

$$\epsilon(\beta) = \sum_{k_x} \left(\left| \widetilde{S}(\beta) \right| - \left| \widetilde{S}_0(\beta) \right| \right)^2 + \frac{1}{N} \sum_x \left(|S(\beta)| - 1 \right)^2, \tag{2.27}$$

where N is the number of points in the x-dimension of the array representing $|S(\beta)|$. This term gives equal weighting to the error in position and momentum-space, because the discrete deconvolution process normalizes $\widetilde{S}_0$, such that $\sum_{k_x} \left| \widetilde{S}_0(\beta) \right|^2 = 1$

After the phase of $S(\beta)$ is successfully retrieved, a sinogram is formed with the region beyond maximum rotation padded with zeros. The range of rotation that should be measured will depend on the aspect ratio of the periodic structure. Once the rotation of the sample in radians exceeds its aspect ratio, the sample diffraction will be much weaker, if even measurable. Thus padding the sinogram with zeros as described provides a good estimation of the full sinogram.

2.4.1.2 Tomographic Reconstruction

The tomographic reconstructions of the recovered position-space phase are completed with a filtered back projection [Str09]. A Hann filter is used in this algorithm, though other filtering functions may be selected. The aspect ratio of the reconstructed image is found by performing the filtered back projection, forming a binary image, then Radon-transforming the resulting image and computing the error when compared to the original, recovered phase sinogram. The error is minimized with respect to the aspect ratio of the reconstruction. This is a local minimum in the neighborhood of the aspect ratio as predicted by the known scattering length density of silicon, the grating period measured using the diffraction peak positions and Equation 2.13, and the amplitude of the recovered phase sinusoid when the grating is approximately aligned with the beam.

The binarization of the reconstruction is completed by setting all the reconstruction values below zero to zero and all the values above zero to one. The average value of the reconstructions is zero because of the previously-mentioned padding for large rotation angles. The offset of the measured

and padded portions of the phase sinogram does not affect the reconstruction because of the initial filtering step in the filtered back projection. Note that other methods for discrete tomography [Kri05] may also be useful for samples made of a single material and cut to a certain shape. A comparison of the reconstructions and the SEM are shown in Figure 2.10. The grating color was set to gray with the white outline added to make the images easier to compare.

2.4.1.3   Diffraction Spectrum Truncation

High-order diffraction peaks are difficult to measure, both because their amplitudes tend to die off with increasing n, and because spanning large momentum transfer requires longer measurement times. However, the resolution of the reconstruction will go like $2\pi/Q_{\text{tot}}$, where Q_{tot} is the total range in wavenumber transfer probed. Thus, there is a cost-benefit to measuring higher diffraction orders versus taking more sample rotation steps. However, tomographic reconstructions of the retrieved phase may also improve the spatial resolution of the reconstruction. This is because lower diffraction orders in the measured diffraction spectra $\widetilde{S}(\beta)$ are a mixture of higher-order diffraction peaks. For example, the $n = 1$ diffraction peak in $\widetilde{S}(\beta)$, is a mixture of the $n = 1$ Fourier coefficient of the underlying phase profile and the product of the $n = 2$ and $n = -1$ coefficients, corresponding to the first-order and second-order term in the Born series for $e^{-i\phi(x)}$, respectively. The optimal choice in whether larger diffraction orders or a higher density of sample rotations should be pursued will depend on the overall phase shift of the sample. If samples with large phase shifts are measured, more information is contained in the amplitudes of the low diffraction orders as a function of sample rotation, as more terms in the Born series are relevant. However, the samples considered here, both virtual and experimental, have overall amplitudes of less than 2π.

   To study the performance of the tomographic phase retrieval algorithm as well as how truncating $\widetilde{S}(\beta)$ affects the reconstructions, diffraction spectra from the image shown in Figure 2.12 were simulated. Diffraction spectra were obtained from phase profiles of the Radon-transformed image from -19 degrees to 19 degrees in 2 degree steps. The diffraction spectra were then set to zero after the first, second, or third-order diffraction peaks. The real-space phase was then reconstructed with (1) the phase of the truncated $\widetilde{S}(\beta)$ left intact and (2) after passing $\left|\widetilde{S}(\beta)\right|$ through the described phase retrieval algorithm.

   The reconstructions and the original image are shown in Figure 2.12. The spatial resolution of the reconstructed images increases with increasing $|n|_{\text{max}}$. The reconstructions where the phase was retrieved provide good estimations of the reconstructions using the known phase. However, some artifacts are evident for the phase-retrieved case. There tends to be a region of high-fidelity, with distortions worsening further away horizontally. The region that best estimates the original image is not necessarily centered, nor at the edge of the reconstruction because as previously discussed in Section 2.4.1.1, phase retrieval algorithms produce translationally-invariant solutions. The distortions
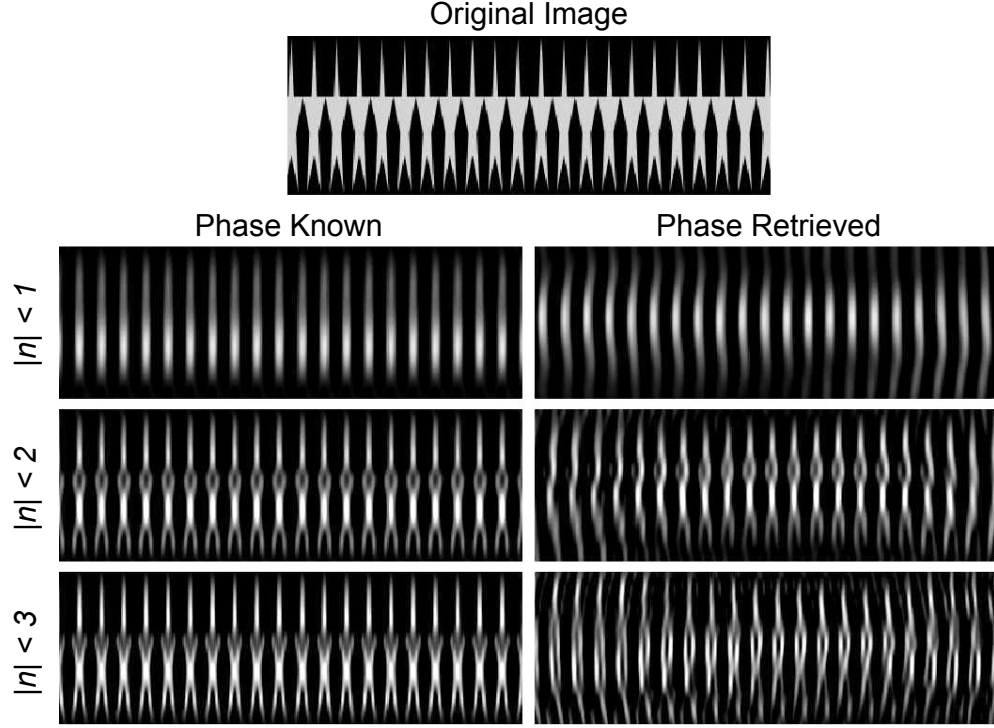
Figure 2.12 Results of phase retrieval algorithm and tomographic reconstruction with the FFT of a Radon transformed image as inputs. A comparison of reconstructions after truncating $\widetilde{S}(\beta)$ past n^{th} order (rows) with the phase of $\widetilde{S}(\beta)$ left intact (left column) and with the phase retrieved (right column).

are of similar character for each level of diffraction order truncation. Similar effects were seen in the reconstructions of the neutron phase-gratings. The best region of the reconstruction was selected visually, as shown with the dashed line in Figure 2.11.

2.4.2 Conclusion

The neutron diffraction spectra of silicon phase-gratings as a function of grating rotation can be used to tomographically reconstruct the shape of the gratings. These reconstructions rely on the periodic structure of the gratings, but nonetheless have a spatial resolution of around 300 nm, which is more than an order of magnitude smaller than other forms of neutron tomography. In principle, even smaller structures may be probed, in which case the spatial resolution of the reconstruction is nominally $\sim 2\pi/Q_{\text{tot}}$, with $Q_{\text{tot}} = \frac{2\pi}{\lambda}(\theta_{\text{max}} - \theta_{\text{min}})$, given by the rotational range of the double crystal diffractometer. However, neutron scattering length densities for most materials are such that tens of micrometers of material are ordinarily required for a 2π phase amplitude given typical neutron wavelengths. Thus it may be difficult to measure structures with amplitudes less than a hundred nanometers.

An upper limit on the length scale to which this type of tomography is sensitive is set by the neutron coherence length of approximately 35 μm. However, the addition of a PSD and possible combination of phase recovery with the USANS refractive signal [Tre03] would allow for much larger reconstructions. Combining phase recovery with other tomography signals is intended for future work.

Further optimization of the phase retrieval and reconstruction algorithms is likely possible. For example, selection of the width of the Gaussian filter employed in the deconvolution step is related to the noise present in the measurement of the diffraction spectra. Analysis of both real and simulated noisy data sets may elucidate how to best set this parameter. Optimization of the cost-benefit between measuring larger ranges in the diffraction spectrum, versus taking a higher density of scans through β-space is also of interest. This problem is likely dependent on the overall phase amplitude of the sample. One may study how these and other changes to the algorithm impact the reconstruction of digital phantoms when the FFT power spectra of the Radon-transformed image are used as inputs for the reconstruction, similar to Figure 2.12. Despite the need for further improvements to the tomographic phase retrieval algorithm, the results presented here indicate that high quality tomographic reconstructions with sub-micrometer resolution of the retrieved phase are possible.

Two-dimensional phase retrieval and three-dimensional tomography could be achieved if data is taken as a function of more than one sample axis of rotation. For a USANS setup, this would likely be a combination of y-axis and z-axis rotation in Figure 2.1a, since only diffraction along the x-axis is measured. For SANS data, where the diffraction spectra are inherently two-dimensional, only one axis of rotation is required for three-dimensional tomography.

In the same way that neutron CT from other signals can be used to visualize materials in a way that is complementary to x-rays [Str09], phase-retrieved neutron tomography can provide unique information about a sample. For example, a periodic structure buried in a matrix would produce a signal for neutrons, but may appear opaque to other forms of radiation, which could be especially beneficial for probing tissue scaffolds such as those described by [Dvi11]. In the case of phase-gratings, creating SEM micrographs entails cleaving the gratings, while neutron phase-recovered CT is both non-destructive and samples a much-larger area of the gratings. Lithium-ion batteries can be imaged using neutrons [Sie11], and batteries with electrode layers that are too thin for traditional neutron imaging, such as those described in [Zha11], could benefit from this method. If the algorithm is adapted to SANS data, in addition to measuring the spacing of oriented biological membranes [Nag11], SANS data could be used to probe the shape of the membranes. The technique could also easily be extended to polarized beams to study magnetic samples. For example, the depth profile of magnetic vortices could be probed [Esk09; KF11; But18]. Additionally, with the recent demonstration of measuring skyrmion lattices using SANS [DS18], it may be possible to generate three-dimensional renderings of skyrmions and provide important insights into their shape [Gil18]. Furthermore, any other sample with periodic structures that have a macroscopic ordering and can

produce diffraction peaks in SANS or USANS data are candidates for phase-recovered neutron tomography. In an unpolarized test case, the shape of neutron phase-grating walls was successfully imaged, and the quality of the tomographic reconstructions was confirmed with SEM micrographs.

CHAPTER 3

DYNAMICAL DIFFRACTION IN PERFECT CRYSTAL NEUTRON INTERFEROMETERS

3.1   Introduction

This chapter details the efforts of three experiments. The first measures Bragg plane misalignments in a neutron interferometer by characterizing multi-crystal rocking curve interference structures in a neutron interferometer (Section 3.3). The results were published in 2017 [Hea17] and are related to the long-standing discrepancy between theory and experiment for the COW gravitationally-induced quantum interference measurements, where COW refers to the authors (Collela, Overhauser, and Werner) of the first paper demonstrating the effect. The second experiment (Section 3.4) examines the effect of annealing a poorly-functioning interferometer, the results of which were published in 2018 [Hea18c]. Finally, in Section 3.5 the relief of subsurface damage in a newly-fabricated "two-blade" neutron interferometer from a combination of annealing and chemical etching is characterized throughout the multistep process. A manuscript detailing the results is in preparation [Hea p]. Before describing each experiment in detail, the effects of dynamical diffraction in neutron interferometers must be described.

3.2   Dynamical Phase Effects in Neutron Interferometers

Dynamical phases are incurred from the momentum-space-dependent filling of the Borrmann fan, as shown in Figure 3.1. For each incoming neutron momentum mode, two degenerate states are excited within the crystal. These two states, $\{\alpha, \beta\}$, are linear combinations of the transmitted, $|\vec{k}\rangle$, and diffracted, $|\vec{k} + \vec{H}\rangle$, states, and propagate in a direction through the crystal that is a function of the incoming momentum mode's misalignment from Bragg. The definition of these states are given in
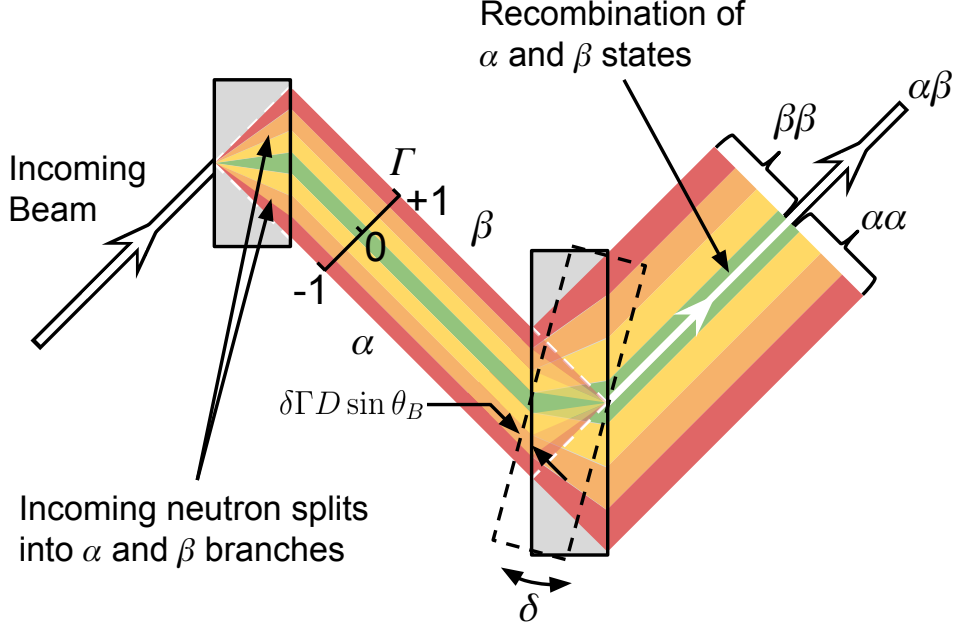
Figure 3.1 Illustration of an incoming neutron beam splitting into the $|\alpha\rangle$ and $|\beta\rangle$ states upon Bragg diffraction in the Laue geometry. The two states are subsequently recombined in a second crystal of equal thickness. Neutron momentum states at the exact Bragg condition (green), occupy the center of the Borrmann fan, while the edges of the Borrmann fan (red) are filled by momentum states that deviate from the Bragg condition. Slightly rotating one crystal relative to the other creates a Γ-dependent phase shift, where Γ is the normalized position in the Borrmann fan. Note that an equivalent diagram exists for cool colors with green in the center and violet at the edges of the Borrmann fan, and the misalignment from the exact Bragg condition is in the opposite direction.

Section 1.4.1. Neutron momentum modes that are exactly on-Bragg propagate orthogonally to $\vec{H}$. Off-Bragg components pass through the crystal at an angle [RW15]

$$\Omega = \pm \arctan \left\{ \frac{(K_H^2 - K^2) \tan \theta_B}{\sqrt{(K_H^2 - K^2)^2 + |v_H|^2}} \right\}, \tag{3.1}$$

where θ_B is the Bragg angle; $\vec{K}$ is the incident momentum mode inside the crystal; and $\vec{K}_H = \vec{K} + \vec{H}$. Note that $K_H^2 - K^2 = 0$ is another way of writing the Bragg condition, such that $\Omega = 0$ at the exact Bragg condition and $\Omega \to \pm \theta_B$ for increasingly off-Bragg momenta. Often the deviation from the Bragg condition is written in terms of an angular misalignment; however, this implies that the Bragg condition is a function of the neutron transverse momentum. In reality, deviation from the Bragg condition is a function of the neutron momentum along the $\vec{H}$ direction, which is a function of both the longitudinal and transverse momenta. Thus, in Figure 3.1 deviation from Bragg is described as a color, with a white beam diffracted from the crystal.

48
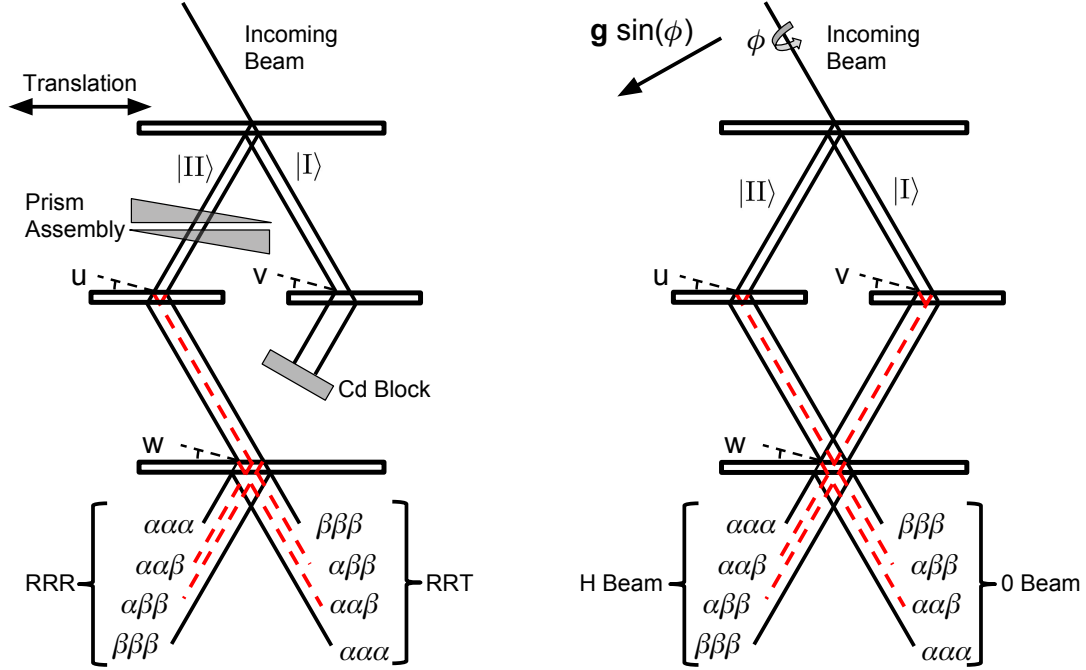
(a) Experimental setup used to measure intrinsic misalignments in an interferometer.

(b) The Mach-Zehnder neutron interferometer geometry used in the COW experiments. Here the direction of gravity is denoted by $\vec{g}\sin(\phi)$, where ϕ is the interferometer tilt about the incoming beam axis.

Figure 3.2 Experimental geometries for (a) measuring Bragg plane misalignments in a neutron interferometer and (b) the COW experiments.

In the case of multiple diffracting crystals, the two-fold degenerate splitting of each incoming $|\vec{k}\rangle$ continues, such that there is a 2^N splitting after N crystals. The α and β states are labeled according to the first crystal, corresponding to the sign of the current density, $J_x^{\alpha,\beta} = \pm\text{sign}\,(H_{x0})\,|J_x|$, relative to $\vec{H}$ for the first crystal, $\vec{H}_0$. If all of the crystals have the same thickness, there are $N+1$ combinations of α and β reflections or transmissions leaving the Nth crystal with $N-1$ recombination points (Figure 3.2). If the crystals are perfectly aligned and have the same thickness, then there is no phase shift between the permutations of α and β states for each of the $N-1$ recombination points. However, if one crystal is misaligned with respect to another, a momentum-dependent phase shift arises, which quickly leads to dephasing and a loss of contrast in the interferometer. This effect is why perfect crystal neutron interferometers must be cut from single, float-zone grown silicon ingots. Additionally, the interferometer blades are made to have the same thickness to a few micrometers to avoid similar dephasing effects.

3.2.1 Two Crystal Geometry

Because the structure factor determines the width of the momentum space acceptance of the crystal, the deviation from the exact Bragg condition is usually normalized by the structure factor

$$\eta = \frac{K_0^2 - K_H^2}{2v_H}, \tag{3.2}$$

such that the Darwin width spans from $\eta = -1$ to $\eta = +1$. Bragg diffraction in the Laue geometry results in a dispersion relation that places large-η momentum components at the edges of the Borrmann fan and small-η components closer to the center. The phase that governs this dispersion relation is given by

$$\varphi_D(\eta) = \pm \tan \theta_B \frac{v_H D}{H} \sqrt{\eta^2 + 1} \tag{3.3}$$

for a crystal of thickness D and is positive (negative) for the α (β) branches. If two crystals are operated successively, then four beams exit the second crystal, corresponding to the permutations of the α and β branches for each crystal. For thick crystals, the $|\alpha\alpha\rangle$ and $|\beta\beta\rangle$ do not overlap, but the $|\alpha\beta\rangle$ and $|\beta\alpha\rangle$ states are able to interfere with each over for all η.

If the Bragg planes in the two crystals are slightly misaligned, such that $\epsilon = \eta_2 - \eta_1$ and $\eta = (\eta_1 + \eta_2)/2$, then the phase shift between the two states to first order in ϵ is

$$\Delta\varphi_D = \epsilon \tan \theta_B \frac{v_H D}{H} \left(\frac{\eta}{\sqrt{\eta^2 + 1}} \right) = \epsilon \frac{\pi D}{\Delta_H} \Gamma = HD\Gamma\delta, \tag{3.4}$$

where $\Delta_H \sim (10 \text{ to } 100) \ \mu$m is the pendellösung length; δ is the angular misalignment between the Bragg planes of the two crystals; and

$$\Gamma = \frac{\eta}{\sqrt{\eta^2 + 1}}, \tag{3.5}$$

which has a range of -1 to $+1$. This phase shift also has a geometric interpretation, with Γ giving the position in the Borrmann fan. In this case Γ in terms of Ω is [RW15]

$$\Gamma = \frac{\tan(\Omega)}{\tan(\theta_B)}. \tag{3.6}$$

With the spatial definition of Γ, the resulting difference in path length between the $|\alpha\rangle$ and $|\beta\rangle$ branches for a small rotation δ of the second crystal is then $2\delta\Gamma D \sin \theta_B$ as is shown in Figure 3.1. Thus the phase shift between the $|\alpha\beta\rangle$ and the $|\beta\alpha\rangle$ states is

$$\Delta\varphi_D = k\Delta x = k(2\delta\Gamma D \sin \theta_B) = HD\Gamma\delta \tag{3.7}$$

where k is the neutron wave vector outside the crystal; θ_B is the Bragg angle; Δx is the change in path length from rotating the crystal; and I have used Bragg's law to write this expression in terms of H. This matches Equation 3.4, which illustrates the geometric interpretation of the phase shift.

Using the η-dependent reflection coefficients (Section 1.4.1) and dynamical phase shift φ_D, the intensity in the twice-diffracted beam of two slightly misaligned crystals of the same thickness D is

$$I_{RR}(\delta) = \int_{-1}^{1} d\Gamma \sqrt{1 - \Gamma^2} \cos\left(HD\Gamma\delta\right) = \pi \frac{J_1(HD\delta)}{HD\delta}, \tag{3.8}$$

where $J_1(x)$ is a Bessel function of the first kind. This function is a sharp peak with respect to δ with a FWHM on the order of of 10 nrad to 100 nrad depending the the thickness of the crystal and the Bragg condition. The integral is taken over all Γ, because the Darwin width of the crystal is generally much smaller than the divergence and/or wavelength spread of the incoming beam. The $\sqrt{1 - \Gamma^2}$ envelope is the result of the higher reflectivity for $\Gamma \to 0$, compared to $\Gamma \to \pm 1$.

If the two crystals are allowed to have unequal thicknesses, and all terms included, the intensity for a twice Bragg reflected neutron is (up to a normalization constant)

$$\begin{aligned}
I_{RR} = \int d\Gamma dk_\zeta \, |\langle\psi|k_\zeta\rangle|^2 \, \sqrt{1 - \Gamma^2} \Bigg\{ & 1 - P(D_2) + \\
& + \frac{1}{2} \cos\left(HD\delta\Gamma\right) \left[P(D_2 - D_1) - 2P(D_1) + P(D_1 + D_2) \right] \Bigg\},
\end{aligned} \tag{3.9}$$

where D_1 and D_2 are the thicknesses of the first and second diffracting crystals; δ is the angular Bragg-plane misalignment of the two crystals in the $\vec{k}, \vec{H}$ plane; k_ζ is the neutron momentum along the Bragg planes (see Figure 3.3); and $|\langle k_\zeta|\psi\rangle|^2$ is the momentum-space intensity profile of the incoming wave packet along z. The function $P(D)$ is

$$P(D) = \cos\left(\frac{D|v_H|}{k_\zeta\sqrt{1 - \Gamma^2}}\right), \tag{3.10}$$

which is the origin of pendellösung interference and is treated in detail in Chapter 4. Except for $P(D_2 - D_1)$, the $P(D)$ terms correspond to the overlap of states with different combinations of α and β reflections.

The width of $|\langle k_\zeta|\psi\rangle|^2$ is determined by the preparation of the beam, including the phase space density of neutrons reflected down the guide, the monochromator crystal, and any slits between the monochromator and the interferometer. For the NIST interferometry beamlines, typically $\sigma_{k_\zeta}/k_\zeta \sim 0.002\,\mathrm{rad}$, and for typical interferometer crystal thicknesses $|v_H|D/k_\zeta \sim 200$. As a result,
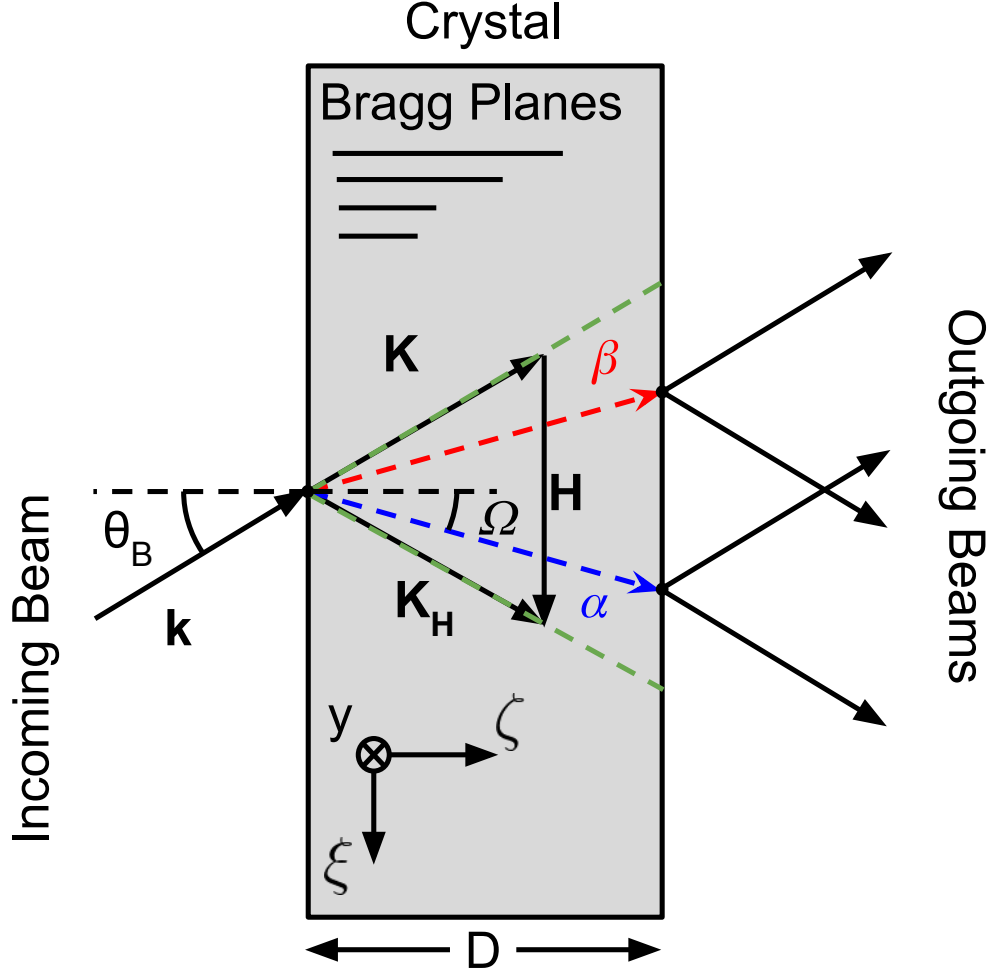
Figure 3.3 An incoming momentum state, $|\vec{k}\rangle$, excites two degenerate, $\{\alpha, \beta\}$, states within the crystal. These two states become spatially separated according to the μrad misalignment of $|\vec{k}\rangle$ from the exact Bragg condition. Each incoming neutron wave packet fills the *entire* Borrmann fan (outlined by green-dashed lines).

the $P(D)$ term is attenuated by only a few percent after the integration of $|\langle\psi|k_\zeta\rangle|^2$ over k_ζ. However, the range of Γ of $\{-1, 1\}$ and the $\sqrt{1-\Gamma^2}$ envelope ensures that the highly oscillatory term

$$P(D) = \cos\left(\frac{|v_H|D}{k_\zeta\sqrt{1-\Gamma^2}}\right) \sim \cos\left(\frac{200}{\sqrt{1-\Gamma^2}}\right) \tag{3.11}$$

integrates to a small value. In other words, pendellösung interference terms dephase very quickly for the crystal thicknesses typically used in neutron interferometers of $D \sim 2.5\,\mathrm{mm}$, when the entire Borrmann fan is filled. If a slit after the crystal is used to select only small values of Γ, then

pendellösung interference can be resolved (see Chapter 4). For the purposes of neutron interferometers $P(D)$ terms are often ignored, and most authors use the approximation

$$I_{RR} \rightarrow \int d\Gamma \sqrt{1 - \Gamma^2} \left\{ 1 + \frac{1}{2} \cos\left(HD\delta\Gamma\right) \right\} = \frac{\pi}{2}\left(1 + \frac{J_1(u)}{u}\right), \tag{3.12}$$

where J_1 is the first order Bessel function of the first kind, and $u = HD\delta$. This approximation of letting $P(D) \rightarrow 0$ is usually a good one and can be extended to any geometry of diffracting crystals.

3.2.2 Dynamical Phases in a Mach-Zehnder Interferometer

The typical Mach-Zehnder geometry is depicted in Figure 3.2b, where two spatially separated, coherent beams (I and II) are produced in the first crystal "blade" of the interferometer, where blade refers to the fact that each of the diffracting components of the interferometer are blade-like protrusions emanating from a common base. The two beams are recombined in the final blade, resulting in two interfering beams, the 0 Beam and H Beam. The COW experiments utilize this geometry. The response of a Mach-Zehnder neutron interferometer to misalignments may be described with three independent variables, $\{u, v, w\}$ (Figure 3.2), which describe the misalignment between the two mirror and analyzer crystal blades relative to the initial splitter crystal blade. Typically, this relative alignment between the blades is assumed to be perfect, even over the relatively large dimensions of the crystal ($\sim 10\,\text{cm}$). This assumption, however, is only justified at the microradian level while outside this alignment the interferometer would cease to function. Considered here is how the relative imperfect alignment of these blades at levels over one hundred times smaller than the Darwin width $\Theta_D \sim 10^{-5}$ rad impacts the performance of the interferometer due to interference effects arising from dynamical Bragg diffraction. To characterize the effects of blade misalignment, consider the state leaving the interferometer:

$$|\psi\rangle = |\text{I}\rangle + |\text{II}\rangle, \tag{3.13}$$

where the states from paths I and II are coherently added together. Then let

$$|\psi\rangle \rightarrow |\text{I}(v, w)\rangle + |\text{II}(u, w)\rangle e^{i\phi_0}, \tag{3.14}$$

where ϕ_0 is the non-dynamical phase shift between the two paths of the interferometer and $|\text{I}(v, w)\rangle$ and $|\text{II}(u, w)\rangle$ are states that depend on the misalignments $\{u, v, w\}$. Notice that $|\text{I}\rangle$ is not a function u and $|\text{II}\rangle$ is not a function v, so that the misalignment of the mirror crystals for each path need not be the same. Comparing the intensity of the two beams exiting the interferometer to the measured interferogram gives

$$\langle\psi|\psi\rangle = A + B\cos\left(\phi_0 + \varphi_D\right) = \left(\langle\text{I}| + \langle\text{II}|e^{-i\phi_0}\right)\left(|\text{I}\rangle + |\text{II}\rangle e^{i\phi_0}\right). \tag{3.15}$$

The measured, dynamical phase, φ_D is then [Wer88]

$$\varphi_D = \arctan\left\{-\frac{\mathrm{Im}\left(\langle\mathrm{I}|\mathrm{II}\rangle\right)}{\mathrm{Re}\left(\langle\mathrm{I}|\mathrm{II}\rangle\right)}\right\}, \tag{3.16}$$

and the contrast is given by

$$C = \frac{B}{A} = \frac{2\sqrt{\mathrm{Im}\left[\langle\mathrm{I}|\mathrm{II}\rangle\right]^2 + \mathrm{Re}\left[\langle\mathrm{I}|\mathrm{II}\rangle\right]^2}}{\langle\mathrm{I}|\mathrm{I}\rangle + \langle\mathrm{II}|\mathrm{II}\rangle}. \tag{3.17}$$

In general $|\mathrm{I},\mathrm{II}\rangle$ may be written in terms of the $\{\alpha,\beta\}$ branches

$$|\mathrm{I},\mathrm{II}\rangle = |\alpha,\alpha,\alpha\rangle_{\mathrm{I},\mathrm{II}} + |\beta,\beta,\beta\rangle_{\mathrm{I},\mathrm{II}} + \left(|\alpha,\alpha,\beta\rangle_{\mathrm{I},\mathrm{II}} + |\alpha,\beta,\alpha\rangle_{\mathrm{I},\mathrm{II}} + |\beta,\alpha,\alpha\rangle_{\mathrm{I},\mathrm{II}}\right) + $$
$$\left(|\alpha,\beta,\beta\rangle_{\mathrm{I},\mathrm{II}} + |\beta,\alpha,\beta\rangle_{\mathrm{I},\mathrm{II}} + |\beta,\beta,\alpha\rangle_{\mathrm{I},\mathrm{II}}\right). \tag{3.18}$$

Different combinations of α and β reflections/transmissions give pendellösung terms similar to those already discussed in reference to Equation 3.9. Therefore, in the pendellösung dephasing approximation, the overlap between states with different numbers of α and β reflections/transmissions are taken to be zero when forming $\langle\mathrm{I},\mathrm{II}|\mathrm{I},\mathrm{II}\rangle$. Expressions for $\langle\mathrm{I},\mathrm{II}|\mathrm{I},\mathrm{II}\rangle$ for the 0 Beam are given in Appendix B.1.

Intrinsic Bragg plane misalignments in a neutron interferometer may be measured by assessing the structure of multiple-reflection rocking curves (Figure 3.2). In the pendellösung dephasing limit, the interfering portion of a neutron undergoing three Bragg reflections is [PR84]

$$\begin{aligned}
I_{RRR} &= \int_{-1}^{1} d\Gamma (1-\Gamma^2)^{\frac{3}{2}} \left\{3 + 2\cos\left[(u-w)\Gamma\right] + 2\cos\left[u\Gamma\right] + 2\cos\left[w\Gamma\right]\right\} \\
&= 6\pi\left(\frac{3}{16} + \frac{J_2(u-w)}{(u-w)^2} + \frac{J_2(u)}{u^2} + \frac{J_2(w)}{w^2}\right),
\end{aligned} \tag{3.19}$$

where $u = HD\delta_{1,2}$ and $w = HD\delta_{1,3}$, with $\delta_{i,j}$ the angular misalignment between the ith and j^{th} crystals. The term u in Equations 3.12 and 3.19 are equivalent which allows for an absolute measurement of the misalignment

$$HD\delta_{2,3} = u - w. \tag{3.20}$$

To measure such rocking curves, subsequent crystals need to be rotated at the nanoradian level. This would be very difficult experimentally. Fortunately, by using a refracting prism, very small deflections can be generated. The beam deflection due to a refracting prism is

$$\delta_p = \left(\frac{\lambda^2}{2\pi} \sum_i N_i b_i \right) \tan\gamma \sin\phi \left(\cos\theta + \sin\theta \frac{\tan\gamma \sin\phi + \tan\theta}{1 - \tan\gamma \sin\phi \tan\theta} \right), \quad\quad (3.21)$$

where γ is the pitch of the prism; θ is the angle between the prism rotation axis and the neutron beam; λ is the neutron wavelength; α is the pitch of the prism; ϕ is the tilt of the prism about the beam axis; and the sum is over the number densities N_i and scattering lengths b_i of each species.

3.3 Dynamical Diffraction and Gravitationally-Induced Quantum Interference

One of the first neutron interferometry measurements demonstrated that Earth's gravitational field could be used to create a phase shift between paths in the interferometer by rotating the interferometer about the incoming beam axis. This launched a twenty-five year effort to perform a precision measurement of the neutron's acceleration in Earth's gravity g. These experiments, beginning in 1975 are commonly referred to as the COW experiments after Colella, Overhauser and Werner, the authors of the first measurement [Col75]. When other forms of matter wave interferometry showed extremely precise measurements of g to agree with measurements made with macroscopic objects [RW15], the effort to do so with perfect crystal interferometry stalled, leaving a still long-standing discrepancy between theory and experiment for the measurement of g using perfect crystal neutron interferometers [Wer88; Lit97; Lit98]. Specifically, gravitationally-induced quantum interference has since been found to agree with theory at the 0.1% level using a spin-echo neutron interferometer [Haa14] and at 0.08% with a very cold grating neutron interferometer [Zou00]. Atom interferometer experiments have confirmed theory at the part per billion level [RW15]. What follows is an experiment that demonstrates the intrinsic Bragg plane misalignments within typical perfect crystal neutron interferometers exists on the order of 10 nrad. This misalignment attenuates the magnitude of the dynamical phase corrections employed by precision versions of the COW experiments and is shown to be of the correct size to explain the over twenty-year discrepancy between theory and experiment.

3.3.1 Measuring Bragg Plane Misalignments in a Neutron Interferometer

Intrinsic Bragg plane misalignments may be probed by creating multi-crystal rocking curves, whose functional form is given by Equations 3.12 and 3.19. Measurements were made with two of the NIST neutron interferometers, one of which is shown in Figure 3.4. For the first interferometer, a single set of RR and RRR curves were measured over a long period of time, so that the uncertainty in the peak position would be low and the fine structure ($P(D) \neq 0$) of the RR curve could be analyzed (see Section 3.3.4). For the second interferometer, the RR and RRR curves were measured as a function
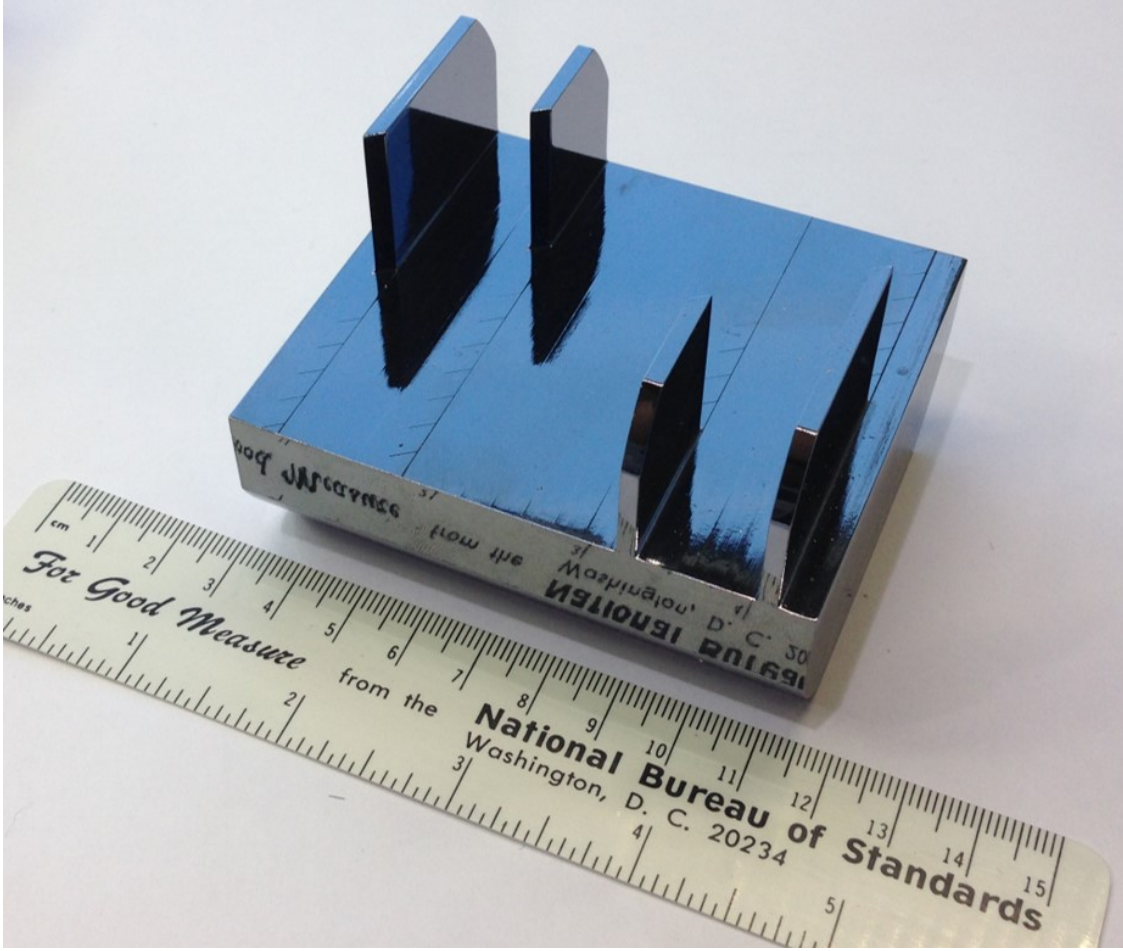
Figure 3.4 The crystal interferometer used for measuring intrinsic Bragg plane misalignments. Four blades protrude from a common base.

of interferometer translation to measure any spatial dependence of the Bragg plane misalignments between crystal blades.

To measure rocking curve interference peaks, an assembly of two fused silica prisms, each with a pitch of 6°, was placed between the first and second blades of a three-blade interferometer (Figure 3.2a). The prism assembly is the same as the one used in [Pus07]. The beam transmitted through the first crystal blade was blocked. The prisms were counter-rotated to deflect the neutron beam in the $\vec{k}, \vec{H}$ plane, generating interference peaks in two detectors, labeled RRR and RRT. The $RRR+RRT$ (equivalent to RR) and RRR signals are of interest here and are given by Equations 3.12 and 3.19, respectively. The prisms are counter-rotated (Figure 3.5) and deflect the beam according to Equation 3.21. For the first set of measurements, the prism assembly was aligned parallel to the interferometer blades, so that $\theta \simeq \theta_B$.

For the second set of measurements, the prism assembly was aligned perpendicular to the beam such that $\theta \simeq 0$. The horizontal spatial dependence of the rocking curve peak positions was measured by translating the interferometer relative to the beam by 1 cm in 1 mm steps, with rocking curves taken for each translational position (Figure 3.7). With the translation of the interferometer, the crystal volume probed by neutrons is also shifted. Rocking curve position vs translation thus gives a one dimensional map of the Bragg-plane misalignment between crystal blades as a function of position.

3.3.2 Peak Location and Sensitivity

To assess a rocking curve's tendency to drift (similar to the way the phase of a Mach-Zehnder neutron interferometer drifts), the peak position of each RR rocking curve for the first crystal was found by fitting to Equation 3.30, which is defined in the next section. The set of 89 rocking curve positions fit a Gaussian distribution $(\exp[-(x-\mu)^2/(2\sigma^2)])$, with $\mu = (16.9 \pm 0.4)$ nrad and $\sigma = (3.24 \pm 0.34)$ nrad (Figure 3.6). The peak locations are stable, and the uncertainty matches that which is predicted by counting statistics; the average peak location uncertainty was 2.94 nrad. Furthermore, averaging the 89 individual rocking curve positions gives (16.78 ± 0.31) nrad, which is indistinguishable from fitting the combined data to Equation 3.30. This yields a peak location of (16.37 ± 0.31) nrad. The average reduced χ^2 (DOF $= 31 - 4$) for the 89 individual rocking curve fits was 1.1. The reduced χ^2 for the combined fit was 2.8.

The interference structure outside the central peak is undetectable in an individual rocking curve, yet can be resolved from summing many rocking curves together. Complications arising from pendellösung interference may explain why the χ^2 from the single rocking curve is inferior to the χ^2 from 89 individual fits (See Section 3.3.4). The uncertainty in the central peak location corresponds to an angular resolution for the setup used here of 0.35 nrad misalignment between crystals for two days of measurement. This sensitivity can conceivably be increased by two or more orders of magnitude by using thicker diffracting crystals, blocking the non-interfering portions of the outgoing beam, and running a dedicated experiment for $\sim$1 month, making angular deflection measurements at the picoradian level a possibility.

3.3.3 Intrinsic Bragg-Plane Misalignment

Intrinsic misalignment of Bragg planes has been observed in two-blade interferometers before by Arthur et al. [Art85]. In this experiment the intrinsic misalignment between the second and third blade is measured. The intrinsic misalignments elsewhere in the interferometer are indistinguishable from the relative alignment of the prisms. Fit functions are formed by substituting
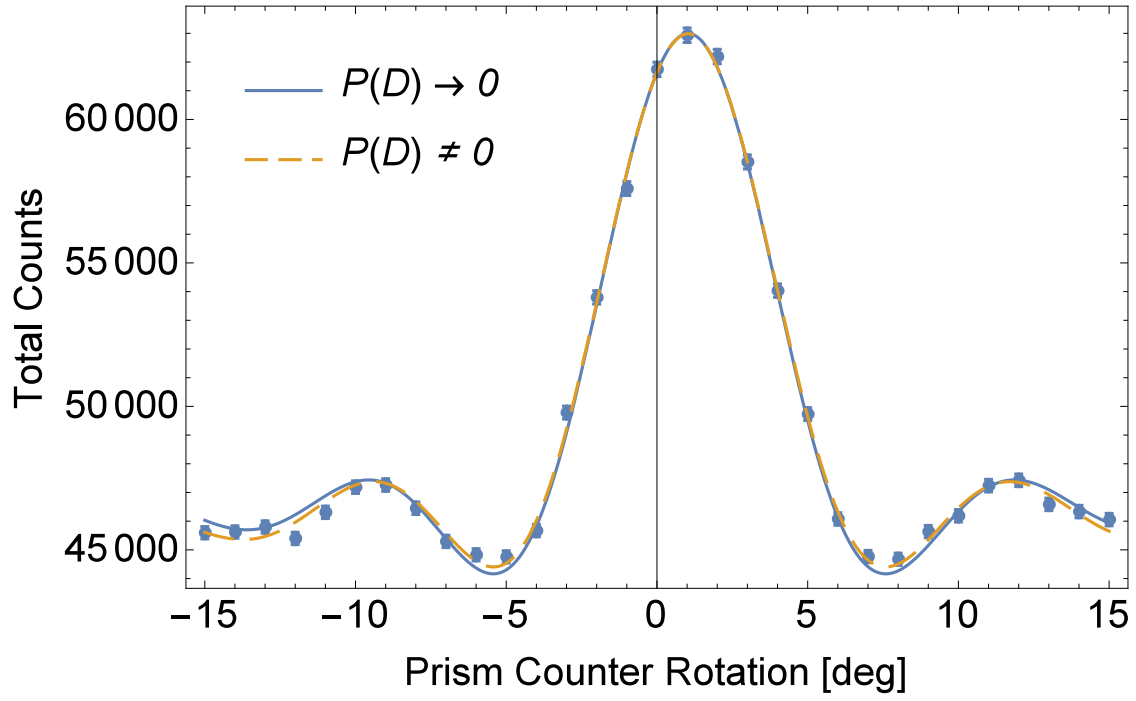
(a) *RR* Intensity. The $P(D) \to 0$ fit uses Equation 3.30, and the $P(D) \neq 0$ fit is explained in Section 3.3.4.
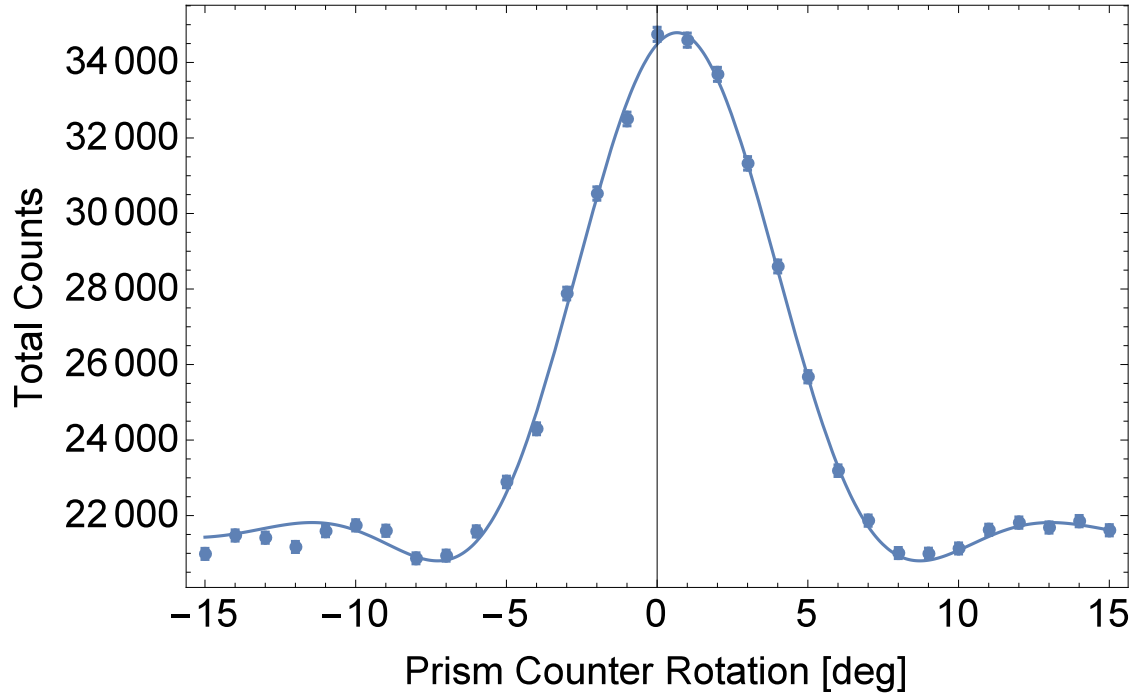
(b) The *RRR* Intensity with the fit to Equation 3.25.

Figure 3.5 *RR* and *RRR* summed intensity with fits. Integrated count time was 89 min. per point. Each plot is the sum of 89 individual rocking curves.
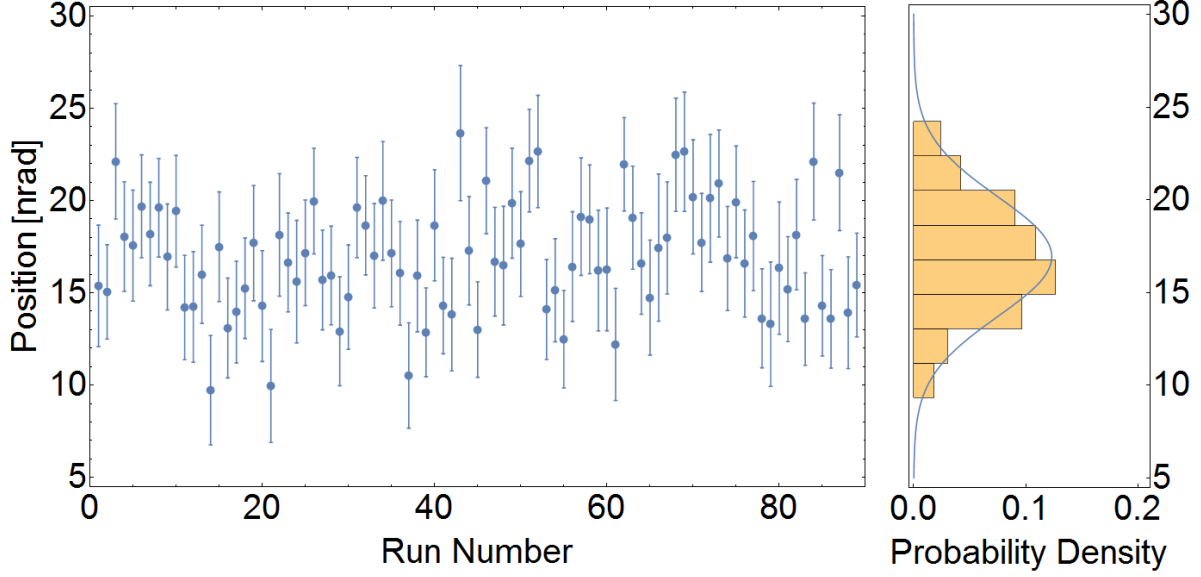
Figure 3.6 Fitted peak locations follow the distribution predicted by counting statistics. The average uncertainty in the individual rocking curve peak positions was 2.94 nrad. This is to be compared to fitting the set of 89 rocking curve peak positions to a Gaussian distribution, which gives $\sigma = (3.24 \pm 0.34)$ nrad.

$$u \to a\delta_p + u_0$$
$$w \to a\delta_p + w_0 \tag{3.22}$$

into Equations 3.12 and 3.19, where a is a fit parameter that has to do with the prism material and neutron wavelength, and δ_p is given by Equation 3.21. If there is an offset in the prism counter rotation, $\phi \to \phi + \phi_0$ in Equation 3.21, then to first order in ϕ_0 this adds the same constant offset to u_0 and w_0. Inserting Equation 3.22 into Equation 3.19, the form of the RRR beam intensity is given by

$$I_{RRR} \propto \frac{J_2(u_0 - w_0)}{(u_0 - w_0)^2} + \frac{J_2(a\delta_p + u_0)}{(a\delta_p + u_0)^2} + \frac{J_2(a\delta_p + w_0)}{(a\delta_p + w_0)^2}. \tag{3.23}$$

The first term only changes the peak baseline, which is absorbed into the A and B fit parameters below. Combing this result with the RR result, I now have two fit functions with related parameters:

$$I_{RR} = A_1 + B_1 \frac{J_1(a\delta_p + u_0)}{(a\delta_p + u_0)^2} \tag{3.24}$$

$$I_{RRR} = A_2 + B_2 \left[\frac{J_2(a\delta_p + u_0)}{(a\delta_p + u_0)^2} + \frac{J_2(a\delta_p + w_0)}{(a\delta_p + w_0)^2} \right], \tag{3.25}$$

where $\{A_{1,2}, B_{1,2}, a, u_0, w_0\}$ are fit parameters, and δ_p is the independent variable given by the prism counter rotation (Equation 3.21). Here I have let the prism counter rotation misalignment be absorbed into u_0 and w_0, such that

$$u_0 \rightarrow u_c + u_p = u_c + w_p$$

$$w_0 \rightarrow w_c + w_p = w_c + u_p, \tag{3.26}$$

where the c and p subscripts refer to the intrinsic crystallographic misalignment and the effective misalignment from an unknown offset in the prism counter rotation, respectively, and I have noted that $w_p = u_p$. In short, the RR peak is located at u_0 and the RRR peak location is $(u_0 + w_0)/2$. As a result, computing the misalignment $u_0 - w_0 = u_c - w_c$ automatically removes the effective misalignment from the prism counter rotation offset, ϕ_0.

Fitting the RR curve (Figure 3.5a) to Equation 3.24 gives $\frac{u_0}{HD} = (16.37 \pm 0.31)\,\mathrm{nrad}$. Combining this result with the RRR fit of Figure 3.5b to Equation 3.25 yields $\frac{w_0}{HD} = (4.75 \pm 0.66)\,\mathrm{nrad}$, leading to a measured absolute misalignment, $\frac{u_0 - w_0}{HD} = \frac{u_c - w_c}{HD} = (11.57 \pm 0.89)\,\mathrm{nrad}$ for the first interferometer. Both fits have reduced χ^2 (DOF $= 31 - 4$) of 2.8. The uncertainties quoted here do not use expanded error bars to decrease the reduced χ^2 to 1. Doing so increases the quoted uncertainties by a factor of $\sqrt{2.8} \simeq 1.7$.

When the second interferometer was translated, variation in misalignment on the order of $4\,\mathrm{nrad/mm}$ emerged. Shown in Figure 3.7 are the measured rocking curve positions as a function of interferometer translation. This suggests that the variation in crystallographic misalignment within each diffracting crystal is large enough to be relevant. If crystallographic misalignments are taken to be fields instead of constants, then the integrals over Γ as well as the solutions to Shrödinger's equation within the crystal are perturbed. These effects, which are not taken into account in the fits of the RR and RRR intensity, as well as the discussion in the next section, help explain the poor reduced χ^2 for both the RR and RRR fits.
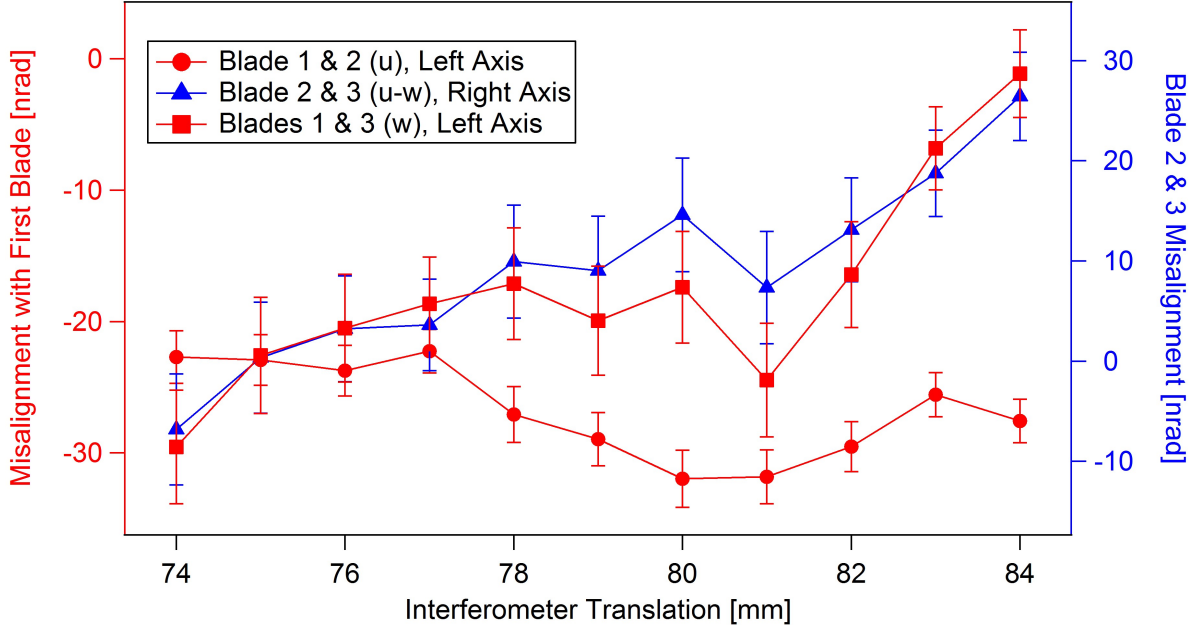
Figure 3.7 Misalignments as a function of interferometer translation. The measured misalignments between Blades 1 & 2 and Blades 1 & 3 are shifted depending on a possible offset in the prism counter rotation (red data, left axis), while the misalignment between Blades 2 & 3 is an absolute measurement (blue data, right axis).

3.3.4 Rocking Curve Fine Structure

If the $P(D)$ terms in Equation 3.9 are not neglected in regards to the RR curve, the fit can be improved. An outline of the fit functions used is given in Appendix B.2. Keeping the $P(D)$ terms adds three more parameters to the fit

$$\left\{ \frac{|v_H|(D_2 - D_1)}{k_\zeta}, \frac{|v_H|D}{k_\zeta}, \frac{\sigma_{k\zeta}}{k_\zeta} \right\}. \tag{3.27}$$

In this context D is the average of the crystal thicknesses. The reduced χ^2 (DOF $= 31 - 4$) when using Equation 3.24 as a fit function was 2.8. If $|v_H|D/k_\zeta$ is allowed to be a fit parameter, the reduced χ^2 (DOF $= 31 - 5$) falls to 1.9. It was found that $|v_H|(D_2 - D_1)/k_\zeta$ and $\sigma_{k\zeta}/k_\zeta$ did not impact the quality of the fit. However, a range for each can be computed given what is known about the thicknesses of the interferometer blades and the phase space profile of the incoming neutron beam. For the beam used here, $\sigma_{k\zeta}/k_\zeta \sim 0.0015\,\mathrm{rad}$, which only attenuates the $P(D)$ terms by a few percent, and the crystal thicknesses are thought to be the same to a few micrometers.

Even though the parameters $|v_H|(D_2 - D_1)/k_\zeta$ and $\sigma_{k\zeta}/k_\zeta$ do not improve the fit, they are covariant with u_0 and $|v_H|D/k_\zeta$. As such, assuming a possible range of values for the difference in

crystal thicknesses and the beam divergence slightly changes the best fits for the rocking curve peak position and silicon structure factor. A systematic uncertainty when reporting rocking curve peak positions should then be reported. By performing fits over the acceptable ranges of $|v_H|(D_2 - D_1)/k_\zeta$ and $\sigma_{k\zeta}/k_\zeta$, a systematic uncertainty emerges in $\frac{u_0}{HD}$ and $|v_H|D/k_\zeta$ of 0.08 nrad and 0.15 nrad, respectively. This results in $x \pm \sigma_{\text{stat}} \pm \sigma_{\text{sys}}$ of $\frac{u_0}{HD} = (-16.49 \pm 0.32 \pm 0.08)$ nrad and $|v_H|D/k_\zeta = (220.29 \pm 0.25 \pm 0.15)$ with $\chi^2_{\text{red}} = 1.9$ for DOF $= 31 - 5$. The still large reduced χ^2 of 1.9 indicates there may be additional complications to the rocking curve structure. This is likely due to *variation* in crystallographic misalignment between crystal blades demonstrated in Section 3.3.3.

The fit of $|v_H|D/k_\zeta$ corresponds to a sensitivity to v_H of one part in 10^{-3}, which is the level at which the neutron electron scattering length impacts v_H. However, the uncertainty in the Debye-Waller factor prevents a measurement of the neutron electron scattering length from being performed with only one Bragg reflection [SL03], Chapter 4. The sensitivity to v_H is not surprising, as two-crystal rocking curves have been used to measure the x-ray silicon structure factor [TB84]. In that case the impact of the incoming momentum space profile has also been studied [BT82]. While the net misalignment between the two diffracting crystals of the RR curve does not affect a measurement of v_H, the same cannot be said for other interferometry setups [Spr09; Zaw10; Pot15; Wie06], where extra diffracting crystals are placed in a Mach-Zehnder neutron interferometer. A measurement of v_H using pendellösung interference is described in Chapter 4, in which case linear strain gradients can affect the result.

3.3.5 Implications for Gravitationally-Induced Quantum Interference Experiments

In the COW gravitationally-induced quantum interference experiments, a Mach-Zehnder neutron interferometer is tilted about the incoming beam axis to induce a gravitational phase shift between paths of the interferometer from Earth's gravitational field (Figure 3.2b). The resulting phase shift versus $\sin\phi$, where ϕ is the interferometer tilt angle, is predicted to be linear, with the slope, q_{grav}, the measured value to be compared to theory. The primary contribution to q_{grav} is due to the path separation in Earth's gravitational field, but a few corrections are needed.

Dynamical phase effects contributed a perturbation in the expected phase shift for the COW experiments. The Sagnac effect constituted another correction, and bending of the interferometer crystal itself was accounted for using simultaneous neutron, x-ray measurements [Wer88]. Later experiments used two neutron wavelengths to account for the crystal bending [Lit97; Lit98]. I will focus on data from [Wer88], which used the x-ray technique, because it is more easily analyzed from information given in the article. For a history and more thorough description of the COW experiments see [RW15].
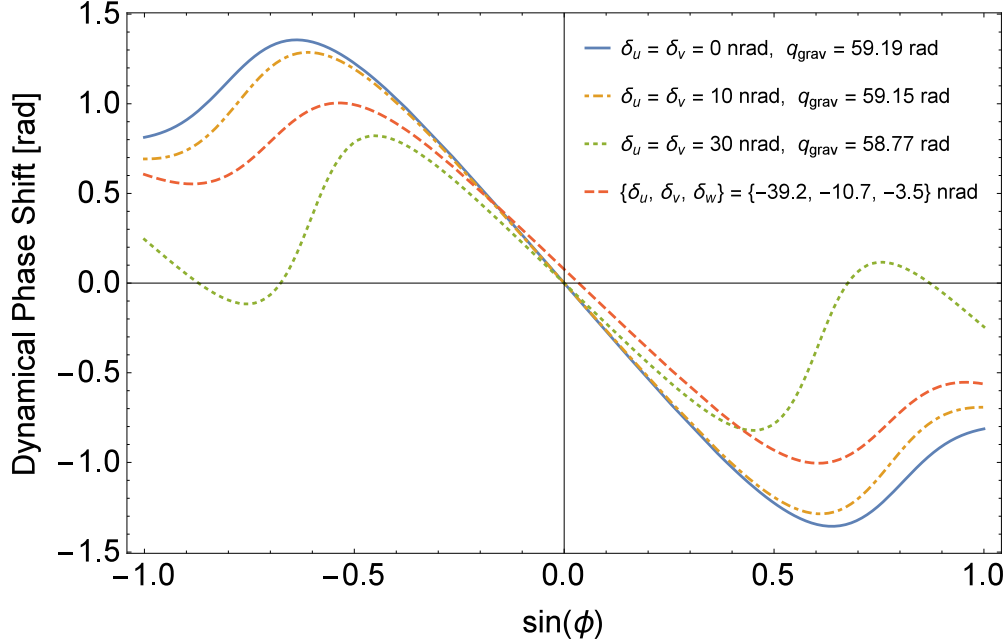
Figure 3.8 Dynamical phase (Equation 3.16) for the interferometer used in [Wer88] were it to have intrinsic misalignments. The corresponding theoretical values of q_{grav} are given in the legend. The final curve has q_{grav} set to the measured value of $(58.72 \pm 0.03)\,\text{rad}$ [Wer88].

When the interferometer is tilted in the COW geometry, the beam between crystal blades is deflected by up to about 100 nrad by gravity, leading to the dynamical phase correction. The previous rocking curve analysis indicates the existence of misalignments between diffracting crystals on the order of 10 nrad to 40 nrad. The relative size of the intrinsic misalignments and gravitational deflection imply that the natural misalignment of the interferometer is large enough to perturb the predicted dynamical phase shift. This is a likely explanation for the dynamical phase in the COW experiments being consistently smaller than predicted. Recalculating the dynamical phase contribution to the gravitationally-induced phase shift while allowing for intrinsic crystal misalignment attenuates the dynamical phase contribution (Figs. 3.8 and 3.10) and also impacts the predicted loss of contrast as a function of interferometer tilt (Figure 3.9). Here I have assumed the phase shift due to the bending of the interferometer under its own weight to already be accounted for by the simultaneous x-ray measurement. The distortion of the theoretical contrast and dynamical phase contribution are due to net misalignments that I have not allowed to change upon tilting the interferometer. The correction from reasonable misalignments as measured in this work is of the correct size to account for the discrepancy between theory and experiment in [Wer88].

There are too many relevant parameters that would need to be measured to recompute the dynamical phase correction for previous COW experiments with intrinsic crystallographic misalign-

63
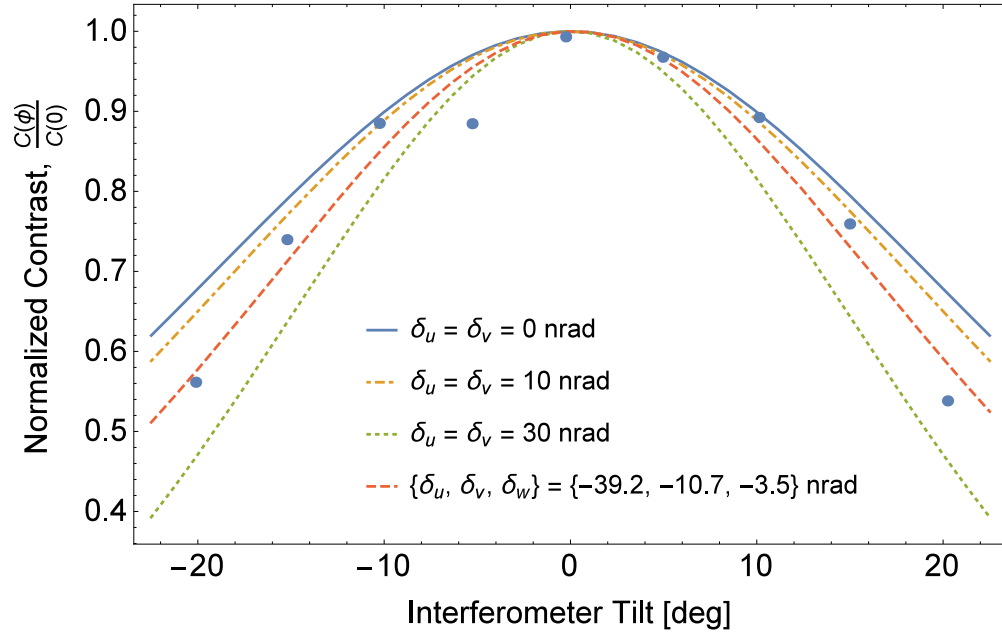
Figure 3.9 Normalized contrast (Equation 3.17) vs. tilt for the interferometer used in [Wer88] were it to have intrinsic misalignments. Data points are from [Wer88]. Uncertainties were not reported.
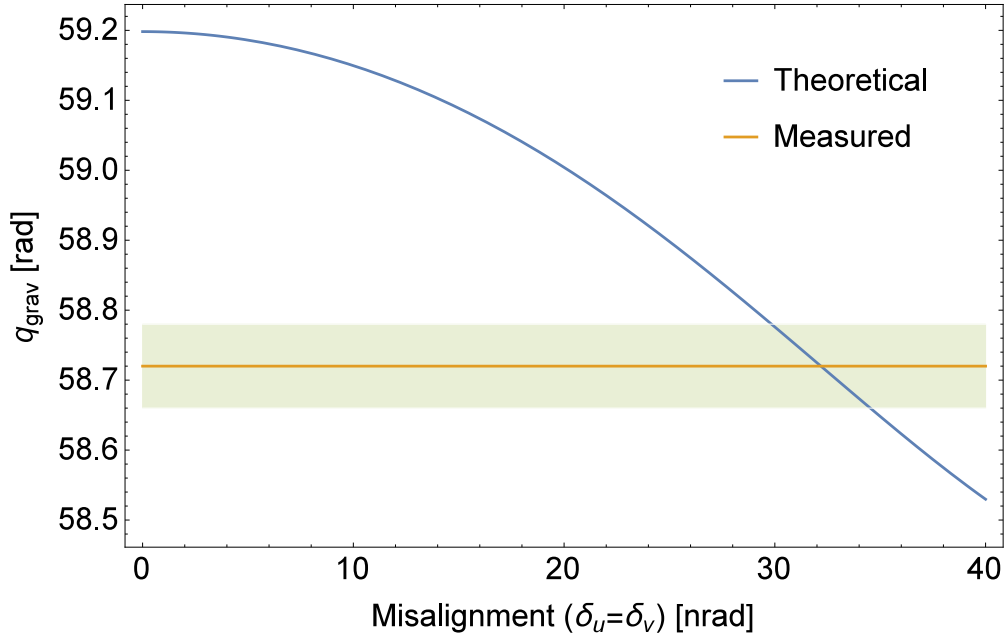
Figure 3.10 Theoretical slope of the gravitational phase shift as a function of $\delta_u = \delta_v$ crystal misalignment with $\delta_w = 0$. Experimental results $\pm 2\sigma$ from [Wer88] are also shown.

ments in the interferometer crystal included. However, for the interferometer used in [Wer88], a set of misalignments

$$\frac{\{u_c, v_c, w_c\}}{HD} = \{\delta_u, \delta_v, \delta_w\} = \{-39.2\,\mathrm{nrad}, -10.7\,\mathrm{nrad}, -3.5\,\mathrm{nrad}\}$$

that were consistent with q_{grav} and fitted to normalized contrast, $\frac{C(\phi)}{C(0)}$ (Figure 3.9) is consistent with the experimental results. A fit to contrast versus tilt angle cannot determine all three misalignment parameters. As a result, the fit to contrast was performed with the theoretical value of q_{grav} fixed to be the value measured in [Wer88]. Additionally, to see that misalignments tend to decrease the theoretical value of q_{grav}, Figure 3.10 shows q_{grav} as a function of misalignment with $\delta_u = \delta_v$ and $\delta_w = 0$, compared to the measured value from [Wer88].

The predicted contrast at no tilt with $\{\delta_u, \delta_v, \delta_w\} = \{-39.2\,\mathrm{nrad}, -10.7\,\mathrm{nrad}, -3.5\,\mathrm{nrad}\}$ for the interferometer used in [Wer88] is 81 %, to be compared with the measured value of 59 %. Fits to absolute contrast, instead of normalized contrast, yielded poor results, suggesting that there are other factors contributing to loss of contrast in this interferometer. The variation in misalignments within diffracting crystals as discussed in Section 3.3.3, differences in crystal thicknesses, or environmental factors such as vibrations are possible culprits.

The effect of intrinsic misalignments in neutron interferometers does not end with gravitationally-induced quantum interference. In the experiment performed in [Spr09], a measurement of the dynamical phase upon Laue transmission resulted in a weaker dynamical phase response than predicted. It is unclear whether including nonzero intrinsic interferometer misalignments would explain the discrepancy.

3.3.6 Conclusion

Measurements that rely on dynamical phases in neutron interferometry require careful characterization of imperfections in the interferometer crystal. Crystal misalignments on the 10 nrad to 40 nrad level, as well as a dependence on pendellösung oscillations have been measured for two monolithic silicon neutron interferometers at the NCNR. Such crystallographic imperfections may affect future precision measurements of the silicon structure factor and provide a likely explanation for the discrepancy between theory and experiment in the COW gravitationally-induced quantum interference measurements. Rocking curve interference peaks have the potential to measure very small deflections (on the order of picoradians) of the neutron beam in an interferometer, as well as characterize the strain in Mach-Zehnder neutron interferometers.

3.4 Impact of Annealing a Neutron Interferometer

Considering that neutron interferometers have very small levels of strain that can produce systematics for some experiments, the next logical question is whether such strain can be fixed. Fortunately, as is demonstrated here, there is hope in annealing. Unlike silicon crystals grown by the Czochralski (Cz) method, whose oxygen content causes strain in the crystal structure to increase with annealing, crystal planes become more highly ordered with annealing for float zone (Fz) crystals [New82], of which all silicon neutron interferometers are constructed. What follows is a description of a poorly-functioning interferometer that was tested, annealed, then retested. The improvement in performance of the interferometer was astonishing. After the initial success, the subsequent annealing of additional interferometers had neither have positive nor negative results, with the exception of the interferometer described in Section 3.5. The lack of reproducibility between interferometers is likely due to differences in thicknesses of the diffracting blades, upon which annealing has no impact. However, nonuniform blade thicknesses are thought to be caused primarily by the chemical etching process, where the entire interferometer is chemically etched in a mixture of nitric, hydrofluoric, and sometimes acetic acids. Currently under investigation is whether annealing can lessen the required etching depths, or even eliminate this step in the process entirely. What follows are the results of the first interferometer that was annealed at the NIOF.

Neutron interferometers are chemically etched iteratively by removing tens of micrometers with each etch, then checking contrast, where etching is believed to relieve strain in the crystal caused by machining damage [Zaw10]. However, as the total etching depth increases, the parallelism and uniform thicknesses of the crystal blades degrade due to uneven etch rates. If too much material is etched away, the contrast begins to drop. Additionally, it is well established that neutron interferometer contrast varies depending on where the incident beam strikes the splitter blade and for different wavelengths. The finding of the previous section, where intrinsic Bragg plane misalignments on the order of tens of nanoradians exist in neutron interferometers, is confirmed here, as well as a variation in the blade thicknesses across the particular interferometer used in this experiment.

Interferometers constructed under similar conditions can show wildly different contrasts. Previously, machining accuracy was thought to be a major source of this variation. However, modern machining processes eliminate this as a possibility. This work demonstrates that the lack of reproducibility in interferometer construction is likely due to thickness variations of the interferometer blades from uneven etch rates as well as fluctuating or large (greater than 10 nrad) Bragg plane misalignments between the blades. It is then shown that Bragg plane misalignment can be reduced by annealing the interferometer after fabrication.

If machining inaccuracies or uneven etch rates cause the two beam paths in a neutron interferometer (Paths $|I\rangle$ and $|II\rangle$ in Figure 3.2a) to be displaced relative to each other outside of the pendellösung length, then the interferometer contrast suffers. This sets the machining tolerances
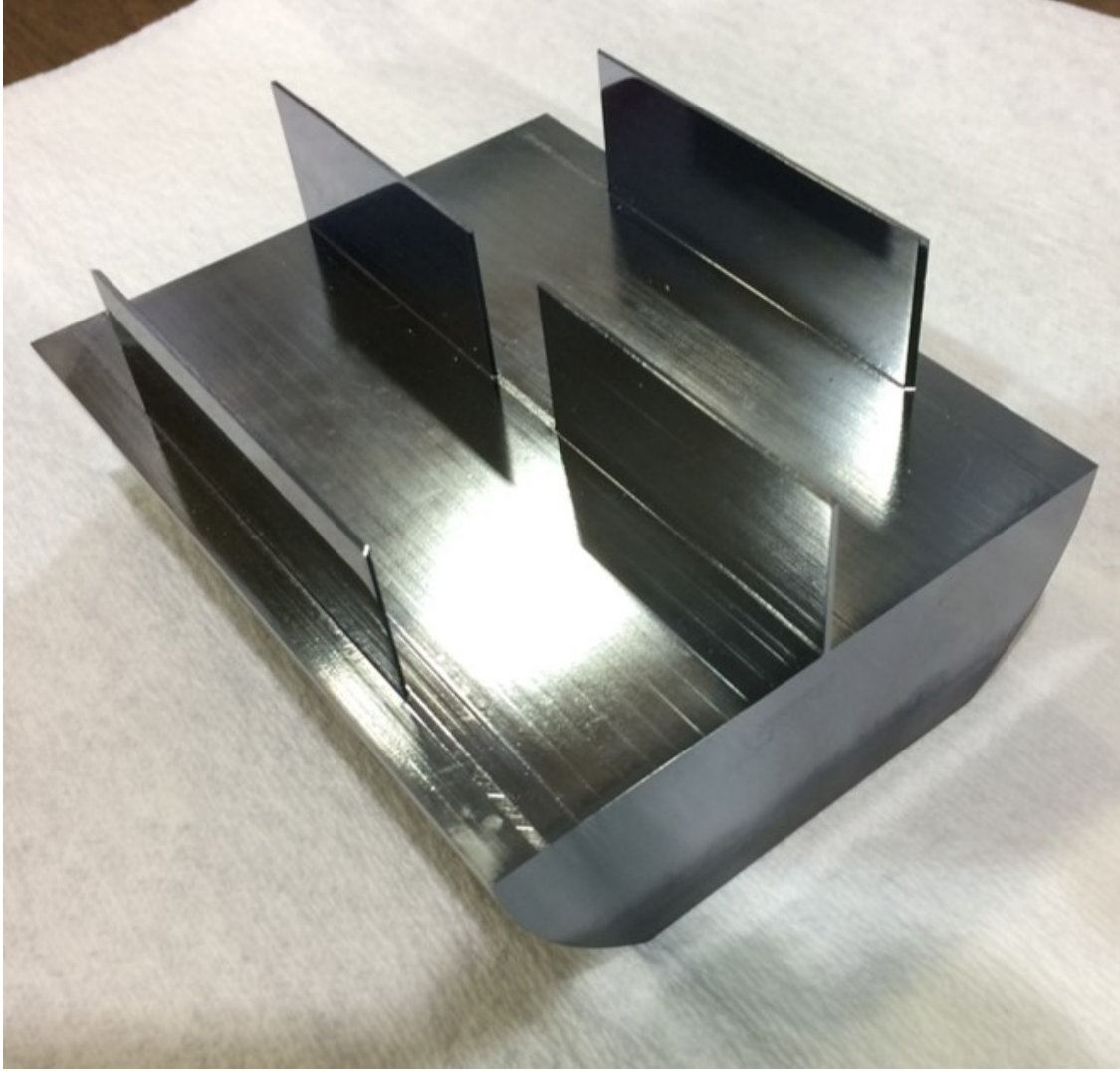
Figure 3.11 The neutron interferometer annealed in this experiment. The base is roughly 10 cm x 10 cm. The blades are 3 cm tall.

for the interferometer blades, indicating that the parallelism, thickness, and spacing of the crystal blades should be uniform to a level much smaller than the pendellösung length [RW15].

Similar to the previous Section, to characterize the impact of annealing on Bragg plane alignment of the interferometer blades, the oscillatory rocking curve structure of multiple Bragg diffractions in one arm of the interferometer as a function of rotation of a fused silica prism was measured [Bon77; PR84; Art85; Hea17]. The relative Bragg plane alignment of the interferometer blades shifted by about 100 nrad after annealing. The structure of each peak is perturbed by unequal crystal thicknesses on the pendellösung length scale, and the overall structure of each peak does not change

with annealing. The rocking curve structure thus differentiates between the detrimental effects of unequal blade thicknesses and Bragg plane misalignments in the interferometer and shows that the post fabrication annealing of the interferometer can improve the latter.

3.4.1 Experiment

This work was performed on both the NIOF and NIOFa beamlines, and all three wavelengths were utilized (2.7 Å at NIOF and 2.2 Å and 4.4 Å at NIOFa). See Section 1.5.

The interferometer was annealed in a tube furnace with an inner diameter of 208 mm under constant argon flow at 800 °C for ten hours, not including ramping time. The ramping rate was 5 °C/min. Lapped Fz silicon crystal slabs (142 mm x 45 mm x 6 mm) were annealed in the furnace under the same conditions before attempting to anneal the interferometer. The full width half maximum (FWHM) of the Cu Kα_1 diffraction peak fit to a Voigt function of a lapped sample dropped from 168(3) arc sec to 102(3) arc sec.

The interferometer that was annealed uses the (111) Bragg reflection. In the past, the interferometer had exhibited a maximum contrast of 23 % at 2.7 Å [Woo14]. Immediately before annealing, it was tested for contrast at 2.2 Å and 4.4 Å, though no visible contrast was found. When searching for contrast, an interferometer is translated vertically and horizontally along the splitter blade thus making a "contrast map" (see Figure 3.15). The interference structure of misaligning the mirror and analyzer blades, relative to the splitter, was also studied before annealing. In a similar fashion to the previous experiment, a fused silica prism was placed so that its 6 deg pitch was oriented at a right angle to the diffraction plane of the interferometer to within a few degrees. By then rotating the prism about the beam axis, deflection of the beam from the prism enters the diffraction plane, which causes the same effect as rotating the analyzer and mirror blades relative to the splitter blade at the nanoradian level.

In the previous Section, the effect of $P(D) \to 0$ was small, allowing the structure of the rocking curves to be described according to Appendix B.2. For this interferometer, it was found that the thickness difference between blades was large enough that the RR and RRR peaks needed to be defined in terms of two special functions

$$\mathcal{I}(\alpha, \beta) = \int_{-1}^{1} d\Gamma \sqrt{1 - \Gamma^2} \cos{(\alpha\Gamma)} \cos{\left(\frac{\beta}{\sqrt{1 - \Gamma^2}} \right)} \tag{3.28}$$

$$\mathcal{J}(\alpha, \beta) = \int_{-1}^{1} d\Gamma \left(1 - \Gamma^2 \right)^{\frac{3}{2}} \cos{(\alpha\Gamma)} \cos{\left(\frac{\beta}{\sqrt{1 - \Gamma^2}} \right)}. \tag{3.29}$$

Here α is related to the peak position and Bragg plane misalignments; $\beta \neq 0$ is a correction to the standard results [PR84] for unequal crystal thicknesses; and the integration over Γ is an integration over the Borrmann fan [RW15]. For $\beta = 0$, these reduce to Equations 3.9 and 3.19.

The RR peak is given by

$$I_{\mathrm{RR}} = A \left\{ \pi + \mathcal{I} \left[B \left(\delta(\phi) + \delta_{S,M}^{\mathrm{rel}} \right), \; \Delta_{M,S} \right] \right\}, \tag{3.30}$$

where A, B, $\Delta_{M,S}$, and $\delta_{S,M}^{\mathrm{rel}}$ are fit parameters, and $\delta(\phi)$ is given by Equation 3.21 as a function of the the prism rotation ϕ. The RRR peak was fit to

$$
\begin{aligned}
I_{\mathrm{RRR}} = \quad A' \Bigg\{ & \frac{9}{16}\pi + \mathcal{J} \left[B \left(\delta(\phi) + \delta_{S,M}^{\mathrm{rel}} \right), \; \Delta_{M,S}^{\mathrm{rel}} \right] + \mathcal{J} \left[B(\delta_{S,M}^{\mathrm{rel}} - \delta_{S,A}^{\mathrm{rel}}), \; \Delta_{A,S} - \Delta_{M,S} \right] \\
& + \mathcal{J} \left[B(\delta(\phi) + \delta_{S,A}^{\mathrm{rel}}), \; \Delta_{A,S} \right] \Bigg\},
\end{aligned}
\tag{3.31}
$$

where A', $\Delta_{A,S}$, and $\delta_{S,A}^{\mathrm{rel}}$ are fit parameters, and B, $\Delta_{M,S}$ and $\delta_{S,M}^{\mathrm{rel}}$ are the same parameters as those appearing in Equation 3.30. For each incident beam position, global fits were performed by fitting I_{RRR} to the RRR beam intensity, and $I_{\mathrm{RR}} - I_{\mathrm{RRR}}$ to the RRT beam intensity. All fits had $42 - 7$ degrees of freedom; the reduced χ^2 were between 0.6 and 1.1.

The $\Delta_{i,j}$ fit parameters are interpreted as the thickness difference between the splitter, mirror, or analyzer blades (subscripts S, M, or A, respectively) scaled by the pendellösung length Δ_H

$$\Delta_{i,j} = 2\pi \frac{D_i - D_j}{\Delta_H}. \tag{3.32}$$

The $\delta_{i,j}^{\mathrm{rel}}$ are interpreted as the angular misalignments between the i and j interferometer blades (again labeled S, M, or A), with an offset due to the unknown absolute alignment of the prism rotation ϕ with the diffraction plane of the interferometer. An offset in the readout of the prism's rotational positioning stage creates $\phi \to \phi + \phi_0$ in Equation 3.21. The prism was rotationally aligned to the interferometer by eye, so the offset ϕ_0 is less than $\sim \pm 10°$ and Equation 3.21 can be expanded such that $\delta(\phi) \to \delta(\phi) + \delta_p$, where $\delta_p = \delta(\phi_0)$. This creates the same constant offset δ_p for the $\delta_{S,M}^{\mathrm{rel}}$ and $\delta_{S,A}^{\mathrm{rel}}$ fit parameters. The offset is the same for the RR and RRR peaks both before and after annealing. The absolute Bragg plane alignment between the i and j blades are related to the fit parameters by

$$\delta_{i,j}^{\mathrm{abs}} = \delta_{i,j}^{\mathrm{rel}} - \delta_p. \tag{3.33}$$

Note that the unknown values of $\delta_{i,j}^{\mathrm{abs}}$ prevent the prism rotation ϕ from being aligned with neutrons. Finally, the absolute alignment between the mirror and analyzer blades is available by noting that

$$\delta_{A,M}^{\text{abs}} = \delta_{S,M}^{\text{rel}} - \delta_{S,A}^{\text{rel}}, \tag{3.34}$$

which is the same relation as described by Equation 3.26.

Figs. 3.12 and 3.13 show the fitted functions for a few incident beam positions on the interferometer at 4.4 Å. In addition to measuring Bragg plane misalignments, the structure of the peak lends information to the difference in thickness between the interferometer blades through the $\Delta_{i,j}$ fit parameters. This effect can be clearly seen in the widening and double peak structure within Figure 3.12 as the interferometer is translated. The clearly visible gradient in the peak centroids in Figure 3.13(a) before annealing is diminished after annealing. All curves shift to around 8 degrees of prism rotation after annealing, suggesting $\phi_0 \sim 8°$. The larger scatter in Figs. 3.12(b) and 3.13(b) is likely due at least in part to shorter count times resulting in a higher error per point in the RR and RRR rocking curves.

These effects are all reflected in Figure 3.14, where the peak centroids, converted to units of Bragg plane misalignment are plotted. Absolute misalignments between the mirror and analyzer blades are shown in Figure 3.14b. Gradients in the Bragg plane misalignments drop from about 10 nrad/mm to less than 5 nrad/mm after annealing, and the absolute misalignment between the mirror and analyzer blades also lessens for some some portions of the interferometer. The fused silica prism was left in place while the interferometer was annealed, keeping δ_p constant before and after annealing. This allowed for an absolute measurement of the shift in the Bragg plane alignment of the splitter blade and the mirror and analyzer blades of about 100 nrad from annealing, because δ_p drops out when taking the difference between $\delta_{i,j}^{\text{rel}}$ before and after annealing.

The fitted $\Delta_{i,j}$ parameters can be seen as the worsening visible distortion in the RR peak, and less so for the RRR peak, as the interferometer is translated (Figs. 3.12 and 3.13). This indicates that the thickness difference between the mirror and splitter blades changes by about 20 % of the pendellösung length over 20 mm, which corresponds to about a 7 μm thickness difference, given the 34 μm pendellösung length for the (111) reflection at 4.4 Å. The same is not true of the RRR peak, indicating that the mirror blade likely has a varying thickness. Alternatively, the mirror blade could be flat with the splitter and analyzer blades having a similar, distorted shape.

The technique of using the refracting prism to measure Bragg plane misalignments only applies to one of the mirror blades, leaving the other unmeasured. One therefore cannot predict the contrast solely from the fits of the RR and RRR peak positions and structure. The interferometer contrast is a function of the difference in thickness between the splitter and analyzer blades and the two mirror blades separately. However, the mean count rate of an interferogram is at its highest when all four diffracting crystals have the same thickness.

Before annealing, there was no contrast visible at 2.2 Å or 4.4 Å. After annealing, the interferometer was tested at 4.4 Å and 2.7 Å. There was up to 20 % contrast observed at 4.4 Å after annealing.

(a) Before Annealing
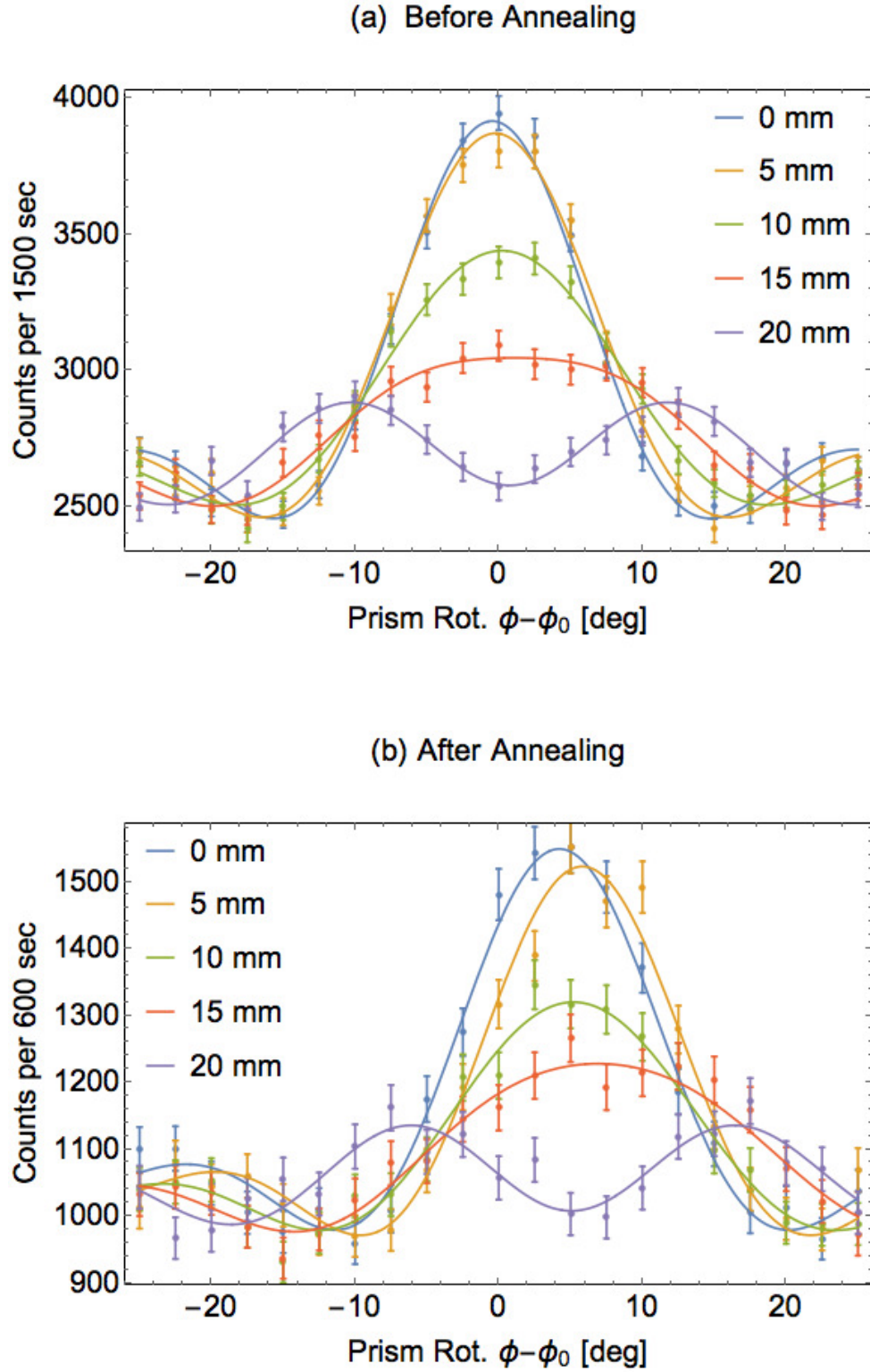
(b) After Annealing

Figure 3.12 The RR peaks before (a) and after annealing (b) with best fits. Each curve is for a different translation of the interferometer relative to the incoming beam.
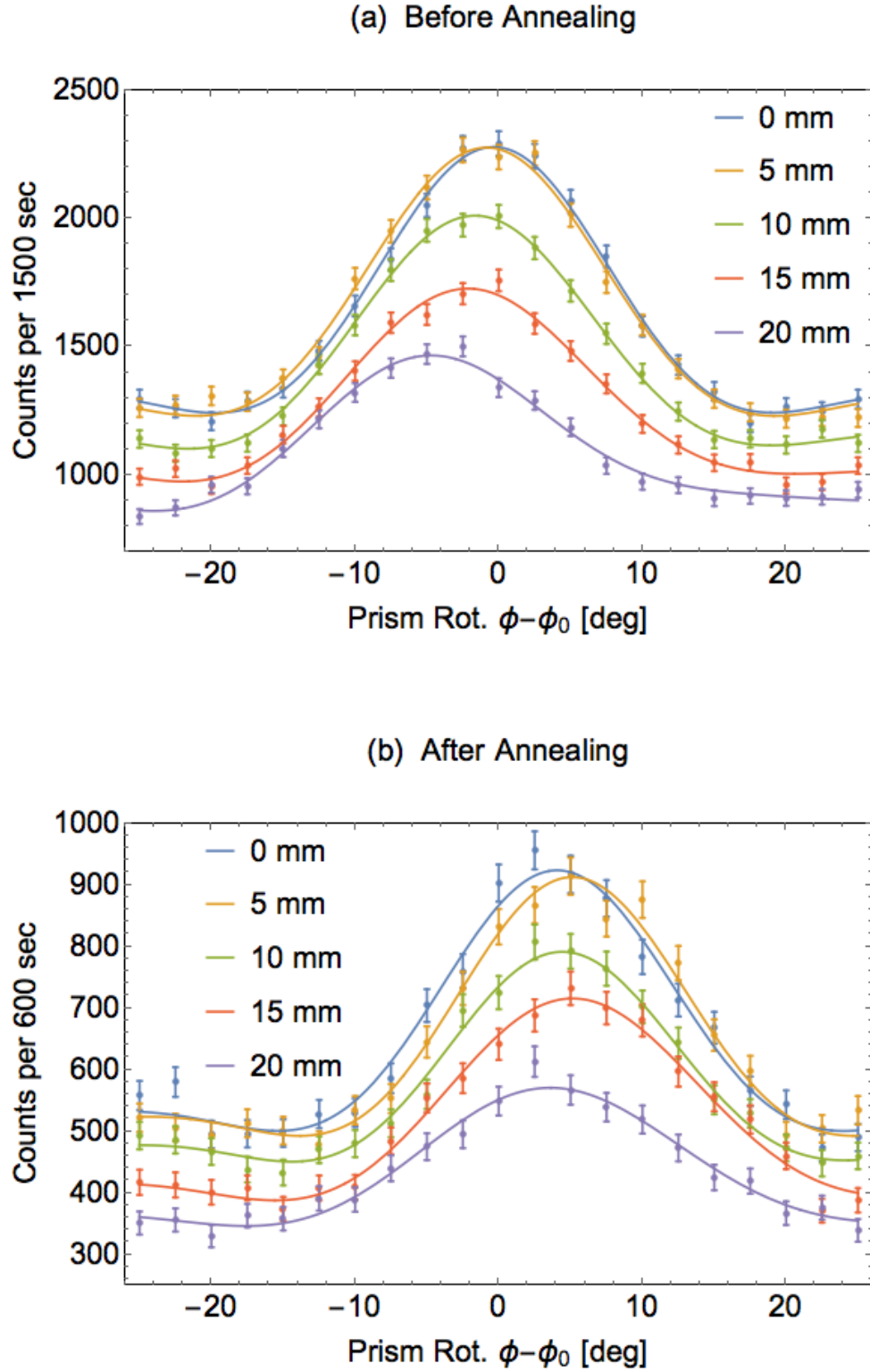
Figure 3.13 The RRR peaks before (a) and after (b) annealing with best fits. Each curve is for a different translation of the interferometer relative to the incoming beam.

(a) Relative Misalignments

(b) Absolute Misalignments

(c) Thickness Differences
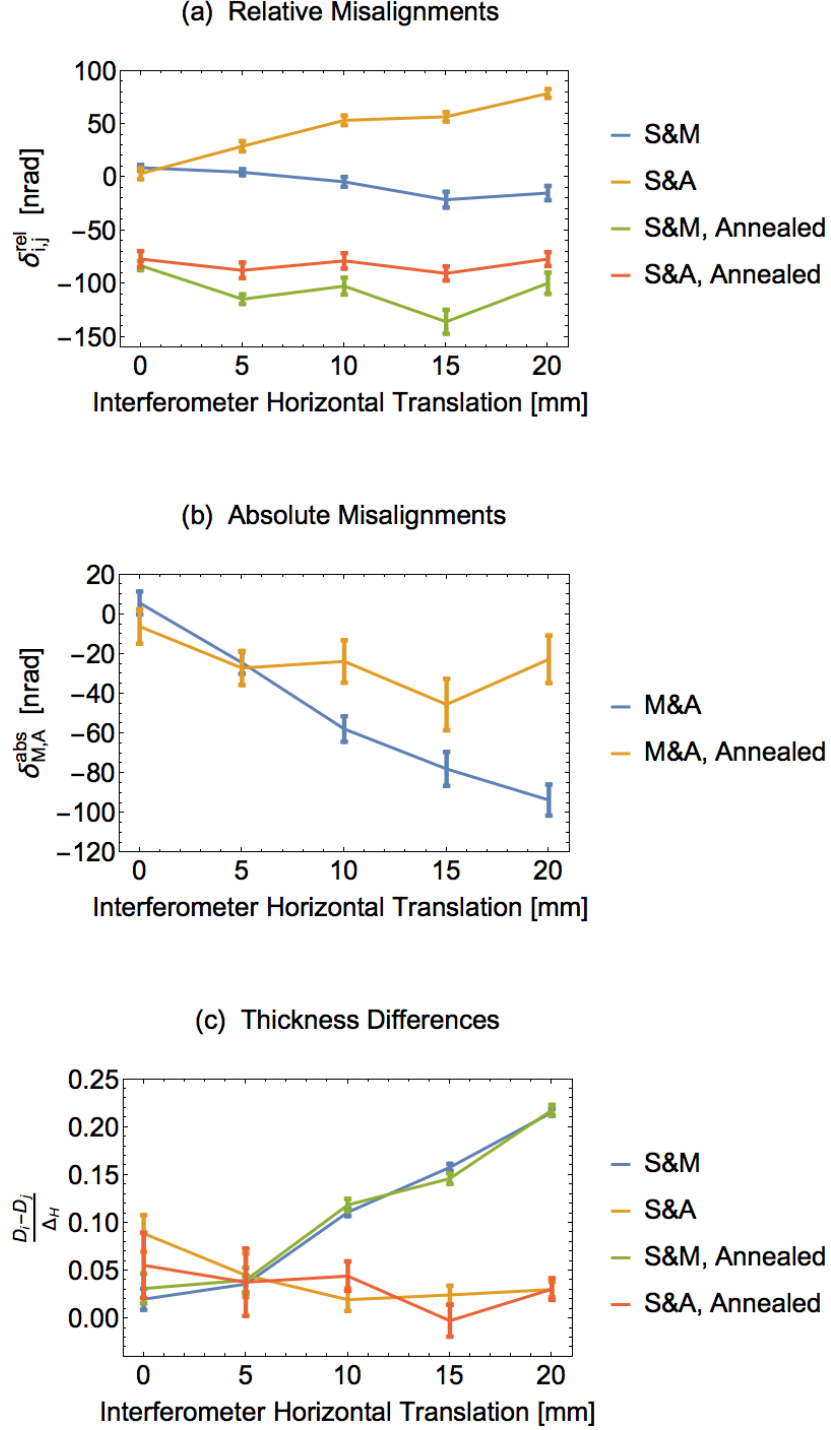
Figure 3.14 Bragg plane misalignments and thickness differences before and after annealing. Shown is (a) the relative Bragg plane misalignment between the splitter and the mirror and analyzer blades, (b) the absolute misalignment between the mirror and the analyzer blades, and (c) the thickness differences as a function of interferometer translation. S, M, and A refer to the splitter, mirror, and analyzer blades.

The contrast at 2.7 Å was excellent, improving from 23 % [Woo14] to 90 %. A contrast map is shown in Figure 3.15. Also shown in Figure 3.15 is a contrast map of the previously highest-contrast interferometer at NIST. While the peak contrasts are similar, the range over which the contrast is high is larger for the the annealed interferometer. This implies that the annealed interferometer may be especially useful for phase imaging, where the incoming beam is much larger (typically ~ 1 cm in diameter).

The improved contrast at 2.7 Å, compared to 4.4 Å, for the annealed interferometer is likely due in part to the better vibrational and environmental isolation provided by the different facility. The more severe Bragg angle at 4.4 Å ($44.5°$ versus $25.6°$), also creates a larger path separation, rendering the interferometer more sensitive to vibrations. However, the dependence of contrast on wavelength may also be due in part to thickness variations across the interferometer blades. It is conceivable that the demonstrated thickness variation in the mirror blade that was measured at 4.4 Å (Figure 3.14c) is less pronounced for the 2.7 Å beam geometry. Finally, the pendellösung length at 2.2 Å is approximately 71 μm, compared to 34 μm at 4.4 Å. The interferometer contrast is therefore twice as sensitive to thickness variation at 4.4 Å, compared to 2.2 Å.

3.4.2 Conclusions

This study shows that annealing a neutron interferometer can refine Bragg plane misalignments enough to drastically improve contrast. While the Bragg plane alignment can be improved by annealing, the only way to fix thickness variations in the interferometer blades would be to remachine and etch the interferometer again. The variation in blade thickness is believed to be a principle cause of the lower contrast at 4.4 Å when compared to 2.7 Å for the interferometer annealed in this work. It is possible that with the addition of annealing treatments to the neutron interferometer post-machining fabrication process, less etching will be required. If this is the case, then the annealing step may also prevent thickness variation in the crystal blades caused by deep etching depths, resulting in higher quality interferometers with blades that are more uniform and parallel and that have better Bragg plane alignment.

3.5 Construction of a Two-Blade Neutron Interferometer

This section details the post fabrication treatments of a "two-blade" neutron interferometer constructed in collaboration with NCSU, NIST, Nagoya University, and RIKEN. While in a different geometry than the more typical Mach-Zehnder geometry, this particular interferometer is the first to have been annealed prior to chemical etching and is the first interferometer to show any, albeit modest, contrast without any etching. Two-blade interferometers have thicker crystal blades than Mach-Zehnder interferometers, and achieve interference fringes by filling the Borrmann fan with
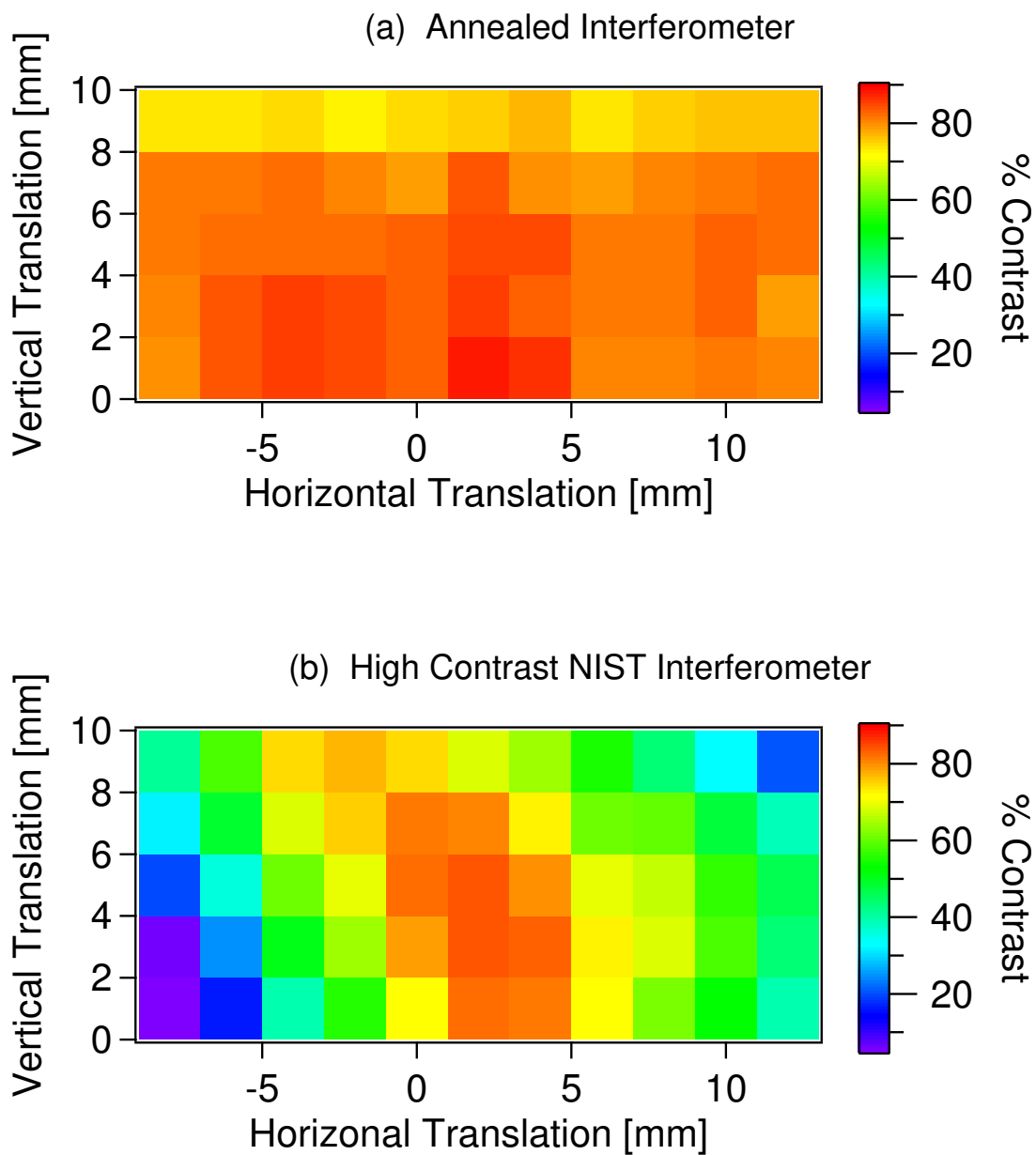
Figure 3.15 Contrast Maps at 2.7Å for (a) the annealed interferometer and for (b) the previously highest-contrast NIST interferometer. The incoming beam passes through a 2 mm x 8 mm slit in both cases. The peak contrast of the annealed interferometer is only slightly higher, but it shows high contrast over a wider spatial range.
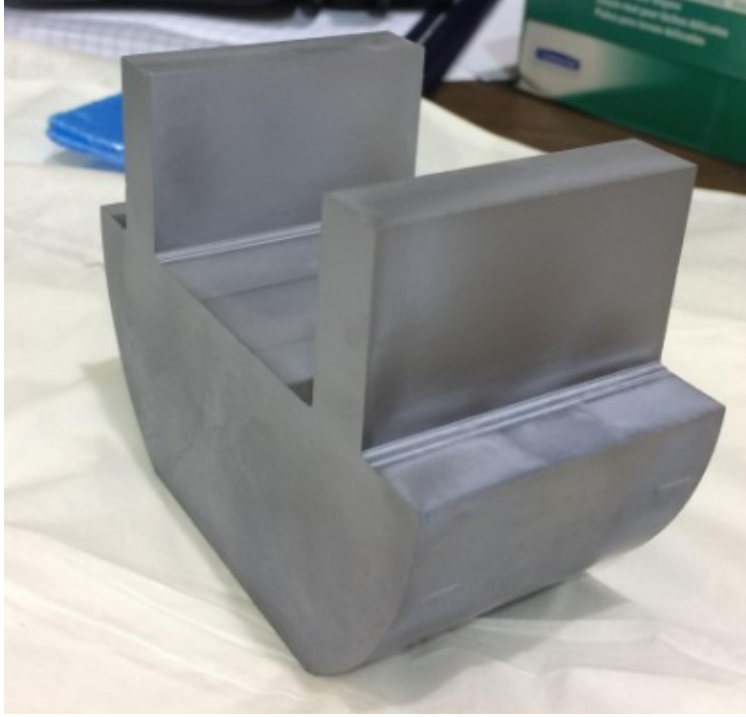
Figure 3.16 The two-blade interferometer machined at RIKEN after all post fabrication steps were completed.

one crystal reflection in the Laue geometry, then coherently recombining all the components of the Borrmann fan in a second crystal of the same thickness, as shown in Figure 3.1. Two other two-blade interferometers have been constructed in the past. Both were constructed about forty years ago but are not in use today. The original interferometers were used as an angle amplifier [Kik78], to probe dynamical diffraction in a magnetic field [ZS79], demonstrate neutron interferometry in a rotating frame of reference [Atw84], and test for nonlinear terms in the Shrödinger equation [Shu80]. The two-bade neutron interferometer can be used in conjunction with a cadmium mask as a traditional neutron interferometer with a sinusoidal signal [Kik78; Shu80]; or a very narrow interference peak is observable by placing a refracting prism between the blades [Art85], as described previously in this chapter.

3.5.1 Non-Ideal Effects

Unlike the first interferometer that was annealed (Section 3.4), the two-blade interferometer has very uniform crystal thicknesses, but also thicker crystals, which magnifies any strain effects within the Borrmann fan. It is most useful to look again at small perturbations to the RR rocking curve with $P(D) \neq 0$, except in this case I will need to consider more functional forms of P and allow P

to be be a function of Bragg plane misalignment δ within the Borrmann fan. In this case the RR peak intensity can be described by

$$I \propto_{RR} \int d\Gamma d\delta \ \sqrt{1-\Gamma^2} \cos(HD\delta\Gamma) \, P(\delta, \Gamma). \tag{3.35}$$

For the case of strain in the crystal, δ is averaged over some distribution. For random strain deviations

$$P(\delta, \Gamma) = \frac{1}{\sigma_\delta \sqrt{2\pi}} \exp\left[-\frac{(\delta - \delta_0)^2}{2\sigma_\delta^2}\right] \tag{3.36}$$

where δ_0 is the average misalignment, which gives

$$I \propto \int d\Gamma \ \sqrt{1-\Gamma^2} \cos[HD\delta_0\Gamma] e^{-\frac{1}{2}(HD\Gamma\sigma_\delta)^2} \tag{3.37}$$

after integrating over all δ. While this integral does not have a closed form solution, its solution may be taken as the definition of a special function with arguments $HD\delta_0$ and $HD\sigma_\delta$ to perform the necessary fitting procedures.

Integrating $P(\delta, \Gamma)$ over δ in effect perturbs the $\sqrt{1-\Gamma^2}$ envelope. Specifically, the new Γ-envelope reduces the weight of larger Γ when computing the interference pattern of the interferometer as a function of δ_0, which is varied using a refracting prism again according to Equation 3.21. In effect, the coherence of the Borrmann fan edges is reduced by strain in the crystal and may be parameterized by σ_δ.

Other non-ideal effects similarly alter the Γ-envelope and tend to decrease the coherence of the Borrmann fan edges. For example, slowly-varying gradients in the Bragg plane alignment across the Borrmann fan may be introduced by letting $\delta_0 \to \delta_0 + \delta_0'\Gamma + \delta_0''\Gamma^2....$ A non-zero δ_0' likewise decreases the coherence for large Γ in the Γ-envelope. The net effect is then that the FWHM of the $I(\delta)$ peak in Equation 3.8 increases, and the amplitude decreases. Unequal crystal thicknesses, create a similar effect, with

$$P(\delta, \Gamma) = \cos\left(2\pi \frac{D_2 - D_1}{\Delta_H \sqrt{1-\Gamma^2}}\right). \tag{3.38}$$

Notice the return of the dependence on the pendellösung length Δ_H, which ultimately determines the dimensional tolerances of the interferometer. This function may also be averaged with respect to $D_2 - D_1$ over a Gaussian distribution with standard error R_A, corresponding to the surface roughness of the interferometer blades

$$P(\delta, \Gamma) = \exp\left[-\frac{1}{2}\left(2\pi \frac{R_A}{\Delta_H \sqrt{1-\Gamma^2}}\right)^2\right]. \tag{3.39}$$

The surface roughness of approximately 400 nm after annealing makes this term very small.

In this study, a non-zero σ_δ in Equation 3.21 is found to be the dominant factor after annealing, but before etching. After etching, the crystal was so lightly strained, that distinguishing between the listed effects is impossible. Consider expanding I_{RR} to leading order in σ_δ, δ_0', $(D_2 - D_1)$, and R_A

$$I = \int d\Gamma \sqrt{1-\Gamma^2} \cos\left[HD\Gamma\delta_0\right] \left\{ 1 - \frac{1}{2}\left(HD\sigma_\delta\right)^2 \Gamma^2 - \frac{1}{2}\left(HD\delta_0'\right)^2 \Gamma^4 + \right.$$
$$\left. - \frac{1}{2}\left[\left(2\pi\frac{D_2 - D_1}{\Delta_H}\right)^2 + \left(2\pi\frac{R_A}{\Delta_H}\right)^2\right]\frac{1}{1-\Gamma^2} \right\} \tag{3.40}$$

From this equation it is clear that low levels of strain in the interferometer may be interpreted as a decreased coherence in the Borrmann fan edges. For the purposes of minor perturbations from an ideal interferometer the RR peak may be fit to

$$I(\phi) = A + B\left[I_0(\phi) + a_2 I_2(\phi) + a_4 I_4(\phi) + a_D I_D(\phi)\right] \tag{3.41}$$

where

$$I_n(\phi) = \int d\Gamma \, \Gamma^n \sqrt{1-\Gamma^2} \cos\left[HD\delta_p(\phi)\right], \tag{3.42}$$

and

$$I_D(\phi) = \int d\Gamma \, \frac{\cos\left[HD\delta_p(\phi)\right]}{\sqrt{1-\Gamma^2}} \tag{3.43}$$

with $\delta_p(\phi)$ defined by Equation 3.21 in which λ, α, and $\sum_i N_i b_i$ are all computed from the known characteristics of the fused silica prism. If a prefactor in Equation 3.21 containing these variables were allowed to be a fit parameter, as was the case in Sections 3.3 and 3.4, then it would not be possible to distinguish between peak broadening from strain and a prism with a smaller pitch than expected. Both the I_n and I_D may be written in terms of Bessel functions $J_i(x)$ and their arguments, similar to Equation 3.8 (see Appendix B.3). Thus, a non-zero a_2 indicates small levels of strain; a_4 indicates a gradient in the Bragg plane alignment; and a_D occurs for unequal crystal thickness or a rough surface. When performing fits to this function, the a_i parameters tend to be highly covariant. Thus, while I cannot distinguish between a strained interferometer versus an interferometer whose blades have rough surfaces, I can use the fits to compute the FWHM of the resulting function. When the covariance of the a_i are taken into account, the uncertainty in the FWHM of $I(\delta)$ is independent of the exact fit function used, and the FWHM is thus used as the figure of merit for assessing subsurface damage in the interferometer.

3.5.2 Fabrication Process

The entire fabrication process was performed at the RIKEN Center for Advanced Photonics. First, the interferometer was cut from a Fz silicon ingot with its growth axis in the (111) direction. The rounded edges of the base, as can be seen in Figure 3.16, comprise the original outer surface of the ingot. The bulk of the raw material was removed with a diamond band saw. The shape of the interferometer, to within $\sim 20~\mu$m was refined using a 150 grit electroplated diamond grinding wheel on a coordinate milling machine. The four large surfaces on the two blades where neutrons penetrate were then machined to one micrometer precision using a ultra-high-precision grinding (UHPG) process in two steps. A 400 grit and a 1200 grit resin-bonded diamond grinding wheel was used in the first and second steps, respectively. The grinding wheels were dressed and trued before mounting the interferometer to the grinding tool. The grinding was completed in multiple passes. The depth of the finishing passes was 2 μm with a feed rate of 500 mm/min and a feed pitch of 2.0 mm. The thickness and parallelism of the blades were checked in the regions where the neutron beam is diffracted with a coordinate measuring machine. The blades were found to be of uniform thickness and parallel at the one micrometer level. The interferometer itself was too large to be mounted to the available white light interferometer for measuring surface roughness. However, silicon test pieces ground under the same conditions showed a surface roughness of about 200 nm.

Tests of the interferometer and all post fabrication measures were performed at the NCNR. The interferometer was tested at the NIOF beamline with 2.7 Å neutrons. Each post-fabrication step that occurred prior to a new neutron assessment is shown in Table 3.1. First, the interferometer was tested with no post-fabrication processes (Step N). Next, annealing was performed in the same quartz tube furnace described previously. Annealing the two-blade interferometer resulted in modest fringe visibility, making this the first interferometer to be annealed prior to etching, and to my knowledge, the only neutron interferometer to have ever shown contrast without chemical etching. The interferometer was not treated at temperatures greater than 800 °C, because the surfaces of test samples showed visible surface pitting after being annealed at those temperatures. Instead, the interferometer was annealed for a longer time (Step II). However, this did not result in another increase in the quality of the measured interference fringes. After annealing, the previously shiny surfaces took on a matted appearance, signifying that the surface roughness increased upon annealing. Similar effects have be characterized previously [Jas07].

Etching was performed with a 60:1 mixture of nitric and hydrofluoric acid, following a similar prescription to the one given in [Zaw10]. Typically, etching depths of 30 μm to 60 μm are required for contrast for Mach-Zehnder neutron interferometers. Here, only 4 μm was etched away from each surface, but resulted in a dramatic increase in fringe visibility (Step III). Because over-etching can cause the interferometer to lose its carefully machined shape, another round of etching was not

Table 3.1 Summary of post fabrication steps and neutron interferometric results.

Fabrication step	"Twist"	FWHM
N. UHPG	N/A	N/A
I. Annealed, 10 h at 800° C	8 nrad/mm	30 nrad
II. Annealed, 72 h at 800° C	8 nrad/mm	30 nrad
III. Etched, 4 μm	0.2 nrad/mm	22 nrad
IV. Annealed, 10 h at 800° C	0.2 nrad/mm	22 nrad

performed. However, the interferometer was annealed one final time (Step IV). When this did not result in an improvement to the interferometer, the post-fabrication process was concluded.

3.5.3   Analysis

Measurements of the interferometer's interference fringes was performed after each step in the post-fabrication process. After all post fabrication was completed, the surface roughness of the interferometer was measured using a white light interferometer to be 400 nm. The interferometer was also mapped on a coordinate measuring machine. The one micrometer tolerances remain intact for the portions of the interferometer that were measured between machining steps. However, the portions of the interferometer that were not measured between UHPG steps show deviations of up to 5 μm (Figure 3.17).

3.5.3.1   No Post-Fabrication Treatment

While no contrast was found before any post-fabrication measures were taken, an image of the twice-reflected beam was taken (Figure 3.18a). This image shows extra "wings" on the fringes of the beam profile that are not predicted for a perfect crystal. The extra wing-like structures indicate a thin damaged layer at the crystal surface with a mosaic that is comparable to the crystal's Darwin width. Mosaic crystals have a higher overall reflectivity than a perfect crystal. However, unfortunately, mosaic crystals are unsuitable for interferometers, because the sum over mosaic blocks in the crystal is incoherent [Sea97a; Sea97b].

Adding an empirical Green's function to the known result for two perfect crystals and fitting to the measured beam profile allowed the reflecting power and depth of the damaged Bragg planes to be measured. The derivation of this function is given in Appendix B.4. The result is to have the two Green's functions, one for a perfect crystal and one for a crystal with reflective surfaces, convolved with the same incoming beam, which is taken to be a Gaussian of width σ_x convolved with a slit of width S (given by a sum of error functions, see Appendix B.4)

$$\mathcal{I}_f(x) = \int dx' \left[G_{2P}(x - x') + R G_{2S}(x - x', \lambda) \right] \mathcal{I}_i(x', \sigma_x, S), \tag{3.44}$$
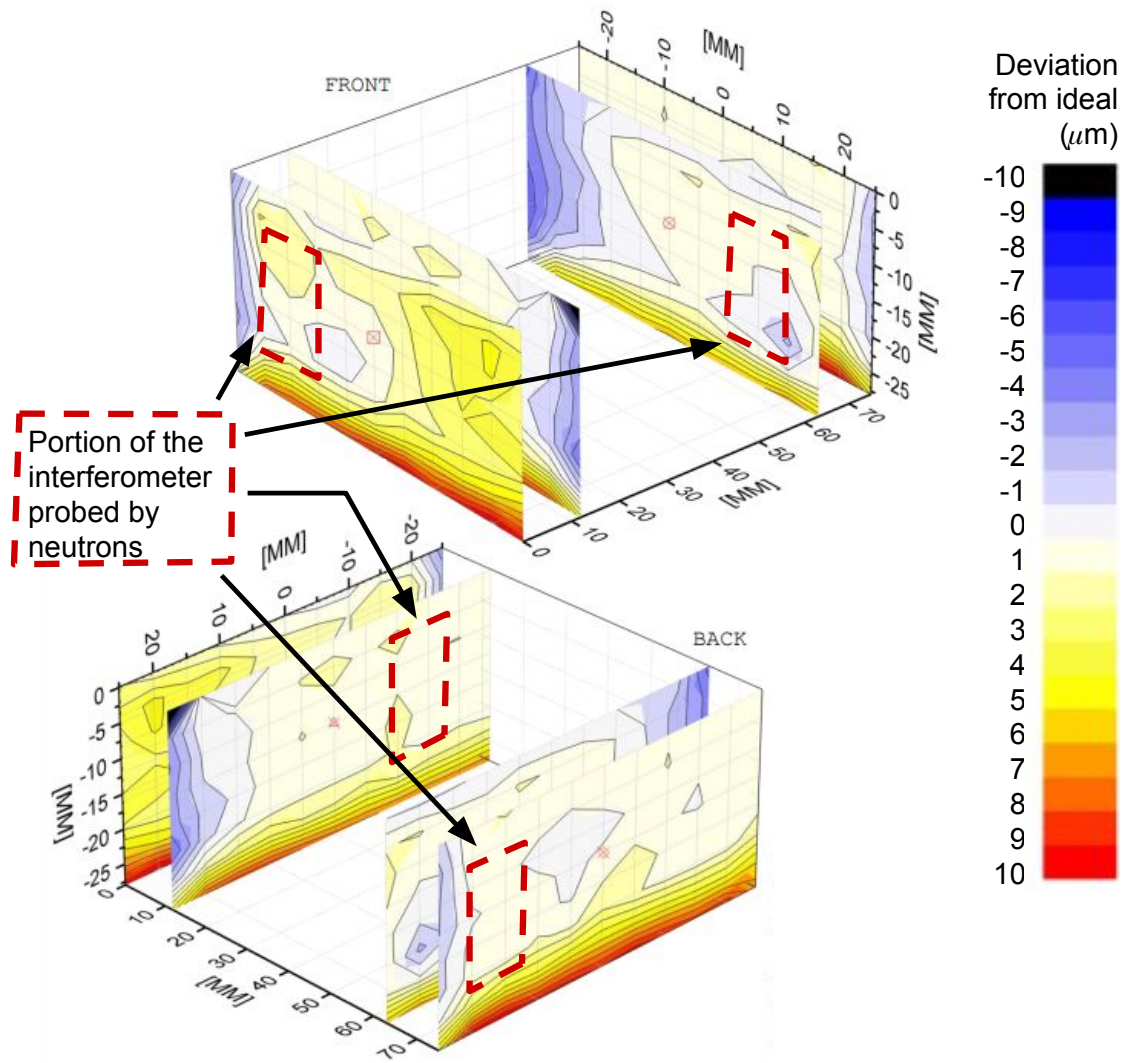
Figure 3.17 Map of the interferometer after all post fabrication steps. The color scale gives deviations from the ideal geometry. The red dashed outlines show the portion of the interferometer probed by neutrons. This was also the approximate place measured by the coordinate measuring machine in between UHPG steps. Coordinate measuring and plot courtesy of Ivar Taminiau.

where G_{2P} and G_{2S} are the position space Green's functions for two perfect crystals and two crystals with strained surfaces, respectively. The two Green's functions are normalized such that R is the reflectivity of the crystal surfaces, relative to the reflectivity of the bulk, which is related to the mosaic of the damaged crystal surfaces

$$R \sim \frac{\sigma_W}{\Theta_D}, \tag{3.45}$$

where σ_W is the mosaic spread of the crystal, and Θ_D is the crystal Darwin width. The depth of the Bragg plane damage is given by λ. In short, R and λ give the amplitude and shape of the rocking curve wings, respectively.

The beam profile $\mathcal{I}(x)$ was then computed numerically over the relevant ranges and fit to the measured beam profiles. From fitting the beam profile before any post fabrication treatments (Figure 3.18a), distortions of the crystallographic planes exist on the order of $R = 1.44 \pm 0.06$ times the reflectivity of the bulk, extending $\lambda = 1.36 \pm 0.03$ mm into the crystal from each surface. The relatively shallow 4 μm etching depth performed in Step III indicates that the subsurface damage from machining itself did not extend this deep into the crystal. However, the data suggests the subsurface damage strains the Bragg planes at the level of the Darwin width and to a depth that is much deeper than the damage itself.

3.5.3.2 First and Second Heat Treatments

The entire interferometer was annealed at 800°C for ten hours. After annealing, the interferometer showed modest fringe visibility, but the interference peak width was larger than theory predicted. Additionally, the peak position moved as the interferometer was translated (see Figure 3.19a), indicating the Bragg planes within each of the diffracting blades exhibit a "twist" relative to one another of 8 nrad/mm.

The distortions of peak structure were large enough that the expansion leading to Equation 3.40 is not valid. Allowing strain in the crystal blades, parameterized by σ_δ in Equations 3.36 and 3.37, was suitable for performing fits. An example of the typical peak structure after annealing for 72 hours at 800°C is shown in Figure 3.20a. The FWHM of the peaks, as a function of interferometer translation is shown in Figure 3.21. The FWHM of the interference peak was 15 nrad to 20 nrad larger than expected. Thus, after annealing, the strain caused by subsurface damage was reduced from roughly the Darwin width of 10^{-5} to 10^{-8}, as given by the difference in the expected and measured FWHM.

3.5.3.3 Chemical Etching

The interferometer was etched in a 60:1 mixture of nictric and hydroflouric acids for seven minutes. 2.5 g of silicon powder was added to the 2.5 L of acid for five minutes to warm the bath and begin
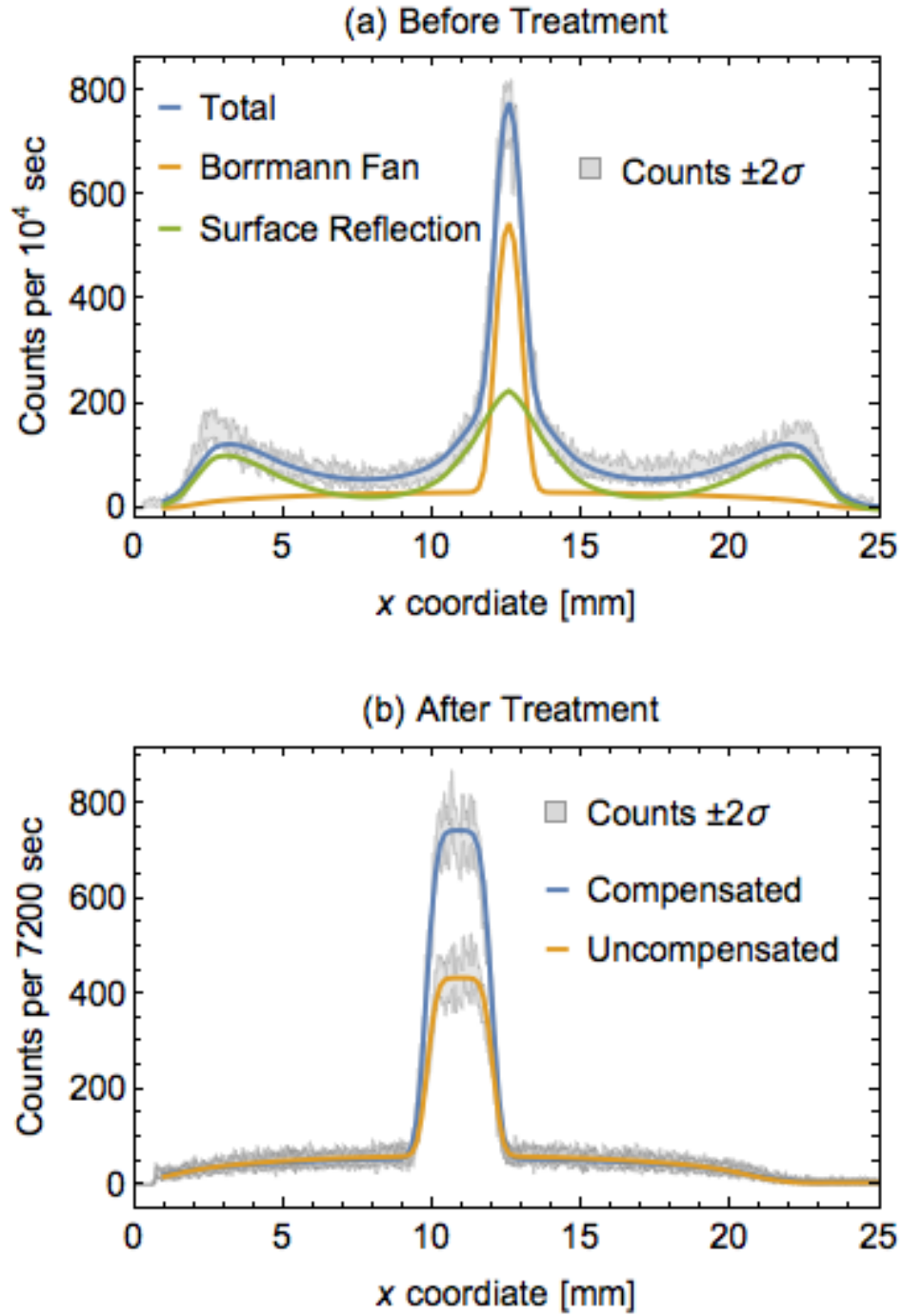
Figure 3.18 Horizontal beam profile (a) before (step N) and (b) after (step IV) annealing and chemical etching. The compensated beam profile has the prism in the beam and rotated to the rocking curve maximum. The uncompensated beam profile has no prisms in the beam. The extraneous "wings" demonstrate the reflectivity and depth of strain in the crystal. The images were taking with an incoming slit of 1 mm and 2 mm for parts (a) and (b), respectively. Uncertainties are from Poisson counting statistics.
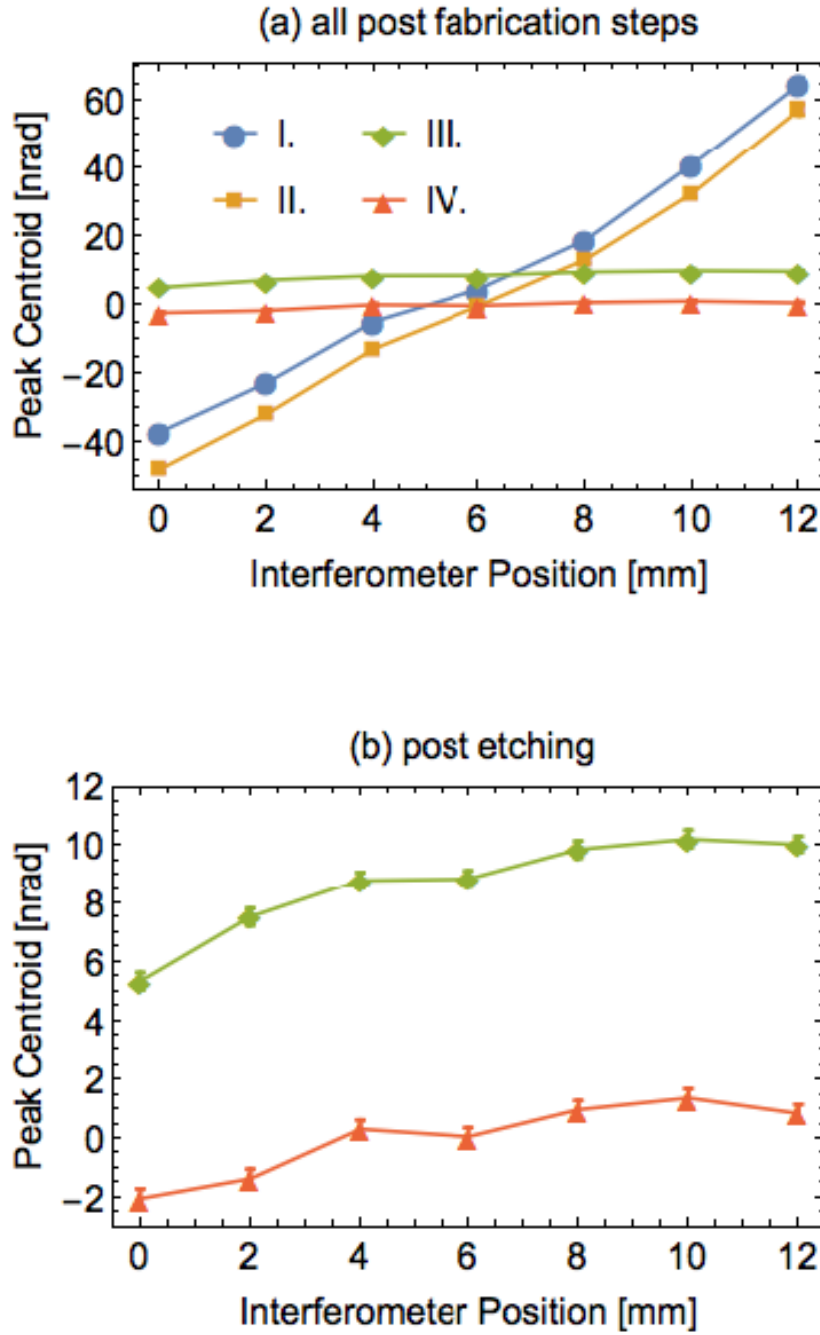
Figure 3.19 Location of peak centroids in terms of Bragg plane misalignment (a) for all post fabrication steps and (b) rescaled to show post fabrication steps after annealing. Post fabrication steps (in order) are I. 12 hour annealing, II. 72 hour annealing, III. chemical etching, and IV. 8 hour annealing. Annealing alters the offset of the curves, but not the overall structure, indicating that heat treatments primarily impact the interferometer base while etching relives subsurface damage in the blades.
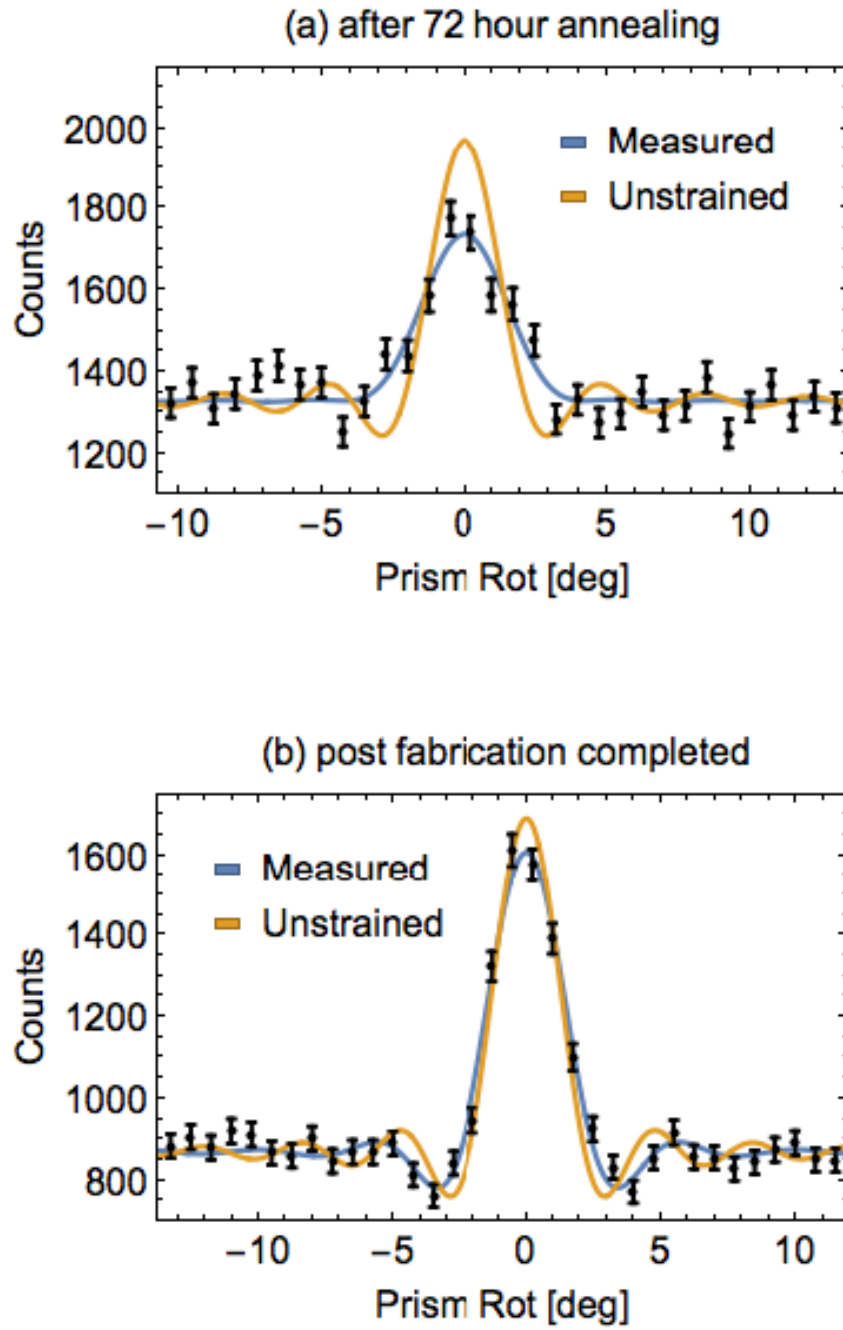
Figure 3.20 Structure of peak (a) after annealing for 72 hours (Step II) and (b) after all post fabrication steps completed (Step IV). Etching changed the peak structure remarkably which suggests that the perturbed peak structure occurred from subsurface damage.

85
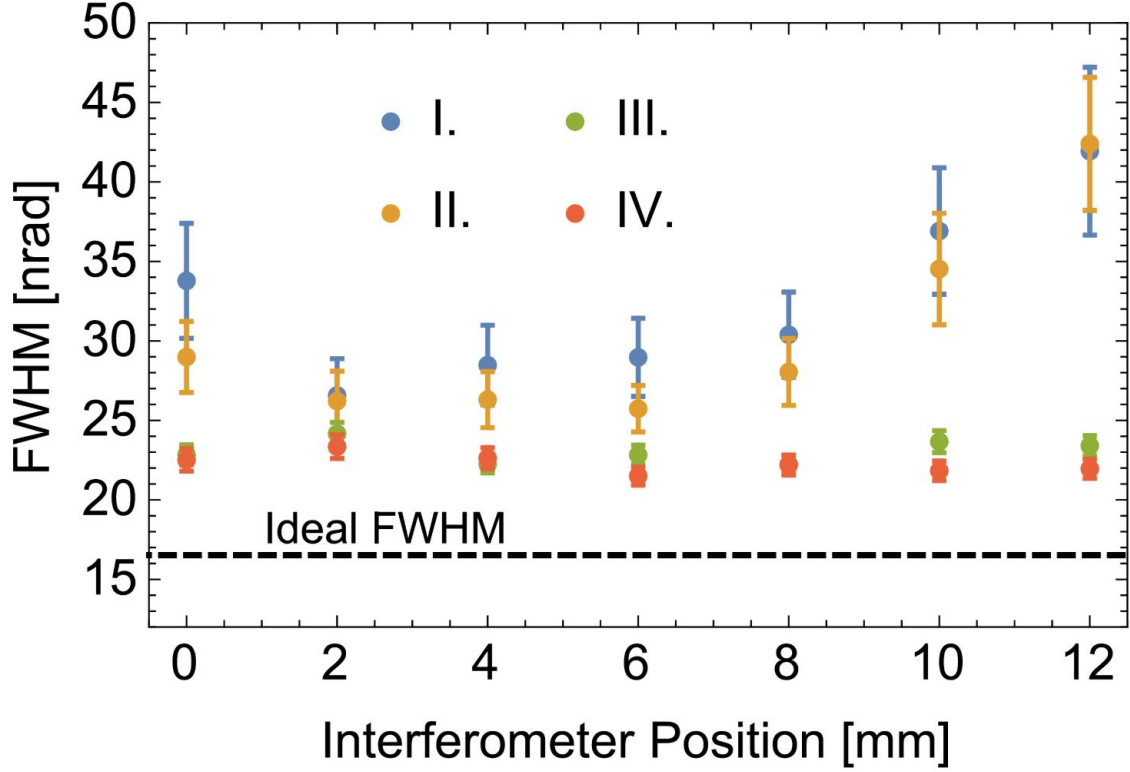
Figure 3.21 Full width at half maximum (FWHM) for each post fabrication step. Etching dramatically reduces the FWHM of the interference curves.

the reaction. The interferometer was submerged upside down in the acid bath and agitated by hand to prevent bubbles from forming on the surfaces.

The peak structure after etching was much improved, as shown in Figure 3.20b. The measurement of the interferometer dimensions concluding all post-fabrication steps indicated that 4 μm of material was removed from each surface. This is much less than the amount required of interferometers in the past, indicating that either the UHPG produces less subsurface damage than traditional techniques, or that less material needs to be removed to fix subsurface damage when chemical etching is used in conjunction with annealing.

The typical FWHM of 22 nrad after etching is much closer to the theoretical value of 17 nrad. The deviations from ideal were parameterized using Equation 3.40, in which case the expansion was found to be a good approximation. The fitted a_i parameters were highly covariant, which prevented the identification of the principle mechanism for peak broadening. It is likely that all the listed effects: strain within the diffracting blades, slowly-varying Bragg plane misalignment, and crystal roughness all contributed. Previous two-blade neutron interferometers also exhibited a FWHM that was wider than expected [Art85]. In conclusion, etching relieved the equivalent of about 15 nrad

of strain caused by subsurface machining damage. Most strikingly, the Bragg plane twist in the interferometer, seen in Figure 3.19, was reduced by over an order of magnitude from 8 nrad/mm to approximately 0.2 nrad/mm after chemical etching. Therefore, chemical etching removes subsurface damage that propagates more-deeply into the diffracting crystal, relieving overall twist in the Bragg planes.

3.5.3.4   Third Heat Treatment

Another chemical etching treatment was not performed, because etching rates are never constant across the interferometer blades and deep etching tends to result in nonuniform blade thicknesses and reduced contrast. It was decided, however, to anneal again, this time for ten hours at 800°C. The peak structures and FWHM did not change appreciably. However, while twist in the Bragg planes remained relatively unchanged, there was an overall shift in the peak positions, indicating that some strain in the base may have been relieved (Fig 3.19b). However, the intensity at the center of the twice-diffracted beam without the prism present was much less than with the prism rotated to the peak maximum (see Figure 3.18b), indicating that the overall angular offset between the Bragg planes of the two diffracting crystals was greater than the width of the peak itself. The overall absolute misalignment of the Bragg planes in the two blades is unknown because the absolute alignment of the refracting fused silica prism to the interferometer Bragg planes is also unknown. This does not greatly impact the functionality of the interferometer, because a global offset in the angular alignment of the two crystals can be corrected with the prism. However, the same cannot be said for Mach-Zehnder interferometers, where an angular misalignment between Bragg planes of two diffracting crystals reduces interference fringe visibility. Fortunately, the blades of Mach-Zehnder neutron interferometers are typically only about 2 mm, making the FWHM of the rocking curves about five times wider than the peaks studied here. While annealing did not appreciably change the FWHM for the two-blade interferometer, the change in global offset from annealing can greatly improve interferometer Mach-Zehnder performance, as was previously shown in Section 3.4.

3.5.4   Conclusion

A high-fidelity two-blade neutron interferometer was successfully fabricated with indicators of subsurface damage monitored throughout the post-fabrication process. A flow diagram showing the response of the interferometer to each post fabrication treatment is shown in Figure 3.22. While subsurface damage from UHPG extended down less than 4 μm into the crystal surfaces, strain in the Bragg planes on the order of the Darwin width caused by subsurface damage extended down about 1.4 mm into the crystals. Some of this damage could be alleviated using annealing, but etching 4 μm off of each surface was necessary to reach high contrast and a small FWHM. Annealing a final time did not change the peak structure, but changed the global offset. This indicates that

annealing Mach-Zehnder neutron interferometers can relieve strain in the interferometer base that causes misalignments between the Bragg planes of separate diffracting crystal blades on the order of 10 nrad.

The NIOF program and collaborators are now currently investigating whether UHPG creates less subsurface damage, or if the addition of annealing allows less material to be etched away. In particular, a wide range of grinding and diamond turning parameters for the purposes of making interferometer fabrication more reproducible is being explored and tested, with the efforts lead by Dmitry Pushin and Ivar Taminiau of the University of Waterloo Institute for Quantum Computing.

N. UHPG

Distorted Bragg
Planes

I.&II. Annealed

Surface Damage

8 nrad / mm twisted
Bragg planes

Surface Damage
Removed

Relieved
strain in base

IV. Reannealed

III. Etched
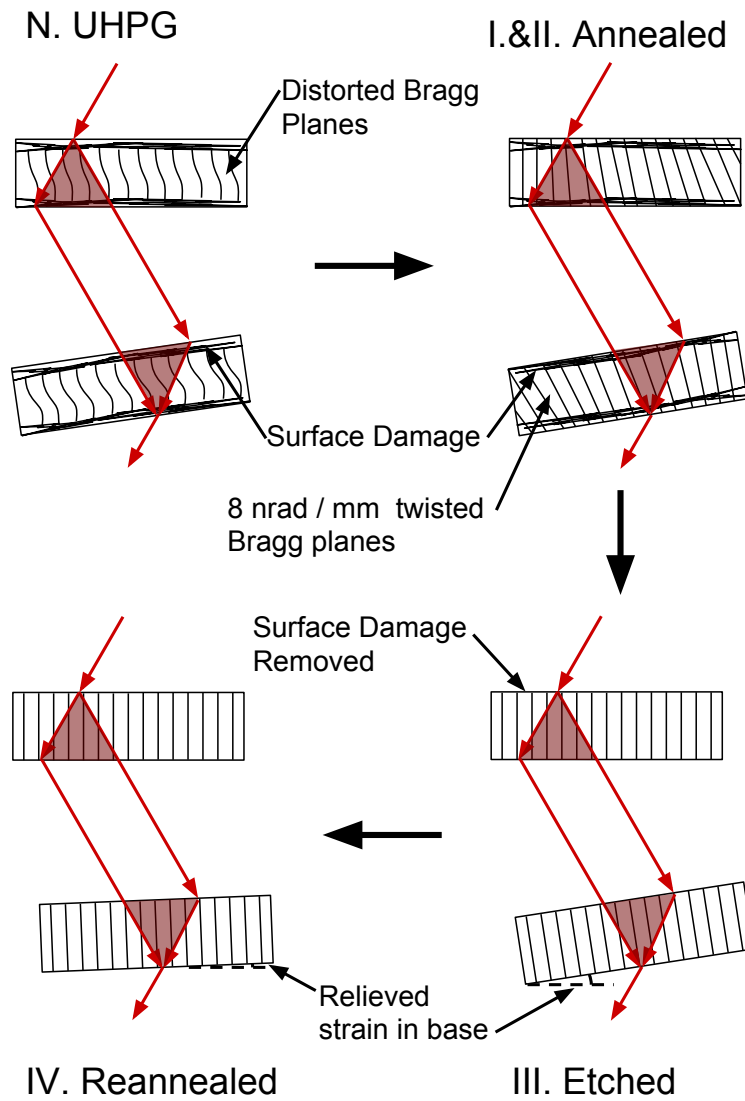
Figure 3.22 Schematic of post fabrication and the hypothesized effect of each step. Beam paths are shown as red arrows. The relevant volume of crystal for interferometric experiments is colored red.

CHAPTER 4 ──────────────────────────────────────

PRECISION STRUCTURE FACTOR MEASUREMENTS USING
PENDELLÖSUNG INTERFEROMETRY

4.1 Introduction

This chapter describes an experiment to measure the neutron silicon structure factors for three Bragg reflections. The data provides a measure of the silicon Debye-Waller factor (DWF) and the neutron charge radius. The data is also used to place limits on an ångström-scale fifth force. While x-ray structure factors in silicon have been measured in the past, the relative uncertainties were generally on the order of $\gtrsim 5 \times 10^{-4}$ [Spa86; CH88], whereas this work results in relative uncertainties of $\gtrsim 5 \times 10^{-5}$. For neutrons in silicon, only the (111) structure factor has been measured with precision [SO72], although this experiment marks a factor of four improvement in precision over the previous result.

The ability to measure neutron structure factors with relatively small uncertainties is due to the very low absorption of neutrons compared to x-rays. Pendellösung measurements with x-rays require the use of thin crystals that are usually cut in a wedge shape, allowing for the pendellösung fringes to be resolved in a position sensitive detector, with tens of pendellösung periods within the crystal [KL59; Hat65; TK72; AH73]. Neutron pendellösung interference, on the other hand, may be resolved after the neutron wave has passed through hundreds of pendellösung periods. The fringes can then either be modulated by changing the neutron wavelength [Shu68] or the effective crystal thickness [Sip65], which is accomplished most easily by tilting the crystal [Som78]. The tilted crystal approach is the one adopted by this experiment. Perhaps most promising, pendellösung at a pulsed neutron source has recently been demonstrated [Ito18]. In this case integer multiples of the same structure factor may be measured in a single apparatus, providing multiple avenues for limiting systematics, as has previously been proposed for x-rays [DH85]. Because the neutron wave passes

through more pendellösung periods and all measurements are made $\text{Mod}(2\pi)$ with regard to the phase of the interference fringes, very precise measurements of neutron structure factors can be made using crystals with thicknesses on the order of 1 cm.

The utility of pendellösung oscillations was first realized for precision measurements of the silicon and germanium coherent scattering lengths [Shu68; SO72; SS73]. However, neutron interferometers have proved a superior tool for measuring the coherent scattering length density of a sample, because the sample need not be crystalline and there is no need to account for neutron electron scattering or the DWF. However, as was pointed out by [SL02; SL03], pendellösung interferometry can be used to measure the neutron charge radius. Because the structure factor still depends on the coherent scattering length, [Wie06] pointed out that measuring diffraction inside an interferometer could lead to a very precise measure of the neutron charge radius. However, it has been realized since that strain and unequal crystal thicknesses severely disrupts such analyses [Pot15]. Despite these difficulties, this experiment is designed to combine aspects of the pendellösung [SL02; SL03] and modified interferometer [Wie06] approaches, by performing the pendellösung interferometry experiment, then placing the sample in a neutron interferometer to measure the forward coherent scattering phase shift. The ratio of the phase shifts measured in each portion of the experiment is independent of the crystal thickness and is not limited by the uncertainty of the silicon coherent scattering length. The most precise measure of the neutron coherent scattering length also had a relative uncertainty of 5×10^{-5} and was ultimately limited by the global parallelism of the silicon sample that was used [Iof98].

Pendellösung interferometry measures the pendellösung phase shift

$$\phi_P = \frac{2D \tan \theta_B}{H} \sqrt{v_H v_{-H}}, \tag{4.1}$$

where D is the thickness of the crystal slab; H is the reciprocal lattice vector; θ_B is the Bragg angle; and v_H is the reduced structure factor (See 1.31 and Section 4.2.3).

Measurement of the crystal thickness is necessary to isolate the structure factor. During the forward scattering measurement, the pendellösung crystal is placed in the neutron interferometer such that the relevant irradiated volume is the same for both portions of the experiment. Because the pendellösung and interferometer phase shifts are both proportional to the crystal thickness, the ratio of the two measurements no longer depends on the crystal thickness. Additionally, the interferometer measures the coherent scattering amplitude, so the resulting quantity is the ratio of the structure factor evaluated for a reciprocal lattice vector with Miller indices hkl to that of $h = k = l = 0$ multiplied by a geometric factor that depends on the Bragg angle of the pendellösung and interferometer crystals.

$$\frac{\phi_P}{\phi_I} = \frac{2\sqrt{v_H v_{-H}} \tan \theta_{BP} H_I}{v_0 \sin \theta_{BI} H_P}, \tag{4.2}$$

where the P and I subscripts refer to the values for the pendellösung and interferometer Bragg reflections, respectively.

The three structure factors measured in this work converge to a result for the mean square neutron charge radius of $\langle r_n^2 \rangle = -0.1088(93)$ fm^2, assuming no preferred value for the DWF. This is to be compared with the Particle Data Group (PDG) value of $\langle r_n^2 \rangle = -0.1166(22)$ fm^2 [Tan18]. Assuming the PDG value and uncertainty for the neutron charge radius, the measured Debye-Waller B parameter is $B = 0.47711(70)$ Å^2 at 295.5 K, where $\langle u^2 \rangle$ is the mean squared displacement of silicon atoms in the lattice due to thermal vibrations. This can be compared to the lattice dynamical value of $B = 0.47266(165)$ (scaled to 295.5 K) as computed according to [FS99] using neutron inelastic scattering data fit to a Born-von Kármán (BvK) lattice dynamics model. The slight disagreement between the values may be due to the choice of the lattice dynamical model that is used, implying that it may be possible for precision structure factor measurements to distinguish between lattice dynamical models. Specifically, it may be possible to compare results with the recent theoretical and experimental advances in the interpretation of neutron inelastic scattering data [Kim15; Kim18].

The measured structure factors may also be used to constrain the coupling strength of a beyond the standard model of particle physics (BSM) force mediator with mass in the 10 eV to 10 keV range. Limits are improved by between one and two orders of magnitude in this range. Repeating the experiment with germanium would further increase limits by about a factor of five.

The rest of this chapter outlines the physical contributions to the neutron silicon structure factor (Section 4.2), the theoretical background necessary for precision pendellösung interferometry (Section 4.3), followed by the experimental details (Section 4.4) and results (Section 4.5). It is possible to skip to Sections 4.4 and 4.5, while referencing prior sections as one's interests lead them.

4.2   Neutron Silicon Structure Factor

The structure factor arises from cross terms in the dynamical diffraction Hamiltonian in the $|\vec{K}\rangle$, $|\vec{K} + \vec{H}\rangle$ basis, which is related to the amplitude of the diffraction operator, as described in Chapter 1. To derive the neutron structure factor I begin with the neutron-crystal potential

$$\mathcal{V} = \sum_{\vec{\ell},v} V_{\vec{\ell},v} \left(\vec{x} - \vec{x}_{\vec{\ell},v} \right), \tag{4.3}$$

where $V_{\vec{\ell},v}$ is the neutron-scattering site potential for the scattering site located at $\vec{x}_{\vec{\ell},v}$; the vector of integers $\vec{\ell}$ indexes the unit cell; and v denotes one of eight positions within the silicon unit cell. The goal is to write this potential in momentum space while also summing over all the scattering centers in the relevant crystal volume. Writing the crystal potential in momentum space gives

$$\widetilde{\mathcal{V}} = \sum_{\vec{\ell},v} \widetilde{V}_v e^{i\vec{q}\cdot\vec{x}_{\vec{\ell}v}} \ , \tag{4.4}$$

with the same summation over unit cells $\vec{\ell}$, as well as the positions within the unit cell v. Note that the Fourier transformed potential of the scattering center is assumed to depend on its position in the unit cell, as indexed by v, and not on which unit cell it inhabits; hence the v and not $\vec{\ell}$ subscript for $\widetilde{V}_v$.

The position of the scattering centers $\vec{x}_{\vec{\ell},v}$ is parameterized by

$$\vec{x}_{\vec{\ell},v} = \vec{\ell}a + \vec{u}_{\vec{\ell}} + \vec{x}_v + \vec{u}_v. \tag{4.5}$$

In this case I have assumed a cubic unit cell with volume $\Omega_0 = a^3$. The displacements from equilibrium of the unit cell and scattering centers within the unit cell are $\vec{u}_{\vec{\ell}}$ and $\vec{u}_v$, respectively. I can then identify $\vec{u}_{\vec{\ell}}$ with displacements arising from acoustic phonons, and $\vec{u}_v$ as displacements from optical phonons in the long wavelength limit. See Section 4.2.2.

To compute the sum over $\vec{\ell}$, I need to make the transformation

$$\sum_{\vec{\ell}} \to \frac{1}{\Omega_0} \int d^3x. \tag{4.6}$$

Performing this integral would normally give a delta function $\delta^3(\vec{q})$. However, for any value of $\vec{q}$ such that $\vec{q}\cdot\vec{\ell}a = n2\pi$ is also a solution. This is to say

$$\sum_{\vec{\ell}} e^{i\vec{q}\cdot\vec{\ell}a} = \sum_{\vec{\ell}} e^{i(\vec{q}+\vec{H})\cdot\vec{\ell}a}, \quad \text{for } \vec{H} = \frac{2\pi}{a}\vec{\ell}', \tag{4.7}$$

where $\vec{H}$ are the reciprocal lattice vectors. One would then expect for there to be no dependence of the result on $\vec{H}$, except for the existence of $\vec{u}_{\vec{\ell}} + \vec{x}_v + \vec{u}_v$. The solution to the discrete sum is the volume integral and a summation over all the possible $\vec{H}$

$$\widetilde{\mathcal{V}} = \sum_{\vec{\ell},v} \widetilde{V}_v e^{i\vec{q}\cdot\vec{x}_{\vec{\ell},v}} = \frac{1}{a^3} \sum_{\vec{H},v} \int d^3x \, \widetilde{V}_v \exp\left[i\left(\vec{q}+\vec{H}\right)\cdot\vec{x} + \vec{q}\cdot\left(\vec{u}(\vec{x}) + \vec{x}_v + \vec{u}_v(\vec{x})\right)\right], \tag{4.8}$$

where I have let $\vec{u}_{\vec{\ell}} \to \vec{u}(\vec{x})$ and noted that $\vec{u}_v$ can also have a long range dependence by writing $\vec{u}_v(\vec{x})$ as a function of position. The volume integration over $\vec{x}$ generates a function that is sharply peaked at $\vec{q} = \vec{H}$. However, smearing of what would be a delta function without $\vec{u}(\vec{x})$, depends on the displacements from equilibrium as a function of position, which itself contains a great deal of physics. The interpretation of $\vec{u}(\vec{x})$ and $\vec{u}_v(\vec{x})$ includes

1. **Debye-Waller Factor (DWF)** - This is the smearing that occurs when averaging over thermal oscillations with the momentum transfer $\vec{q}$ still sharply peaked around the reciprocal lattice vector $\vec{H}$.

2. **Inelastic neutron-phonon scattering** - The average over thermal oscillations can lead to a nonzero contribution from the term that is first order in $\vec{u}(\vec{x})$. This scattering is inelastic with the neutron absorbing or emitting phonons. While not probed by this experiment, phonon dispersion curves may be measured using neutron inelastic scattering. See for example [Kul94; FS99; Kim18].

3. **Thermal diffuse scattering (TDS)**- Inelastic scattering of the diffracted wave $\vec{q} \neq \vec{H}$ can impact structure factor measurements when the inelastically scattered state overlaps with the momentum space acceptance of the experimental apparatus. This thermal scattering is referred to as diffuse, because it occurs over the entire range of $\vec{q}$, as opposed to Bragg scattering which is much more sharply peaked at $\vec{q} = \vec{H}$. This is very important for experiments which measure the integrated reflectivity of a Bragg diffracting crystal. The contribution of thermal diffuse scattering to the measured structure function depends on the experimental details and is difficult to compute [Wil69; Wil70; WM17] . Fortunately, the TDS correction is likely very small and is not generally considered in x-ray pendellösung measurements [Spa86; CH88].

4. **Cubic anharmonic effects** - The lowest order, imaginary part of $e^{i\vec{q}\cdot\vec{u}}$ with $\vec{q} = \vec{H}$ is the $\vec{u}^3$ term, which takes on a nonzero value from three-phonon terms in the interatomic potential. As will be described, in the case of silicon this only impacts certain Bragg reflections, and exists at the detection limit for this experiment. Extension of this experiment to higher-order Bragg reflections could provide a direct measure of the anharmonic force contributions.

5. **Quartic and higher-order anharmonic effects** - Higher order terms in the interatomic potential also exist, causing the Debye-Waller factor to not be strictly Gaussian in H. These effects can be quite important for the study of phonon-light scattering [Bal83], however they exist outside the detection limit for this experiment.

For the case of Bragg diffraction from a monochromatic beam, only one reciprocal lattice vector will be relevant, leaving a single term in the sum over H to be retained

$$\widetilde{\mathcal{V}}_H = \frac{1}{a^3} \widetilde{V}(H) \left\langle \sum_v e^{i\vec{H}\cdot\vec{x}_v} \right\rangle (2\pi)^3 \, \delta^3 \left(\vec{q} - \vec{H}\right) \tag{4.9}$$

where the Brackets indicate the thermal average, and I have assumed $\widetilde{V}$ to be the same for each of the scattering centers in the unit cell. This is true for silicon, but not valid for multi-species crystals such as quartz. The extension to such crystals is straightforward, though the lack of symmetry gives
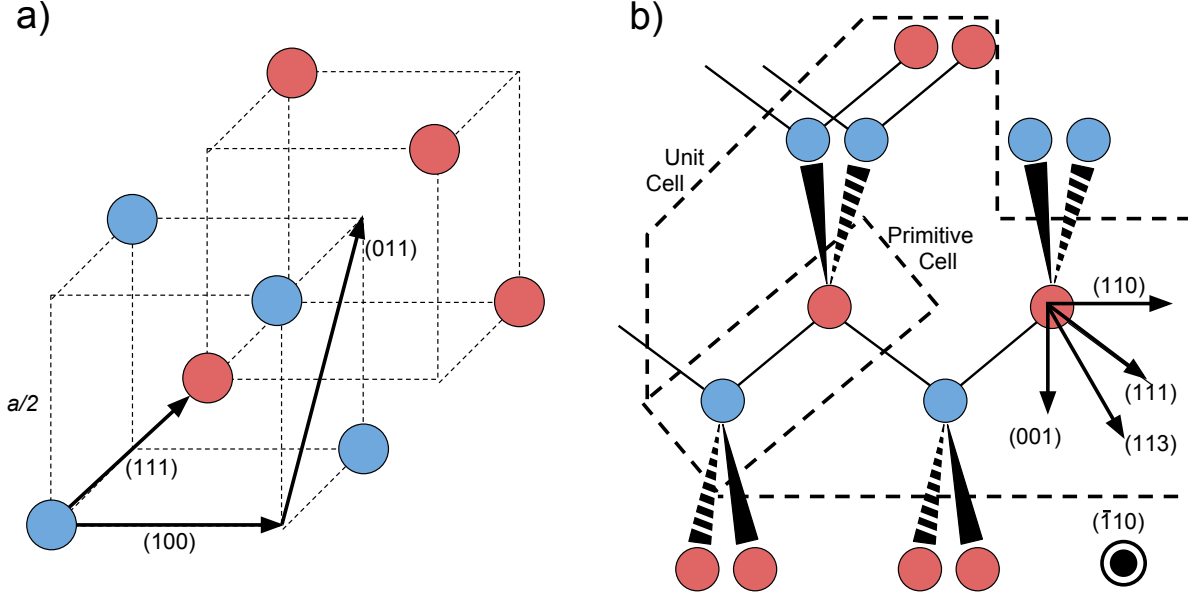
Figure 4.1 (a) Eight atoms make up a diamond unit cell. Two sets of four atoms with opposite tetrahedral bonding parities, indicated as red and blue circles, form interspersed cubes. Atoms only form bonds with the opposite parity. The (100) direction points along the cube edges; the (110) direction points between the two oppose corners of a cube face; and the (111) direction points along bond axis, between opposite corners of a cube. Shown in (b) is a view of the plane formed by two bonds with nearest neighbors.

rise to spin-dependent effects which are not observable in silicon. See [FV18] and the references therein; there is also some discussion of these effects in Section 4.2.3.2. The reduced structure factor

$$v_H = \frac{2m}{a^3} \widetilde{V}(H) \left\langle \sum_v e^{i\vec{H}\cdot\vec{x}_v} \right\rangle \tag{4.10}$$

is the term appearing in the dynamical diffraction Hamiltonian in Chapter 1. I will now continue with a discussion of the term in angle brackets, leaving the explanation for the potential $\widetilde{V}(H)$ for Section 4.2.3.

The high degree of symmetry is such that the sum over phase factors $\sum_v e^{i\vec{H}\cdot\vec{x}_v}$ add to zero for some Bragg conditions. This leads to what are called forbidden reflections. To see the origin of allowed versus forbidden reflections, consider the silicon unit cell. Silicon has a diamond unit cell containing eight atoms, all in tetrahedral bonding geometries in one of two parities. Four of the atoms with the same bonding tetrahedral form a cube with atoms occurring in cross-diagonal locations. A second identical cube, except for the bonding parity of the atoms, is displaced from the first by $\Delta\vec{x} = \frac{a}{4}(1,1,1)$. See Figure 4.1.

Because a primitive cell (Figure 4.1b) consists of two atoms sharing a bond, and there are four, unique bonding directions, there are a total of eight atoms in the unit cell, and if the unit cell is chosen as four primitive cells with the same bonding geometry, there must also be phase factors carried by the position of each bond. The four bonding locations for the unit cell shown in Figure 4.1a, are $\frac{a}{8}(1,1,1)$, $\frac{a}{8}(5,5,1)$, $\frac{a}{8}(5,1,5)$, and $\frac{a}{8}(1,5,5)$.

When summing these phase factors over the four primitive cells within the unit cell, a Bragg condition is allowed only if all the Miller indices are either all odd or all even and add to a multiple of four. i.e. (111) and (444) are allowed, but (222) is forbidden. For these purposes, zero is considered even: For example, (110) is forbidden but (220) is allowed. The two types of reflections, all the Miller indices odd or even, lead to two different magnitudes for

$$\left| \sum_v e^{i\vec{H}\cdot\vec{x}_v} \right| = \begin{cases} \sqrt{32}, & \text{odd} \\ \\ 8, & \text{even} \end{cases}. \tag{4.11}$$

The classification of certain reflections as being even, odd, or forbidden, depends only on the average position of the unit cells. I will now consider the effect of thermally smearing Equation 4.11.

4.2.1 Debye-Waller Factor

The Debye-Waller factor (DWF) occurs due to the thermal smearing of the ideal structure factor. The smearing is determined by the distribution of vibrations exhibited by the crystal at some temperature. To derive the DWF consider the average atomic positions $\vec{x}_v$ and their displacements from average $\vec{u}$

$$\left\langle e^{i\vec{H}\cdot\vec{x}_v} \right\rangle \rightarrow e^{i\vec{H}\cdot\vec{x}_v} \left\langle e^{i\vec{H}\cdot\vec{u}_v} \right\rangle. \tag{4.12}$$

Note, however, that the displacement vectors $\vec{u}$ may be written in terms of phonon raising and lowering operators:

$$\vec{u}(\vec{x}) = \int d^3k \sqrt{\frac{1}{2m\omega_k}} \left(\vec{a}_k + \vec{a}^\dagger_{-k} \right) e^{i\vec{k}\cdot\vec{x}}, \tag{4.13}$$

where a_k annihilates a phonon

$$a_k \left| n_k \right\rangle = \sqrt{n_k} \left| n_k - 1 \right\rangle \tag{4.14}$$

with n_k the number of phonons with wave vector k, and $a^\dagger$ creates a phonon

$$a^\dagger_k \left| n_k \right\rangle = \sqrt{n_k + 1} \left| n_k + 1 \right\rangle. \tag{4.15}$$

In this case, the Bloch identity [Lov84] (pg 95) allows me to form the DWF

$$\left\langle e^{i\vec{H}\cdot\vec{u}} \right\rangle = e^{-\frac{1}{2}\left\langle \left(\vec{H}\cdot\vec{u}\right)^2 \right\rangle} = e^{-\frac{1}{2}\langle\vec{H}\cdot U\cdot\vec{H}\rangle} = e^{-W} \tag{4.16}$$

where U is the mean-square displacement matrix $U_{ij} = u_i u_j$; the components of U are called the anisotropic displacement parameters (ADP) [Erb13]. The occurrence of off-diagonal elements in U-depends on the symmetry of the system. Silicon's symmetry is such that U is diagonal, and can be given by one parameter, which is $U_{ii} = \frac{1}{3}\langle u^2 \rangle$ for cubic systems, and the exponent of Equation 4.16 takes on a simplified form

$$W = \frac{1}{2}\left\langle \vec{H}\cdot\vec{u} \right\rangle^2 = \frac{1}{2}\vec{H}\cdot U\cdot\vec{H} = \frac{1}{6}\vec{H}^2\langle u^2\rangle = \frac{B}{16\pi^2}\vec{H}^2, \tag{4.17}$$

where B is the Debye-Waller B parameter, and the relationship between the mean square displacement $\langle u^2 \rangle$, ADP U, and Debye-Waller B parameter for silicon has been made explicit. Note that there is some notational discrepancy in what is meant by $\langle u^2 \rangle$. Some authors, for example [FS99], take this to be the same as U_{ii}, while others such as [Lov84], take $\langle u^2 \rangle = 3U_{ii}$. Confusingly, both are called the mean square displacement. I have adopted the latter notation, as it corresponds to the expectation value of $\langle \vec{u}^2 \rangle$, whereas the prior refers a single component of $\vec{u}$: $\langle u_x^2 \rangle = \langle u_y^2 \rangle = \langle u_z^2 \rangle = U_{ii}$. The meaning of B, however, is universal, so to avoid confusion I have reported the results of this experiment in terms of B.

Computing the exponent gives [Lov84]

$$\left\langle \left(\vec{u}\cdot\vec{H}\right)^2 \right\rangle = \sum_{k\in\text{BZ}} \frac{\left|\sigma_k\cdot\vec{H}\right|^2}{2M_{\text{Si}}N\omega_k}\left(2n_k + 1\right), \tag{4.18}$$

where the sum is taken over the first Brillouin zone and phonon polarizations for a given $\vec{k}$; σ_k is the phonon polarization; M_{Si} is the mass of the silicon nucleus; N is the number of nuclei in the experimental volume; ω_k is the frequency, as given by the phonon dispersion relations; n_k is the number operator, and a function of temperature. Clearly, $(2n_k + 1)/N$ is a density, and this is most easily computed using the phonon density of states.

4.2.2   Anharmonicity in Silicon

The difference in the bonding parities of the A and B portions of the silicon lattice create extra degrees of freedom and with it optical phonons. While acoustic phonons vibrate the entire unit cell, the optical phonons change the spacing between the A and B portions of the unit cell. The separate bonding geometries cause A and B atoms to see different potentials, which can be seen in the crystal Hamiltonian [HA13]

$$\mathcal{H} = \frac{p_i^\alpha p_i^\alpha}{2m_i} + \frac{1}{2}\Phi_{ij}^{\alpha\beta}u_i^\alpha u_j^\beta + \frac{1}{3!}\Psi_{ijk}^{\alpha\beta\gamma}u_i^\alpha u_j^\beta u_k^\gamma, \tag{4.19}$$

where Roman indices denote individual atoms; Greek indices denote Cartesian coordinates; repeated indices of both varieties are summed over; and Φ and Ψ are the harmonic and anharmonic force matrices, respectively. A nonzero cubic force constant $\Psi \neq 0$ is required for thermal expansion, and given silicon's anomalous thermal expansion at low temperatures, Ψ is of great interest [Kim18].

Next, consider how optical phonons and acoustic phonons differ in constructing the silicon structure factor by splitting the sum over the eight scattering centers in the unit cell into a sum over the A and B portions thereof. I can rewrite the equilibrium displacements in terms of $\vec{u}_{\rm ac} = (\vec{u}_A + \vec{u}_B)/2$ and $\vec{u}_{\rm op} = (\vec{u}_A - \vec{u}_B)/2$, labelled acoustic and optical in the long phonon wavelength limit

$$\left\langle \sum_v e^{i\vec{H}\cdot\vec{x}_v} \right\rangle = \left\langle \sum_{v\in A} e^{i\vec{H}\cdot(\vec{u}_{\rm ac}+\vec{u}_{\rm op}+\vec{x}_v)} + \sum_{v\in B} e^{i\vec{H}\cdot(\vec{u}_{\rm ac}-\vec{u}_{\rm op}+\vec{x}_v)} \right\rangle, \tag{4.20}$$

where I have noted that the sign of $\vec{u}_{\rm op}$ is opposite for the A and B atoms in the lattice. Letting the B sites be translated relative to the A sites by $\frac{a}{4}(1,1,1,)$, the phase factor for the B sites is

$$\exp\left[i\vec{H}\cdot(\vec{x}_B - \vec{x}_A)\right] = \begin{cases} i, & h+k+l = 4n+1 \\ -i, & h+k+l = 4n-1 \\ 1, & h+k+l = 4n \\ -1, & h+k+l = 4n\pm 2 \end{cases}. \tag{4.21}$$

This phase shift between the A and B atoms, creates interference for the optical phonon oscillations, and I can write the structure factor for each of the four cases as

$$\left\langle \sum_v e^{i\vec{H}\cdot\vec{x}_v} \right\rangle = \begin{cases} 4(1-i)\left\langle e^{i\vec{H}\cdot\vec{u}_{\rm ac}}\left[\cos\left(\vec{H}\cdot\vec{u}_{\rm op}\right) - \sin\left(\vec{H}\cdot\vec{u}_{\rm op}\right)\right]\right\rangle, & h+k+l = 4n-1 \\ & h,k,l \in \text{Odd} \\[2ex] 4(1+i)\left\langle e^{i\vec{H}\cdot\vec{u}_{\rm ac}}\left[\cos\left(\vec{H}\cdot\vec{u}_{\rm op}\right) + \sin\left(\vec{H}\cdot\vec{u}_{\rm op}\right)\right]\right\rangle, & h+k+l = 4n+1 \\ & h,k,l \in \text{Odd} \\[2ex] 8\left\langle e^{i\vec{H}\cdot\vec{u}_{\rm ac}}\cos\left(\vec{H}\cdot\vec{u}_{\rm op}\right)\right\rangle, & h+k+l = 4n \\ & h,k,l \in \text{Even} \\[2ex] i8\left\langle e^{i\vec{H}\cdot\vec{u}_{\rm ac}}\sin\left(\vec{H}\cdot\vec{u}_{\rm op}\right)\right\rangle, & h+k+l = 4n\pm 2 \\ & h,k,l \in \text{Even} \end{cases} \tag{4.22}$$

The averaging over $\vec{u}_{\text{ac}}$ and $\vec{u}_{\text{op}}$ leads to the traditional Debye-Waller for the $\cos(\vec{H} \cdot \vec{u}_{\text{op}})$ terms. The $\sin(\vec{H} \cdot \vec{u}_{\text{op}})$ terms give cubic anharmonic effects. Consider expanding the anharmonic terms to third order in $u_{\text{ac,op}}$. Despite that for elastic scattering the single phonon terms are zero

$$\left\langle \vec{H} \cdot \vec{u}_{\text{op}} \right\rangle = 0, \tag{4.23}$$

the cubic terms in a tetrahedral geometry are nonzero

$$\left\langle \left(\vec{H} \cdot \vec{u}_{\text{op}} \right)^3 \right\rangle \neq 0 \tag{4.24}$$

$$\left\langle \left(\vec{H} \cdot \vec{u}_{\text{op}} \right) \left(\vec{H} \cdot \vec{u}_{\text{ac}} \right)^2 \right\rangle \neq 0. \tag{4.25}$$

Such terms are related to the phonon lifetime matrix elements [HA13]. To motivate the necessity of three phonon terms, consider perturbing a spherical harmonic oscillator with the cubic interaction potential

$$\mathcal{H}_{\text{int}} = \frac{1}{3!} \Psi_{ijk}^{\alpha\beta\gamma} u_i^\alpha u_j^\beta u_k^\gamma. \tag{4.26}$$

The perturbed energy eigenstates are then

$$|\vec{n}\rangle^{(1)} = |\vec{n}\rangle + \sum_{\vec{n}' \neq \vec{n}} \frac{|\vec{n}'\rangle \langle \vec{n}'| \mathcal{H}_{\text{int}} |\vec{n}\rangle}{\omega \sum(n^{\alpha'} - n^\alpha)}, \tag{4.27}$$

where $|\vec{n}\rangle$ is the energy eigenstate of the three dimensional harmonic oscillator with energy $E = \sum_\alpha (n^\alpha + 1/2)\omega$. The three phonons created (annihilated) by $\mathcal{H}_{\text{int}}$ must be annihilated (created) by an operator O in order for the expectation value $\langle O \rangle$ to be perturbed by $\mathcal{H}_{\text{int}}$

$$\sum_{\vec{n}' \neq \vec{n}} \frac{\langle \vec{n}| O |\vec{n}'\rangle \langle \vec{n}'| \mathcal{H}_{\text{int}} |\vec{n}\rangle}{\omega \sum_\alpha (n'^\alpha - n^\alpha)} \neq 0, \quad \text{only if } O \text{ is order 3 in } u. \tag{4.28}$$

The connection to phonon lifetimes is clear, because $\mathcal{H}_{\text{int}}$ can annihilate one phonon while creating two more. For example, an optical phonon can decay into two acoustic phonons travelling in opposite directions, while still respecting momentum and energy conservation, via terms similar to Equation 4.25.

Treating the cubic anharmonic perturbation classically, Dawson and Willis [DW67] were able to show

$$\left| \left\langle e^{i\vec{H}\cdot\vec{x}_v} \right\rangle \right| = \begin{cases} \sqrt{32}e^{-W}\left[1 - T_a(hkl)\right], & \begin{aligned} &h + k + l = 4n - 1 \\ &h, k, l \in \text{Odd} \end{aligned} \\[2em] \sqrt{32}e^{-W}\left[1 + T_a(hkl)\right], & \begin{aligned} &h + k + l = 4n + 1 \\ &h, k, l \in \text{Odd} \end{aligned} \\[2em] 8e^{-W}, & \begin{aligned} &h + k + l = 4n \\ &h, k, l \in \text{Even} \end{aligned} \\[2em] 8e^{-W}T_a(hkl), & \begin{aligned} &h + k + l = 4n \pm 2 \\ &h, k, l \in \text{Even} \end{aligned} \end{cases} , \tag{4.29}$$

where

$$T_a(hkl) = \left(\frac{B}{4\pi a}\right)^3 \frac{\beta}{k_B T} hkl, \tag{4.30}$$

corresponds to the three phonon terms; k_B is the Boltzmann constant; and T is the temperature. In this case a single parameter is used for the anharmonic force constant $\beta = \Psi_{iii}^{xyz}$, which does not take into account the nearest neighbor, next to nearest neighbor, etc. interactions. For temperatures approaching and above the Debye temperature $\Theta_{D,\text{Si}} \sim 640$ K, B is linear in temperature, and Equation 4.30 takes on a quadratic temperature dependence, which was utilized for measuring the anharmonic force constant using forbidden reflections at high temperatures [FS99; Kea71; Rob74; HB75]. However, at room temperature B is not linear with respect to temperature, and at all temperatures β will have its own temperature dependence [MW76]. While not entirely correct, the T^2-dependence was shown to be a decent approximation above 600 K. Additionally, the (222) structure factor has been measured close to room temperature [Rob74], which provides the anharmonic correction to the odd structure factors. Fortunately, Equation 4.22 indicates that the common term to the forbidden and odd reflections is a general result and does not depend on classical versus quantum phonon statistics or the number of anharmonic force constants that are considered.

Using the measured (222) forbidden reflection close to room temperature [Rob74], $T_a(111) \simeq 3 \times 10^{-5}$, which should be compared to the measured relative uncertainty of this experiment for the (111) structure factor of 5.4×10^{-5}. While $T_a(111)$ is below the detection limit, $T_a(333)$ would be 27 times larger at 81×10^{-5}. Thus, when the (333) structure factor is measured using pendellösung interferometry, the anharmonic term will be detectable. Finally, note that the $T_a(111)$ taken from the measured $T_a(222)$ is twice the size of $T_a(111) = 1.5 \times 10^{-5}$ computed using a single anharmonic force constant derived from fitting high temperature data to a T^2 model [FS99]. This suggests that the T^2-dependence of $T_a(hkl)$ is invalid at room temperature. In any case, measurement of the (333)

structure factor, especially as a function of temperature, could settle the disagreement between the limited data and the classical anharmonic force model at temperatures below the Debye temperature.

4.2.3 The Scattering Length and Q-Dependence

I now turn toward the structure of neutron-scattering center potential $\widetilde{V}$ in Equation 4.10. The principle contribution to $\widetilde{V}$ is nuclear scattering from the strong force. Because the strong force has a range that is much smaller than the neutron wavelength, it may be estimated by a single parameter b, the bound scattering length via the Fermi pseudopotential

$$V_N \simeq \frac{2\pi}{m} b \delta^3(\vec{x} - \vec{x}_N), \tag{4.31}$$

where $\vec{x}_N$ is the position of the scattering site, which is $\vec{x}_N = \vec{x}_{\vec{\ell},v}$ for a scattering center in the silicon lattice. The Fourier transform of this potential is

$$\widetilde{V}_N = \frac{2\pi}{m} b. \tag{4.32}$$

The presence of additional interactions simply add to $\widetilde{V}_N$. Of interest here are the nuclear scattering contribution, V_N, neutron scattering via electromagnetic interactions V_{EM}, and any BSM physics V_5. While the Fourier transform of the Fermi pseudopotential has no momentum space structure, the same cannot be said about the other interactions. Additionally, the neutron spin may interact with the crystal potential via Schwinger scattering. Because $\widetilde{V}_N$ is related to the scattering length b by a factor if $\frac{2\pi}{m}$, it is customary to simply apply a Q-dependence to b and write

$$\widetilde{V} = \frac{2\pi}{m} \left[b_N + b_{EM}(Q, \vec{\sigma}) + b_5(Q, \vec{\sigma}) \right] \tag{4.33}$$

where I have explicitly noted that b_{EM} and b_5 may be spin-dependent. For the purposes of this experiment, spin-dependent terms are out of phase with the primary nuclear contribution and can be neglected. This is due to the high degree of symmetry in the silicon scattering potential. When less symmetric crystals are used, this is no longer the case, and spin-dependent terms are prevalent. This has lead to large body of work centered around spin transport in non-centrosymmetric crystals. See [FV18] and the references therein for a summary. It is also possible to measure such effects in silicon by placing a pendellösung experiment within a resonant laboratory magnetic field [Fin87; Hor88]. Alternatively, an entirely different geometry that maximizes the total number of Bragg reflections in a silicon channel-cut crystal also has a spin-dependence [Dom01].

Combining Equation 4.33 with Equations 4.16 and 4.17, the Q-dependence of the structure factor appearing in the dynamical diffraction Hamiltonian itself is, with $\vec{Q} \to \vec{H}$

$$v_H = \frac{4\pi}{a^3} e^{-W(H)} \left[1 + f_{\mathrm{an}}(H)\right] \sum_v e^{i\vec{H}\cdot\vec{x}_v} b(H) \tag{4.34}$$

where f_{an} is the contribution from anharmonic effects discussed in the previous section.

4.2.3.1 Electronic Structure

Neutron electronic scattering can be understood given its Dirac F_1 and Pauli F_2 form factors [Isg99]

$$\widetilde{V}(Q) = j_n^\mu \widetilde{A}_\mu(Q) = \bar{u}(p') \left(\gamma^\mu F_1 + \frac{\sigma^{\mu\nu} q_\nu}{2m_n} F_2\right) u(p)\widetilde{A}_\mu(Q), \tag{4.35}$$

where the u are Dirac spinors; γ^μ are the Dirac matrices; $\sigma^{\mu\nu} = \frac{i}{2}[\gamma^\mu, \gamma^\nu]$; the four momentum transfer $(p'-p)^2 = -Q^2 = -\vec{q}^2$ is for low energy scattering $|p'-p|^2 = Q^2 \ll m^2$, and $\widetilde{A}$ is the Fourier transform of the crystal four vector potential. In the low energy limit, this expression can be expanded in Q^2. The zeroth order contribution to F_1 is the electric charge, and the zeroth order contribution to F_2 is the anomalous magnetic moment. In the case of the neutron, $F_1 = 0$, and because the entire magnetic moment is anomalous $F_2 = \mu$. The Dirac and Pauli form factors are related to the electric G_E and magnetic G_M form factors by

$$G_E = F_1 - \frac{Q^2}{4m^2} F_2 \tag{4.36}$$

$$G_M = F_1 + F_2. \tag{4.37}$$

Experimentally, these form factors are what are measured. Magnetic scattering is spin-dependent and will be treated in Section 4.2.3.2. For now, I will focus on $G_E(Q^2)$, which is the coupling of the neutron current j_n^μ to the electrostatic potential A^0.

For neutrons, the large Q^2 regime of the electronic form factor $G_E(Q^2)$ is measured using neutron electron scattering, where relativistic electrons are scattered from a target containing neutrons [GC11]. This leads to a straightforward physical interpretation of the neutron mean square charge radius as proportional to the slope of $G_E(Q^2)$ at zero momentum transfer, Figure 4.2. As pointed out by the authors of [GC11], this information can be used in conjunction with higher energy scattering data to fit $G_E(Q^2)$ to a functional form, which itself can be motivated either empirically or by predictions from quantum chromodynamics (QCD).

Expanding $G_E(Q^2)$ to first order in Q^2 yields [Isg99]

$$G_E = \left(\frac{\partial F_1}{\partial (Q^2)}\right) Q^2 - \frac{F_2}{4m^2} Q^2 = -\frac{1}{6}\langle r_n^2 \rangle Q^2 \tag{4.38}$$

where $\langle r_n^2 \rangle$ is the mean square neutron charge radius. Combing this with Equations 4.35 and 4.33
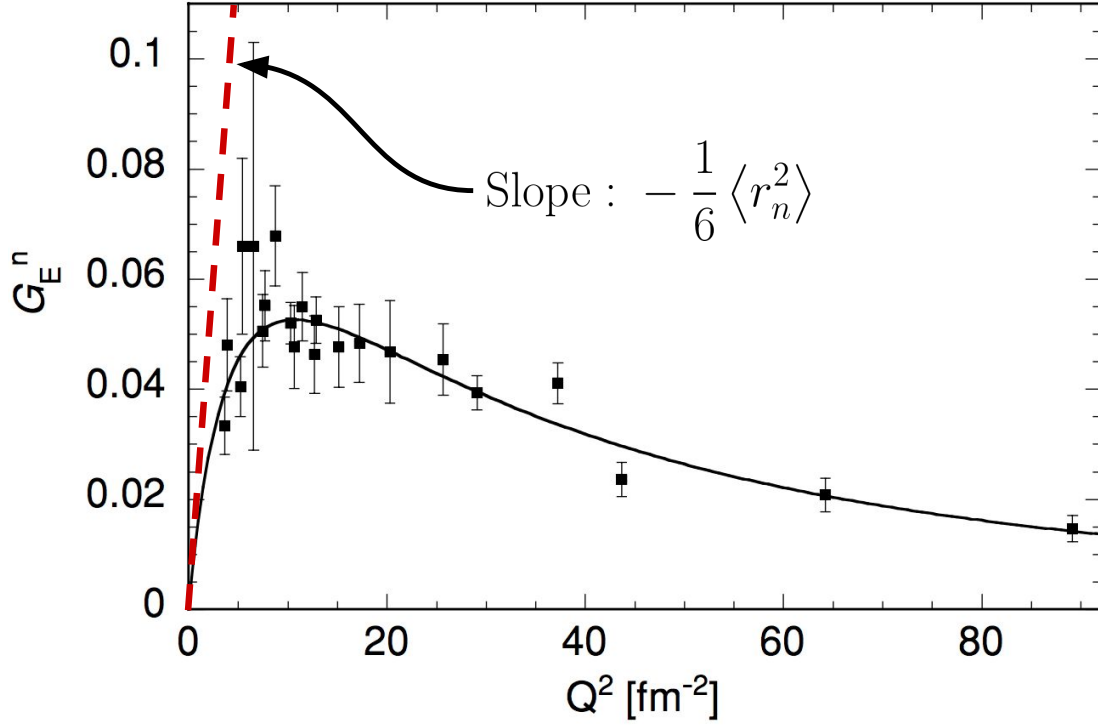
Figure 4.2 Illustration of the neutron charge radius as the slope of G_E. Plot is from [GC11] with the red line showing the slope at $Q^2 = 0$ added.

$$b_E(Q) = -\frac{m}{2\pi}\frac{1}{6}Q^2 \langle r_n^2 \rangle \widetilde{A}^0, \tag{4.39}$$

where I have split up b_{EM} into its electric b_E and magnetic b_M components.

The computation of $\widetilde{A}^0$ is completed by considering the charge density of the crystal

$$A^0(\vec{x}) = \frac{1}{4\pi}\int d^3x' \frac{\rho(\vec{x}')}{|\vec{x} - \vec{x}'|}, \tag{4.40}$$

the Fourier transform of which yields

$$\widetilde{A}^0 = \frac{\widetilde{\rho}(Q^2)}{Q^2}. \tag{4.41}$$

The Fourier transform of the charge density is

$$\widetilde{\rho}(Q^2) = Ze\left|\widetilde{\psi}_N\right|^2 - e\left|\widetilde{\psi}_e\right|^2 = e[Z - f_e(Q)], \tag{4.42}$$

where $\widetilde{\psi}_N$ is the momentum space wave function of the nucleus, and $\widetilde{\psi}_e$, is the Z-electron momentum space wave function of the electrons. The second equality assumes that the nuclear wave function is well-estimated by a delta function. The electronic form factor $f_e(Q)$ can be measured with x-ray Bragg scattering or calculated by lattice dynamics [Spa86; CH88; Erb13]. Note that traditionally in the neutron literature $f_e(Q)$ is written as the single electron form factor. In keeping the x-ray literature however, I will take $f_e(Q)$ to be the form factor for the entire atom, containing Z electrons. Ultimately, this experiment is dependent on the accuracy of the previously measured or calculated values of the electron form factors at the 2% level, whereas the form factors are known at $\sim 5 \times 10^{-4}$ relative uncertainties.

Inserting this result into Equation 4.39 gives [Sea86]

$$b_E(Q) = -\left(\frac{m\alpha}{3}\right)\langle r_n^2\rangle\left[Z - f_e(Q)\right] = -b_{ne}\left[Z - f_e(Q)\right], \tag{4.43}$$

where $\alpha \simeq \frac{1}{137}$ is the fine structure constant, and the neutron charge radius has units of fm^2, as opposed to $e\,\mathrm{fm}^2$. The neutron-electron scattering length b_{ne} is related to $\langle r_n^2\rangle$ by a factor of $\frac{3}{m\alpha} = 86.34$ fm. Note that despite being termed the neutron-electron scattering length, b_{ne} is actually the scattering length associated with the neutron scattering from a charge density which is apparent from the factor of $Z = f_N(Q)$. At $b_{ne} = -1.345(25) \times 10^{-3}$ fm [Tan18], and $(Z - f_e(Q))$ at most 14 but between approximately 3.4 and 7.0 for this experiment depending on the Bragg reflection, the total electronic scattering length b_E is between 0.1 % and 0.2 % of the magnitude of the nuclear scattering length b_N for this experiment.

Finally, it is worth noting that the effective electric field in the crystal is $\sim 10^8$ V cm^{-1}, which is approximately two orders of magnitude larger than what can safely be produced in the laboratory. This fact enables this experiment to probe the neutron charge radius. Additionally, the large interatomic fields of quartz have been used to place limits on the neutron electric dipole moment [Fed10].

4.2.3.2 Spin-Dependence

There is also a spin-dependence in Equation 4.35. In this case

$$b_M(Q) = -\frac{m}{2\pi}\mathcal{F}\left\{\vec{\mu}\cdot\vec{B}\right\} = -\frac{m}{2\pi}\mathcal{F}\left\{\vec{\mu}\cdot\nabla\times\vec{A}\right\} = i2\vec{\mu}\cdot\left(\vec{Q}\times\vec{p}\right)\frac{\widetilde{\rho}(Q)}{Q^2} \tag{4.44}$$

where $\vec{p}$ is the neutron momentum. Using the definition of $\widetilde{\rho}(Q)$ from Equation 4.42 [Sea86]

$$b_M(Q) = i2\vec{\mu}\cdot\frac{\vec{Q}\times\vec{p}}{Q^2}e\left[Z - f_e(Q)\right] = ib_F\left[Z - f_e(Q)\right]\vec{\sigma}\cdot\hat{n}\cot\theta_B \tag{4.45}$$

where

$$b_F = \frac{e\mu}{4\pi} = g_n \frac{\alpha}{2m} = -1.468 \times 10^{-3} \text{ fm} \tag{4.46}$$

is the Foldy scattering length with $g_n = -1.91$ the neutron gyromagnetic ratio; $\vec{\sigma}$ is the vector of Pauli matrices and is pointed in the direction of the neutron spin; and $\hat{n}$ points in the $\vec{Q} \times \vec{p}$ direction [Sea86]. This interaction is referred to as Schwinger scattering.

Noting that b_M is out of phase with b_N and b_E, the same can be said of the structure factor itself, because when summing over all the scattering centers in a unit cell, $b(Q)$ factors out. However, in the case of a multi-species crystal, such as quartz, the magnetic component of $\widetilde{V}$ of one scattering center can interfere with the nuclear components of neighboring scattering centers and b_M is no longer out of phase with b_N and b_E. When computing the structure factor for silicon $b_N + b_E$ add in quadrature with b_M, and the total contribution of b_M is on the order of $(b_F/b_N)^2 \sim 10^{-6}$, which is far below the detection level for this experiment.

4.2.3.3 Beyond the Standard Model Forces

A BSM force mediator that acts between the neutron and the atoms in a crystal would provide a unique signature in regards to either its spin-dependence or its range. Such new particles are motivated by a variety of BSM physics, including the ultraviolet completion of General Relativity, light dark matter [Fay07], explanations of dark energy [Zee04], and the origins of neutrino masses [AHD02]. While any given theory may or may not have a preferred mass scale, the exclusion plot for a BSM force mediator spans many order of magnitude in coupling strength and range, spanning from celestial ($\sim 10^9$ m) to collider ($\sim 10^{-20}$ m). In general, constraints drop off rapidly at 100 μm, and gravitation itself has never been detected on length scales shorter than 10 μm [MT15]. The measure of structure factors naturally probes forces with a ~ 1 Å range, which corresponds to a mass of 2 keV. I will assume a Yukawa parameterization, which gives [GG07]

$$b_5(Q) = -\frac{m}{2\pi} g^2 Q_n Q_N \frac{\lambda_5^2}{1 + Q^2 \lambda^2} = \alpha_G 2G m^2 M \left(\frac{\lambda_5^2}{1 + Q^2 \lambda_5^2} \right), \tag{4.47}$$

where g is the coupling of the force mediator, and Q_n and Q_N are the charges of the neutron and scattering center, respectively. The second equality assumes the new force mediator couples to mass $Q_n = m$ and $Q_N = M$, and I have written the interaction normalized to the strength of gravity, with the dimensionless parameter $\alpha_G = 1$ for g^2 equal to that of gravity, with G the gravitational force constant [GG07]. For silicon this reduces to

$$b_5(Q) = -1.6 \times 10^{-26} \alpha_G \frac{\lambda_5^2}{1 + Q^2 \lambda_5^2} \tag{4.48}$$

with λ_5 in ångströms and b_5 in femtometers. Note that in the presence of a Yukawa fifth force the forward scattering amplitude is also modified, causing the coherent scattering length to deviate from the nuclear term b_N. This is an important detail, because this experiment fundamentally measures $b(Q)/b(0)$.

The coupling g^2 in Equation 4.47 can correspond to a vector or scalar force mediator. Coupling to an axial vector boson, both vector and axial vector bosons, or scalar-pseudoscalars are also possible. Each of these interactions may create spin-dependent forces, which may be probed using a polarized neutron beam, with the neutron spin coupling to the $\vec{p}$, $\vec{Q}$, or $\vec{p} \times \vec{Q}$ directions. Interactions proportional to $\vec{\sigma} \cdot \vec{p}$ violate parity; $\vec{\sigma} \cdot \vec{Q}$ violates time reversal symmetry; and $\vec{p} \times \vec{Q}$ violates no fundamental symmetries and would need to have a Q-dependence or coupling that is unique from Schwinger scattering to be detectable, necessitating the use of either multiple Bragg reflections or multiple crystal types. Because $\vec{\sigma} \cdot \vec{Q}$ and $\vec{\sigma} \cdot (\vec{Q} \times \vec{p})$ are linear in $\vec{Q}$, and $b(Q) = b(-Q)^*$ (except in the case of absorption) these terms will be out of phase with the nuclear potential and be highly suppressed for centrosymmetric crystals. However, the $\vec{\sigma} \cdot \vec{Q}$ term corresponds to a nonzero neutron electric dipole moment or a scalar-pseudoscalar coupling to a new particle, both of which have been limited by spin transport in quartz [Vor09]. While transmission-style diffraction experiments with silicon are not sensitive to $\vec{\sigma} \cdot \vec{Q}$ or $\vec{\sigma} \cdot (\vec{Q} \times \vec{p})$ terms, resonating geometries such as the one demonstrated in [Jer96; Jae05], are sensitive to such interactions [Dom01]. Neutron pendellösung interference in a resonant magnetic field [Fin87; Hor88] may also have possibilities for probing terms of odd order in Q.

4.2.3.4   Total Q-Dependence for Silicon Pendellösung Measurements

Combining the results from the previous sections, I can write the total Q-dependence of $b(Q)$, while also folding in the Q-dependence of the DWF and anharmonic corrections,

$$b(Q) = e^{-W(Q^2)} \left[1 + f_{\mathrm{anh}}(Q^3) \right] \left(b_N - [Z - f_e(Q)] b_{ne} + b_5(Q) \right) \tag{4.49}$$

where I have not included the spin-dependent terms that are out of phase with the nuclear potential, and it is understood that $f_{\mathrm{anh}}(Q^3)$ only affects odd reflections. Fundamentally this experiment actually measures $b(Q)/b(0)$, and the presence of a new force would change $b(0) \neq b_N$. Letting

$$e^{-W'} = e^{-W} \left(1 + f_{\mathrm{anh}} \right), \tag{4.50}$$

I can compute the theoretical value for a measurement of $b(Q)/b(0)$

$$\frac{b(Q)}{b(0)} = e^{-W'} \left(1 - [Z - f_e(Q)] \frac{b_{ne}}{b(0)} + \frac{b_5(Q) - b_5(0)}{b(0)} \right). \tag{4.51}$$

106
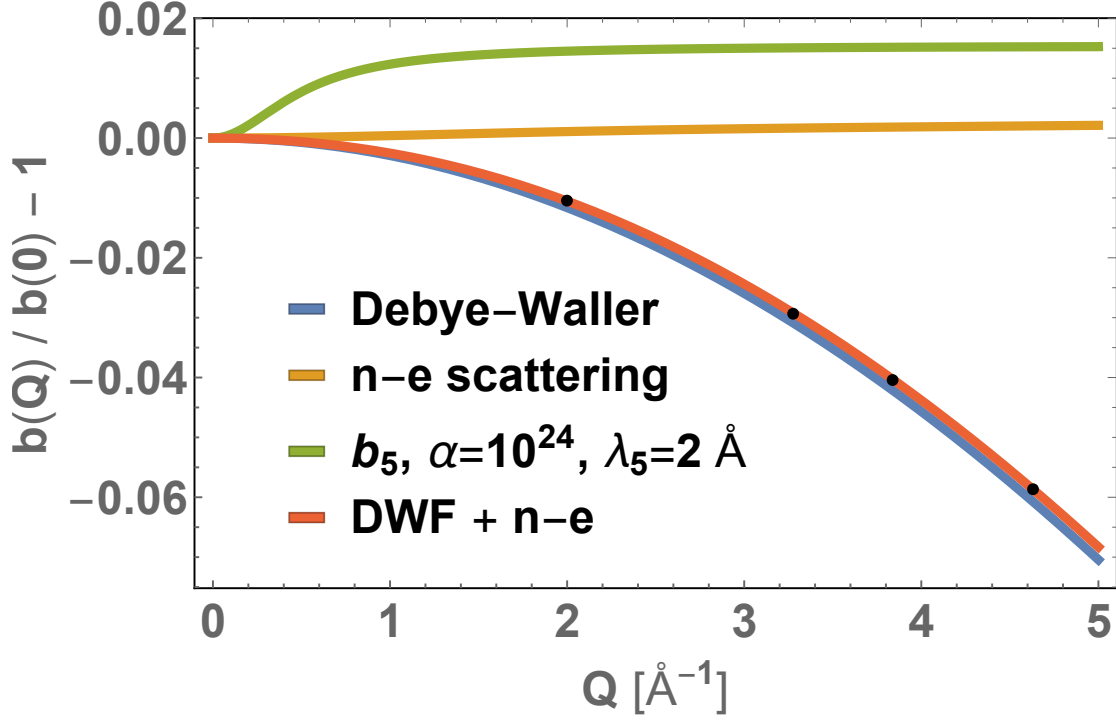
Figure 4.3 Contributions to $b(Q)/b(0)$ from the DWF, electronic scattering, and a BSM force carrier. The black points show evaluations corresponding to the (111), (220), (311), and (400) Bragg reflections. While the DWF is the dominant effect, other interactions are measurable because of the very low experimental relative uncertainties ($\sim 5 \times 10^{-5}$) and well defined functional form of the DWF with respect to Q^2.

For the case of $b_5(Q)$ given by a vector boson with mass $m_5 = \lambda_5^{-1}$ (Section 4.2.3.3) that couples to mass, with M given by the nuclear mass of silicon

$$\frac{b(Q)}{b(0)} = e^{-W_{\mathrm{anh}}} \left[1 - [Z - f_e(Q)]\frac{b_{ne}}{b(0)} + \alpha_G \left(3.9 \times 10^{-12} \ \text{\AA}^{-2} \ \lambda_5^2 \right) \left(\frac{Q^2 \lambda_5^2}{1 + Q^2 \lambda_5^2} \right) \right]. \qquad (4.52)$$

where I have absorbed the measured value of $b(0) = 4.1507(2)$ [Iof98] into the numerical factor in Equation 4.48. The various contributions to $b(Q)/b(0)$ are shown in Figure 4.3. From the the plot, it is clear that the DWF is the dominant term. Thus any deviation from the traditional functional form of the DWF would severely complicate the analysis of the experiment.

4.3 Pendellösung Interferometry

Pendellösung interference depends on both the average momentum of the neutron beam along the Bragg planes, as well as the position space slit geometry used. Further complicating the scenario is the fact that the crystal's selection in momentum space causes a wavelength-dependence in position space. Characterization of these effects and minimization of the systematic uncertainties they produce are discussed in this section. I describe how beam collimation and slit sizes affect the measurement of neutron pendellösung oscillations. Both affect the predicted contrast, and more importantly, slit size and positioning alters the measured pendellösung phase shift. This must be well-understood for precision measurements. Experimental demonstration of the pendellösung oscillation phase shift as a function of slit size and positioning is provided.

The dynamical diffraction Hamiltonian, and correspondingly the Green's function inside the crystal, is most easily solved in a coordinate system $(\hat{\xi}, \hat{\zeta})$ with $\hat{\xi}$ parallel to $\vec{H}$, and $\hat{\zeta}$ parallel to the neutron's average momentum $\vec{p}$. In the Laue geometry, $\hat{\xi}$ is parallel and $\hat{\zeta}$ is perpendicular to the crystal surface. The Greek letter coordinate system is used for the crystal coordinates, while a Latin letter coordinate system is used for the beam coordinates. For the beam coordinates $\hat{z}$ is in the longitudinal direction, and $\hat{x}$ is in the transverse direction (see Figure 4.4).

Because the pendellösung phase shift

$$\frac{2\pi D}{\Delta_H} = \frac{v_H D}{k_\zeta} \tag{4.53}$$

is a function of k_ζ, the measured pendellösung oscillations are averaged over the incoming momentum space distribution of the beam. However, because the Bragg condition carves out a narrow strip of momentum space in the $\hat{\xi}$-direction, there is a correlation between k_ζ and x. The k_ζ-dependence of the pendellösung phase shift causes smearing of the interference pattern upon averaging over the distribution of k_ζ, which depends on the preparation of the beam. These effects are addressed in Section 4.3.5.

In addition to loss of interference fringe visibility from the k_ζ-dependence of the pendellösung phase shift, pendellösung oscillations are only resolvable at the center of the Borrmann fan. To illustrate this point, consider the position space neutron profile in the diffracted beam with respect to the beam coordinates

$$|\langle x \,|\, \psi \rangle|^2 = \int dk_\zeta \, |\langle k_\zeta | \psi_0 \rangle|^2 \, \frac{1 + \sin\left[\frac{2\pi D}{\Delta_H} \sqrt{1 - \left(\frac{x'-x}{D \sin\theta_B}\right)^2}\right]}{\sqrt{1 - \left(\frac{x'-x}{D \sin\theta_B}\right)^2}}, \tag{4.54}$$
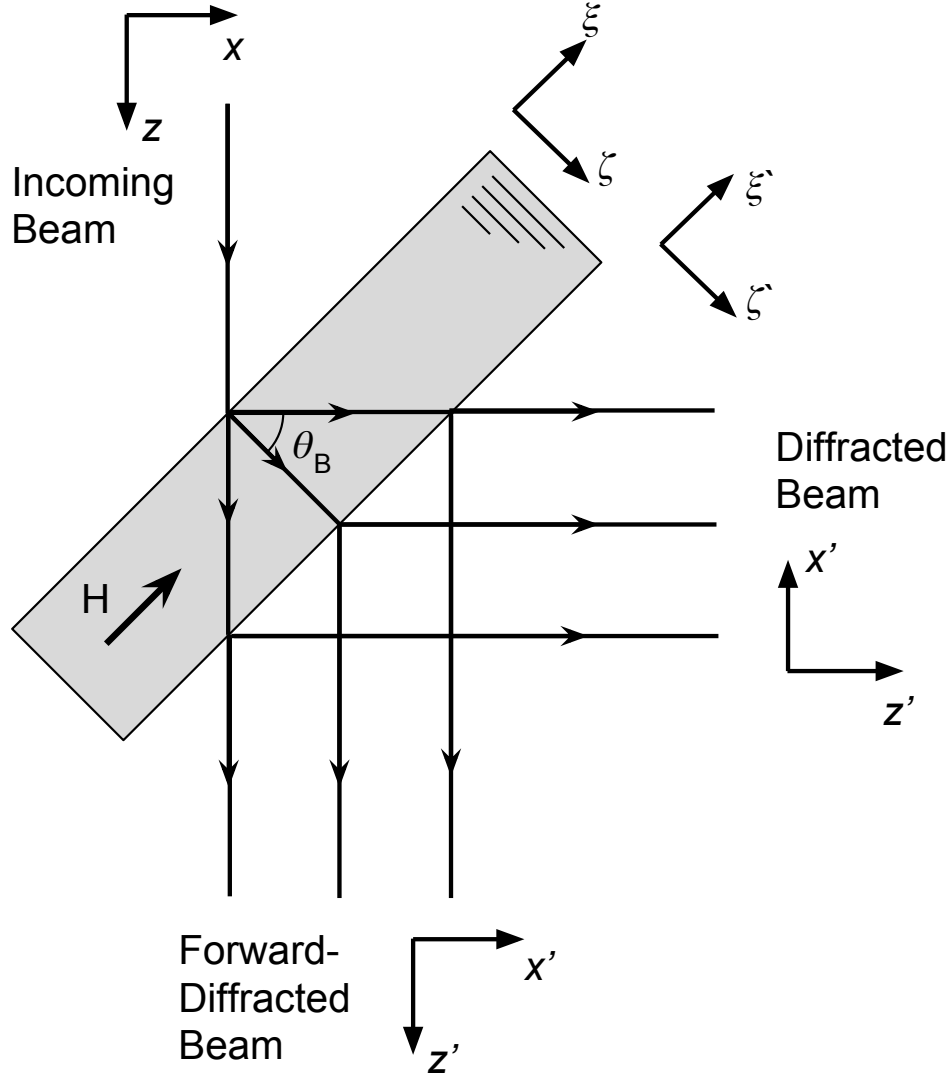
Figure 4.4 Beam and crystal coordinates. $\vec{\xi}$ refers to the diffraction plane of the crystal with $\hat{\xi}$ parallel to $\vec{H}$, and $\vec{x}$ is defined by the transverse and longitudinal components of the incoming beam

where x is the incoming wave packet displacement and must be averaged over the incoming slit, while x' is the outgoing position and will ultimately be averaged over the outgoing slit. This equation is consistent with [SO72; Kat61a; Kat61b] for the "spherical wave" case. Because the Borrmann fan is defined by $-D\sin\theta_B < (x' - x) < D\sin\theta_B$, the denominator and argument of the sin function are always real. For the crystal thicknesses used in this experiment the crystal thickness is much larger than the pendellösung length $D \gg \Delta_H$, causing the sinusoidal portion of Equation 4.54 to become highly oscillatory at the edges of the Borrmann fan $(x' - x) \to \pm D\sin\theta_B$. This function is
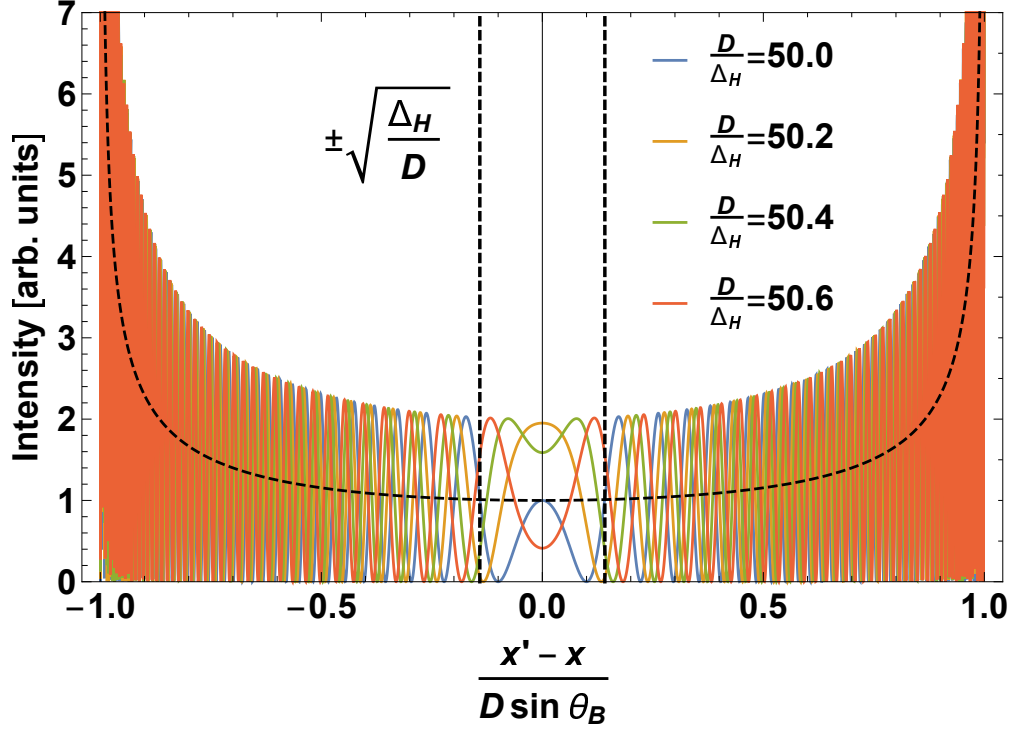
Figure 4.5 Pendellösung position space profile. The envelope is shown as a dashed line. Also shown is the slit size after which oscillations begin to wash out.

plotted in Figure 4.5. Resolvable pendellösung oscillations only occur at the center of the Borrmann fan, in the region defined by $-\sqrt{D\Delta_H}\sin\theta_B < (x' - x) < \sqrt{D\Delta_H}\sin\theta_B$.

Before going into more detail in regards to beam profiles, slit sizes, etc., it will be helpful to discuss the manipulation of the crystal in the neutron beam.

4.3.1 Crystal Manipulation

A pendellösung interferogram is measured by tilting a Bragg-diffracting crystal about the axis defined by the reciprocal lattice vector $\vec{H}$. The intensity in the forward diffracted beam is measured over a range of crystal tilts, such that a few periods may be measured. The intensity in the diffracted beam shows oscillations of the form

$$\mathcal{I}_{\text{meas}}(\theta_P) = A + B\cos\left(\frac{2\pi C}{\cos(\theta_P - \theta_{P0})} + \phi_{\text{calc}}\right) \tag{4.55}$$

where A, B, C, and θ_{P0} are fit parameters. The pendellösung fringe number C is the main parameter of interest. The quantity ϕ_{calc}-depends on the geometry of the collimating slits and is discussed in Section 4.3.6. A typical pendellösung interferogram is shown in Figure 4.6.
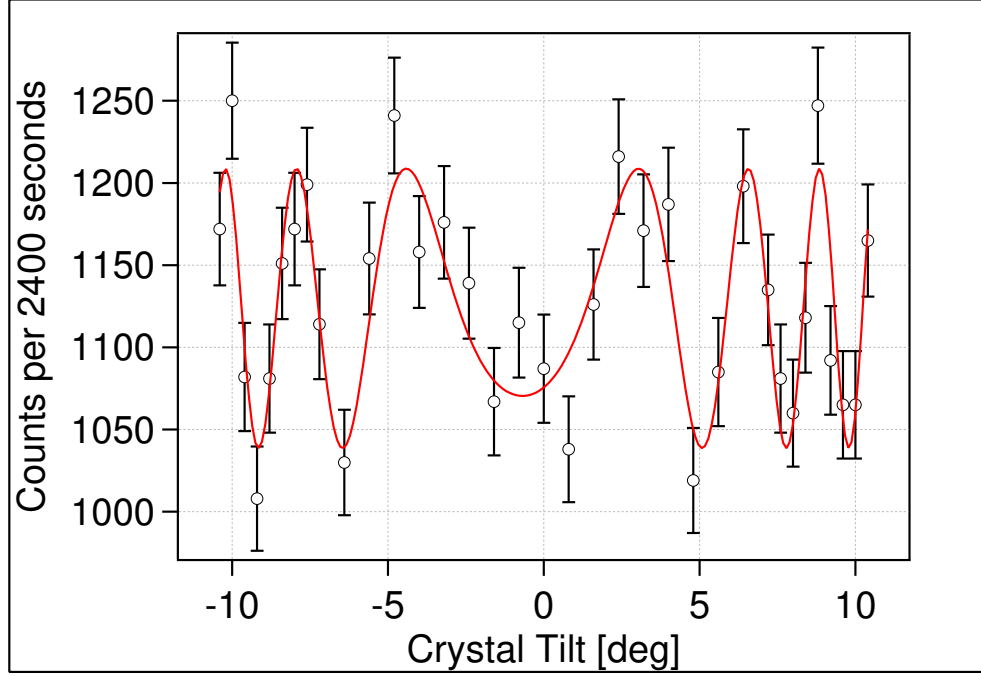
Figure 4.6 Typical pendellösung interferogram taken over 24 hours for the 220 Bragg reflection, using the 2.2 Å component of the NIOFa neutron beam. The data is fitted (red line) to Equation 4.55, and the error bars are from Poisson counting statistics.

In order to generate a pendellösung interferogram, the reciprocal lattice vector $\vec{H}$ must be aligned to tilt axis of the positioning stage. To perform this alignment, the crystal is fixed to a goniometer with three rotation axes (Figure 4.7). A Bragg peak occurs as the crystal is rotated by θ_B in Figure 4.7 through the Bragg condition where

$$\sin \theta_B = \frac{H}{2K}. \tag{4.56}$$

In this case, K has a distribution which depends on the upstream monochromator and slits that is much wider than the Darwin width. If $\vec{H}$ and the pendellösung tilt axis are aligned, then rotating by some angle θ_P will not change the angular position of the Bragg peak. If the tilt axis and $\vec{H}$ are misaligned vertically, then ϵ in Figure 4.7 takes on a nonzero value. The projection of $\vec{H}$ in the plane perpendicular to rotation axis of the stage that controls θ_B is then dependent on θ_P. The result is that the angular position of the Bragg peak depends linearly on θ_P, where the peak centroid changes more rapidly for larger magnitude ϵ.

To align $\vec{H}$ of the crystal in its mount to the tilt stage that controls θ_P, a three dimensional alignment scan is used. First θ_T is altered to intentionally induce a nonzero ϵ. Bragg peak centroids are then measured for a few values of θ_P. The Bragg peak centroids versus θ_P are fit to a line. The
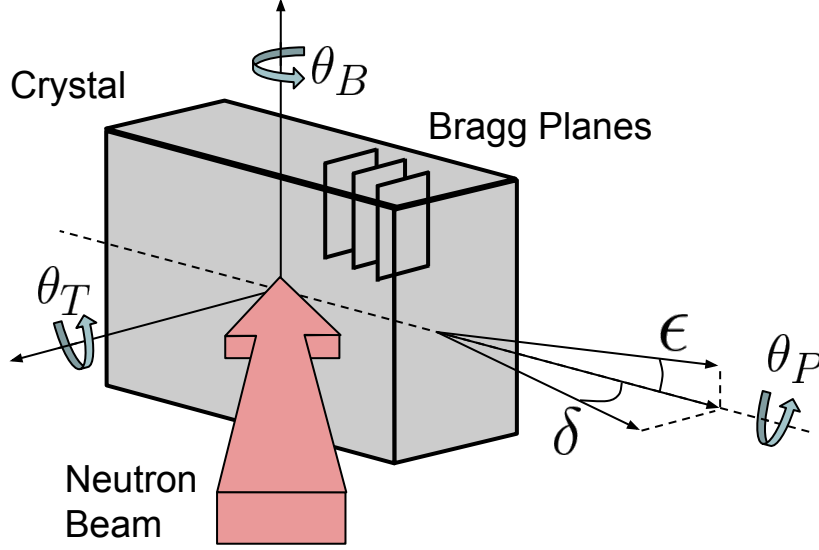
Figure 4.7 Crystal rotation axes. Rotations by θ_P create pendellösung interferograms. Rotations by θ_B change the wavelength. The angle θ_T is aligned such that the misalignment ϵ of the of the θ_P tilt axis and $\vec{H}$ is minimized.

slope of this line for each value of θ_T also forms a line, and the value of θ_T for which the Bragg peak centroid is unaltered by a change in θ_P can be computed from the fits. Using this alignment method ϵ can be limited to less than about 0.1 deg.

A nonzero ϵ impacts the pendellösung interferogram by causing θ_P to take on a wavelength dependence. The pendellösung fringe number is proportional to $\tan \theta_B$. Letting θ_B be dependent on θ_P, and also expanding $1/\cos \theta_P$ to second order in θ_P

$$\frac{2\pi C}{\cos \theta_P} \to 2\pi C \left(1 + \frac{1}{2}\theta_P^2 + \frac{\epsilon \theta_P}{\cos \theta_B \sin \theta_B} + \mathcal{O}(\epsilon^2, \theta_P^3) \right), \tag{4.57}$$

assuming $\frac{d\theta_B}{d\theta_P} = \epsilon$. This has a minimum at

$$\theta_{P0} = -\frac{\epsilon}{\cos \theta_B \sin \theta_B}. \tag{4.58}$$

The net result is that the interferogram would be shifted left or right in Figure 4.6. If ϵ is nonzero, then the interferogram shifts in the opposite direction for plus and minus θ_B. Because pendellösung interferograms are taken at both plus and minus θ_B as a way of measuring the incoming neutron wavelength (see Figure 4.8), the difference in the fitted center of the interferograms θ_{P0} gives an extra indication of ϵ. In addition to shifting the curve left or right, the phase at θ_{P0} is altered by

$$2\pi C \to 2\pi C \left(1 - \frac{1}{2}\theta_{P0}^2\right) = 2\pi C \left[1 - \frac{1}{2}\left(\frac{\epsilon}{\cos\theta_B \sin\theta_B}\right)^2\right] \tag{4.59}$$

This relation makes correcting the measured C simple. However, with the previously described alignment of θ_T to minimize ϵ, this correction is very small at $\frac{1}{2}\theta_{P0}^2 \lesssim 5 \times 10^{-6}$.

The alignment of $\vec{H}$ to the θ_P tilt axis in the plane perpendicular to the θ_B axis (δ is Figure 4.7) depends on the machining tolerances of the parts holding the crystal and is estimated to be $\delta \lesssim 2.5$ deg. The pendellösung fringe number as a function of θ_P is altered

$$\frac{2\pi C}{\cos\theta_P} \to \frac{2\pi C}{\sin^2\delta + \cos^2\delta\cos\theta_P}\left(1 + \frac{(1-\cos\theta_P)\sin\delta}{\sin\theta_B\cos\theta_B}\right). \tag{4.60}$$

The change in the $\cos\theta_P$ term in the denominator is a geometric effect (as δ increases, the thickness change as a function of θ_P decreases), and the $(1-\cos\theta_P)$ term is due to a change in wavelength. The wavelength term is linear in δ and therefore dominates. Expanding Equation 4.60 to second order in θ_P

$$\frac{2\pi C}{\cos\theta_P} \to 2\pi C\left[1 + \frac{1}{2}\left(1 + \frac{\sin\delta}{\sin\theta_B\cos\theta_B}\right)\theta_P^2\right], \tag{4.61}$$

it is clear that the relationship between the pendellösung fringe position C and the rate at which the phase is modulated by changing the crystal tilt θ_P is altered by the δ angular misalignment.

When fitting the pendellösung interferograms, one has the choice of using Equation 4.55, or allowing the pendellösung fringe position and $1/\cos\theta_P$ terms to be different

$$\mathcal{I}_{\text{meas}}(\theta_P) = A + B\cos\left[2\pi C_0\left(\frac{1}{\cos\theta_P} - 1\right) + 2\pi C + \phi_{\text{calc}}\right], \tag{4.62}$$

which would allow for a nonzero δ misalignment without biasing the fitted pendellösung fringe position C.

However, because of the extra parameter C_0, the uncertainty in the fitted pendellösung fringe position is larger when the pendellösung interferograms are fit to Equation 4.62. Fortunately, $\delta/(\sin\theta_B\cos\theta_B)$ carries opposite signs for plus and minus θ_B. While C and C_0 cannot be fixed to be the same, a combined fit for the pendellösung interferograms at plus and minus θ_B may be constrained such that $C_0 \to C \pm \Delta C_0$

$$\mathcal{I}_{\text{meas}}(\theta_P) = A + B\cos\left[2\pi(C \pm \Delta C_0)\left(\frac{1}{\cos\theta_P} - 1\right) + 2\pi C + \phi_{\text{calc}}\right], \tag{4.63}$$

where the $\pm$ refers to the plus and minus θ_B interferograms, with ΔC_0 the only fit parameter shared between the two interferograms. This takes advantage of the common origin of C and C_0, while still allowing C_0 to be perturbed by a nonzero crystal tilt axis misalignment δ.

When constraining the fits according to Equation 4.63, the fitted pendellösung fringe positions C at plus and minus θ_B become covariant. To account for this issue, a global fit for the plus and minus θ_B interferograms is performed

$$\mathcal{I}_{\text{meas}}(\theta_P) = A + B\cos\left[2\pi(C_0 \pm \Delta C_0)\left(\frac{1}{\cos(\theta_P - \theta_{P0})} - 1\right) + 2\pi(C \pm \Delta C) + \phi_{\text{calc}}\right], \quad (4.64)$$

where C_0 is fixed; C, ΔC_0, and ΔC are shared fit parameters between the two interferograms; A, B, and θ_{P0} are fit parameters unique to each interferogram; and $\pm$ refers to the plus and minus θ_B interferograms. In this procedure, C is the average pendellösung fringe number and the parameter of interest. Doing the global analysis in this way takes advantage of the the fact that δ and ϵ misalignments of the crystal tilt axis relative to $\vec{H}$ cause a shift in the fitted pendellösung phase fringe position that has opposite signs for the plus and minus θ_B interferograms. If the crystal holder is remade to higher tolerances, it is likely that ΔC_0 can be constrained to be zero.

4.3.2   Collimation Requirements

As discussed in the previous section, pendellösung oscillations are measured by tilting the crystal over the range of a few degrees, then fitting intensity in the forward-diffracted beam to a functional form. The uncertainty from the fits will generally go like $1/\sqrt{\mathcal{I}}$, for an average intensity $\mathcal{I}$. Additionally, the fitted pendellösung phase shift is measured $\text{Mod}(2\pi)$, such that the uncertainty in the pendellösung phase shift is some fraction of a full period that depends on the intensity of the beam and the fringe visibility of the oscillation. The relative uncertainty σ_{rel} thus decreases as the number of full pendellösung periods inside the crystal increases

$$\sigma_{\text{rel}} \sim \frac{\sigma_P}{N_P}, \quad (4.65)$$

where σ_P is the uncertainty in the $\text{Mod}(2\pi)$ pendellösung phase shift, and $N_P = D/\Delta_H$ is the number of pendellösung oscillations that occur inside the crystal. It would seem then that an arbitrarily small uncertainty could be achieved by using very thick crystals. However, there are two caveats: (1) Only the central portion of the Borrmann fan results in a resolvable interference pattern. The useful fraction of the Borrmann fan is $\sqrt{\Delta_H/D}\sin\theta_B$ (Figure 4.5), and the signal intensity decreases with increasing D. (2) There is a need for high collimation or monochromacy with increasing N_P, because the pendellösung phase shift is a function of k_ζ. If Equation 4.54 is integrated over too large of a range in k_ζ, the the interference fringe visibility of the oscillations will suffer. The level of dephasing is determined by the incoming momentum space envelope $|\langle k_\zeta|\psi_0\rangle|^2$. The required level of collimation *or* monochromacy is

$$\Theta_{\text{col}} < \frac{\Delta_H}{D} \quad \text{or} \quad \frac{\delta\lambda}{\lambda} < \frac{\Delta_H}{D} \quad . \tag{4.66}$$

Either a monochromatic or well-collimated beam may be used, because the Bragg condition selects a narrow strip in momentum space perpendicular to $\vec{H}$

$$\frac{\delta k_\xi}{k_\xi} \sim \frac{v_H}{Hk} \sim 10^{-5}, \tag{4.67}$$

which is two orders of magnitude more narrow than the collimation or monochromacy requirements. Furthermore, because the Darwin width and the pendellösung phase shift are both ultimately set by the magnitude of the structure factor v_H, allowing the crystal itself to define wave packet's coherence length allows the pendellösung phase shift to be predicted with very little systematic uncertainty. In practice, it is easier to collimate the beam, which is the strategy adopted by this experiment. However, with higher collimation, the total intensity must decrease. Taking the intensity to be roughly proportional to the collimation $\mathcal{I} \propto D^{-1}$, provided there is enough space available between the slits. The requirement that $\Theta_{\text{col}} = S/L$, were S is the slit width and L is the distance between the slits, requires there be $L \sim D^{\frac{3}{2}}\Delta_H^{-\frac{1}{2}}$, amount of space available between the beam port and the experiment.

Using $\sigma_p \sim \mathcal{I}^{-\frac{1}{2}}$, the uncertainty of the pendellösung interferogram increases with increasing crystal thickness $\sigma_p \propto \sqrt{D}$. Inserting this into Equation 4.65, σ_{rel} is still expected to decrease with increasing D, but not linearly

$$\sigma_{\text{rel}} \propto \frac{1}{\sqrt{D}}. \tag{4.68}$$

This relationship may be optimized with regards to the background count rates of the apparatus and available space between the beam port and the experiment. For the NCNR NIOFa beamline, crystal thicknesses of around 1 cm are convenient for silicon. However, the background neutron count rates are still relatively high, and reasonably large gains could be made if the backgrounds can be reduced. In practice, however, this can be difficult, because the interfering portion of the forward diffracted beam is only translated by a few millimeters relative to the direct beam, which itself is about 10^3 times more intense than the forward diffracted beam.

4.3.3 Slit Size

The fringes shown in Figure 4.5 should be integrated over any incoming or outgoing slits. The coordinate x is integrated over the incoming slit, and the x' coordinate is likewise integrated over the outgoing slit. There are two limiting cases, a narrow slit and a wide slit case, with the two cases shifted by $\frac{\pi}{4}$ in the pendellösung phase shift. The narrow and wide slit cases are defined by

$$S_2 \text{ and } S_3 \ll \sin\theta_B \sqrt{\Delta_H D} \quad \text{narrow} \tag{4.69}$$

$$S_2 \text{ or } S_3 > \sin\theta_B \sqrt{\Delta_H D} \quad \text{wide} \tag{4.70}$$

with S_2 and S_3 the widths of the slits immediately before and after the crystal, respectively, as defined in Figure 4.8. In the narrow slit limit, the pendellösung fringe position may be read off the argument of the sin function in Equation 4.54. In this case a translational misalignment of the slits leads to a shift in the pendellösung phase shift that is in the opposite direction of the plane wave prediction. The proper direction of the change in the pendellösung phase shift as being from the spherical wave solution as computed by [Kat61a; Kat61b] was confirmed by [SO72]. However, in the limit that the second slit is suitably wider than both the first slit and $\sqrt{D\Delta_H}\sin\theta_B$, the increasingly rapid oscillations as a function of $x' - x$ in Figure 4.5 cease to shift the pendellösung fringe position as a function of slit size. Therefore, the wide slit case is less sensitive to a translational misalignment of S_3.

For the wide slit case, integrating $x' - x$ over $\pm\frac{S}{2}$, and taking S to be large enough such that the integration bounds over the sin function in Equation 4.54 can be estimated to be $\pm\infty$ one obtains

$$\mathcal{I} = \int dk_\zeta \, |\langle k_\zeta | \psi_0 \rangle|^2 \left\{ 2\sin^{-1}\left[\frac{S}{2D\sin\theta_B}\right] + \sqrt{\frac{\Delta_H}{D}}\sin\left[2\pi\frac{D}{\Delta_H} - \frac{\pi}{4}\right] \right\}. \tag{4.71}$$

The shift the pendellösung phase shift by $\frac{\pi}{4}$ for the wide slit case relative to the narrow slit case is readily apparent. For intermediate slit sizes, the pendellösung fringe position shifts smoothly by $\frac{\pi}{4}$ as the slit sizes change on the $\sqrt{D\Delta_H}\sin\theta_B$ length scale and the integration over x' and x must be performed numerically. The predicted beam profile for a few pendellösung phase shifts as a function of x' after an integration over x is shown in Figure 4.9.

4.3.4 Pendellösung Green's Function

The position space Green's function for the forward diffracted beam in the Laue geometry is given by [Ito18]

$$G_P\left(\vec{\xi'}, \vec{\xi}\right) = \delta\left(\zeta' - \zeta - D\right) \frac{\left(1 - \frac{\xi' - \xi}{D\sin\theta_B}\right)^{\frac{1}{4}}}{\left(1 + \frac{\xi' - \xi}{D\sin\theta_B}\right)^{\frac{3}{4}}} \cos\left(\frac{v_H D}{2k_\zeta}\sqrt{1 - \left(\frac{\xi' - \xi}{D\sin\theta_B}\right)^2} + \frac{\pi}{4}\right). \tag{4.72}$$

This function has historically been referred to as the "spherical wave" case as measured by [SO72] and derived by [Kat61a; Kat61b]. The spherical wave Green's function is shifted by $\frac{\pi}{2}$ in the pendellösung
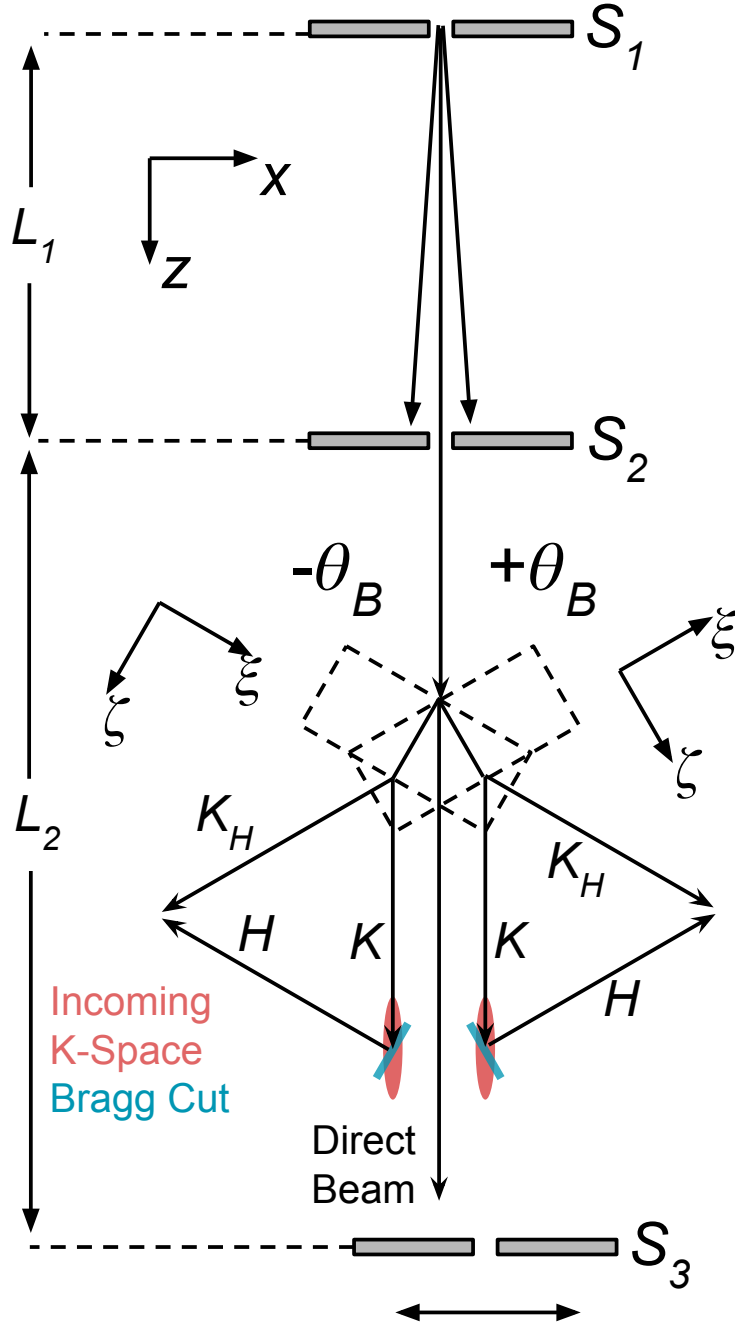
Figure 4.8 Using slits to collimate the beam ("Incoming Phase Space" in red) causes a correlation between the x-coordinate and the transverse momentum. This is passed into a correlation between k_ζ and x in the forward-diffracted beam, because the Bragg condition selects momenta according to the k_ξ ("Bragg cut" in blue), and the Darwin width is much smaller than the divergence of the beam. The collimation of the beam thus sets the distribution of k_ζ (overlap of the red and blue regions). The x-k_ζ correlation modifies the x-dependence of the pendellösung phase shift.
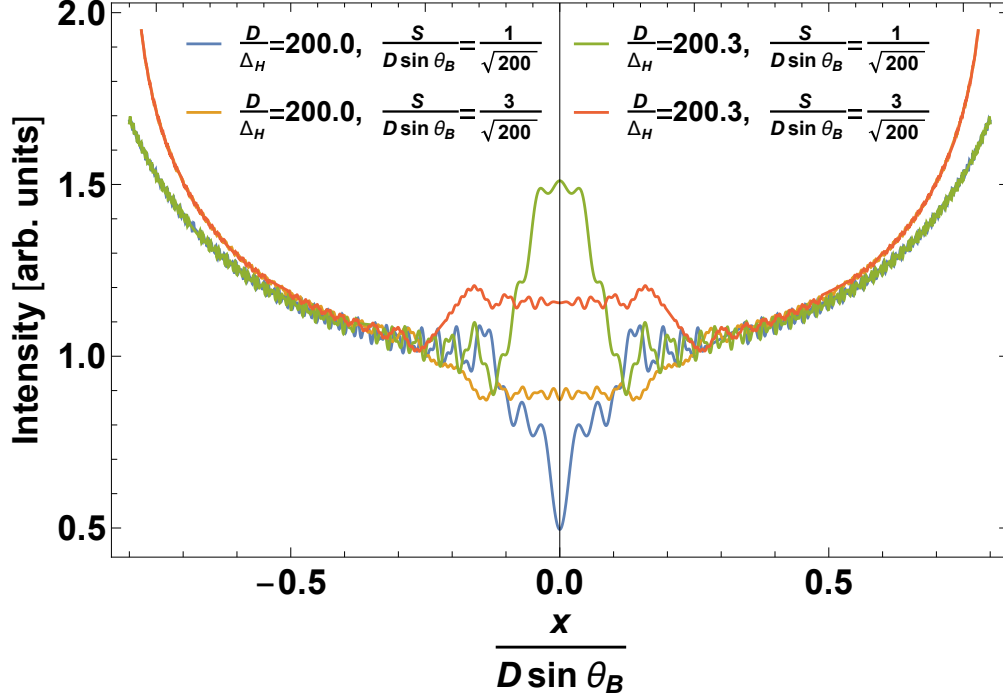
Figure 4.9 Pendellösung profile at different crystal effective thickness or k_ζ and incoming slit sizes.

phase shift when compared to the result of assuming a single plane wave entering and exiting the crystal. Because the Darwin width of the crystal limits the momentum space extent of the neutron wave packet, the plane wave case is relevant only if the incoming beam is collimated in such a way that the momentum space spread of the incoming beam along $\vec{H}$ is smaller than the Darwin width. In practice, achieving this scenario experimentally with neutrons would be very difficult, and only the spherical wave case will be relevant. Finally, it should be noted that the incoming wave need not be spherical at all. The distinguishing feature between the "spherical" and plane wave cases is whether the momentum space spread of the incoming wave packet is much larger or much smaller than the Darwin width of the crystal, respectively.

The crystal Green's function may be convolved with free space Green's functions to form the wave function at S_3

$$\psi_{3P}(x') = \int d\xi' d\xi dx \, G_3(x' - D\sin\theta_B - \xi'\cos\theta_B)G_P(\xi' - \xi)G_2(\xi\cos\theta_B - x)\psi_2(x), \qquad (4.73)$$

where G_2 and G_3 are the free space Green's functions from S_2 to the crystal, and from the crystal to S_3, respectively in Figure 4.8, and $\psi_2(x)$ is the incoming neutron wave function at S_2. Performing the integration over ξ' and ξ by changing variables $\Upsilon = \xi' - \xi$ and $\Xi = \xi' + \xi$, I obtain

$$\psi_{3P}(x') = \int d\Upsilon d\Xi dx\, G_3\left(x' - D\sin\theta_B - \frac{\Xi + \Upsilon}{2}\cos\theta_B\right)G_P(\Upsilon)G_2\left(\frac{\Xi - \Upsilon}{2}\cos\theta_B - x\right)\psi_2(x). \tag{4.74}$$

Noting that

$$\int dx'\, G_3(x'' - x')G_2(x' - x) = G_{2,3}(x'' - x) \tag{4.75}$$

is the Green's function for propagation from S_2 to S_3, I can rewrite Eqn. 4.74 as

$$\psi_{3P}(x') = \int d\Upsilon dx\, G_{2,3}\left(x' - D\sin\theta_B - \Upsilon\cos\theta_B - x\right)G_P(\Upsilon)\psi_2(x). \tag{4.76}$$

This can be further simplified by noting that the wave function at S_3 in the absence of the crystal is

$$\psi_3(x') = \int dx\, G_{2,3}(x' - x)\psi_2(x) \tag{4.77}$$

which gives

$$\psi_{3P}(x') = \int d\Upsilon\, G_P(\Upsilon)\psi_3(x' - D\sin\theta_B - \Upsilon\cos\theta_B) = G_P * \psi_3 \tag{4.78}$$

and the resulting spatial intensity

$$\mathcal{I} = |G_P * \psi_3|^2. \tag{4.79}$$

The wave function at S_3 may be well-modelled by assuming a spherical source of width S_1 at the first slit. This is a good approximation, as the geometry of the slits results in a beam divergence of 0.06 deg, which is about an order of magnitude smaller than the mosaic of the monochromator crystal or the angle of total external reflection for the NG7 guide (both ~ 0.5 deg). In this case the measured intensity becomes

$$\mathcal{I}(x') = \int dx\, |G_P * G_{1,3}(x' - x)|^2\, \Theta\left(\frac{S_1}{2} - |x|\right). \tag{4.80}$$

where Θ is the heaviside step function, and

$$G_{1,3}(x'' - x) = \int dx'\, G_{2,3}(x'' - x')G_1(x' - x)\Theta\left(\frac{S_2}{2} - |x'|\right). \tag{4.81}$$

Note that the heaviside step function in this expression is for the S_2, not S_1 as in Equation 4.80. The coherence length of ψ_3 is $\frac{1}{\sigma_{kx}} \sim 200$ nm, which is much smaller than the relevant length scale for $G_P(x)$ of $\sin\theta_B\sqrt{\Delta_H D} \sim 450\ \mu$m. The estimation

$$\mathcal{I} = |G_P * G_{1,3}|^2 * \Theta\left(\frac{S_1}{2} - |x|\right) \simeq |G_P|^2 * |G_{1,3}|^2 * \Theta\left(\frac{S_1}{2} - |x|\right) = |G_P|^2 * \mathcal{I}_3, \qquad (4.82)$$

where $\mathcal{I}_3$ is the beam profile in the absence of the crystal, is then valid. This assumes the crystal does not drastically change the collimation of the beam, which is a fair approximation, because the divergence of the beam is much smaller than the wavelength spread $\Delta\lambda/\lambda$ of the beam before the crystal. In other words, it is effectively the longitudinal component of the beam that is altered by the crystal. However, because the crystal is a momentum selector in the $\vec{H}$ direction, a covariance is generated between wavelength and transverse momentum. At the detector x and k_ζ are correlated, which in turn implies that x and the pendellösung phase shift are correlated via modification of the $\frac{v_H D}{k_\zeta}$ term

$$\frac{v_H D}{k_\zeta} \rightarrow \frac{v_H D}{k_\zeta}\left[1 - \frac{\delta k_\zeta}{k_\zeta} - \frac{1}{k_\zeta}\frac{\partial \delta k_\zeta}{\partial x}x\right]. \qquad (4.83)$$

Fortunately, the $\partial k_\zeta/\partial x$ correlation term may be predicted from the slit geometry with a suitable precision so as not to present a serious systematic uncertainty to the experiment. To perform this calculation the phase space of the incoming beam must be analyzed.

4.3.5   Beam Phase Space

The beam is selected from the main neutron guide by a pyrolitc graphite monochromator with a mosaic of ~ 0.5 deg. A series of slits then defines the transverse momentum spread, a schematic of which is shown on in Figure 4.8. For this experiment $L_1 = 1.420$ m, $L_2 = 0.480$ m, and the slit sizes were of variable sizes between 0.6 mm and 1.6 mm, leading to nominal beam divergence of ~ 0.06 deg, which is much smaller than the mosaic of the monochromator, allowing the phase space of the beam to be determined by the pendellösung crystal Bragg angle and the slit geometry.

Modelling the phase space of the beam and characterizing any correlations between position and momentum can be achieved by constructing the Wigner quasiprobability distribution [RW15] (pg 154 to 159)

$$P(x, k_x) = \int dy \; \psi^*(x - y)\psi(x + y)e^{i2yk_x}. \qquad (4.84)$$

Also called the Wigner function, $P(x, k_x)$ is related to the wave functions in position and momentum space by

$$|\psi(x)|^2 = \int dk_x \; P(x, k_x)$$

$$\left|\widetilde{\psi}(k_x)\right|^2 = \int dx \, P(x, k_x) \tag{4.85}$$

and is useful for computing the expectation values of an operator that may be functions of both position and momentum

$$\langle O \rangle = \int dx dk_x \, P(x, k_x) \hat{O}(x, k_x) \tag{4.86}$$

The Wigner function for the slit geometry in Figure 4.8 transparently shows any correlations between position and momentum and elucidates the resulting dependence of the measured pendellö-sung phase phase shift on the alignment of S_3. Under the assumption that the free space Green's function may be estimated as

$$G \sim \exp\left[-i\frac{2\pi}{L\lambda}(x' - x)^2\right], \tag{4.87}$$

where L is the distance between the slits and λ is the neutron wavelength, the Wigner function for the direct beam is (up to a normalization constant)

$$P(x, k_x) = \left\{ \mathrm{Si}\left[\frac{4\pi}{L_1\lambda}\left(\frac{S_2}{2} - \left|\frac{L_2\lambda}{2\pi}k_x - x\right|\right)\left(\frac{S1}{2} - \frac{(L_1 + L_2)\lambda}{2\pi}k_x + x\right)\right] + \right.$$
$$\left. - \mathrm{Si}\left[\frac{4\pi}{L_1\lambda}\left(\frac{S_2}{2} - \left|\frac{L_2\lambda}{2\pi}k_x - x\right|\right)\left(\frac{S1}{2} + \frac{(L_1 + L_2)\lambda}{2\pi}k_x - x\right)\right] \right\} \Theta\left(\frac{S_2}{2} - \left|\frac{L_2\lambda}{2\pi}k_x - x\right|\right) \tag{4.88}$$

where

$$\mathrm{Si}(z) = \int_0^z dx \, \frac{\sin x}{x}. \tag{4.89}$$

For the typical slit sizes and separations used in this experiment, Equation 4.88 is well-estimated by the simplification

$$P(x, k_x) \simeq \Theta\left[\frac{S_1}{2} - \left|\frac{(L_1 + L_2)\lambda}{2\pi}k_x - x\right|\right] \Theta\left[\frac{S_2}{2} - \left|\frac{L_2}{2\pi}k_x\right|\right], \tag{4.90}$$

which this is identical to the beam trace result. Figure 4.10 shows both functions; the only difference is the appearance of diffraction spots for the exact result.

4.3.6 Beam Phase Space and the Calculated Pendellösung Phase Shift

To account for a correlation between k_ζ and x, I can construct the Wigner function for the forward-diffracted beam. Writing the pendellösung phase shift in terms of the beam's transverse momentum k_x gives

(a) Exact solution.

(b) Estimated solution.
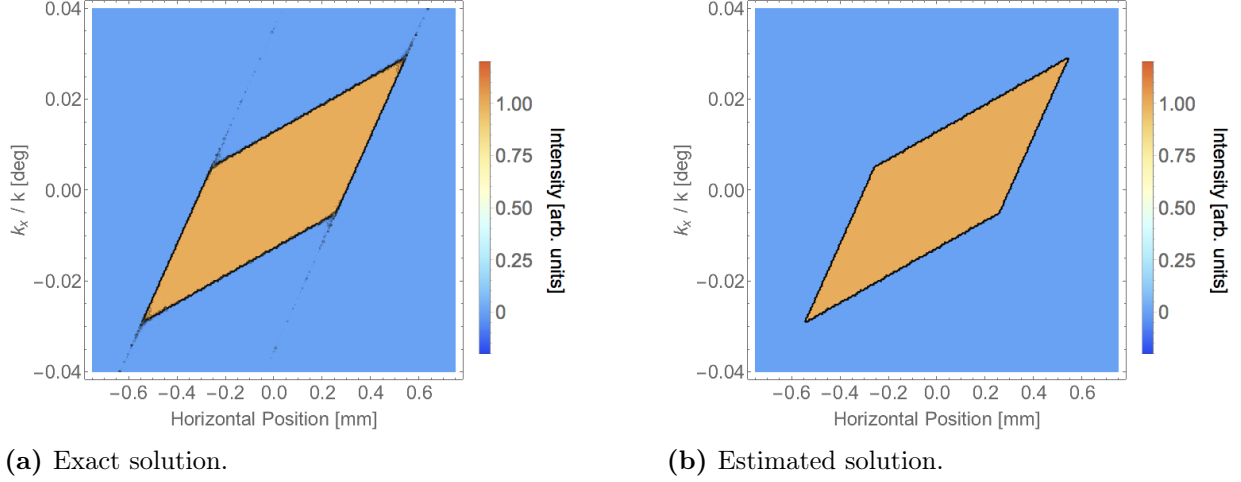
Figure 4.10 Direct beam Wigner function at S_3 for $S_1 = 0.85$ mm, $S_2 = 0.6$ mm, $L_1 = 1.420$ m, and $L_2 = 0.480$ m. The x-coordinate and k_x/k are correlated, because of the use of slits to collimate the beam.

$$\frac{v_H D}{k_\zeta} \to \frac{v_H D}{k_\zeta}\left(1 - \frac{\delta k_\zeta}{k_\zeta}\right) = \frac{v_H D}{k_\zeta}\left(1 - \frac{k_x}{k}\sec\theta_B \csc\theta_B\right). \tag{4.91}$$

Note that this is valid for both $\pm\theta_B$. By the same arguments leading to Equation 4.82, the Wigner function for the forward diffracted beam is

$$P_{\mathrm{F}}(x', k_x) = \int dx\, P_0(x' - x, k_x) G_p^2(x, k_x), \tag{4.92}$$

where P_0 is the Wigner function of the incoming direct beam at S_3; G_P^2 is the modulus-square of the crystal Green's function, the k_x-dependence of which is from the expanding the pendellösung phase shift according to Equation 4.91. The measured intensity in terms of the slit positions and sizes is

$$\mathcal{I}_{\mathrm{meas}} = \int dx\, dk_x\, P_{\mathrm{F}}(x, k_x)\Theta\left(\frac{S_3}{2} - |x - x_3|\right) \tag{4.93}$$

where x_3 is the shift of S_3 with respect to x from $D\sin\theta_B$ (with θ_B positive or negative). The Wigner function for the forward diffracted beam with $D = 11.85$ mm and $\Delta_H = 32.7$ μm is shown in Figure 4.11.

A systematic uncertainty is caused by an unknown shift in x_3, and to a lesser extent the widths of S_1, S_2, and S_3. Fortunately, these parameters can be checked against the direct beam profile as a measured by translating S_3 with a known width through the direct beam (Figure 4.14). The phase shift ϕ_{calc} in Equation 4.55 is computed by simulating pendellösung interferograms with a crystal thickness and pendellösung length close to the experimental parameters. A simulated interferogram is generated by computing data sets according to Equation 4.93 over the experimental range of
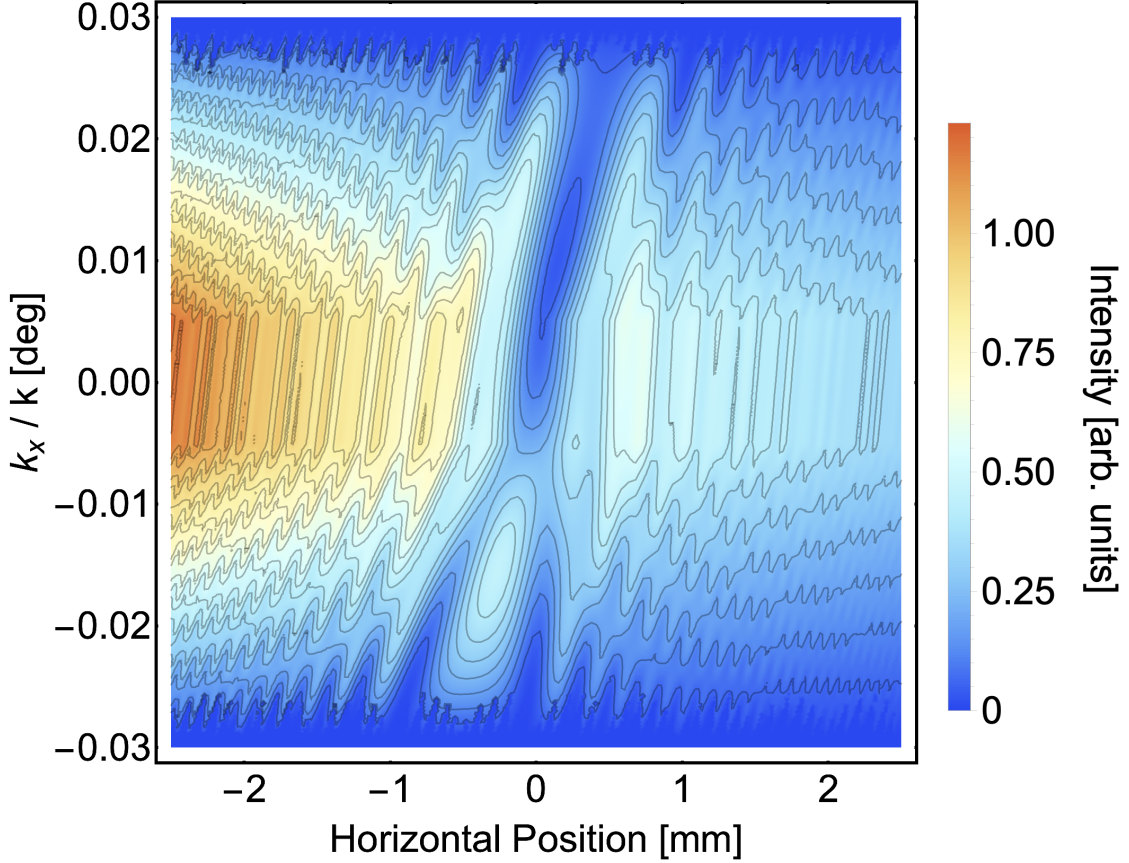
Figure 4.11 Forward-diffracted beam Wigner function at S_3 for $S_1 = 0.85$ mm, $S_2 = 0.6$ mm, $L_1 = 1.420$ m, $L_2 = 0.480$ m, $D = 11.85$ mm, $\Delta_H = 32.7$ μm, $\lambda = 4.4$ Å, and $\theta_B = 44.6$ deg. The correlation between the x-coordinate and the phase of the pendellösung interference fringes is visible.

θ_P. The simulated data is fit to Equation 4.55, except C is fixed, and ϕ_{calc} is a fitted parameter. In this way, ϕ_{calc} may also be computed as a function of x_3, S_1, S_2, S_3, etc., and the uncertainties associated with these parameters can be used to compute the resulting systematic uncertainty in the measured pendellösung phase shift.

The computations for ϕ_{calc} were also be used to help to *select* optimal slit widths. This is done by ensuring the gradient of $\phi_{\mathrm{calc}}(x_3, S_1, S_2, S_3)$ with respect to x_3 and the size of each slit is not too large. For example, $S_1 = 0.9$ mm, $S_2 = 0.6$ mm, and $S_1 = 1.4$ mm, leads to a smaller $\partial\phi_{\mathrm{calc}}/\partial x_3$ than $S_1 = 0.9$ mm, $S_2 = 0.6$ mm, and $S_1 = 0.6$ mm as shown in Figure 4.12. All of the pendellösung interferograms used in the production data for measuring the silicon structure factors used slits with widths $S_1 = 0.9$ mm, $S_2 = 1.1$ mm, and $S_3 = 1.6$ mm, that where $L_1 = 1.42$ m and $L_2 = 0.48$ m apart. The $\phi_{\mathrm{calc}}(x_3)$ functions for each Bragg reflection is shown in Figure 4.13.
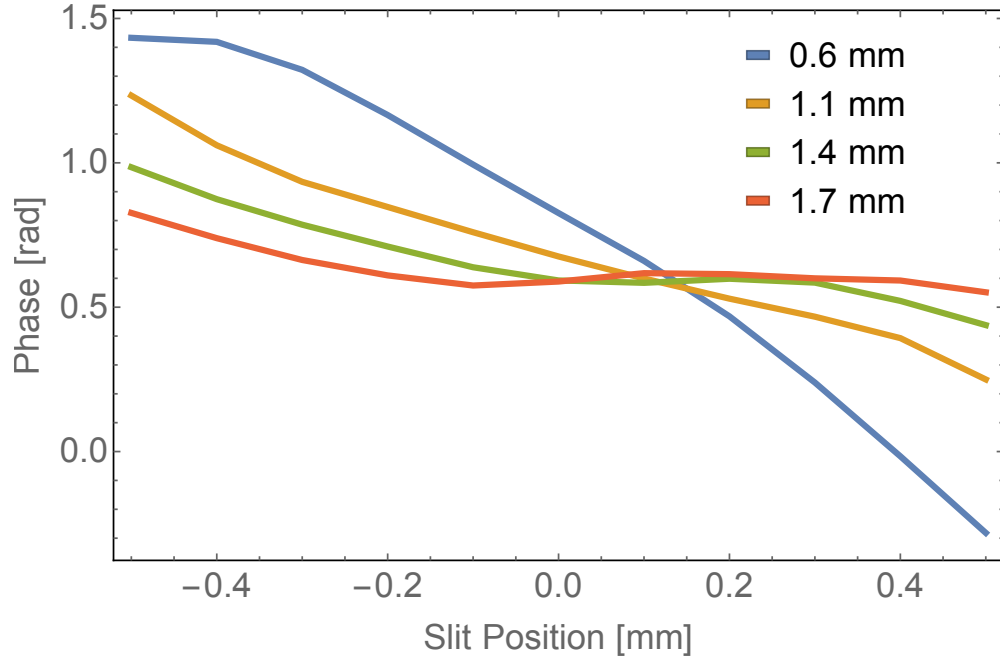
Figure 4.12 Phase versus slit position for varying widths of S_3 for $S_1 = 0.9$ mm, $S_2 = 0.6$ mm, $L_1 = 1.42$ m, $L_2 = 0.48$ m, $D = 11.84$ mm, $\Delta_H = 35.19$ μm, and $\theta_B = 44.56$ deg. The phase gradient is minimal for $S_3 = 1.4$ mm

.
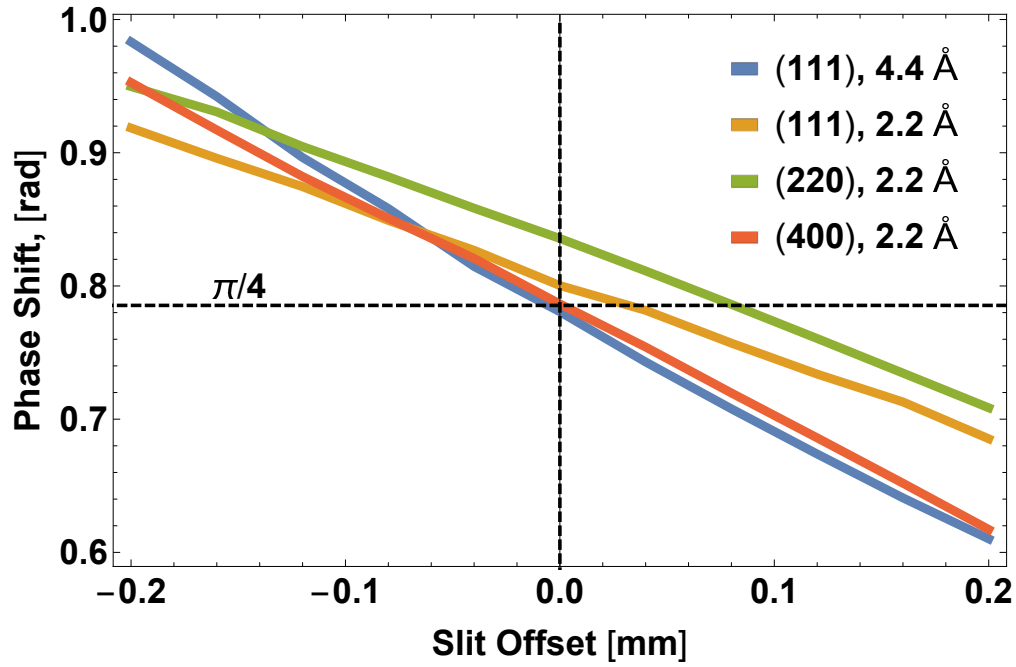
Figure 4.13 Phase offsets for each Bragg reflection in silicon, given the experimental parameters for the precision structure factor measurements: $S_1 = 0.9$ mm, $S_2 = 1.1$ mm, $S_3 = 1.6$ mm, and $D = 9.847$ mm.

4.3.7 Experimental Demonstration of the Pendellösung Phase Correction

To demonstrate that the Wigner function for the direct beam P_0 may computed using the known slit geometry, Figure 4.14 shows that the beam profile measured by passing a 1.1 mm slit through the direct beam is well predicted by P_0 given the known slit sizes and distances apart.

The correlation of the pendellösung phase shift and the x-coordinate was demonstrated experimentally by translating S_3 in the forward-diffracted beam for a few crystal tilts. A pendellösung interferogram was created by tilting the RIKEN two-blade interferometer described in Chapter 3 such that the neutron beam was only hitting one of the crystal blades with S_3 approximately in the center of the Borrmann fan. The S_3 slit was scanned for four crystal tilts, corresponding to the maximum, minimum, and largest-magnitude positive and negative slope points of the interferogram. The results, compared to theory, are shown in Fig 4.15.

Additionally, the pendellösung phase as a function of slit translation was measured. Pendellösung interferograms were measured over a range of S_3 translations for two different slit sizes (Figure. 4.16). The slope of the pendellösung phase as a function of position depends on the width of the slit S_3, with the larger slit width corresponding to a smaller slope.

Finally, note that the linear dependence of the pendellösung phase shift with respect to x_3 is very different from the narrow slit case, or when the correlation between k_ζ and x is not taken into account. Previously, the predicted quadratic dependence of the pendellösung phase shift on slit translation has been measured with slits widths of $\sim 100~\mu$m [SO72]. However, the data presented in this section indicates that the phase correction becomes linear in the wide slit case, with the slope of $\phi_{\rm calc}$ versus x_3 decreasing with increasing final slit width S_3. In short, in the narrow slit case, the pendellösung phase as a function of slit translation is quadratic and equal to $\phi_{\rm calc} = \pi/2$ when the slit is centered in the Borrman fan. In the wide slit case, and also accounting for the k_ζ-x correlation, the pendellösung phase shift is linear with respect to slit translation, and $\phi_{\rm calc} = \pi/4$ when the slit is centered.

4.3.8 Pendellösung in a Strained Crystal

Linear strain gradients along $\vec{H}$ cause a systematic shift in the pendellösung phase which depends on the wavelength and thickness of the crystal slab. The origin of this effect was derived by [Kat63; Kat64a; Kat64b]. The effect has been confirmed by intentionally inducing a temperature gradient across a crystal and measuring the shift in pendellösung fringes using x-rays [Har66]. For the neutron case, pendellösung interference where a component of $\vec{H}$ is in the direction Earth's gravitational field gives a similar result. A thorough description of the theory applied to the neutron case is given by [Wer80], and readers with an interest in this topic are also encouraged to see [Mah89], where experiments detailing neutron dynamical diffraction in mechanically bent silicon crystals are described. Pendellösung in the presence of both strain and Earth's gravity has also been demonstrated
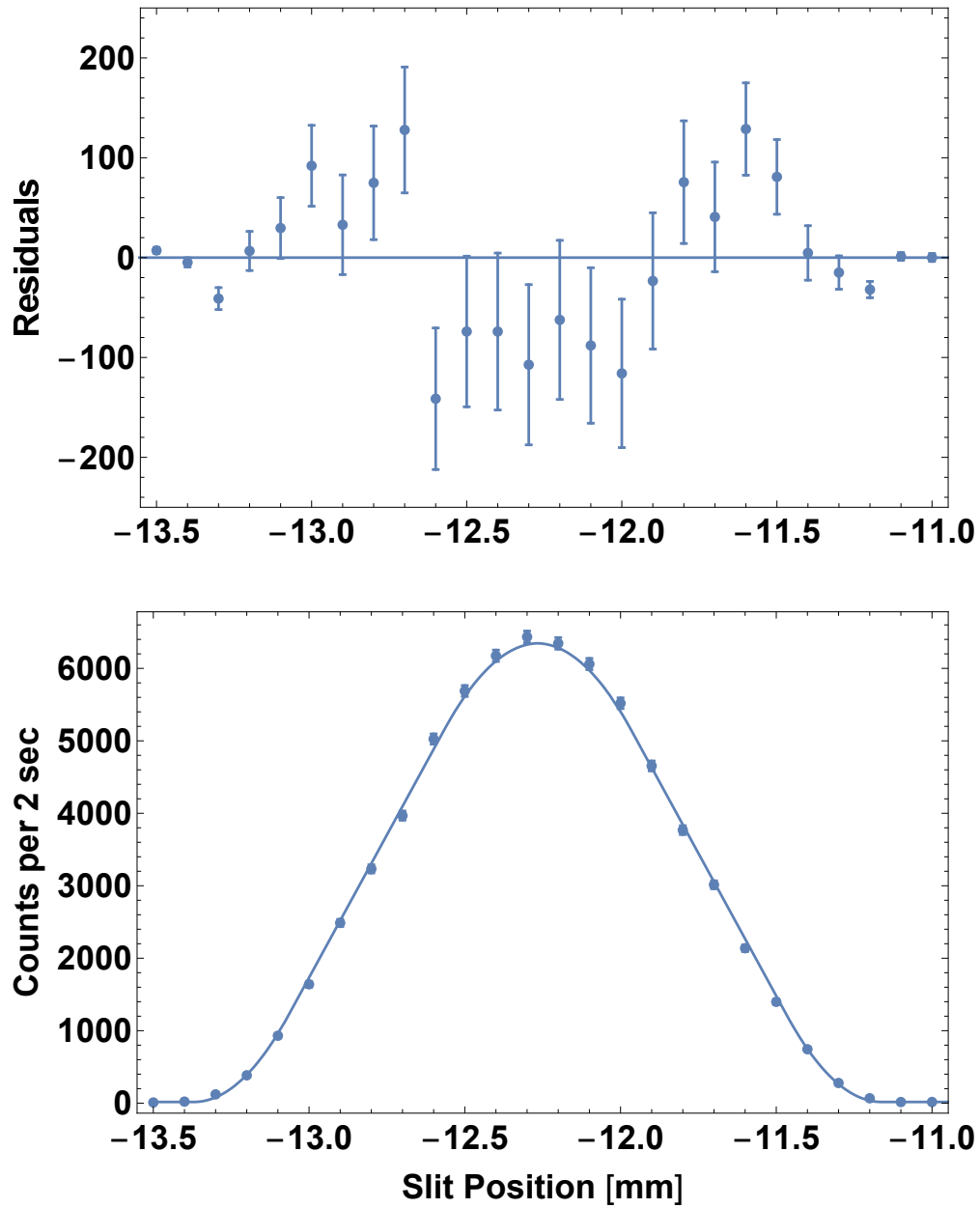
Figure 4.14 Measured beam profile from passing a $S_3 = 1.1$ mm slit through the direct beam, with $S_1 = 0.9$ mm, $S_2 = 0.6$ mm, $L_1 = 1.42$ m, and $L_2 = 0.48$ m. The only fit parameters are the offset in slit position and the amplitude. The shape is fixed by the known slit widths and distances between slits.
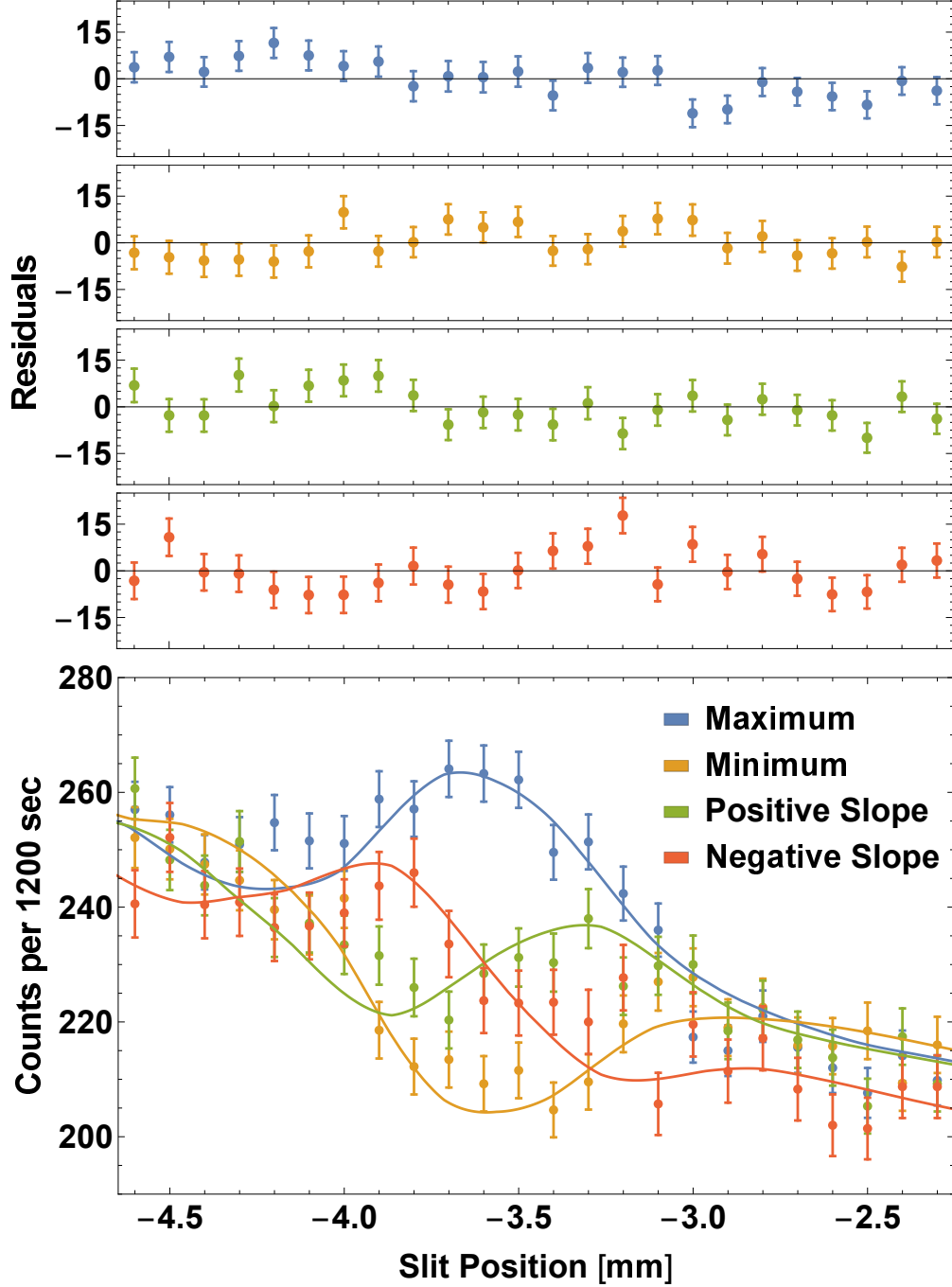
Figure 4.15 Beam profile from scanning a $S_3 = 0.6$ mm slit through the forward diffracted beam of a crystal with thickness $D = 11.85$ mm (one of the blades of the RIKEN two-blade interferometer). The different curves are for the maximum, minimum, and positive and negative slopes of the fitted oscillation upon tilting the crystal with a $S_3 = 1.1$ mm slit in the forward diffracted beam. If there were no correlation between the slit position and transverse momentum, then the positive slope and negative slope curves would not contain the visible, single oscillation. The curves were allowed to have different backgrounds, but the relative amplitudes of the oscillations were the fixed to be same.
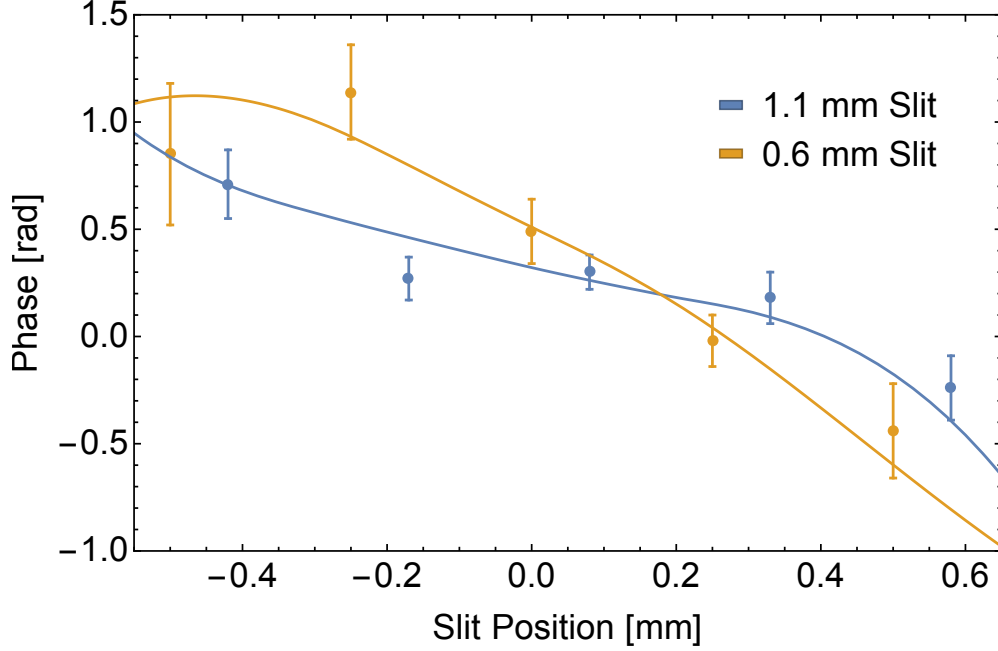
Figure 4.16 Measured phase shift versus position using one blade of the RIKEN two-blade interferometer ($D = 11.85$ mm), with $S_1 = 0.85$ mm, $S_2 = 0.9$ mm, $L_1 = 1.42$ m, and $L_2 = 0.48$ m for both $S_3 = 1.1$ mm and $S_3 = 0.6$ mm compared to theory. The larger error bars for larger magnitude slit positions are due to reduced interference fringe visibility.

using neutrons in quartz [Ale88]. In regards to Earth's gravity, $\vec{H}$ in this experiment is aligned horizontally, so it does not affect the measured pendellösung phase shift.

The effect of strain gradients on the measured pendellösung phase shift shift may be understood by noting that when computing the pendellösung phase shift, the canonical momentum in the $\hat{\zeta}$ direction is integrated from one side of the crystal to the other

$$\phi_P = \int_0^D d\zeta \left(K_\zeta^\alpha - K_\zeta^\beta \right) \tag{4.94}$$

where the α and β superscripts refer to the $|\alpha\rangle$ and $|\beta\rangle$ degenerate solutions to the dynamical diffraction Hamiltonian (See Chapter 1). Normally, $K_\zeta^{\alpha,\beta}$ has no dependence on ζ, and the integral simply evaluates to a factor of the crystal thickness D. However, in the presence of a strain gradient neutrons travelling through different portions of the Borrmann fan see slightly different lattice constants. This causes the otherwise straight trajectories in the Borrrmann fan to become curved. The simplest way to take this into account is to classically solve the dynamical diffraction Hamiltonian, then evaluate the phase shift in the semi-classical limit. This is the Eikonal approximation, which in Chapter 1, I claimed was not suitable for crystalline dynamical diffraction on account of the crystalline potential varying on the same length scale as the neutron wavelength. However, this is

only true of applying solutions of the free particle Hamiltonian to the crystalline potential. In the case of a linear strain gradient, I am claiming that perturbations to the $|\alpha\rangle$ and $|\beta\rangle$ solutions of the dynamical diffraction Hamiltonian may be treated in the Eikonal approximation, where the strain gradient does not vary appreciably over the neutron wavelength.

Beginning with the crystalline dynamical diffraction Hamiltonian in the α, β basis (Equation 1.34)

$$\mathcal{H}^{\alpha,\beta} = \frac{1}{2m}\left(K_\zeta^2 + \frac{1}{4}H^2 + v_0 \pm v_H\sqrt{\eta^2+1}\right) \tag{4.95}$$

where for simplicity, I have let $\sqrt{v_H v_{-H}} \to v_H$ and written the Hamiltonian in terms of $\eta = \delta K H/v_H$. I can then identify K_ζ and $\eta\,(v_H/H)$ as the canonical momenta conjugate to ζ and ξ, respectively.

To perturb the Hamiltonian let K_ζ^2 and H^2 above be the average values with the strain field perturbing each in the following way

$$H^2 \to \frac{H^2}{\left(1+\frac{\delta a}{a}\right)^2} \simeq H^2\left[1 - 2h\left(\vec{\xi}\right)\right] \tag{4.96}$$

$$K_\zeta^2 \to \frac{H^2}{4\left(1+\frac{\delta a}{a}\right)^2}\cot^2\theta_B \simeq \frac{1}{4}H^2\left[1 - 2h\left(\vec{\xi}\right)\right]\cot^2\theta_B = K_\zeta^2 - \frac{1}{2}H^2\cot^2\theta_B\, h\left(\vec{\xi}\right) \tag{4.97}$$

where $h\left(\vec{\xi}\right) = \delta a/a$ is the position-dependent strain field. Inserting this into Equation 4.95, the perturbative potential is given by

$$\mathcal{H}^{\alpha,\beta} = \mathcal{H}_0^{\alpha,\beta} - \frac{H^2}{4m\sin^2\theta_B}h\left(\vec{\xi}\right), \tag{4.98}$$

which clearly indicates that a gradient in the strain field will act like a force inside the crystal [Wer80].

To compute the phase shift from a strain gradient, I need to start by solving Hamilton's equations in the crystal:

$$\dot{\zeta} = \frac{\partial\mathcal{H}}{\partial K_\zeta} = \frac{K_\zeta}{m} \tag{4.99}$$

$$\dot{K}_\zeta = -\frac{\partial\mathcal{H}}{\partial\zeta} = \left(\frac{H^2}{4m}\right)\frac{\partial h\left(\vec{\xi}\right)}{\partial\zeta} \tag{4.100}$$

$$\dot{\xi} = \left(\frac{H}{v_H}\right)\frac{\partial\mathcal{H}}{\partial\eta} = \pm\frac{H}{2m}\frac{\eta}{\sqrt{\eta^2+1}} \tag{4.101}$$

$$\dot{\eta} = -\left(\frac{H}{v_H}\right) \frac{\partial \mathcal{H}}{\partial \xi} = \left(\frac{H^3}{4mv_H \sin^2 \theta_B}\right) \frac{\partial h\left(\vec{\xi}\right)}{\partial \xi}. \tag{4.102}$$

Noting that the $|\alpha\rangle$ and $|\beta\rangle$ states which interfere to form the pendellösung phase shift have the same energy, I can write

$$K_\zeta^\alpha - K_\zeta^\beta = \frac{v_H}{K_{\zeta B}} \sqrt{\eta^2 + 1} \tag{4.103}$$

where $K_{\zeta B} = \sqrt{k^2 - \frac{1}{4}H^2 - v_0}$ is the average momentum along the Bragg planes. The pendellösung phase shift then becomes

$$\phi_P = \frac{v_H}{K_{\zeta B}} \int_0^D d\zeta \sqrt{\eta^2 + 1} = \frac{v_H}{K_{\zeta B}} \int_{\eta(0)}^{\eta(D)} d\eta \frac{\dot{\zeta}}{\dot{\eta}} \sqrt{\eta^2 + 1} \tag{4.104}$$

For the simplest case of a linear strain gradient, let the strain gradient be constant and in the $\hat{\xi}$ direction, $\hat{\zeta} \cdot \nabla h(\vec{\xi}) = 0$ and $\hat{\xi} \cdot \nabla h(\vec{\xi}) = h_\xi$. In this case

$$\dot{\eta} = \left(\frac{H^3}{4mv_H \sin^2 \theta_B}\right) h_\xi \tag{4.105}$$

is a constant, and Equation 4.102 may be integrated giving $\eta(t) = \eta + \dot{\eta}t$. With $\dot{\zeta}$ and $\dot{\eta}$ both constant, the integral in Equation 4.104 can be evaluated

$$\phi_P = \frac{v_H}{K_{\zeta B}} \frac{\dot{\zeta}}{\dot{\eta}} \frac{1}{2} \left(\eta \sqrt{\eta^2 + 1} + \sinh^{-1}(\eta)\right)\Big|_{\eta(0)}^{\eta(D)}. \tag{4.106}$$

However, it is easier to expand $\sqrt{\eta^2 + 1}$ around the average value of η

$$\phi_p = \frac{v_H}{K_{\zeta B}} \int_{-t/2}^{t/2} dt \, \dot{\zeta} \left\{ \sqrt{\eta^2 + 1} + (\dot{\eta}t) \frac{\eta}{\sqrt{\eta^2 + 1}} + \frac{1}{2}(\dot{\eta}t)^2 \left(\eta^2 + 1\right)^{-\frac{3}{2}} \right\} \tag{4.107}$$

which evaluates to

$$\phi_P = \frac{v_H}{K_{\zeta B}} D \left\{ \sqrt{\eta^2 + 1} + \frac{1}{6} \left(\frac{\dot{\eta}t}{2}\right)^2 \left(\eta^2 + 1\right)^{-\frac{3}{2}} \right\} \tag{4.108}$$

where I have used $D = t\dot{\zeta}$. The $\dot{\eta}t/2$ term is half the change in η the the neutron experiences as it passes through the crystal. In the notation of [Har66]

$$p = \frac{\dot{\eta}t}{2} = \frac{\dot{\eta}D}{2\dot{\zeta}} = \left(\frac{H^2 D}{4v_H \sin \theta_B \cos \theta_B}\right) h_\xi. \tag{4.109}$$

Finally, the pendellösung phase shift becomes

$$\phi_P = \frac{v_H D}{K_\zeta} \sqrt{\eta^2 + 1} \left\{ 1 + \frac{1}{6} p^2 \frac{1}{(\eta^2 + 1)^2} \right\}. \tag{4.110}$$

Normally, computing the pendellösung Green's function using the reflection operator in momentum space

$$G_P \propto \int d\eta \exp \left[\pm i \frac{1}{2} \phi_P(\eta) + i \frac{v_H}{H} \eta (\xi' - \xi) \right] \tag{4.111}$$

is accomplished via the stationary phase method. The argument of the exponential is evaluated at the value of $\eta = \eta_0$ such that

$$\pm \frac{1}{2} \frac{\partial}{\partial \eta} \phi_P + \frac{v_H}{H} (\xi' - \xi) = 0. \tag{4.112}$$

In the absence of strain, the solution to this equation is

$$\eta_0 = \pm \frac{\gamma}{\sqrt{1 - \gamma^2}}, \tag{4.113}$$

where

$$\gamma = \frac{\xi' - \xi}{D \tan \theta_B}. \tag{4.114}$$

Instead of solving Equation 4.112 for the case of a strained crystal, I can use the solution for η_0 in the absence of strain, by noting that the phase of the resulting position space Green's function will be the same to first order in p^2 (see Equation B.9)

$$\phi_P(\xi' - \xi) = \pm \frac{v_H D}{2 K_\zeta} \sqrt{1 - \gamma^2} \left\{ 1 + \frac{1}{6} p^2 (1 - \gamma^2)^2 \right\}. \tag{4.115}$$

For small γ (the center of the Bormann fan), the pendellösung phase is shifted by a factor of $p^2/6$, and the phase shift from a linear strain gradient is *positive definite*.

In the case of a temperature gradient

$$h_\xi = \alpha \frac{dT}{d\xi}, \tag{4.116}$$

which has been used to demonstrate the validity of these treatments [Har66]. During data allocation for this experiment, there was some evidence of temperature gradients that were large enough to cause a shift in the measured pendellösung phase shift. This prompted the use of two calibrated temperature probes placed on the crystal to monitor the absolute temperature and any gradients within the crystal. After adjusting the temperature control system, the temperature gradients could be made small enough to not affect the measured pendellösung phase shift.

To avoid strain gradients causing a systematic uncertainty, $\frac{1}{6}p^2$ should be less than the relative uncertainty of the measured pendellösung phase shift. This was not the case for the first precision neutron pendellösung measurements carried out by [SO72; SS73]. Instead, the authors measured tens of full pendellösung oscillations by rotating a crystal in a polychromatic neutron beam. The fitted pendellösung phase shift then followed the $1/(\cos\theta_B \sin\theta_B)$ functional form, allowing the neutron structure factor to be isolated. These experiments required the crystals be polished and very flat, because in order to isolate v_H, the crystal thickness had to be very well known.

From the slope of the measured pendellösung phase shift as a function of $1/(\cos\theta_B \sin\theta_B)$, the authors of [SO72] measured strain gradients on the order of $h_\xi = 1/R = 1/(10^4 \text{ m}) = 100$ nrad mm^{-1}, where R is the radius of curvature, which refers to the strain gradient that would occur from elastically bending a crystal to have radius of curvature R. Compared to the Bragg plane twists measured in Chapter 3 for a number of neutron interferometers, this level of strain is enormous! Typical values for the interferometers in Chapter 3 are $\lesssim 5$ nrad mm^{-1}. The best interferometer with regards to minimal Bragg plane twist was the RIKEN two-blade interferometer with 0.2 nrad mm^{-1}. Strain gradients at this level would produce no discernible systematic uncertainty to the experiment.

Producing strain free crystals using methods similar to what is used for neutron interferometers, however, comes at the cost of flatness and parallelism of the slab, because chemical etching is inevitably uneven. The RIKEN two-blade interferometer exhibited the smallest strain gradients and required relatively little chemical etching, likely do the ultra-high precision grinding process producing less subsurface damage. The pendellösung samples were ground and etched by similar methods (though the crystal was not annealed). Even so, measuring the thickness of the crystal to isolate v_H from the measured pendellösung phase shift is not an option, because the crystal cannot be made flat enough without creating strain gradients. However, the method of placing the sample in a neutron interferometer, such that the irradiated volume of the crystal is roughly the same as for the pendellösung portion of the experiment alleviates the need to measure the crystal thickness using other means.

4.4   Experiment

Both the pendellösung and forward scattering measurements were performed on the NIOFa beamline at the NCNR (see Section 1.5). The 2.2 Å component of the beam was used to measure the (220) and (400) pendellösung interferograms, and the 4.4 Å component was used for measuring the (111) pendellösung interferograms and completing the forward scattering measurements using a neutron interferometer. Pendellösung interferograms for the (111) reflection were also measured at 2.2 Å; however, parasitic reflections rendered the data unsuitable for inclusion in the measurement of the (111) structure factor. See the Section 4.4.1.1 for details concerning parasitic reflections.

The neutron interferometer used in this experiment predates this work by a number of years. The geometry and fringe visibility were convenient for the experiment so there was no need to construct a new interferometer. The pendellösung sample did need to be fabricated; a diagram of the sample is shown in Figure 4.17a. The neutron beam enters the main face of the crystal. By aligning the surface normal of the major face to the ($\bar{2}$20) planes, there are a number of accessible reflections available whose lattice vectors are parallel to the surface. For three of these reflections, flats were cut so that the sample could fit in between the blades of the interferometer. The beam profiles for the interferometry and pendellösung measurements are also shown in Figure 4.17a. The (111), (220), and (004) reflections were all measured. In principle, the sample may also be used to measure the (113) reflection, though this has not yet been completed. In the following discussion, the (004) reflection in Figure 4.17 will usually be referred to as the (400) reflection.

The pendellösung sample was aligned to the Bragg planes and cut from a float zone grown silicon ingot by Albert Henins of the NIST Diffraction and Metrology Standards Group. The alignment of the ($\bar{2}$20) Bragg planes to the major surface is < 0.25 deg. The major surfaces of the sample were finished using the ultra-high precision grinding capabilities at the RIKEN Center for Advanced Photonics. The grinding was performed in a similar manner to the two-blade interferometer described in Chapter 3. Approximately 5 μm of material was chemically etched from each side of the crystal to remove machining damage. Two-dimensional profiles of the change in crystal thickness were measured for each side of the crystal using a helium-neon laser interferometer. The two profile measurements were added together to form a map of the crystal's thickness variation, which is shown in Figure 4.17b. The profile measurements were completed before the crystal was etched; however, while etching changes the absolute thickness of the sample, it is unlikely that the profile changed appreciably.

4.4.1   Pendellösung Interferograms

Pendellösung interferograms were measured for the (111), (220), and (400) reflections by rotating the crystal about the $\hat{\xi}$-axis, which is defined by $\vec{H}$. The slits widths were $S_1 = 1.4$ mm, $S_2 = 1.1$ mm and $S_3 = 1.6$ mm with the distances between the slits $L_1 = 1.42$ m and $L_2 = 0.48$ m in Figure 4.8. The corresponding computed phase shifts were 0.78 rad, 0.84 rad, and 0.79 rad for the (111), (220), and (400) reflections, respectively. The computed phase shift for the (111) reflection at $\lambda = 2.2$ Å was 0.80 rad. The correction from the wide slit case of $\phi_{\text{calc}} = \frac{\pi}{4} = 0.785$ is small for all the reflections. See Section 4.3.6 for details concerning the calculated pendellösung phase shift.

The S_1 and S_2 slits remained stationary, while the S_3 slit and detector for the forward-diffracted beam could be translated into position. The central value for the translation of S_3 was measured by translating the slit through the direct beam, and finding the centroid of the resulting peak. The slit was moved into the forward diffracted beam by translating the slit by $\pm D \sin \theta_B$. Lead screw and
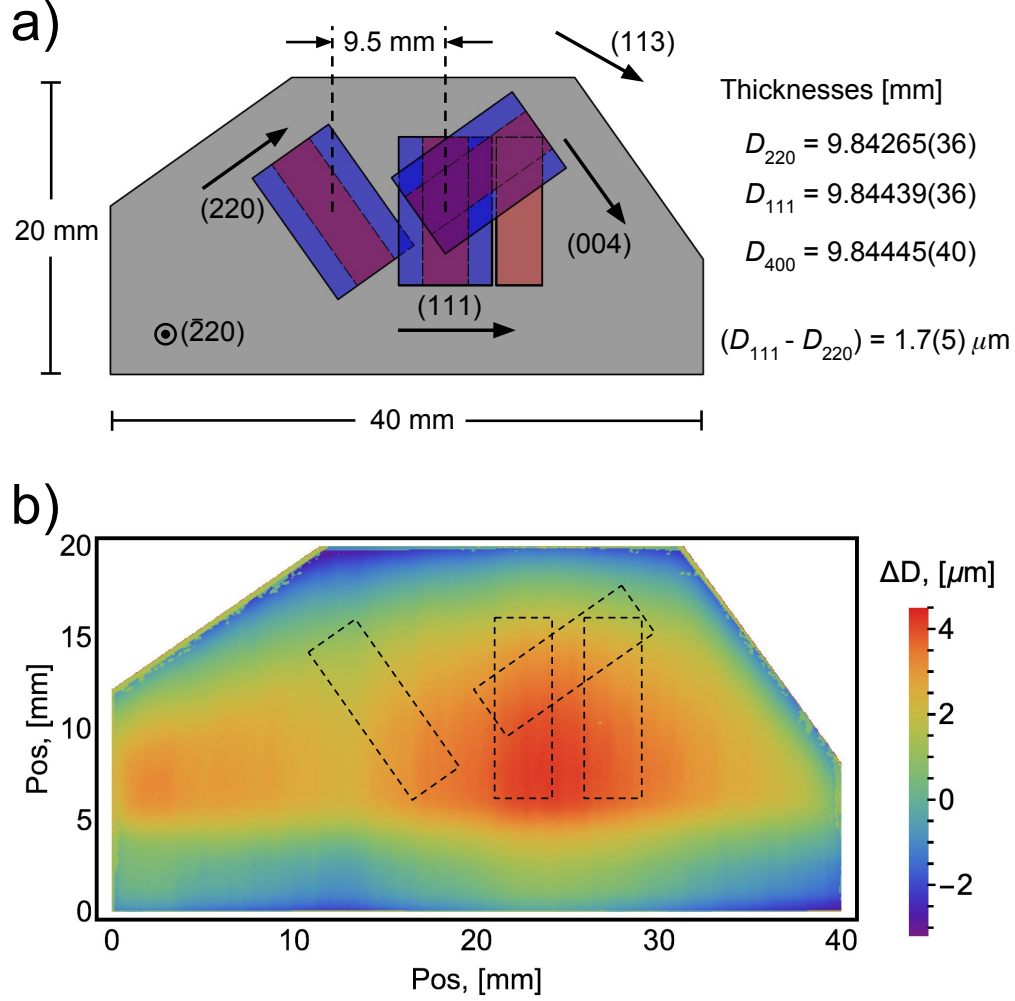
Figure 4.17 Diagram (a) and thickness variation map (b) of the pendellösung crystal. Thicknesses for (a) are computed from the interferometer phase shift and known scattering length density of silicon. The uncertainty of the silicon scattering length density is not included in the quoted thickness uncertainties, because it is common to all three measurements. The blue sections are the approximate interferometer beam profile, which is most sensitive to the crystal thickness at its center. The red sections are the areas probed by the pendellösung measurements. The outlines of the pendellösung beam profiles are shown as dashed lines in (b). A portion of the (111) data was shifted by 5 mm to the right, as shown. A small correction was applied based on the profile map. See text for details.

stepper motor accuracy of the translation stage causes a ~ 4 μm systematic uncertainty in the slit position, and the angular misalignment of the translation stage is taken to be at most 2.5 deg, which causes a $\lesssim 8$ μm misalignment of S_3. Given the slope of the ϕ_{calc} with respect to the position of S_3, the systematic uncertainty caused by the positioning error of the final slit is small and given in Table 4.1.

Table 4.1 Uncertainty budget for the pendellösung interferogram measurements. The correction to the measured pendellösung phase shift is $\Delta\phi_P$. The total phase shifts for ϕ_P were approximately 10×10^4 deg, 6×10^4 deg and 8×10^4 deg for the (111), (220), and (400) reflections, respectively.

Source	Uncertainty	$\Delta\phi_P$ (deg)	$\sigma_P/\phi_P \times 10^{-5}$	hkl
		0.0	0.5	111
S_3 Translation	10 μm	1.1	0.4	220
		2.9	0.3	400
			1.0	111
Bragg Stage, θ_B	3×10^{-4} deg		0.8	220
			1.6	400
	0.1×10^{-5}	0.2	0.1	111
Temperature Gradient, $p_T^2/6$	0.2×10^{-5}	0.4	0.2	220
	2.1×10^{-5}	3.7	2.1	400
	0.20 K	-1.0	0.7	111
Absolute Temperature	0.06 K	-1.0	0.6	220
	0.08 K	3.2	1.5	400
Crystal Profile	0.14 μm	1.4	1.4	111
Anharmonic Correction, $f_{\mathrm{anh}}(hkl)$	1×10^{-5}	2.9	1.0	111
			2.2	111
Total Sys.			1.1	220
			3.1	400
	2.6 deg		2.5	111
$\boldsymbol{\phi_P}$, **Stat.**	3.3 deg		5.4	220
	6.3 deg		7.8	400
			3.0	111
Total			**5.5**	220
			8.4	400

Interferograms were measured at both plus and minus θ_B. To extract $v_H D$, the measured pendellösung phase shift is multiplied by $\frac{H}{2}\cot\theta_B$, with θ_B taken by the angular position of the rotation stage, which had an embedded encoder with a resolution of 7.5×10^{-5} deg. Estimating the accuracy of the encoder to be four times the resolution, an angular positioning error of 3×10^{-4} deg is assumed. The resulting systematic uncertainties are reported in Table 4.1.

There is inevitably a slight difference in the average wavelength for the plus and minus θ_B measurements. The linear deviations in wavelength caused by a difference in Bragg angle create a
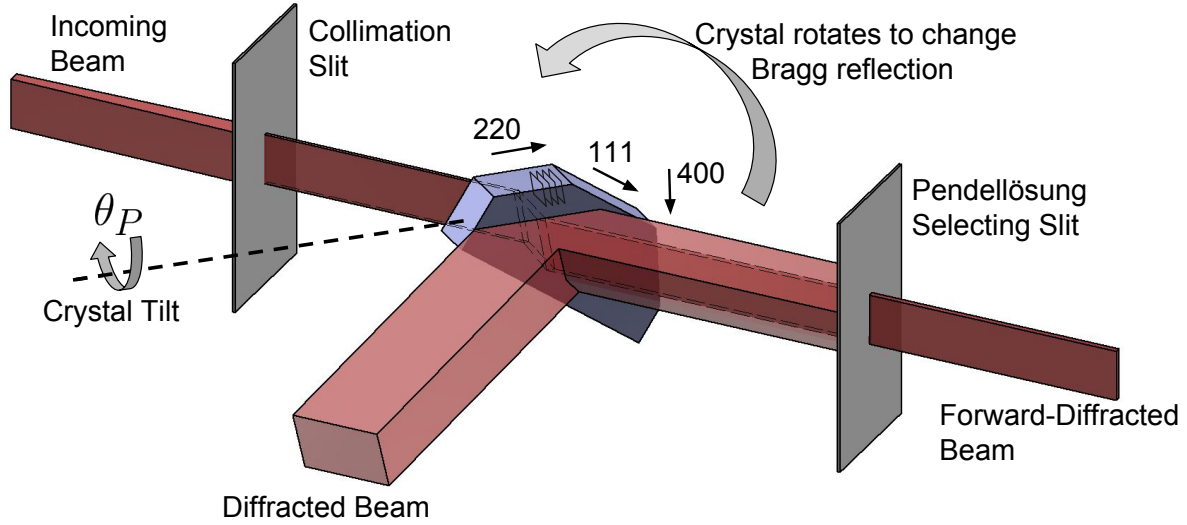
Figure 4.18 Schematic of the experimental setup. Pendellösung interferograms are measured in the forward-diffracted beam.

relative change in the pendellösung phase shift of $\delta\theta_B/(\sin\theta_B\cos\theta_B)$. However, the linear terms drop out upon averaging the plus and minus θ_B phase shifts, and the leading-order term in $\delta\theta_B$ is quadratic, causing a relative shift of $\delta\theta_B^2/\cos^2\theta_B$. This term may be computed from the difference in the fitted pendellösung phase shift for the plus and minus θ_B interferograms. At its largest, the relative correction from the quadratic term is 1×10^{-6} and thus neglected.

Alignment of the θ_P stage's tilt axis was accomplished for each reflection according to Section 4.3.1. To change between reflections, the crystal and its mount could be removed and rotated (Figure 4.18). To generate an interferogram, the crystal was tilted over a range of θ_P in discrete steps, and the number of neutron counts within a set time frame was recorded as a function of θ_P in a ^{3}He detector. The interferograms at plus and minus θ_B were fit together, with some parameters constrained to be the same, as previously described in Section 4.3.1. Interferograms were measured with the crystal translated by ± 1 mm along $\vec{H}$ from the target value. There was no measurable difference in the pendellösung phase shifts as a function of translation. Depending on the local parallelism of the crystal, a systematic uncertainty for misalignment of the beam is considered, but this is ascribed to the interferometer phase shift. See Section 4.4.2.

The temperature of the samples was controlled with a heater plate suspended above the crystal (Figure 4.19a). For the (220) and (400) measurements, a second heater was placed next to the crystal opposite from the larger heater. Both heaters were controlled in a PID feedback loop using temperature probes. Two other calibrated temperature probes were placed on the crystal a known distance apart, typically about 15 mm. The resulting temperatures were recorded for each point
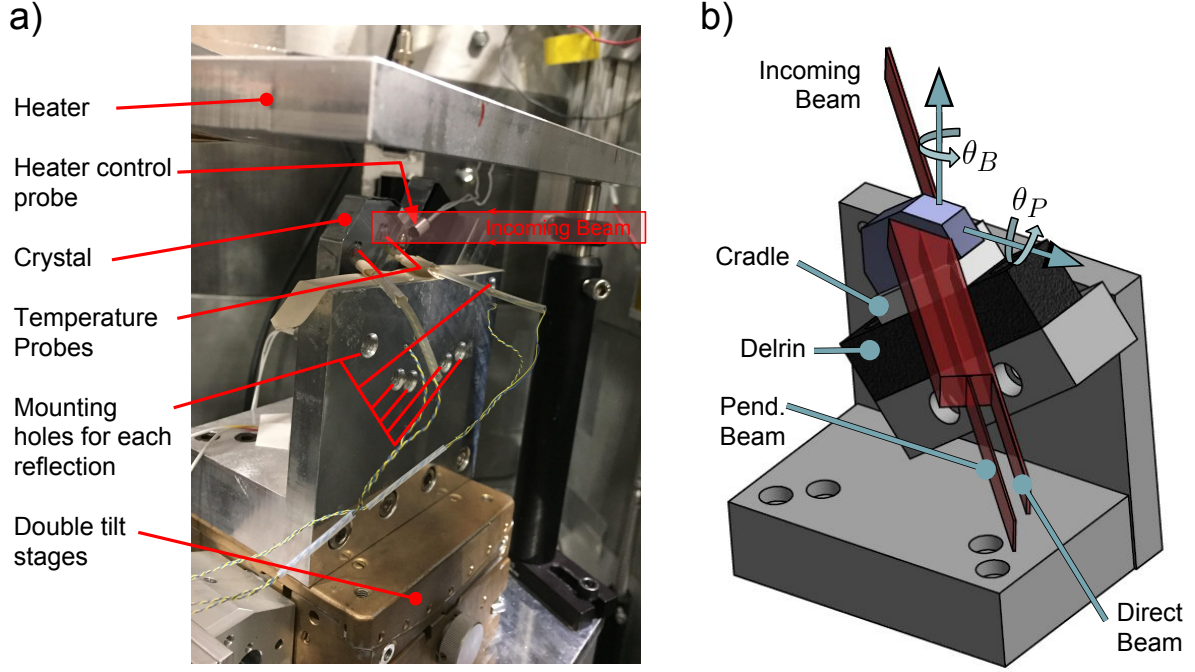
Figure 4.19 (a) Photograph of the pendellösung interferometry setup. (b) Computer model of the experiment showing the beam paths.

of the pendellösung interferograms. The temperature gradient was taken from the difference in measured temperature for the two probes. The resulting value of p_T was computed according to Equations 4.109 and 4.116, with the subscript T denoting the portion of p from temperature gradients. The phase of the interferogram was corrected using the average value of $p_T^2/6$, and the uncertainty was computed as the standard deviation of $p_T^2/6$. See Table 4.1 for the corrections and uncertainties for each Bragg reflection.

A change in the absolute temperature of the pendellösung crystal changes the Debye-Waller B parameter by $B(T + \delta T) \simeq B(T)(1 + \delta T/T)$. The lattice dynamical function of $B(T)$ from inelastic neutron scattering and the BvK model predicts $dB/dT = 0.0014$ Å^2 K^{-1} at 295.5 K, whereas $B/295.5 = 0.0016$ Å^2 K^{-1}; fortunately, this experiment is not sensitive to the difference in dB/dT for the two estimations because all of the measurements were made at similar temperatures. Specifically, $T_{111} = 295.78(20)$, $T_{220} = 295.67(8)$, and $T_{400} = 295.30(8)$, where the uncertainties are taken as the standard deviation of temperature averages of all the pendellösung interferograms for each reflection. The resulting corrections and systematic uncertainties for each Bragg reflection are tabulated in Table 4.1. The corrections are all less than half of the statistical uncertainties. The lattice constant is also a function of temperature; however, the coefficient of thermal expansion

is small $\sim 2.6 \times 10^{-6}$ K^{-1}. A value of $a = 5.431020$ Å, as according to [Kes17], was used when computing $Db(Q)$.

The height of the pendellösung crystal was set by placing a cadmium slit on the crystal mount and lifting the mount through the beam. The crystal was aligned in the horizontal direction separately for both Bragg angles and each reflection. This was accomplished by translating the crystal through the beam past its edge while monitoring the diffracted beam. When the neutron beam misses the crystal, only the background intensity is measured. As the crystal edge is translated into the beam, the diffracted beam intensity is approximately linearly increasing. Diffracted beam counts as a function of translation were measured, and the linear portion of the curve was fit to a line. The intersection of this line with the background count rate was determined to be the edge of the crystal relative to the neutron beam. Using the known beam width and crystal dimensions, the crystal was then translated from its edge to the target position, which was chosen to correspond to the location of the crystal measured by the neutron interferometer in the forward scattering measurement.

A clerical error caused the plus θ_B interferograms for the (111) reflection to be shifted by 5 mm away from the target position (Figure 4.17). This was discovered after data allocation was completed. To compensate for the translation, the average thickness difference between the plus and minus θ_B interferogram positions was computed by averaging the crystal profile map over the beam profiles outlined in Figure 4.17. This was repeated with the beam profiles pseudo-randomly co-translated according to a two dimensional normal distribution (horizontal and vertical translations) with $\sigma_{\text{trans}} = 1$ mm. The average thickness difference for the two beam profiles was 0.28(28) μm, where the average and uncertainty is the average and standard deviation of the resulting thickness difference distribution. (Note that the equal values for the correction and uncertainty is a coincidence.) The difference between the average thickness of the pendellösung beam profiles and the thickness of the crystal at the target position is then 0.14(14) μm (half the average thickness difference), resulting in a 1.4×10^{-5} relative correction and uncertainty applied to the measured pendellösung phase shift for the (111) reflection. The correction and uncertainty are reflected in Table 4.1 under "Crystal Profile." A similar calculation was performed for estimating the uncertainty caused by a misalignment of the pendellösung and interferometer beam profiles, but this uncertainty was ascribed to the interferometer phase shifts. See Table 4.2 and Section 4.4.2.

4.4.1.1 Parasitic Reflections

Pendellösung interferograms for the (111) reflection were measured at 2.2 Å. However, a large distortion in one of the interferograms shown in Figure 4.20 suggested so-called "parasitic" reflections were diffracting neutrons into the forward-diffracted beam detector as a function of θ_P. The distortions were severe enough to severely impede the extraction of the useful data from the 2.2 Å (111)
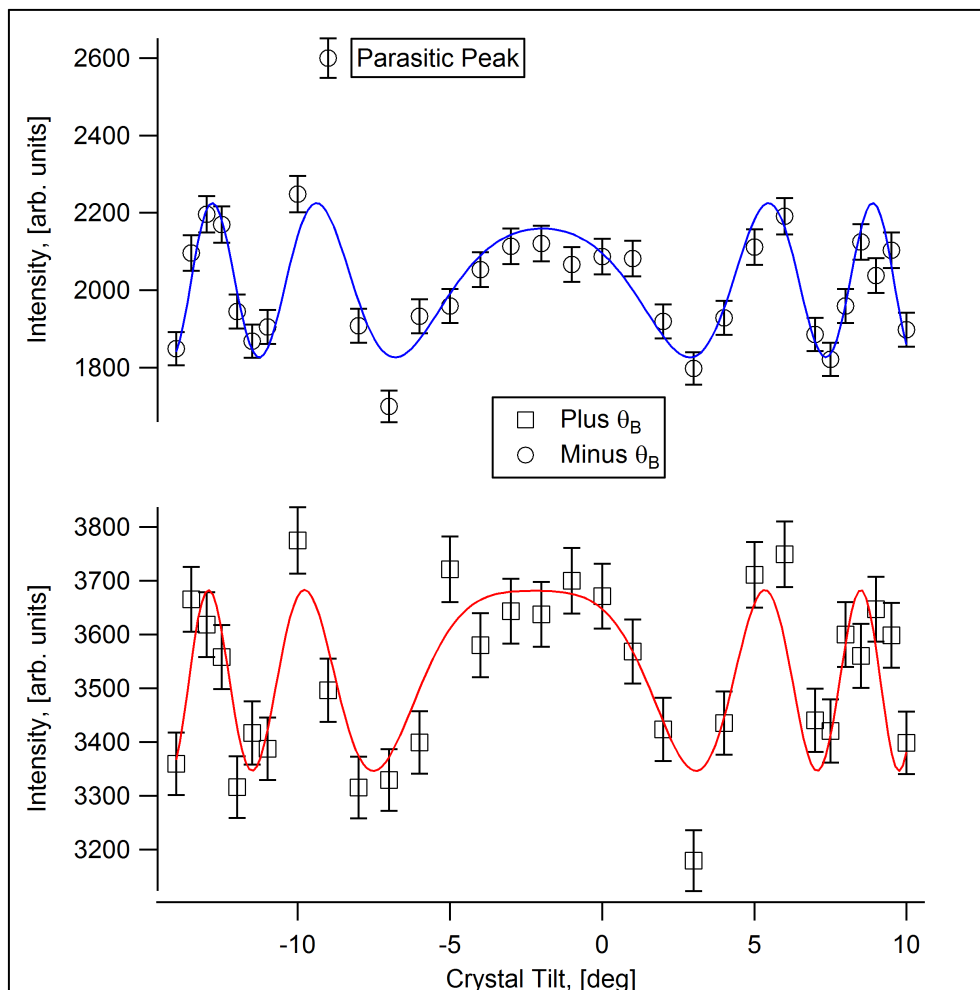
Figure 4.20 Pendellösung interferograms for the (111) reflection using 2.2 Å neutrons. The obvious distortion of the interferogram corresponds to the region where a number of parasitic reflections can occur. The data is fitted with the average phase fixed to that which is predicted by the 4.4 Å interferograms.

interferograms. Even after masking the obvious parasitic peaks within the pendellösung interferogram, the χ^2 sums of weighted residuals of the resulting fits were poor.

To assess whether parasitic reflections were affecting the other pendellösung interferograms, the Bragg conditions for all of the available Bragg vectors were plotted for 2.2 Å and 4.4 Å as a function of θ_B and θ_P. The (220) and (400) pendellösung interferograms were unaffected. Figure 4.21 shows this plot for the (111) reflection. A number of parasitic reflections cross the pendellösung-interfering reflection between $\phi_P = \pm 2.5$ deg for the (111) reflection measured at 4.4 Å. Additionally, the (111) reflection measured with 2.2 Å neutrons shows crossings that are consistent with the observed distortion in the (111) 2.2 Å pendellösung interferograms. Note that the lines in Figure 4.21 are for
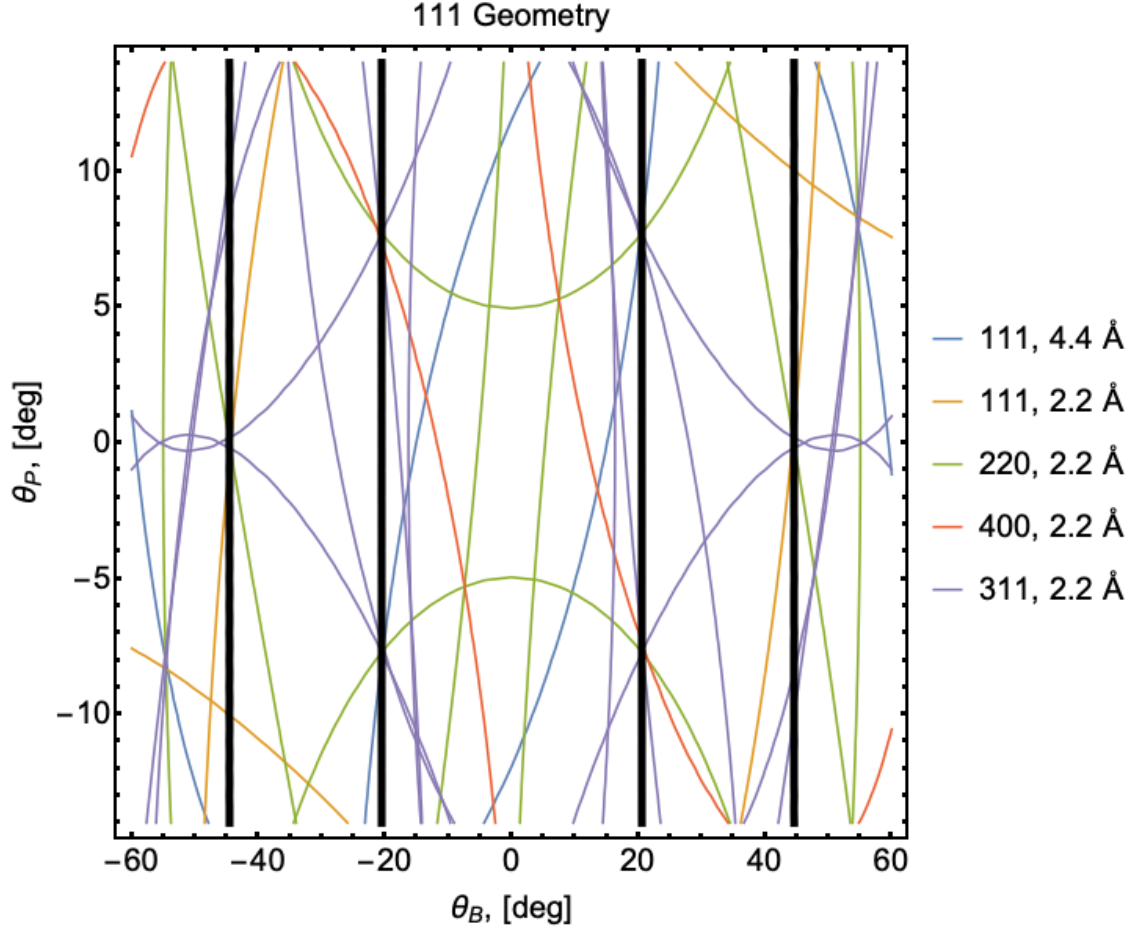
Figure 4.21 Parasitic reflections for the (111) reflection. The black lines refer to the Bragg angles of the experiment. The lines at $\theta_B \sim \pm 20$ deg are for the 2.2 Å component of the beam, while the 4.4 Å component of the beam is located at $\theta_B \sim \pm 45$ deg. Inserting an upstream beryllium filter removes the parasitic reflections that affect the 4.4 Å pendellösung interferograms.

a monochromatic beam. In reality, the complicated shape of the incoming beam's momentum space profile blur the lines on the 0.5 deg angular scale in a way that is difficult to predict.

Fortunately, all of the parasitic reflections that cross the 4.4 Å (111) reflection are from 2.2 Å neutrons. The shorter wavelength was filtered out by placing a beryllium filter upstream, and (111) pendellösung interferograms were remeasured. The resulting oscillations agree with the previous interferograms - except in the portion of the interferogram affected by parasitic reflections. Both data sets were used in the result, but the data set without the beryllium filter was masked in the affected region (Figure 4.22).

This consistency check shifted the resulting (111) measured pendellösung phase shift by about $6\sigma_P$ and improved the χ^2 of the fits. Before the parasitic reflection effect on this experiment was
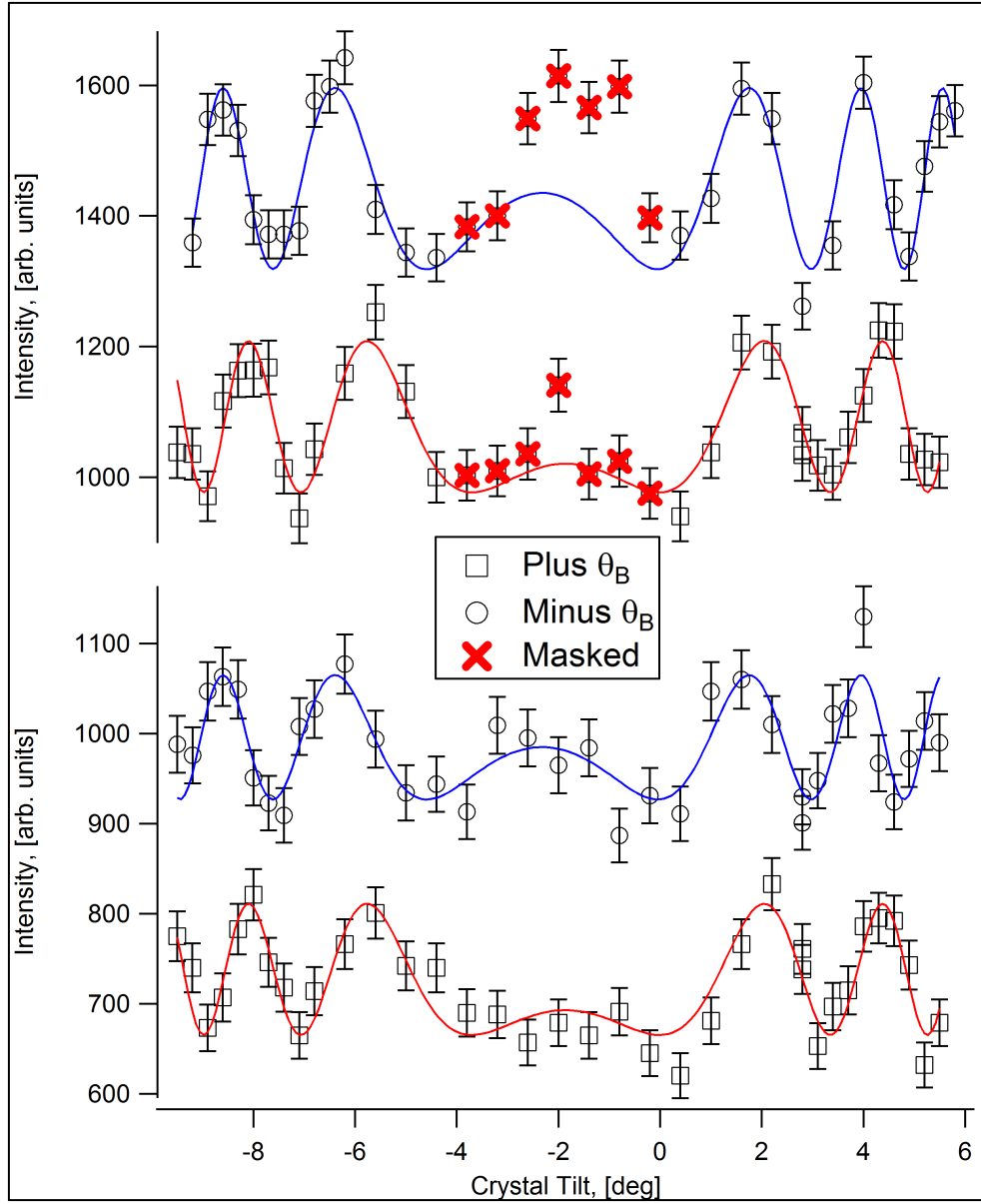
Figure 4.22 Summed pendellösung interferograms for the (111) reflection using $\lambda = 4.4$ Å neutrons. The top pair of curves is with no beryllium filter. The bottom pair is with the beryllium filter in place. The systematic effect of parasitic reflections is clear. A shift in the baseline of some curves was added for clarity.

discovered, the data did not converge on a reasonable region of $\langle r_n^2 \rangle$ and B. Fortunately, after accounting for the parasitic reflections, the results of the experiment converged.

4.4.2 Forward Scattering Measurement

The forward scattering measurement was performed on the same NIOFa beamline. Similar to the pendellösung measurement, data allocation was split between plus and minus θ_B (Figure 4.23). The interferometer phase shift

$$\phi_I = \langle b \rangle \lambda D = \frac{16}{a^2 \sqrt{3}} b(0) D \sin \theta_B \tag{4.117}$$

is proportional to $\sin \theta_B$. The $\sqrt{3}$ in the denominator comes from the fact that the interferometer uses the (111) Bragg reflection. Upon averaging the measured phase shifts, the linear terms in $\delta \theta_B$ again average out, and the quadratic terms are small enough to be neglected. As was the case for the pendellösung interferograms, there is a small systematic uncertainty from the accuracy of the θ_B rotational stage (Table 4.2). The θ_B axis for the interferometer was aligned to be perpendicular to $\vec{H}$ of the interferometer by measuring the angular locations of the plus and minus θ_B Bragg peaks (see Section 4.3.1) as a function of tilt about the θ_T axis (Figure 4.7) of the interferometer. The result is a parabola for $2\theta_B$ as measured by the plus and minus θ_B Bragg peak centroids versus θ_T. The interferometer is brought to the center of this parabola with an estimated uncertainty of 0.04 deg for θ_T, which contributes a negligible uncertainty to θ_B for the plus and minus θ_B interferograms. This is a common alignment technique for Bragg diffracting crystals [RW15].

A forward scattering interferogram is generating by rotating a fused silica phase flag that intersects both beam paths. The phase flag is rotated through a small span in angle (± 1.5 deg), and the difference in optical path length through the phase flag for the two interferometer beam paths is linear in phase flag rotation. This is a standard technique in neutron interferometry [RW15]. The result is a sinusoidal signal which may be fit to

$$\mathcal{I} = A + B \cos \left[C\delta + \phi \right] \tag{4.118}$$

where A, B, C, and ϕ are fit parameters, and δ is the angle of phase flag rotation. The fitted phase of the interferogram is composed of two parts

$$\phi = \phi_0(t) + \phi_I, \tag{4.119}$$

where $\phi_0(t)$ is the intrinsic phase of the interferometer and can drift as a function of time. To isolate the phase shift of the sample, interferograms must be measured with the sample both in and out of the interferometer beam paths (Figure 4.23). The difference in fitted phases of the interferograms is
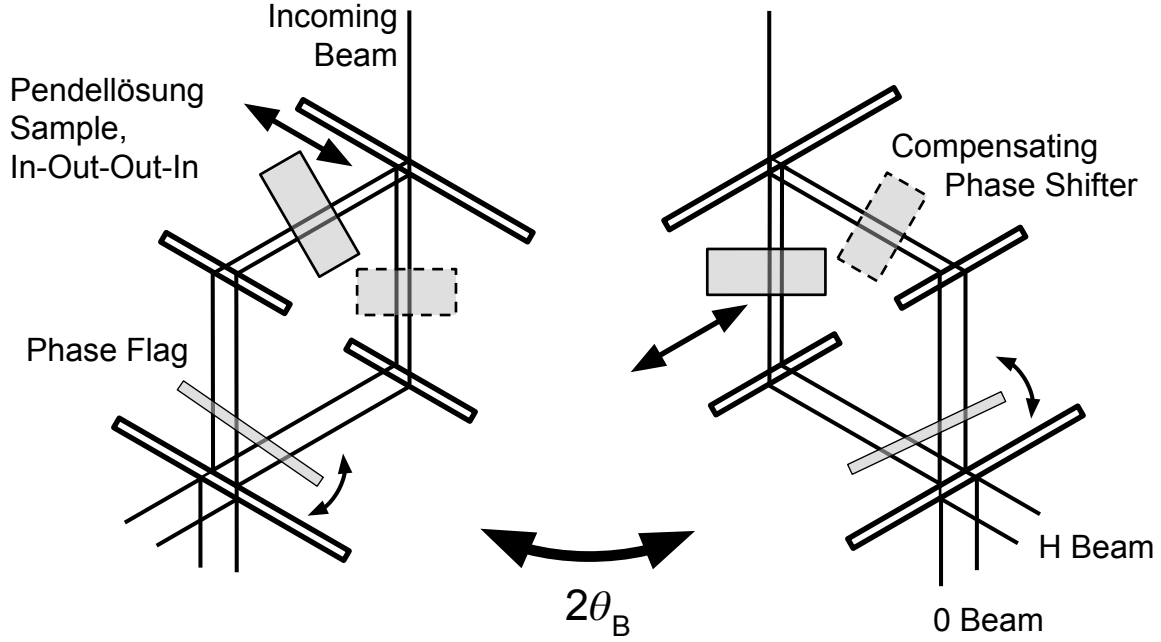
Figure 4.23 The forward scattering phase shift is measured in the same area as the pendellösung interferograms. Half the interferograms are measured at plus and minus θ_B. The angle $2\theta_B$ is measured by an angular encoder embedded in the position stage and used for a wavelength measurement.

then due to the sample. Typical interferograms for the sample in and out of the interferometer are shown in Figure 4.24.

To account for the temporal drifts of $\phi_0(t)$ a series of In-Out-Out-In interferograms are taken. Linear drifts are canceled by this scheme. Additionally, a χ^2 may be computed for each In-Out-Out-In measurement

$$\chi^2 = \sum_{i=1}^{4} \frac{(\phi_i - \bar{\phi} \pm \Delta\bar{\phi})^2}{\sigma_{\phi_i}^2} \tag{4.120}$$

where i indexes the interferogram; σ_ϕ is the uncertainty from fitting the interferogram to Equation 4.118; $\bar{\phi}$ is the average fitted phase of the four measurements; $\Delta\bar{\phi} = (\bar{\phi}_{\text{out}} - \bar{\phi}_{\text{in}})/2$ is the average phase difference; and the $\pm$ sign depends on whether i corresponds to the sample in or out of the interferometer.

The In-Out-Out-In or any drift subtraction scheme breaks down if drifts oscillate too rapidly. To control for this possibility the reduced χ^2 for each In-Out-Out-In sequence (for which there are two degrees of freedom) was computed; if the reduced χ^2 was greater than unity, the uncertainty of the sample phase shift was expanded by a factor of $\sqrt{\chi^2_{\text{red}}} = \sqrt{\chi^2/2}$. For some data points, the error expansion could be quite large. See Figure 4.25.

143
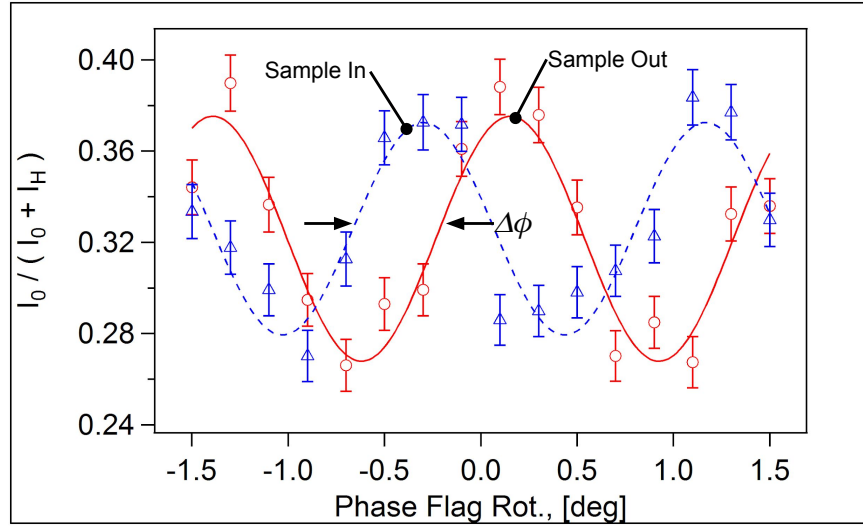
Figure 4.24 Typical sample-in, sample-out interferograms. Uncertainties assume Poisson counting statistics.
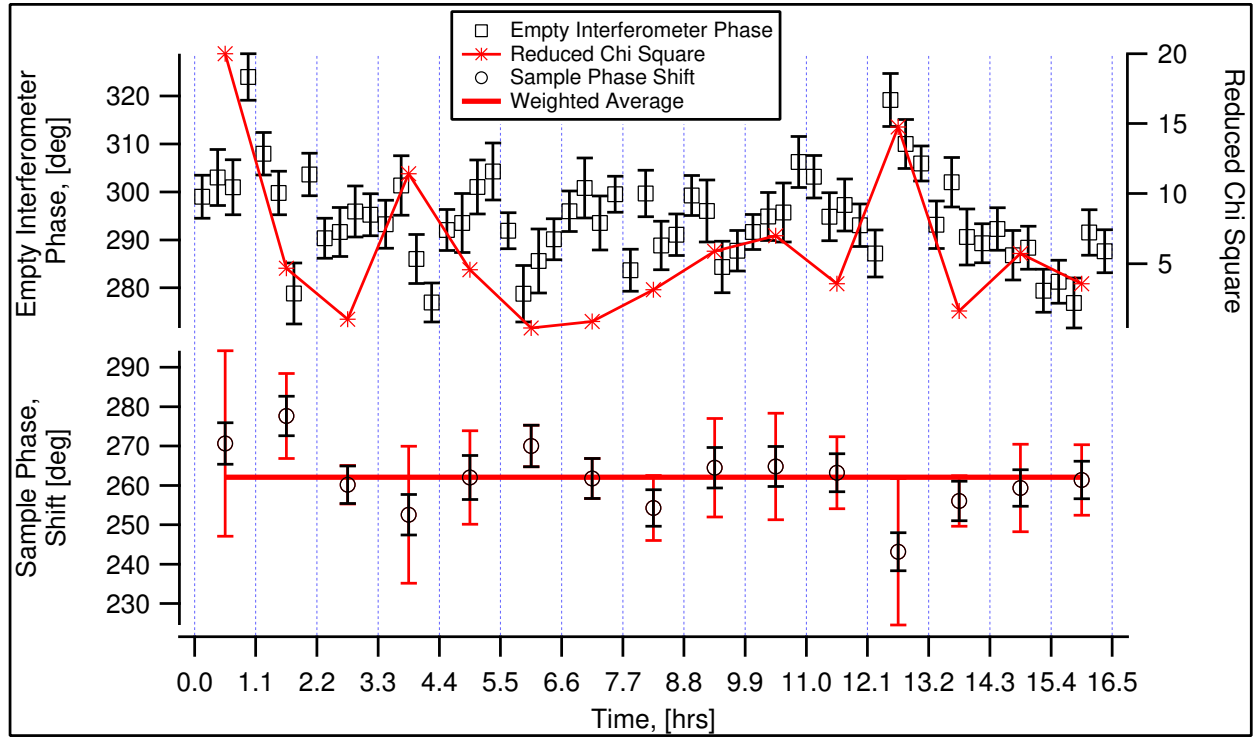
Figure 4.25 Typical interferometer phase and sample phase shifts versus time. Additionally, the reduced χ^2 of each In-Out-Out-In measurement is plotted. The red error bars for the sample phase shift are expanded according the the reduced χ^2. See text for details.

Table 4.2 Uncertainty budget for the forward scattering measurements. The overall phase shift of the sample is approximately 51×10^3 deg.

| Source	Uncertainty	$\Delta\phi_I$ (deg)	$\sigma_I/\phi_I \times 10^5$	hkl
			2.4	111
Crystal Translation	1 mm		2.6	220
			3.8	400
Bragg Stage, θ_B	3×10^{-4} deg		0.7	All
Air Scattering, ϕ_{air}	0.8 deg	105.3 deg	1.6	All
Thermal phase, ϕ_{therm}	0.9 deg	0.6 deg	1.7	All
			3.5	111
Total Sys.			3.5	220
			4.5	400
	1.5 deg		2.9	111
$\boldsymbol{\phi_I}$, **Stat.**	1.5 deg		2.9	220
	1.8 deg		3.5	400
			4.4	111
Total			**4.5**	220
			5.7	400

The overall phase shift of the sample is approximately 51×10^3 deg. Because the phase shift of the sample is proportional to wavelength, averaging the interferogram over the wavelength spread of the interferometer beams causes interference fringe visibility to suffer. This effect becomes more pronounced as the product of the relative wavelength spread of the interferometer and the total phase shift in radians $(\delta\lambda/\lambda)\phi_I$ approaches order one. As a result, sample-in interferograms usually have reduced interference fringe visibility, which increases the total uncertainty of the In-Out-Out-In measurement. The interference fringe visibility of the sample-in and sample-out interferograms were made to be similar by placing a stationary phase compensator in the beam path without the sample, where the phase compensator has a total phase shift of approximately half that of the sample (Figures 4.23 and 4.26b).

In addition to the temporal phase associated with $\phi_0(t)$, there can be a thermal link between the sample and the interferometer. This has been the subject of recent study on the NIOF beamline at the NCNR [Hau p]. As a systematic effect, the thermal link between the sample and the interferometer is particularly damaging, because it depends on whether the sample is in or out of the interferometer. To estimate the size of this effect, series of In-Out-Out-In data sets were taken, but with no sample in the crystal holder. With no material in the beam, the phase shift associated with this measurement

is due only to thermal effects. Initially, the thermal phase was measured to be about 6 deg, which is typical when compared to other thermal phase measurements [Hau p]. To disrupt the thermal link between the sample and the interferometer, a thin layer of aluminum was placed between the sample and the interferometer. This reduced the thermal phase to be less than one degree. The thermal phase was measured in the plus θ_B geometry before measuring the sample phase shifts and again after all the sample phase shifts were measured a few days later, this time in the minus θ_B geometry. The resulting thermal phase measurement was 0.6 ± 0.9 deg, and each forward scattering phase shift was independently corrected by this value. The uncertainty was treated as uncorrelated, because the thermal phase can also drift as a function of time, albeit much more slowly than the intrinsic interferometer phase, as has also been recently demonstrated [Hau p].

All of the interferograms were measured at $\sim 21\,^\circ$C. The lattice constant was taken to be $a = 5.431017$ Å when computing $Db(0)$ from the sample phase shift, with a adjusted to $21\,^\circ$C according to [Kes17]. When taking the ratio of $b(Q)D$ and $b(0)D$, the result was multiplied by a factor of $[1 - 2.6 \times 10^{-6}(1.5)] = (1 - 3.9 \times 10^{-6})$ to correct for the $\sim 1.5\,^\circ$C temperature difference between the pendellösung and interferometer measurements. The relative shift of 3.9×10^{-6} was much smaller than the uncertainties for $b(Q)/b(0)$.

The thickness appearing in Equation 4.117 is the optical thickness. If the crystal slab is misaligned from the beam by some angle ϵ, then the optical thickness is $D/\cos\epsilon \simeq D(1 + \frac{1}{2}\epsilon^2)$. The quadratic dependence of ϵ is utilized to align the sample to the interferometer beam. Before doing the longer set of In-Out-Out-In measurements, the phase shift of the sample is measured as a function of sample tilt (horizontal axis perpendicular to the beam) and rotation (vertical axis). The sample tilt and rotation were set to the central values of the resulting parabolas. The uncertainties for ϵ were on the order of 0.1 deg; the resulting relative change in the sample phase shift of $\sim 1.5 \times 10^{-6}$ is negligible. This is another standard practice in neutron interferometry [RW15].

The height of the pendellösung sample relative to the beam inside of the interferometer was set by tipping off the crystal holder for the forward scattering measurement to the crystal while it was still in the holder for the pendellösung measurement. The horizontal translation of the sample was set by translating a slit in the interferometer beam path for both plus and minus θ_B. Aligning with slits for the forward scattering measurement is easier than for the pendellösung portion of the experiment, because the crystal holder is perpendicular to the beam, alleviating any need for tapered slits. The translational alignment was preserved when switching between the plus and minus θ_B geometries by setting up a fence that was made flush to a plate holding the phase flag and sample positioning stages. The translational alignment was only performed in the (111) geometry, but a set of tapped holes were made in the plate to which the crystal holder was secured, such that the sample could be removed and re-fixed to the mount in a known relative alignment for the portion of the crystal corresponding to the (220) or (400) reflections. The absolute translational accuracy of this method is estimated to be about 1 mm.
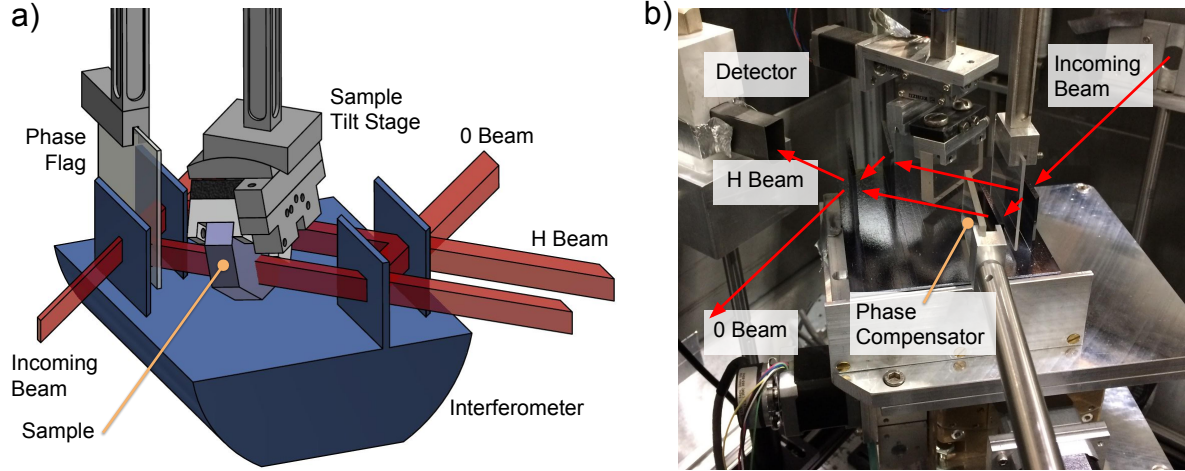
Figure 4.26 Interferometer setup for measuring forward scattering of the pendellösung sample. Shown is (a) a computer model showing the neutron beams and (b) a photograph of the setup. Note the sample being measured in (b) is quartz, not silicon. An aluminum thermal shield was later placed between the interferometer and the sample.

The phase shifts of the (111) and (400) sections agreed within statistics, whereas the (220) section phase shift suggests a thickness difference of 1.7(5) μm. This implies a slight thickness gradient across the crystal, which is why it is important to measure the crystal in the same locations for the pendellösung and forward scattering length measurements. While the interferometer beam profiles are wider than the relevant pendellösung region, the central portion of the interferometer beam has the highest interference fringe visibility. Additionally, the pendellösung sample phase shift was measured with the sample translated over a 2 mm to 4 mm range for all three of the sample sections, and no phase gradients with respect to sample translation were resolvable.

An estimation of how the crystal thickness changes due to an offset of the pendellösung and interferometer beam paths is necessary to compute the systematic uncertainty associated with translational misalignment of the crystal. The pendellösung estimated beam profiles shown as dashed lines in Figure 4.17b were used as a mask and applied to the thickness variation map. The average thickness difference was computed using the profile map as a function of mask translation by pseudo-randomly translating the mask five hundred times according to two dimensional, uncorrelated normal distribution with $\sigma_{\text{trans}} = 1$ mm. The standard deviations of the resulting change in crystal thickness distributions were taken as the crystal thickness uncertainties that occur from translational misalignment of the pendellösung and interferometer beam profiles. The change in thickness uncertainties were 0.24 μm, 0.26 μm, and 0.38 μm for the (111), (220), and (400) sections of the crystal, respectively. The resulting systematic uncertainty in the measured phase shift is the largest systematic uncertainty of the experiment and shown in Table 4.2.

Finally, the measured phase shift has to be corrected by the phase shift of atmosphere in the space occupied by the sample [Iof98; RW15]

$$\phi_{\text{air}} = \langle b \rangle_{\text{air}} \lambda D. \tag{4.121}$$

At 105.3(8) deg, this correction is not small. The uncertainty of the correction is from considering a combination of temperature, which was not as carefully monitored during the forward scattering measurements, barometric pressure, and relative humidity. The uncertainty contributed by that of the scattering lengths of each species is negligible compared to the environmental effects.

It is worth noting that placing the interferometer in vacuum would both help disrupt the thermal coupling between the sample and the interferometer, as well as remove the need for the air scattering correction. It also provides an overall more thermally-stable environment for the interferometer. For these reasons, in-vacuum neutron interferometry is being developed at the NCNR. After a prototype setup showed improved thermal stability [Sag16], a large vacuum chamber has recently been built as a major facility upgrade to the NIOFa beamline.

4.5   Results

Combining the pendellösung and forward scattering phase shifts and their uncertainties provides the measured Q-dependence of the structure factors, given in Table 4.3. Taking after the x-ray community, as more silicon structure factors are measured, this table can be extended. This practice has allowed lattice dynamics researches, for example [Erb13], to test models against readily available diffraction data.

Table 4.3 Measured Q-dependence of structure factors and uncertainties. The (111) anharmonic correction and associated uncertainty is not included. All results are scaled to 295.5 K.

hkl	$b(Q)/b(0) - 1$	Unc. Stat.	Unc. Sys.	Unc. Total
(111)	-0.011 084	0.000 038	0.000 040	0.000 055
(220)	-0.030 216	0.000 059	0.000 036	0.000 069
(400)	-0.060 559	0.000 080	0.000 051	0.000 095

The three measured values of $b(Q)/b(0)$ were fit to

$$\frac{b(Q)}{b(0)} = e^{-B(h^2+l^2+k^2)/(2a)^2} \left(1 - Z\frac{b_{ne}}{b(0)} \right) + f_e(hkl)\frac{b_{ne}}{b(0)} \tag{4.122}$$

where $b_{ne} = \langle r_n^2 \rangle / (86.34 \text{ fm})$ and B are fit parameters that may also be constrained by adding their weighted residuals to the χ^2 minimization, given values and uncertainties. The experiment is only sensitive to the coherent scattering length $b(0)$ at the 1 % level, though $b(0)$ has been measured at the 5×10^{-5} level [Iof98]. The $f_e(hkl)$ are the x-ray structure factors at room temperature, taken directly from diffraction data averages [CH88]. Like the coherent scattering length, the uncertainties in the $f_e(hkl)$ charge densities are much better than is required of this experiment. The fit function is written in such a way that the fitted Debye-Waller factor does not interfere with the measured $f_e(hkl)$, as there has been some speculation that the mean square displacements of the electrons are different for each shell [DH85].

The χ^2-surface with B and $\langle r_n^2 \rangle$ both allowed to vary is shown in Figure 4.27. For comparison, the PDG recommended value and uncertainty for $\langle r_n^2 \rangle$ is shown. Also shown is the lattice dynamical result from fitting neutron inelastic scattering data to a BvK model [FS99]. Note that [FS99] gives formulae for computing B as a function of temperature, so the result was easily scaled from 293 to 295.5 K, in which case $B_{\text{BvK}} = 0.4725(17)$ Å^2. Recent advances in neutron inelastic scattering data, as well as fully anharmonic lattice dynamical models [HA13], have recently shown that simpler models are insufficient for silicon. This is in part due to silicon's negative thermal expansion at low temperatures, which continues to effect lattice dynamics when the thermal expansion is positive at room temperature [Kim15; Kim18]. If this is taken as evidence that the BvK value for B may not be correct, then the value of B measured in this experiment should be checked against predictions for B by various lattice dynamical models. When analyzing the data in the interest of learning something about lattice dynamics, a weighted residual for $\langle r_n^2 \rangle$ based on the PDG recommended value and uncertainty may be added to the χ^2 minimization. If this approach is taken, then $B = 0.47711(70)$ Å^2. Considering the $2.5\,\sigma$ discrepancy, the pendellösung and BvK values do not quite agree with one another.

The anharmonic correction for the (111) reflection is computed using the measured (222) structure factor at room temperature [Rob74] as described in Section 4.2.2; the correction is about one half of the total uncertainty. Because the strength of the anharmonic correction is proportional to $h \times k \times l$, measurement of higher-order odd reflections would be very sensitive to the anharmonic term. This may be useful for comparing measured structure factors to anharmonic lattice dynamical models for silicon. Note that the uncertainty of the anharmanic correction has been expanded by a factor of three from the uncertainty reported in [Rob74], on account of the fact that the measured $f_{\text{anh}}(222)$ at room temperature does not fit the temperature-dependent model [FS99].

The fitted value for the mean square neutron charge radius (allowing B to vary) is $\langle r_n^2 \rangle = -0.1088(93)$ fm^2. This is in agreement with the PDG value of $-0.1161(22)$ fm^2 within statistics. Most of the measurements that make up the PDG value are from epithermal neutron transmission in lead or bismuth [Kop97; Tan18]. One experiment measured a scattering asymmetry of thermal neutrons from a few noble gasses [KR66; KR73]. As pointed out by [SL02], pendellösung interferometery has
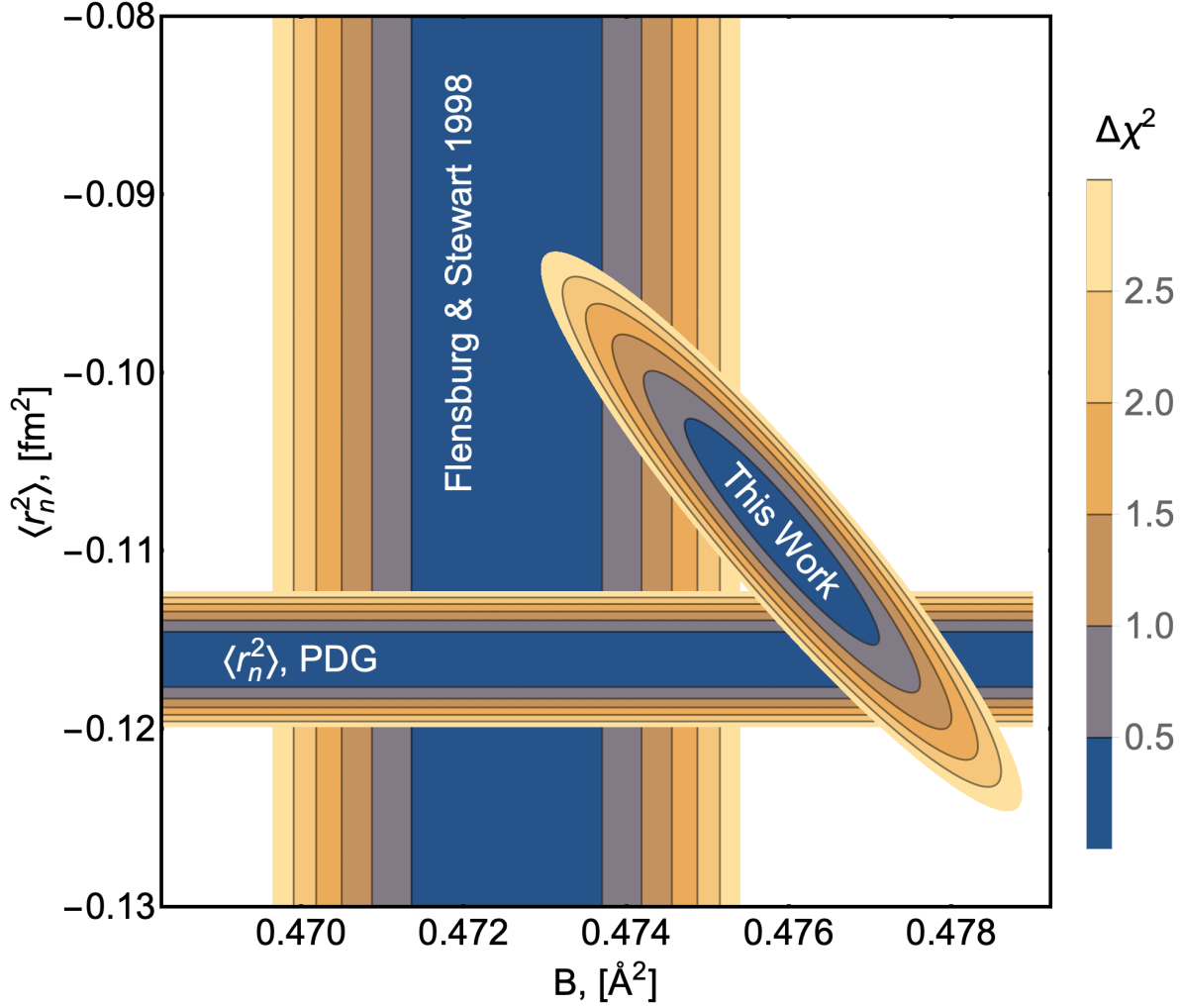
Figure 4.27 $\Delta\chi^2$ surface for the neutron charge radius and silicon Debye Waller B parameter, compared to the PDG value for the charge radius and the value of B from [FS99].

very different systematic uncertainties from the other experiments making up the PDG value for $\langle r_n^2 \rangle$. While this experiment will not lower the uncertainty of the neutron charge radius, the agreement of this experiment with the PDG value is nonetheless encouraging.

If the improved neutron inelastic scattering data and lattice dynamical models can be used to compute B to a high degree of certainty, then it may be possible to constrain B in the fit, leading to an improved uncertainty for $\langle r_n^2 \rangle$. Measurement of more structure factors would also improve the uncertainty in the charge radius measurement. Additionally, an effort to measure the (111), (220), and (400) structure factors in a germanium sample is already underway at the NCNR. If these measurements are added to the fit, then the resulting uncertainty in $\langle r_n^2 \rangle$ is predicted to be on the order of 0.005 fm^2.
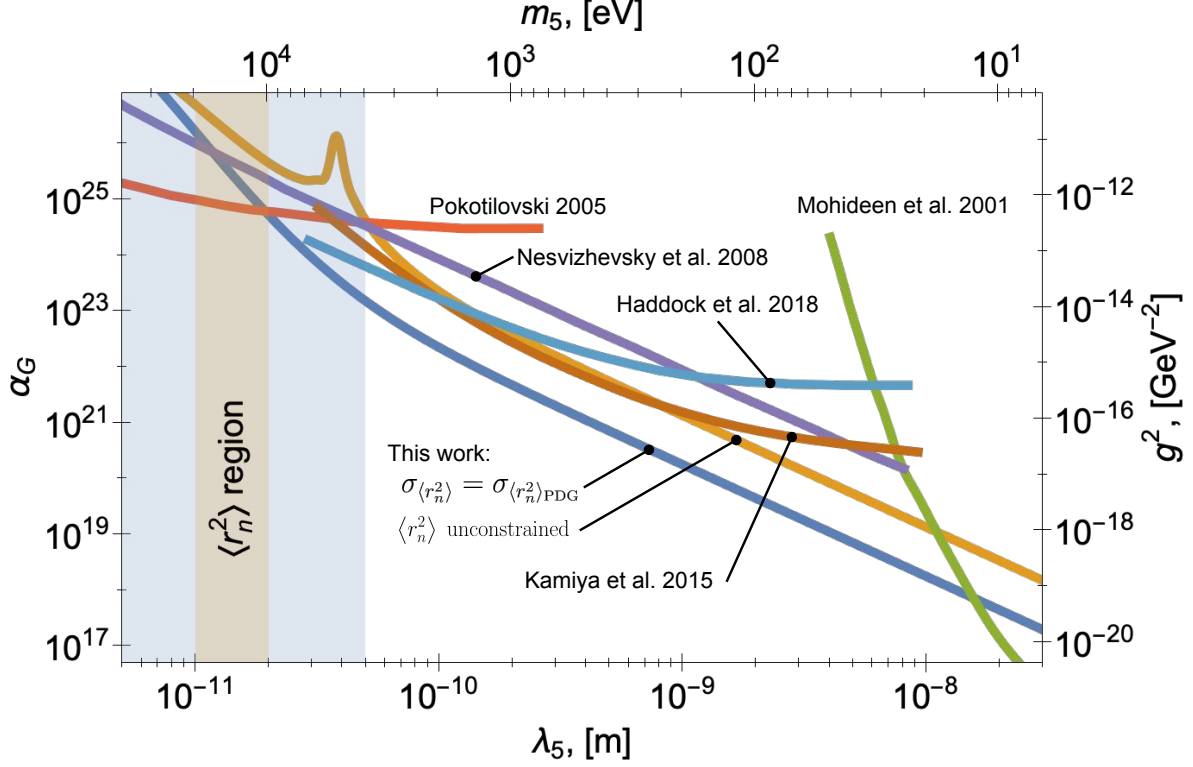
Figure 4.28 Experimental limits (90% confidence interval) on the coupling strength of a BSM force mediator that couples to mass. Area above the lines excluded. Shown are limits assuming the PDG value and uncertainty for the neutron charge radius, as well as limits where $\langle r_n^2 \rangle$ is unconstrained. The region on the plot where the electronic and BSM form factors have a similar shape is shaded. This is well-illustrated by the bump in the limit with the charge radius unconstrained. Each experiment making up the PDG charge radius value would also have a bump, the location of which depends on the mass and charge of the scattering target, as well as the Q-range of the experiment.

4.5.1 Limits on Ångström-Scale Fifth Forces

The data was also used to constrain the coupling strength of a BSM force mediator with length scale $\lambda_5 = 1/m_5$ and coupling to mass g^2, which may also be written relative to the strength of gravity using the dimensionless parameter α_G. See Section 4.2.3.3. Limits are again computed by minimizing the χ^2 sum of weighted residuals. This is repeated with values of λ_5 fixed (see Equation 4.52), resulting in the 90% confidence exclusion plot shown in Figure 4.28. For this analysis a residual for B was added to the χ^2, with $B = 0.475(15)$, the large uncertainty of which encompasses the somewhat disparate set of B from x-ray measurements [Spa86], as well as the BvK lattice dynamical value [FS99].

The decision of whether to constrain the neutron charge radius is more difficult. Any given experiment that is sensitive to the neutron charge radius may be "fooled" out of measuring a fifth
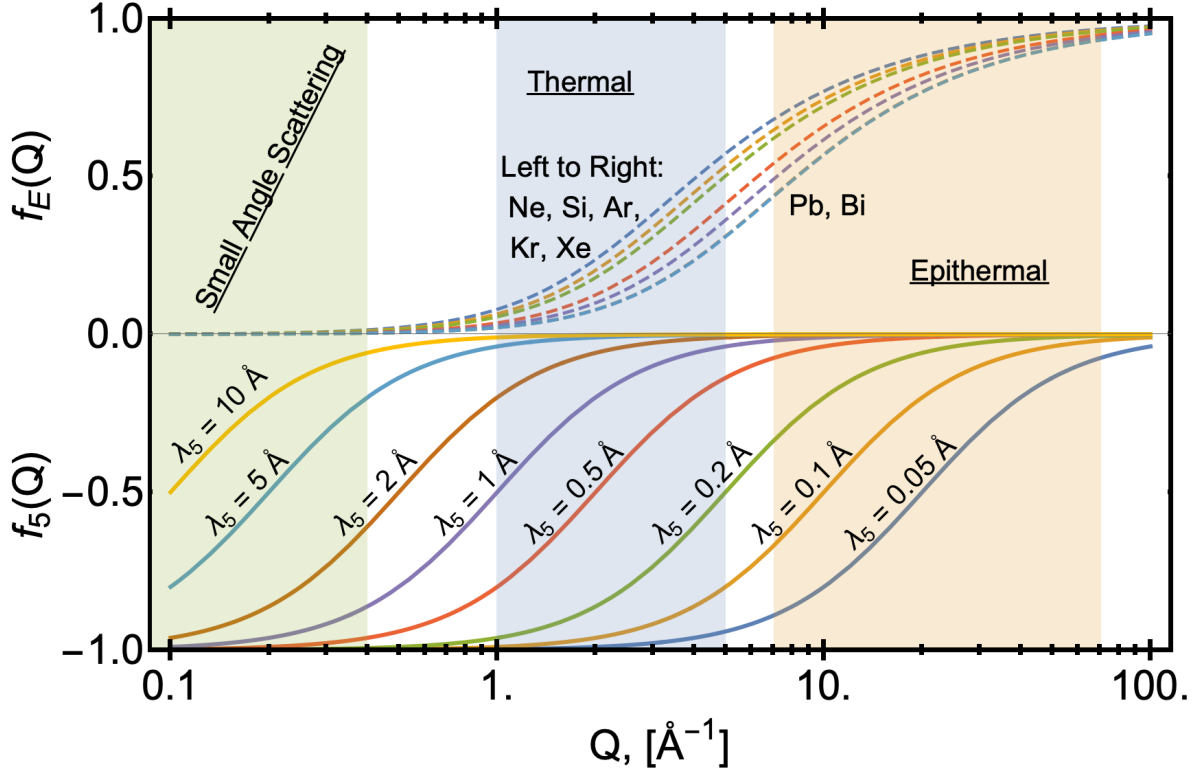
Figure 4.29 Similarity between the shape of the atomic and BSM form factors. The relevant Q-regions are shown for each experiment. Note that the bismuth and lead atomic form factors are indistinguishable on this plot. The ability to distinguish between electronic scattering and a BSM force mediator depends on the Q-range and variety of measured atomic numbers and masses.

force if the structure function of the BSM force mediator and the atomic form factors have a similar shape over the Q-range relevant to the experiment. An illustration of how this could happen is shown in Figure 4.29. For illustrative purposes the electric form factors are estimated given the form in [Sea86], and the form factors are all normalized. The atomic form factors f_E will scale with the atomic number of the target Z and the BSM form factors f_5 will scale with the mass of the target M. Taking measurements over a range of scattering target atomic numbers Z and mass M can help distinguish between the two types of form factors. An experimental program to measure noble gas scattering over a very large range of Q is now underway at Japan Proton Accerator Research Complex (J-PARC) to help distinguish between these effects, as well as measure the neutron charge radius [Hadbm].

Limits on the coupling strength of a BSM force mediator from this experiment compared to previous experiments is shown in Figure 4.28. Two limits are shown. One with $\langle r_n^2 \rangle$ unconstrained and one with $\langle r_n^2 \rangle$ constrained by the PDG value and uncertainty. The effect of the structure factor

shapes can be seen clearly as the spike at $\lambda_5 \simeq 0.3$ Å. The spike is in the long length scale portion of the region labelled $\langle r_n^2 \rangle$. The center of this region corresponds to the approximate danger zone for the lead and bismuth measurements which make up most of the experiments that have measured the neutron charge radius.

There is seemingly not a standard for how to constrain $\langle r_n^2 \rangle$ for the experiments in Figure 4.28. Kamiya et al. 2015 [Kam15] constrains $\langle r_n^2 \rangle$ with the PDG value and uncertainty, as does Haddock et al. 2015 [Had18]. Both of these experiments use small angle scattering from noble gasses to determine their limits. The approximate Q-range for small angle scattering is identified in Figure 4.29. The Pokotilovski 2005 [Pok13] limit is a retro analysis of lead and bismuth scattering data, and has the most competitive limit below 0.2 Å. The author relies on previous neutron charge radius measurements, but does increase the associated uncertainty in $\langle r_n^2 \rangle$.

In any case, the fact that $\langle r_n^2 \rangle$ agrees between experiments that probe different length scales with a disparate set of Z and M scattering targets, suggests that it is fair to constrain $\langle r_n^2 \rangle$ to the PDG value and uncertainty when placing limits on a BSM force mediator. This is certainly the case outside of the $\langle r_n^2 \rangle$ region in Figure 4.28. With all this taken into account, pendellösung interferometry has improved current limits for g^2 by about an order of magnitude over a range of λ_5 that spans almost three orders of magnitude. Pendellösung measurements with germanium are expected additionally improve limits by a factor five. Simulations indicate that whether $\langle r_n^2 \rangle$ is constrained will make little difference, because the BSM form factor cannot mimic the atomic form factors of both silicon and germanium over the relevant range in Q.

4.6   Conclusion

Pendellösung interferometry is a very sensitive probe of lattice dynamics, the neutron charge radius, and BSM physics on the ångström length scale. Extension of the experiment to more structure factors and other scattering species will further all three areas of interest. Following the example of x-ray scattering, where structure factors as large as $(12\,12\,0)$ have been measured [Spa86; CH88], a complete set of neutron structure factors for silicon and germanium would have a deep impact on a wide range of physics. In regards to x-rays, some difficulty exists in distinguishing between contributions to the x-ray structure factors from the electron density and thermal smearing [Deu89]. Because neutrons mainly scatter from the nuclei, most of the Q-dependence in the neutron structure factors is from the DWF. It will be intriguing to see whether B as measured in this experiment can help x-ray scattering experiments distinguish between the two effects, elucidating a more exact measure of the electron density in silicon.

Measuring structure factors over a wide range of temperatures would provide relevant checks to lattice dynamical models. In particular, it would be interesting to measure high-order, odd structure factors in silicon at colder temperatures. The anharmonic contribution to these structure factors

are related to the cubic force constants which in turn are the principle *cause* of the anomalous thermal expansion of silicon. Recent work suggests that the success of the quasi-harmonic theory for predicting the thermal expansion of the silicon was caused by a fortuitous cancellation of errors within the theory [Kim18]. It may be possible for neutron pendellösung interferometry to weigh in on these new results.

In regards to the near future of neutron pendellösung interferometry, the measurement of the (111), (220), and (400) germanium structure factors is already underway. The germanium experiment is expected to improve limits on the coupling strength of a BSM force mediator by a factor of five. The measurement of structure factors at higher Q will require shifting to a neutron beamline with a slightly shorter wavelength ($\lambda \sim 1$ Å to 2 Å) than what is available at NIOFa. In any case, neutron pendellösung interferometry as first proposed by Sparenberg and Leeb [SL02] has exceeded expectations in the amount of relevant physics that it probes. With only three neutron structure factors in a single material having now been measured with precision, the future of pendellösung interferometry is very bright.

The End.

BIBLIOGRAPHY

[Abo02] Abov, Y. G. et al. "Dynamical neutron diffraction on perfect crystals". *Physics of Atomic Nuclei* **65**.11 (2002), pp. 1933–1979.

[AH73] Aldred, P. & Hart, M. "The electron distribution in silicon-I. Experiment". *Proc. R. Soc. Lond. A* **332**.1589 (1973), pp. 223–238.

[Ale88] Alekseev, V. et al. "Gravitational effect in neutron diffraction by a curved quartz single crystal". *Zh. Eksp. Teor. Fiz* **94**.37 (1988), pp. 1–383.

[All00] Allman, B. et al. "Imaging: phase radiography with neutrons". *Nature* **408**.6809 (2000), p. 158.

[AHD02] Arkani-Hamed, N. & Dimopoulos, S. "New origin for approximate symmetries from distant breaking in extra dimensions". *Physical Review D* **65**.5 (2002), p. 052003.

[Art85] Arthur, J et al. "Dynamical neutron diffraction in a thick-crystal interferometer". *Physical Review B* **32**.9 (1985), p. 5753.

[Atw84] Atwood, D. et al. "Neutron phase shift in a rotating two-crystal interferometer". *Physical Review Letters* **52**.19 (1984), p. 1673.

[Bal83] Balkanski, M et al. "Anharmonic effects in light scattering due to optical phonons in silicon". *Physical Review B* **28**.4 (1983), p. 1928.

[Bar05] Barker, J. et al. "Design and performance of a thermal-neutron double-crystal diffractometer for USANS at NIST". *Journal of Applied Crystallography* **38**.6 (2005), pp. 1004–1011.

[BT82] Bonse, U & Teworte, R. "Spherical Wave Treatment of Laue Case Rocking Curves". *Zeitschrift für Naturforschung A* **37**.5 (1982), pp. 427–432.

[Bon77] Bonse, U et al. "Oscillatory structure of laue case rocking curves". *physica status solidi (a)* **43**.2 (1977), pp. 487–492.

[Bro17] Brooks, A. J. et al. "Neutron Imaging of Laser Melted SS316 Test Objects with Spatially Resolved Small Angle Neutron Scattering". *Journal of Imaging* **3**.4 (2017), p. 58.

[Bro18] Brooks, A. J. et al. "Neutron interferometry detection of early crack formation caused by bending fatigue in additively manufactured SS316 dogbones". *Materials & Design* **140** (2018), pp. 420–430.

[Bur11] Burvall, A. et al. "Phase retrieval in X-ray phase-contrast imaging suitable for tomography". *Optics express* **19**.11 (2011), pp. 10359–10376.

[But18]   Butch, N. personal communication. 2018.

[Col75]   Colella, R. et al. "Observation of gravitationally induced quantum interference". *Physical Review Letters* **34**.23 (1975), p. 1472.

[CH88]   Cummings, S & Hart, M. "Redetermination of absolute structure factors for silicon at room and liquid nitrogen temperatures". *Australian Journal of Physics* **41**.3 (1988), pp. 423–432.

[Dav07]   David, C et al. "Fabrication of diffraction gratings for hard X-ray phase contrast imaging". *Microelectronic Engineering* **84**.5-8 (2007), pp. 1172–1177.

[DW67]   Dawson, B & Willis, B. "Anharmonic vibration and forbidden reflexions in silicon and germanium". *Proc. R. Soc. Lond. A* **298**.1454 (1967), pp. 307–315.

[DS18]   DeBeer-Schmitt, L. M. et al. "Realization of magnetic skyrmions in thin films at ambient conditions". *Under Review* (2018).

[DH85]   Deutsch, M & Hart, M. "A new approach to the measurement of X-ray structure amplitudes determined by the Pendellösung method". *Acta Crystallographica Section A* **41**.1 (1985), pp. 48–55.

[Deu89]   Deutsch, M. et al. "Thermal motion of atoms in crystalline silicon: Beyond the Debye theory". *Physical Review B* **40**.17 (1989), p. 11666.

[Dom01]   Dombeck, T et al. "Measurement of the neutron reflectivity for Bragg reflections off a perfect silicon crystal". *Physical Review A* **64**.5 (2001), p. 053607.

[Dvi11]   Dvir, T. et al. "Nanotechnological strategies for engineering complex tissues". *Nature nanotechnology* **6**.1 (2011), p. 13.

[Ede91]   Eder, K. et al. "Diffraction of very cold neutrons at phase gratings". *Physica B: Condensed Matter* **172**.3 (1991), pp. 329–338.

[Erb13]   Erba, A. et al. "Accurate dynamical structure factors from ab initio lattice dynamics: The case of crystalline silicon". *Journal of computational chemistry* **34**.5 (2013), pp. 346–354.

[Esk09]   Eskildsen, M. et al. "Vortices in superconducting Ba (Fe 0.93 Co 0.07) 2 As 2 studied via small-angle neutron scattering and Bitter decoration". *Physical Review B* **79**.10 (2009), p. 100501.

[Fay07]   Fayet, P. "U-boson production in e+ e- annihilations, ψ and Y decays, and Light Dark Matter". *Physical Review D* **75**.11 (2007), p. 115017.

[FV18]   Fedorov, V. & Voronin, V. "Modern Status of Searches for nEDM, Using Neutron Optics and Diffraction in Noncentrosymmetric Crystals". *Proceedings of the International Conference on Neutron Optics (NOP2017)*. 2018, p. 011007.

[Fed10]   Fedorov, V. et al. "Measurement of the neutron electric dipole moment via spin rotation in a non-centrosymmetric crystal". *Physics Letters B* **694**.1 (2010), pp. 22–25.

[Fin87]   Finkelstein, K. D. "Neutron spin-pendellösung resonance". PhD thesis. Massachusetts Institute of Technology, 1987.

[FS99]   Flensburg, C. & Stewart, R. F. "Lattice dynamical Debye-Waller factor for silicon". *Physical Review B* **60**.1 (1999), p. 284.

[GC11]   Gentile, T. R. & Crawford, C. "Neutron charge radius and the neutron electric form factor". *Physical Review C* **83**.5 (2011), p. 055203.

[Gil18]   Gilbert, D. personal communication. 2018.

[Gli98]   Glinka, C. et al. "The 30 m small-angle neutron scattering instruments at the National Institute of Standards and Technology". *Journal of Applied Crystallography* **31**.3 (1998), pp. 430–445.

[GG07]   Greene, G. L. & Gudkov, V. "Neutron interferometric method to provide improved constraints on non-Newtonian gravity at the nanometer scale". *Physical Review C* **75**.1 (2007), p. 015501.

[Grü08]   Grünzweig, C et al. "Design, fabrication, and characterization of diffraction gratings for neutron phase contrast imaging". *Review of Scientific Instruments* **79**.5 (2008), p. 053703.

[GSF12]   Guizar-Sicairos, M. & Fienup, J. R. "Understanding the twin-image problem in phase retrieval". *JOSA A* **29**.11 (2012), pp. 2367–2375.

[Haa14]   Haan, V.-O. de et al. "Measurement of gravitation-induced quantum interference for neutrons in a spin-echo spectrometer". *Physical Review A* **89**.6 (2014), p. 063611.

[Hadbm]   Haddock, C et al. "A search for deviations from the inverse square law of gravity at nm range using a pulsed neutron beam" (submitted).

[Had18]   Haddock, C. C. et al. "Search for deviations from the inverse square law of gravity at nm range using a pulsed neutron beam". *Physical Review D* **97**.6 (2018), p. 062002.

[Har66]   Hart, M. "Pendellösung fringes in elastically deformed silicon". *Zeitschrift für Physik* **189**.3 (1966), pp. 269–291.

[Har17]   Harti, R. P. et al. "Sub-pixel correlation length neutron imaging: Spatially resolved scattering information of microstructures on a macroscopic scale". *Scientific Reports* **7** (2017), p. 44588.

[HB75]   Hastings, J. & Batterman, B. "High-order anharmonic forbidden neutron reflections in silicon". *Physical Review B* **12**.12 (1975), p. 5580.

[Hat65]   Hattori, H. et al. "Absolute Measurement of Structure Factors of Si Single Crystal by Means of X-Ray Pendellösung Fringes". *Journal of the Physical Society of Japan* **20**.6 (1965), pp. 988–996.

[Hau p]   Haun, R. et al. "Sample Induced Thermal Gradient Effects in Neutron Interferometry" (In preparation).

[Hea17]   Heacock, B. et al. "Neutron interferometer crystallographic imperfections and gravitationally induced quantum interference measurements". *Phys. Rev. A* **95** (1 2017), p. 013840.

[Hea18a]   Heacock, B et al. "Optimization of neutron diffraction from phase-gratings". *arXiv preprint arXiv:1812.07097* (2018).

[Hea18b]   Heacock, B et al. "Sub-micrometer resolution neutron tomography". *arXiv preprint arXiv:1808.07476* (2018).

[Hea18c]   Heacock, B. et al. "Increased interference fringe visibility from the post-fabrication heat treatment of a perfect crystal silicon neutron interferometer". *Review of Scientific Instruments* **89**.2 (2018), p. 023502.

[Hea p]   Heacock, B. et al. "Measurement and alleviation of subsurface damage in a thick-crystal neutron interferometer" (In preparation).

[HA13]   Hellman, O. & Abrikosov, I. A. "Temperature-dependent effective third-order interatomic force constants from first principles". *Physical Review B* **88**.14 (2013), p. 144301.

[Hor88]   Horne, M. A. et al. "Neutron spin-pendellösung resonance". *Physica B+ C* **151**.1-2 (1988), pp. 189–192.

[Hus16]   Hussey, D. S. et al. "Demonstration of a white beam far-field neutron interferometer for spatially resolved small angle neutron scattering". *arXiv preprint arXiv:1606.03054* (2016).

[Hus17]   Hussey, D. S. et al. "Neutron imaging detector with 2 μm spatial resolution based on event reconstruction of neutron capture in gadolinium oxysulfide scintillators". *Nuclear Instruments and Methods in Physics Research Section A: Accelerators, Spectrometers, Detectors and Associated Equipment* **866** (2017), pp. 9–12.

[Iof98]   Ioffe, A et al. "Precision neutron-interferometric measurement of the coherent neutron-scattering length in silicon". *Physical Review A* **58**.2 (1998), p. 1475.

[Isg99]   Isgur, N. "Interpreting the Neutron's Electric Form Factor: Rest Frame Charge Distribution or Foldy Term?" *Physical review letters* **83**.2 (1999), p. 272.

[Ito18]   Itoh, S. et al. "Pendellösung interferometry by using pulsed neutrons". *Nuclear Instruments and Methods in Physics Research Section A: Accelerators, Spectrometers, Detectors and Associated Equipment* **908** (2018), pp. 78–81.

[Jae05]   Jaekel, M. R. et al. "New developments in cold neutron storage with perfect crystals". *Nuclear Instruments and Methods in Physics Research Section A: Accelerators, Spectrometers, Detectors and Associated Equipment* **539**.1-2 (2005), pp. 335–344.

[Jas07]   Jasinevicius, R. G. et al. "In-situ raman spectroscopy analysis of re-crystallization annealing of diamond turned silicon crystal". *Journal of the Brazilian Society of Mechanical Sciences and Engineering* **29**.1 (2007), pp. 49–54.

[Jer96]   Jericha, E et al. "Performance of an improved perfect crystal neutron storage cavity". *Nuclear Instruments and Methods in Physics Research Section A: Accelerators, Spectrometers, Detectors and Associated Equipment* **379**.2 (1996), pp. 330–334.

[Kam15]   Kamiya, Y et al. "Constraints on new gravitylike forces in the nanometer range". *Physical review letters* **114**.16 (2015), p. 161101.

[Kat61a]   Kato, N. "A theoretical study of pendellösung fringes. I. general considerations". *Acta Crystallographica* **14**.5 (1961), pp. 526–532.

[Kat61b]   Kato, N. "A theoretical study of pendellösung fringes. II. Detailed discussion based upon a spherical wave theory". *Acta Crystallographica* **14**.6 (1961), pp. 627–636.

[Kat63]   Kato, N. "Pendellösung fringes in distorted crystals i. fermat's principle for bloch waves". *Journal of the Physical Society of Japan* **18**.12 (1963), pp. 1785–1791.

[Kat64a]   Kato, N. "Pendellösung fringes in distorted crystals II. Application to two-beam cases". *Journal of the Physical Society of Japan* **19**.1 (1964), pp. 67–77.

[Kat64b]   Kato, N. "Pendellösung Fringes in Distorted Crystals III. Application to homogeneously bent crystals". *Journal of the Physical Society of Japan* **19**.6 (1964), pp. 971–985.

[KL59]   Kato, N. & Lang, A. "A study of pendellösung fringes in X-ray diffraction". *Acta Crystallographica* **12**.10 (1959), pp. 787–794.

[KF11]   Kawano-Furukawa, H et al. "Gap in KFe 2 As 2 studied by small-angle neutron scattering observations of the magnetic vortex lattice". *Physical Review B* **84**.2 (2011), p. 024507.

[Kea71]   Keating, D. et al. "Forbidden (222) Neutron Reflection in Silicon: Anharmonicity and the Bonding Electrons". *Physical Review B* **4**.8 (1971), p. 2472.

[Kes17]   Kessler, E. G. et al. "The lattice spacing variability of intrinsic float-zone silicon". *J. Res. NIST* **122** (2017).

[Kik78]   Kikuta, S. et al. "Construction of Two Crystal Component Neutron Interferometer". *Journal of the Physical Society of Japan* **45**.2 (1978), pp. 715–716.

[Kim15]   Kim, D. et al. "Phonon anharmonicity in silicon from 100 to 1500 K". *Physical Review B* **91**.1 (2015), p. 014307.

[Kim18]   Kim, D. et al. "Nuclear quantum effect with pure anharmonicity and the anomalous thermal expansion of silicon". *Proceedings of the National Academy of Sciences* **115**.9 (2018), pp. 1992–1997.

[Kop97]   Kopecky, S et al. "Neutron charge radius determined from the energy dependence of the neutron transmission of liquid 208 Pb and 209 Bi". *Physical Review C* **56**.4 (1997), p. 2229.

[Kri05]   Krimmel, S et al. "Discrete tomography for reconstruction from limited view angles in non-destructive testing". *Electronic Notes in Discrete Mathematics* **20** (2005), pp. 455–474.

[KR66]   Krohn, V. & Ringo, G. "Measurement of the electron-neutron interaction by the Asymmetrical scattering of thermal neutrons by noble gases". *Physical Review* **148**.4 (1966), p. 1303.

[KR73]   Krohn, V. & Ringo, G. "Reconsideration of the Electron-Neutron Scattering Length As Measured by the Scattering of Thermal Neutrons by Noble Gases". *Physical Review D* **8**.5 (1973), p. 1305.

[Kul94]   Kulda, J. et al. "Inelastic-neutron-scattering study of phonon eigenvectors and frequencies in Si". *Physical Review B* **50**.18 (1994), p. 13347.

[LaM17]   LaManna, J. et al. "Neutron and X-ray Tomography (NeXT) system for simultaneous, dual modality tomography". *Review of Scientific Instruments* **88**.11 (2017), p. 113702.

[LG09]   Lamoreaux, S. & Golub, R. "Experimental searches for the neutron electric dipole moment". *Journal of Physics G: Nuclear and Particle Physics* **36**.10 (2009), p. 104002.

[Lan08]   Langer, M. et al. "Quantitative comparison of direct phase retrieval algorithms in in-line phase tomography". *Medical physics* **35**.10 (2008), pp. 4556–4566.

[Lem13]   Lemmel, H. "Influence of Bragg diffraction on perfect crystal neutron phase shifters and the exact solution of the two-beam case in the dynamical diffraction theory". *Acta Crystallographica Section A: Foundations of Crystallography* **69**.5 (2013), pp. 459–474.

[Lit97]   Littrell, K. et al. "Two-wavelength-difference measurement of gravitationally induced quantum interference phases". *Physical Review A* **56**.3 (1997), p. 1767.

[Lit98]   Littrell, K. et al. "The effects of dynamical diffraction on the measurement of gravitationally induced quantum phase shifts by neutron interferometry". *Acta Crystallographica Section A: Foundations of Crystallography* **54**.5 (1998), pp. 563–580.

[Lov84]   Lovesey, S. W. *Theory of neutron scattering from condensed matter.* 1984.

[Lyn12]   Lynch, S. et al. "Fabrication of 200 nm period centimeter area hard x-ray absorption gratings by multilayer deposition". *Journal of Micromechanics and Microengineering* **22**.10 (2012), p. 105007.

[Mah89]   Maheswaran, S. "Dynamical theory of neutron diffraction for perfect crystals with and without strain gradients". PhD thesis. Theses (Dept. of Physics)/Simon Fraser University, 1989.

[MW76]   Mair, S. & Wilkins, S. "Anharmonic Debye-Waller factors using quantum statistics". *Journal of Physics C: Solid State Physics* **9**.7 (1976), p. 1145.

[Mar12]   Martin, A. V. et al. "Noise-robust coherent diffractive imaging with a single diffraction pattern". *Optics Express* **20**.15 (2012), pp. 16650–16661.

[Mia16]   Miao, H. et al. "A universal moiré effect and application in X-ray phase-contrast imaging". *Nature physics* **12**.9 (2016), pp. 830–834.

[MT15]   Murata, J. & Tanaka, S. "A review of short-range gravity experiments in the LHC era". *Classical and Quantum Gravity* **32**.3 (2015), p. 033001.

[Nag11]   Nagy, G. et al. "Reversible membrane reorganizations during photosynthesis in vivo: revealed by small-angle neutron scattering". *Biochemical Journal* **436**.2 (2011), pp. 225–230.

[Nes02]   Nesvizhevsky, V. V. et al. "Quantum states of neutrons in the Earth's gravitational field". *Nature* **415**.6869 (2002), p. 297.

[New82]   Newman, R. "Defects in silicon". *Reports on Progress in Physics* **45**.10 (1982), p. 1163.

[Nic09]   Nico, J. S. "Neutron beta decay". *Journal of Physics G: Nuclear and Particle Physics* **36**.10 (2009), p. 104001.

[Ncn]   *NIST Center for Neutron Research Instrument Layout.* https://www.nist.gov/ncnr/neutron-instruments/general-info-and-layout.

[PR84]   Petrascheck, D & Rauch, H. "Multiple Laue rocking curves". *Acta Crystallographica Section A: Foundations of Crystallography* **40**.4 (1984), pp. 445–450.

[Pok13]   Pokotilovski, Y. N. "Strongly coupled chameleon fields: Possible test with a neutron LloydÊijs mirror interferometer". *Physics Letters B* **719**.4 (2013), pp. 341–345.

[Pot15]   Potocar, T. et al. "Neutron interferometric measurement and calculations of a phase shift induced by Laue transmission". *Acta Crystallographica Section A: Foundations and Advances* **71**.5 (2015), pp. 534–541.

[Pus06]   Pushin, D. et al. "Reciprocal space neutron imaging". *Physica B: Condensed Matter* **385** (2006), pp. 1402–1404.

[Pus07]   Pushin, D. et al. "Reciprocal space approaches to neutron imaging". *Applied physics letters* **90**.22 (2007), p. 224104.

[Pus15]   Pushin, D. et al. "Neutron interferometry at the National Institute of Standards and Technology". *Advances in High Energy Physics* **2015** (2015).

[Pus17a]   Pushin, D. et al. "Far-field interference of a neutron white beam and the applications to noninvasive phase-contrast imaging". *Physical Review A* **95**.4 (2017), p. 043637.

[Pus18]   Pushin, D. personal communication. 2018.

[Pus17b]   Pushin, D. A. et al. "Far-field interference of a neutron white beam and the applications to noninvasive phase-contrast imaging". *Physical Review A* **95**.4 (2017), p. 043637.

[RW15]   Rauch, H. & Werner, S. A. *Neutron Interferometry: Lessons in Experimental Quantum Mechanics, Wave-particle Duality, and Entanglement.* Vol. 12. Oxford University Press, 2015.

[Rob74]   Roberto, J. et al. "Diffraction studies of the (222) reflection in Ge and Si: Anharmonicity and the bonding electron". *Physical Review B* **9**.6 (1974), p. 2590.

[Rod13]   Rodriguez, J. A. et al. "Oversampling smoothness: an effective algorithm for phase retrieval of noisy diffraction intensities". *Journal of applied crystallography* **46**.2 (2013), pp. 312–318.

[Sag16]   Saggu, P. et al. "Decoupling of a neutron interferometer from temperature gradients". *Review of Scientific Instruments* **87**.12 (2016), p. 123507.

[SN11]   Sakuraiiii, J. & Napolitano, J. *Modern Quantum Mechanics, 2nd Ed.* Addison Wesley, 2011.

[Sar18]   Sarenac, D et al. "Three Phase-Grating Moiré Neutron Interferometer for Large Interferometer Area Applications". *Physical review letters* **120**.11 (2018), p. 113201.

[Sea78]   Sears, V. F. "Dynamical theory of neutron diffraction". *Canadian Journal of Physics* **56**.10 (1978), pp. 1261–1288.

[Sea86]   Sears, V. F. "Electromagnetic neutron-atom interactions". *Physics Reports* **141**.5 (1986), pp. 281–317.

[Sea89]   Sears, V. F. *Neutron optics: an introduction to the theory of neutron optical phenomena and their applications.* Vol. 3. Oxford University Press, USA, 1989.

[Sea97a]   Sears, V. "Bragg reflection in mosaic crystals. I. General solution of the Darwin equations". *Acta Crystallographica Section A* **53**.1 (1997), pp. 35–45.

[Sea97b]   Sears, V. "Bragg reflection in mosaic crystals. II. Neutron monochromator properties". *Acta Crystallographica Section A: Foundations of Crystallography* **53**.1 (1997), pp. 46–54.

[Sha16]   Shahi, C. et al. "A new polarized neutron interferometry facility at the NCNR". *Nuclear Instruments and Methods in Physics Research Section A: Accelerators, Spectrometers, Detectors and Associated Equipment* **813** (2016), pp. 111–122.

[She15]   Shechtman, Y. et al. "Phase retrieval with application to optical imaging: a contemporary overview". *IEEE signal processing magazine* **32**.3 (2015), pp. 87–109.

[Shu68]   Shull, C. "Observation of Pendellösung fringe structure in neutron diffraction". *Physical Review Letters* **21**.23 (1968), p. 1585.

[SO72]   Shull, C. & Oberteuffer, J. "Spherical-wave neutron propagation and Pendellösung fringe structure in silicon". *Physical Review Letters* **29**.13 (1972), p. 871.

[SS73]   Shull, C. & Shaw, W. "Neutron Pendellösung fringe structure in the Laue diffraction by germanium". *Zeitschrift für Naturforschung A* **28**.5 (1973), pp. 657–661.

[Shu80]   Shull, C. et al. "Search for a nonlinear variant of the Schrödinger equation by neutron interferometry". *Physical Review Letters* **44**.12 (1980), p. 765.

[Sie11]   Siegel, J. B. et al. "Neutron imaging of lithium concentration in LFP pouch cell battery". *Journal of the Electrochemical Society* **158**.5 (2011), A523–A529.

[Sip65]   Sippel, D et al. "Pendellösungs-Interferenzen mit thermischen neutronen an Si-Einkristallen". *Physics Letters* **14** (1965), pp. 174–175.

[Som78]   Somenkov, V. et al. "Observation of dynamical oscillations for neutron scattering by Ge crystals using the inclination method". *Solid State Communications* **25**.8 (1978), pp. 593–595.

[Spa86]   Spackman, M. "The electron distribution in silicon. A comparison between experiment and theory". *Acta Crystallographica Section A* **42**.4 (1986), pp. 271–281.

[SL02]   Sparenberg, J.-M. & Leeb, H. "Neutron charge radius deduced from Bragg reflection technique". *Physical Review C* **66**.5 (2002), p. 055210.

[SL03]   Sparenberg, J.-M. & Leeb, H. "Neutron–electron scattering length deduced from Pendellösung interferometry in neutron Bragg reflections on silicon". *Journal of electron spectroscopy and related phenomena* **129**.2 (2003), pp. 315–317.

[Spr09]   Springer, J et al. "A neutron interferometric measurement of a phase shift induced by Laue transmission". *Acta Crystallographica Section A: Foundations of Crystallography* **66**.1 (2009), pp. 17–21.

[Str04]   Strobl, M et al. "Small angle scattering signals for (neutron) computerized tomography". *Applied Physics Letters* **85**.3 (2004), pp. 488–490.

[Str07]   Strobl, M et al. "The new V12 ultra-small-angle neutron scattering and tomography instrument at the Hahn–Meitner Institut". *Applied Crystallography* **40**.s1 (2007), s463–s465.

[Str08]   Strobl, M et al. "Neutron dark-field tomography". *Physical review letters* **101**.12 (2008), p. 123902.

[Str09]   Strobl, M et al. "Advances in neutron radiography and tomography". *Journal of Physics D: Applied Physics* **42**.24 (2009), p. 243001.

[Tan18]   Tanabashi, M. et al. "Review of particle physics". *Physical Review D* **98**.3 (2018), p. 1654.

[TK72]   Tanemura, S & Kato, N. "Absolute measurement of structure factors of Si by using X-ray Pendellösung and interferometry fringes". *Acta Crystallographica Section A: Crystal Physics, Diffraction, Theoretical and General Crystallography* **28**.1 (1972), pp. 69–80.

[TB84]   Teworte, R & Bonse, U. "High-precision determination of structure factors F h of silicon". *Physical Review B* **29**.4 (1984), p. 2102.

[Tre03]   Treimer, W et al. "Refraction as imaging signal for computerized (neutron) tomography". *Applied physics letters* **83**.2 (2003), pp. 398–400.

[Vor09]   Voronin, V. et al. "Neutron diffraction test on spin-dependent short range interaction". *JETP letters* **90**.1 (2009), pp. 5–7.

[WM17]   Wahlberg, N. & Madsen, A. Ø. "Implications of X-ray thermal diffuse scattering in integrated Bragg intensities of silicon and cubic boron nitride". *Journal of Applied Crystallography* **50**.6 (2017), pp. 1791–1799.

[Wer88]   Werner, S. et al. "Neutron interference induced by gravity: new results and interpretations". *Physica B+ C* **151**.1 (1988), pp. 22–35.

[Wer80]   Werner, S. A. "Gravitational and magnetic field effects on the dynamical diffraction of neutrons". *Physical Review B* **21**.5 (1980), p. 1774.

[Wer75]   Werner, S. A. et al. "Observation of the phase shift of a neutron due to precession in a magnetic field". *Physical Review Letters* **35**.16 (1975), p. 1053.

[Wie06]   Wietfeldt, F. et al. "Measuring the neutron's mean square charge radius using neutron interferometry". *Physica B: Condensed Matter* **385** (2006), pp. 1374–1376.

[Wil12]   Williams, S. et al. "Detection system for microimaging with neutrons". *Journal of Instrumentation* **7**.02 (2012), P02014.

[Wil69]   Willis, B. "Lattice vibrations and the accurate determination of structure factors for the elastic scattering of X-rays and neutrons". *Acta Crystallographica Section A: Crystal Physics, Diffraction, Theoretical and General Crystallography* **25**.2 (1969), pp. 277–300.

[Wil70]   Willis, B. "The correction of measured neutron structure factors for thermal diffuse scattering". *Acta Crystallographica Section A: Crystal Physics, Diffraction, Theoretical and General Crystallography* **26**.4 (1970), pp. 396–401.

[Woo14]   Wood, C. J. et al. "Quantum correlations in a noisy neutron interferometer". *Phys. Rev. A* **90** (3 2014), p. 032315.

[Zaw10]   Zawisky, M et al. "A large-area perfect crystal neutron interferometer optimized for coherent beam-deflection experiments: Preparation and performance". *Nuclear Instruments and Methods in Physics Research Section A: Accelerators, Spectrometers, Detectors and Associated Equipment* **612**.2 (2010), pp. 338–344.

[Zee04]   Zee, A. "Dark energy and the nature of the graviton". *Physics Letters B* **594**.1-2 (2004), pp. 8–12.

[ZS79]   Zeilinger, A & Shull, C. "Magnetic field effects on dynamical diffraction of neutrons by perfect crystals". *Physical Review B* **19**.8 (1979), p. 3957.

[Zha11]   Zhang, H. et al. "Three-dimensional bicontinuous ultrafast-charge and-discharge bulk battery electrodes". *Nature nanotechnology* **6**.5 (2011), p. 277.

[Zou00]   Zouw, G Van der et al. "Aharonov–Bohm and gravity experiments with the very-cold-neutron interferometer". *Nuclear Instruments and Methods in Physics Research Section A: Accelerators, Spectrometers, Detectors and Associated Equipment* **440**.3 (2000), pp. 568–574.

APPENDICES

APPENDIX A

RECURSION FORMULAE FOR PERIODIC POTENTIALS

A.1 Phase Profile and Wave Amplitudes

What follows is the recursion formula for relating the diffracted wave amplitudes a_n to the Fourier coefficients ϕ_n of a periodic phase shifter. Begin with the Fourier transform of the phase profile,

$$\widetilde{\phi} \equiv \mathcal{F}\{\phi(\vec{x})\}, \tag{A.1}$$

then take

$$\widetilde{\psi}_{\text{out}} = \sum_{m=0}^{\infty} \frac{(-i)^m}{m!} \left[\widetilde{\phi}*\right]^m \widetilde{\psi}_{\text{in}}. \tag{A.2}$$

Expanding $\phi(\vec{x})$ as a complex Fourier series gives

$$\phi(\vec{x}) = \sum_{n=-\infty}^{\infty} a_n e^{in\vec{q}_0 \cdot \vec{x}} \tag{A.3}$$

where

$$\vec{q}_0 = \frac{2\pi}{\lambda_G} \hat{g} \tag{A.4}$$

is the magnitude $2\pi/\lambda_G$ and direction $\hat{g}$ of the first-order grating diffraction peak, and a_n are the complex Fourier coefficients. In general, $a_n = a_{-n}^*$, and the phase of a_n gives the position coordinate of the grating. i.e. if I let $\vec{x} \to \vec{x} + \vec{x}_0$ then I added a phase on the a_n. Note that this function is still manifestly real. It is nice to do it in this way, because if I leave this function as a complex Fourier

167

series, it will be easier to see how one can get an asymmetry in the positive and negative first-order diffracted peaks. Now,

$$\widetilde{\phi}(\vec{q}) = \sum a_n \delta^3 \left(\vec{q} - n\vec{q}_0\right), \tag{A.5}$$

and

$$\widetilde{\phi} * \widetilde{\phi} = \sum_{n,m} a_n a_m \delta^3 \left(\vec{q} - (n+m)\vec{q}_0\right). \tag{A.6}$$

In hopes of getting back to $\widetilde{\psi}_{\text{out}}$ via Eqn. A.2,

$$\left[\widetilde{\phi}*\right]^{m-1} \widetilde{\phi} = \sum_{n_1, n_2, \ldots, n_m} \left(\prod_{i=1}^{m} a_{n_i}\right) \delta^3 \left(\vec{q} - \vec{q}_0 \sum_{i=1}^{m} n_i\right) \tag{A.7}$$

which, convolved with $\widetilde{\psi}_{\text{in}}$ gives

$$\left[\widetilde{\phi}*\right]^{m} \widetilde{\psi}_{\text{in}} = \sum_{n_1, n_2, \ldots, n_m} \left(\prod_{i=1}^{m} a_{n_i}\right) \widetilde{\psi}_{\text{in}} \left(\vec{k} - \vec{q}_0 \sum_{i=1}^{m} n_i\right). \tag{A.8}$$

This indicates that

$$\widetilde{\psi}_{\text{out}}\left(\vec{k}\right) = \sum_{n} A_n \widetilde{\psi}_{\text{in}}\left(\vec{k} - \vec{q}_0 n\right). \tag{A.9}$$

The only thing left to do is to relate the A_n coefficients back to the a_n coefficients. I can do this in the following way. Start by rewriting Eqn A.2 as

$$\widetilde{\psi}_{\text{out}}\left(\vec{k}\right) = \sum_{n,m} \frac{(-i)^m}{m!} A_n^m \widetilde{\psi}_{\text{in}}\left(\vec{k} - \vec{q}_0 n\right), \tag{A.10}$$

thus

$$\left[\widetilde{\phi}*\right]^{m} \widetilde{\psi}_{\text{in}} = \sum_{n} A_n^m \widetilde{\psi}_{\text{in}}\left(\vec{k} - \vec{q}_0 n\right) \tag{A.11}$$

and

$$A_n = \sum_{m} \frac{(-i)^m}{m!} A_n^m. \tag{A.12}$$

All that is left to do is to write A_n^m in terms of a_n. First, note that

168

$$\left[\widetilde{\phi}*\right]^m \widetilde{\psi}_{\text{in}} = \left[\widetilde{\phi}*\right]^{m-1} \widetilde{\phi} * \widetilde{\psi}_{\text{in}} = \left[\widetilde{\phi}*\right]^{m-1} \sum_\ell A_\ell^1 \widetilde{\psi}_{\text{in}} \left(\vec{k} - \vec{q}_0 \ell\right) = \sum_{\ell,r} A_r^{m-1} A_\ell^1 \widetilde{\psi} \left(\vec{k} - \vec{q}_0(\ell + r)\right)$$

(A.13)

thus

$$A_n^m = \sum_{\ell,r} A_r^{m-1} A_\ell^1 \delta_{\ell+r,n} = \sum_\ell A_{n-\ell}^{m-1} A_\ell^1$$

(A.14)

I can start with

$$A_n^0 = \delta_{n,0}$$

(A.15)

which immediately gives

$$A_n^1 = a_n$$

(A.16)

such that finally

$$A_n^m = \sum_\ell A_{n-\ell}^{m-1} a_\ell.$$

(A.17)

Fortunately, the a_ℓ tend to fall off rapidly with increasing ℓ so the sum need not be taken to infinity. Because $A_n^m \sim (a_n)^m$, the A_n^m should also fall off as n increases. How many A_n^m one must compute with respect to m depends on the overall magnitude of the phase / thickness of the grating.

Consider taking the modulus square of $\widetilde{\psi}_{\text{out}}$

$$\left|\widetilde{\psi}_{\text{out}}\left(\vec{k}\right)\right|^2 = \sum_{n,m} A_n^* A_m \widetilde{\psi}_{\text{in}}^* \left(\vec{k} - \vec{q}_0 n\right) \widetilde{\psi}_{\text{in}} \left(\vec{k} - \vec{q}_0 m\right)$$

(A.18)

At first it would seem I have to do another set of mixing up my A_n coefficients to find the relative peak amplitudes. However, consider that I must average over a set of phases in the a_n based on the grating translation relative to the wave packet's $\langle\vec{x}\rangle$. Alternatively if I translate the diffracted wave packet $\vec{\Delta x}$, I get $\widetilde{\psi}_{\text{in}} \to \widetilde{\psi}_{\text{in}} e^{i\vec{k}\cdot\vec{\Delta x}}$ and Eqn. A.18 becomes

$$\left|\widetilde{\psi}_{\text{out}}\left(\vec{k}\right)\right|^2 = \sum_{n,m} A_n^* A_m \widetilde{\psi}_{\text{in}}^* \left(\vec{k} - \vec{q}_0 n\right) \widetilde{\psi}_{\text{in}} \left(\vec{k} - \vec{q}_0 m\right) e^{i\vec{q}_0\cdot\vec{\Delta x}(m-n)}$$

(A.19)

which because of the $a_n = a_{-n}^*$ symmetry is still real. Note, however, that $A_n \neq A_{-n}^*$ is how an asymmetry in the first-order diffracted peaks can arise. Neutrons are detected over a large set of $\vec{\Delta x}$ that is much larger than the grating period. Thus, after averaging over $\vec{\Delta x}$ Eqn. A.18 becomes

$$\left|\widetilde{\psi}_{\text{out}}\left(\vec{k}\right)\right|^2 = \sum_n |A_n|^2 \left|\widetilde{\psi}_{\text{in}}\left(\vec{k}-\vec{q}_0 n\right)\right|^2 \tag{A.20}$$

and for a neutron source with a set of wave packets averaged over a large range of $\vec{\Delta}x$, I can identify $|A_n|^2$ as the measurexd, n^{th}-order peak amplitudes.

In summary, with $|A_n|^2$ the peak amplitude, and a_n the Fourier coefficients for the grating of period λ_G, may be computed using the recursion formulae

$$\left|\widetilde{\psi}_{\text{out}}\left(\vec{k}\right)\right|^2 = \sum_n |A_n|^2 \left|\widetilde{\psi}_{\text{in}}\left(\vec{k}-\vec{q}_0 n\right)\right|^2$$

$$A_n = \sum_m \frac{(-i)^m}{m!} A_n^m$$

$$A_n^m = \sum_\ell A_{n-\ell}^{m-1} a_\ell$$

$$A_n^0 = \delta_{n,0}$$

.

A.2 Square Wave Exact Solution

To demonstrate the result from the previous section, I will perform the test case of a square wave. Consider the phase profile of a square wave:

$$\phi(\vec{x}) = \frac{\phi_0}{2}\left[\frac{4}{\pi}\sum_{n \text{ odd}} \frac{e^{i\vec{q}_0 \cdot \vec{x}}}{n2i}\right] \tag{A.21}$$

This is a square wave with amplitude $\phi_0/2$, so that the portion is brackets is a square wave with amplitude ± 1. Consider taking $\phi(\vec{x})$ to an integer power:

$$(\phi(\vec{x}))^n = \begin{cases} \left(\frac{\phi_0}{2}\right)^n \left[\frac{4}{\pi}\sum_{n \text{ odd}} \frac{e^{in\vec{q}_0 \cdot \vec{x}}}{n2i}\right], & n \text{ odd} \\ \left(\frac{\phi_0}{2}\right)^n, & n \text{ even} \end{cases} \tag{A.22}$$

This allows me to write:

$$e^{-i\phi(\vec{x})} = \cos\left(\frac{\phi_0}{2}\right) - i\sin\left(\frac{\phi_0}{2}\right)\left[\frac{4}{\pi}\sum_{n\text{ odd}}\frac{e^{i\vec{q_0}\cdot\vec{x}}}{n2i}\right] \tag{A.23}$$

and the resulting momentum space outgoing wavefunction

$$\widetilde{\psi}_{\text{out}}\left(\vec{k}\right) = \cos\left(\frac{\phi_0}{2}\right)\widetilde{\psi}_{\text{in}}\left(\vec{k}\right) - \sin\left(\frac{\phi_0}{2}\right)\left[\frac{2}{\pi}\sum_{n\text{ odd}}\frac{1}{n}\widetilde{\psi}_{\text{out}}\left(\vec{k} - \vec{q_0}n\right)\right] \tag{A.24}$$

Now, compare this to a derivation using the results from the last section. I will start with

$$A_n^1 = \frac{\phi_0}{in\pi}, \quad n\text{ odd} \tag{A.25}$$

Then forming

$$A_n^2 = \sum_\ell A_{n-\ell}^1 A_\ell^1 = \left(\frac{\phi_0}{i\pi}\right)^2 \sum_{\ell\text{ odd}}\left(\frac{1}{n-\ell}\right)\left(\frac{1}{\ell}\right)\delta_{n-\ell,\text{ odd}} \tag{A.26}$$

If $(n-\ell)$ must be odd and ℓ must be odd, n must also be even. Rewriting this slightly, and combing the positive and negative parts of the summation over ℓ

$$A_n^2 = \left(\frac{\phi_0}{i\pi}\right)^2\sum_{\ell=1,3,...}\left(\frac{1}{(n-\ell)\ell} - \frac{1}{(n+\ell)\ell}\right)\delta_{n,\text{ even}} = 2\left(\frac{\phi_0}{i\pi}\right)^2\sum_{\ell=1,3,...}\left(\frac{1}{n^2-\ell^2}\right)\delta_{n,\text{ even}} \tag{A.27}$$

I need the following identity:

$$\sum_{\ell=1,3,...}\left(\frac{1}{n^2-\ell^2}\right) = -\left(\frac{\pi\tan\left(\frac{n\pi}{2}\right)}{4n}\right) = \begin{cases} -\frac{\pi^2}{8}, & n=0 \\[2mm] 0, & n\text{, even} \\[2mm] \pm\infty, & n\text{, odd} \end{cases} \tag{A.28}$$

Putting this back into my expression for A_n^2

$$A_n^2 = \left(\frac{\phi_0}{2}\right)^2\delta_{n,0} \tag{A.29}$$

Now, using A_n^2 and A_n^1 to form A_n^3, all I must do is note that

$$A_n^2 = \left(\frac{\phi_0}{2}\right)^2 A_n^0 \tag{A.30}$$

which implies

$$A_n^3 = \left(\frac{\phi_0}{2}\right)^2 A_n^1 \tag{A.31}$$

thus for a square wave:

$$A_n^m = \left(\frac{\phi_0}{2}\right)^m \times \begin{cases} \delta_{n,0}, & m \text{ even} \\ \\ \left(\frac{2}{in\pi}\right)\delta_{n,\,\text{odd}}, & m \text{ odd} \end{cases} \tag{A.32}$$

Putting this result into Eqn. A.10

$$\widetilde{\psi}_{\text{out}}\left(\vec{k}\right) = \sum_{m=0,2,\dots} \frac{1}{m!}\left(-\frac{i\phi_0}{2}\right)^m \widetilde{\psi}_{\text{in}}\left(\vec{k}\right) + \sum_{m=1,3,\dots} \frac{1}{m!}\left(-\frac{i\phi_0}{2}\right)^m \left[\frac{2}{i\pi}\sum_{n,\,\text{odd}}\frac{1}{n}\widetilde{\psi}_{\text{in}}\left(\vec{k}-\vec{q_0}n\right)\right]$$

$$= \cos\left(\frac{\phi_0}{2}\right)\widetilde{\psi}_{\text{in}}\left(\vec{k}\right) - \sin\left(\frac{\phi_0}{2}\right)\left[\frac{2}{\pi}\sum_{n,\,\text{odd}}\frac{1}{n}\widetilde{\psi}_{\text{in}}\left(\vec{k}-\vec{q_0}n\right)\right] \tag{A.33}$$

which matches Eqn. A.24.

DYNAMICAL PHASE CALCULATIONS

B.1 Mach-Zehnder Geometry Calculations

Following previous work [Bon77; PR84; Wer88; Lit98], but generalizing to let there be three separate misalignments $\{u, v, w\}$, gives

$$\langle \mathrm{I}|\mathrm{I}\rangle = \pi \left[8\frac{J_1(v-w)}{u-w} - 12\frac{J_2(v-w)}{(v-w)^2} - 12\frac{J_2(v)}{v^2} - 12\frac{J_2(w)}{w^2} + 5 \right] \tag{B.1}$$

$$\langle \mathrm{II}|\mathrm{II}\rangle = \pi \left[8\frac{J_1(u)}{u} - 12\frac{J_2(u-w)}{(u-w)^2} - 12\frac{J_2(u)}{u^2} - 12\frac{J_2(w)}{w^2} + 5 \right] \tag{B.2}$$

$$\mathrm{Im}\left[\langle \mathrm{I}|\mathrm{II}\rangle\right] = 4\pi \left[\frac{J_2\left(\frac{u+v}{2}\right)}{\frac{u+v}{2}} - \frac{J_2\left(\frac{u-v}{2}-w\right)}{\frac{u-v}{2}-w} + \frac{J_2\left(\frac{u-v}{2}+w\right)}{\frac{u-v}{2}+w} - \frac{J_2\left(\frac{u+v}{2}-w\right)}{\frac{u+v}{2}-w} \right] \tag{B.3}$$

$$\mathrm{Re}\left[\langle \mathrm{I}|\mathrm{II}\rangle\right] = 2\pi \left[4\frac{J_1\left(\frac{u-v}{2}\right)}{\frac{u-v}{2}} - 12\frac{J_2\left(\frac{u-v}{2}\right)}{\left(\frac{u-v}{2}\right)^2} + 2\frac{J_1\left(\frac{u+v}{2}\right)}{\frac{u+v}{2}} - 6\frac{J_2\left(\frac{u+v}{2}\right)}{\left(\frac{u+v}{2}\right)^2} + 2\frac{J_1\left(\frac{u-v}{2}-w\right)}{\frac{u-v}{2}-w} + \right.$$
$$\left. -3\frac{J_2\left(\frac{u-v}{2}-w\right)}{\left(\frac{u-v}{2}-w\right)^2} + 2\frac{J_1\left(\frac{u+v}{2}-w\right)}{\frac{u+v}{2}-w} - 6\frac{J_2\left(\frac{u+v}{2}-w\right)}{\left(\frac{u+v}{2}-w\right)^2} + 2\frac{J_1\left(\frac{u-v}{2}+w\right)}{\frac{u-v}{2}+w} - 3\frac{J_2\left(\frac{u-v}{2}+w\right)}{\left(\frac{u-v}{2}+w\right)^2} \right] \tag{B.4}$$

for the 0 Beam. The phase and contrast of a regular interferogram can then be extracted by inserting these expressions into Equations 3.16 and 3.17.

B.2 Rocking Curve Fine Structure

Estimating Equation 3.9 in terms of a set of parameters, $\left\{ HD\delta, \frac{D|v_H|}{k_\zeta}, \frac{\sigma_{k\zeta}}{k_\zeta}, \frac{(D_2 - D_1)|v_H|}{k_\zeta} \right\} = \{\mu, \Delta, \sigma, \epsilon\}$ corresponds to integrals of the form

$$\mathcal{I} = \int d\Gamma \sqrt{1 - \Gamma^2} \cos(\mu\Gamma) \cos\left(\frac{\Delta}{\sqrt{1 - \Gamma^2}} \right). \tag{B.5}$$

Because the blades of the interferometer are nearly the same thickness, the $P(D_2 - D_1)$ term in Equation 3.9 can be expanded in terms of $\Delta \to \epsilon$

$$\mathcal{I} = \int d\Gamma \sqrt{1 - \Gamma^2} \cos(\mu\Gamma) \left(1 - \frac{\epsilon^2}{2(1 - \Gamma^2)} + \mathcal{O}(\epsilon^4) \right) = \pi \left(\frac{J_1(\mu)}{\mu} - \frac{\epsilon^2}{2} J_0(\mu) + \mathcal{O}(\epsilon^4) \right). \tag{B.6}$$

This approximation is found to have an error of less than 0.5% of the peak maximum for $\epsilon = 0.2$ and any value of μ. The $P(D)$ terms in Eqn. 3.9, on the other hand, are extremely oscillatory, so I integrate over $\langle \psi | k_\zeta \rangle \langle k_\zeta | \psi \rangle$ and use a stationary phase method, similar to [Kat61a; Kat61b]. In this case, is better to integrate over η than Γ:

$$\mathcal{I} = \mathrm{Re}\left\{ \int d\eta \, \exp\left[i\mu \frac{\eta}{\eta^2 + 1} + i\Delta\sqrt{\eta^2 + 1} - \frac{1}{2}(\eta^2 + 1)\Delta^2\sigma^2 - 2\log\left(\eta^2 + 1\right) \right] \right\}. \tag{B.7}$$

I can then expand the argument of the exponential, $f(\eta)$, around η_0 which should be close to a minimum of $f(\eta)$. To avoid having to numerically find η_0, I will neglect terms η_0^2 and higher in $f^{(1)}(\eta_0) = 0$, which gives

$$\eta_0 = \frac{i\mu}{\Delta^2\sigma^2 - i\Delta + 4}. \tag{B.8}$$

To compute the integral in the stationary phase approximation, terms in the argument of the exponential of $(\eta - \eta_0)^3$ and higher are neglected, and the integral is completed as Gaussian

$$\mathcal{I} = \mathrm{Re}\left\{ \sqrt{2\pi} \frac{\exp\left[f(\eta_0) - \frac{f^{(1)}(\eta_0)^2}{2f^{(2)}(\eta_0)} \right]}{\sqrt{-f^{(2)}(\eta_0)}} \right\}. \tag{B.9}$$

This function is found to have an error of less that 0.5% of the peak value over the relevant ranges of $\{\mu, \Delta, \sigma\}$.

B.3 Special Functions

A list of closed form solutions for the integrals giving the peak structure of the interferometer are given here.

$$I_0 = \int_{-1}^{1} d\Gamma \ \sqrt{1-\Gamma^2} \cos\left(HD\delta\Gamma\right) = \pi \frac{J_1(HD\delta)}{HD\delta} \tag{B.10}$$

$$I_2 = \int_{-1}^{1} d\Gamma \ \Gamma^2 \sqrt{1-\Gamma^2} \cos\left(HD\delta\Gamma\right) = \pi \frac{J_2(HD\delta)}{(HD\delta)^2} - \pi \frac{J_3(HD\delta)}{HD\delta} \tag{B.11}$$

$$I_4 = \int_{-1}^{1} d\Gamma \ \Gamma^2 \sqrt{1-\Gamma^2} \cos\left(HD\delta\Gamma\right) = \pi(3 - (HD\delta)^2) \frac{J_3(HD\delta)}{(HD\delta)^3} + 2\pi \frac{J_4(HD\delta)}{(HD\delta)^2} \tag{B.12}$$

$$I_D = \int_{-1}^{1} d\Gamma \ \frac{\cos\left(HD\delta\Gamma\right)}{\sqrt{1-\Gamma^2}} = \pi J_0(HD\delta) \tag{B.13}$$

where $J_n(x)$ is the nth Bessel function of the first kind.

B.4 Beam Profile Green's Functions

The Green's function describing the Borrmann fan after two perfect successive Bragg diffracting crystals in the Laue geometry is [RW15]

$$G_{2\text{P}}(x', x) = \frac{1}{2}(1 + C)\delta\left(\frac{x'-x}{D\sin\theta_B}\right) + \frac{1}{2\pi}\text{Re}\left\{\sqrt{1 - \left(\frac{x'-x}{2D\sin\theta_B}\right)^2}\right\}, \tag{B.14}$$

where D is the crystal thickness; θ_B is the Bragg angle; and x and x' are the transverse beam coordinates at the entrance and exit faces of the crystal, respectively. I have also normalized the expression given in [RW15], so that the integral of $G_{2\text{P}}(x', x)$ over all $x' - x$ is unity. The constant C depends on the alignment of the Bragg planes of the two crystals. For two aligned crystals $C = A/B$, where A and B are the central peak amplitude and background, respectively.

Consider an empirical Green's function for spurious reflections from the crystal surfaces, where the reflectivity of the crystal is highest at the surfaces and falls off at some length scale λ

$$G_{1\text{S}}(x', x, \lambda) = \lambda \left(e^{-\frac{x'-x+D\sin\theta_B}{\lambda}} + e^{\frac{x'-x-D\sin\theta_B}{\lambda}} \right) \Theta\left[D^2 \sin^2\theta_B - (x'-x)^2 \right], \tag{B.15}$$

Note that I have also normalized this expression. Forming the Green's function after two crystals gives

$$G_{2S}(x'', x, \lambda) = \int dx' \, G_1(x'', x', \lambda) G_1(x', x, \lambda), \tag{B.16}$$

which does have a closed form solution. I can then write the whole Green's function

$$G_{\text{tot}}(x', x) = G_{2P}(x', x) + R \, G_{2S}(x', x). \tag{B.17}$$

Note that R gives the reflectivity of the surface, relative to the crystal bulk and λ is the depth of higher-reflectivity crystallographic material. The beam profile can then be fit to

$$\mathcal{I}(x) = G_{\text{tot}} * \mathcal{I}_i \tag{B.18}$$

where $*$ is the convolution operator at $\mathcal{I}_i$ is the incoming beam's shape with some parameterization. For the NIOF beamline, $\mathcal{I}_i(x)$ is the convolution of a Gaussian of width σ_x with the incoming slit of width S

$$\mathcal{I}_i(x, \sigma_x, S) = \frac{1}{2} \left[\text{Erf} \left(\frac{\frac{S}{2} - x}{\sigma_x \sqrt{2}} \right) + \text{Erf} \left(\frac{\frac{S}{2} + x}{\sigma_x \sqrt{2}} \right) \right] \tag{B.19}$$